Jānis Braunfelds

DAUDZFUNKCIONĀLAS ŠĶIEDRU OPTISKO SENSORU SISTĒMAS IZVEIDE UN PIELIETOJUMS UZRAUDZĪBAS RISINĀJUMIEM

Promocijas darbs

RĪGAS TEHNISKĀ UNIVERSITĀTE
Elektronikas un telekomunikāciju fakultāte
Telekomunikāciju institūts

Jānis Braunfelds

Doktora studiju programmas „Telekomunikācijas" doktorants

Daudzfunkcionālas šķiedru optisko sensoru sistēmas izveide un pielietojums uzraudzības risinājumiem

Promocijas darbs

Zinātniskie vadītāji:
prof. *Dr. sc. ing.* VJAČESLAVS BOBROVS
prof. *Dr. sc. ing.* JURĢIS PORIŅŠ

Rīga 2023

INDUSTRIĀLAIS DOKTORANTS

1862

RĪGAS TEHNISKĀ UNIVERSITĀTE

lmt

RTU studentu inovāciju granti

NACIONĀLAIS ATTĪSTĪBAS PLĀNS 2020

EIROPAS SAVIENĪBA
Eiropas Reģionālās attīstības fonds

I E G U L D Ī J U M S   T A V Ā   N Ā K O T N Ē

PROMOCIJAS DARBS IZVIRZĪTS ZINĀTNES DOKTORA GRĀDA IEGŪŠANAI RĪGAS TEHNISKAJĀ UNIVERSITĀTĒ

Promocijas darbs zinātnes doktora (*Ph. D.*) grāda iegūšanai tiek publiski aizstāvēts 2023. gada 2. jūnijā Rīgas Tehniskās universitātes Elektronikas un telekomunikāciju fakultātē, Rīgā, Āzenes ielā 12, 201. auditorijā.

APSTIPRINĀJUMS

Apstiprinu, ka esmu izstrādājis šo promocijas darbu, kas iesniegts izskatīšanai Rīgas Tehniskajā universitātē zinātnes doktora (*Ph. D.*) grāda iegūšanai. Promocijas darbs zinātniskā grāda iegūšanai nav iesniegts nevienā citā universitātē.

Jānis Braunfelds ＿＿＿＿＿＿＿＿＿＿＿＿＿＿．

Datums: ＿＿＿．＿＿＿．＿＿＿．

Promocijas darbs sagatavots kā tematiski vienotu zinātnisko publikāciju kopa ar kopsavilkumu latviešu un angļu valodā. Promocijas darbs ir uzrakstīts latviešu, tajā ir ievads, 3 nodaļas, secinājumi, literatūras saraksts, 39 attēli, 5 tabulas, 11 pielikumi, kopā 70 lappuses, neieskaitot pielikumus. Literatūras sarakstā ir 203 nosaukumi. Promocijas darbs apkopo 10 zinātniskos oriģinālrakstus no autoram 19 esošiem, vienu Latvijas Republikas patentu. Zinātniskās publikācijas uzrakstītas angļu valodā un ir indeksētas SCOPUS, IEEE vai WoS datubāzēs, to kopējais apjoms ir 100 lpp. Patents uzrakstīts latviešu valodā, tā apjoms ir 10 lpp.

DOKUMENTS IR PARAKSTĪTS AR DROŠU ELEKTRONISKU PARAKSTU UN SATUR LAIKA ZĪMOGU

Pateicība

Vēlos pateikties promocijas darba vadītājiem profesoram Vjačeslavam Bobrovam un profesoram Jurģim Poriņam, un RTU ETF Telekomunikāciju institūta Sakaru sistēmu Tehnoloģiju izpētes centra vadītājam profesoram Sandim Spolītim par sniegto atbalstu un padomiem promocijas darba izstrādes gaitā.

Strādājot RTU, ETF Telekomunikāciju institūtā par pētnieku, man bija iespēja sadarboties ar daudziem talantīgiem un profesionāliem kolēģiem un studiju biedriem. Paldies visiem par atbalstu, komandas darbu, zināšanām ar kurām viņi dalījās ar mani. Īpaši liels paldies maniem ilggadējiem kolēģiem Andim Supei, Sandim Spolītim, Uģim Seņkānam, Tomam Salgalam, Armandam Ostrovskim, Rihardam Mūrniekam un Elvim Haritonovam⚰.

Paldies SIA Latvijas Mobilais Telefons un RTU Dizaina fabrikas, Doktorantu studiju nodaļas komandai par padomiem, atbalstu un produktīvu sadarbību.

Visbeidzot, vislielākais paldies manai ģimenei un draugiem par sniegto atbalstu un ticību maniem spēkiem. Jūsu atbalsts ir nenovērtējams.

Paldies visiem, ar kuriem kopā esmu strādājis vai kuri mani ir atbalstījuši, bet kuru vārds šeit nav pieminēts.

Saturs

Pielikums I:	**J. Braunfelds**, E. Haritonovs, U. Senkans, I. Murans, J. Porins, S. Spolitis. Designing of Fiber Bragg Gratings for Long-distance Optical Fiber Sensing Networks. Modelling and Simulation in Engineering, 2022, pp.1-13.
Pielikums II:	U. Senkans, **J. Braunfelds**, I. Lyashuk, J. Porins, S. Spolitis, V. Bobrovs. Research on FBG Based Sensor Networks and Their Coexistence with Fiber Optical Transmission Systems. Journal of Sensors, Vol.2019, pp.1-19, 2019.
Pielikums III:	**J. Braunfelds**, U. Senkans, I. Lyashuk, J. Porins, S. Spolitis and V. Bobrovs. Unified Multi-channel Spectrum-sliced WDM-PON Transmission System with Embedded FBG Sensors Network, 2019 PhotonIcs & Electromagnetics Research Symposium - Spring (PIERS-Spring), Rome, Italy, 2019, pp. 3327-3333.
Pielikums IV:	**J. Braunfelds**, K. Zvirbule, U. Senkans, R. Murnieks, I. Lyashuk, J. Porins, S. Spolitis, V. Bobrovs. Application of FWM-based OFC for DWDM Optical Communication System with Embedded FBG Sensor Network. The Latvian Journal of Physics and Technical Sciences, 2021, pp.1-9. (apstiprināta publicēšanai).
Pielikums V:	U. Senkans, **J. Braunfelds**, I. Lyashuk, J. Porins, S. Spolitis, V. Haritonovs, and V. Bobrovs. FBG Sensors Network Embedded in Spectrum-sliced WDM-PON Transmission System Operating on Single Shared Broadband Light Source. No: Proceedings of Photonics & Electromagnetics Research Symposium (PIERS 2019), China, Xiamen, 17 - 20 December, pp.1.-9.
Pielikums VI:	U. Senkans, **J. Braunfelds**, S. Spolitis, V. Bobrovs. Research of FBG Optical Sensors Network and Precise Peak Detection. 2018 Advances in Wireless and Optical Communications (RTUWO), Riga, 2018.
Pielikums VII:	**J. Braunfelds**, S. Spolitis, J. Porins, V. Bobrovs. Fiber Bragg Grating Sensors Integration in Fiber Optical Systems, IntechOpen, 2020.
Pielikums VIII:	**J. Braunfelds,** J. Porins, S. Spolitis, V. Bobrovs. Optisko sensoru signālu apstrādes iekārta ar integrētu optiskā laika apgabala reflektometra funkciju**.** Latvijas Republikas patents, LV15534, 11.12.2019.
Pielikums IX:	**J. Braunfelds**, U. Senkans, P. Skels, R. Janeliukstis, T. Salgals, D. Redka, I. Lyashuk, J. Porins, S. Spolitis, V. Haritonovs, V. Bobrovs, FBG-based sensing for structural health monitoring of road infrastructure, Journal of Sensors, 2021, pp. 1-9.
Pielikums X:	**J. Braunfelds**, U. Senkans, P. Skels, R. Janeliukstis, J. Porins, S. Spolitis, V. Bobrovs. Road Pavement Structural Health Monitoring by Embedded Fiber Bragg Grating Based Optical Sensors. Sensors, 2022, pp.1-13.
Pielikums XI:	**J. Braunfelds**, U. Senkans, P. Skels, I. Murans, J. Porins, S. Spolitis, V. Bobrovs Fiber Bragg Grating Optical Sensors for Road Infrastructure Monitoring Applications, Applied Industrial Optics, 2022, pp.1-2.

Lietoto saīsinājumu saraksts

AADT	Annual Average Daily Traffic	gada vidējā diennakts satiksme
AADTT	Annual Average Daily Truck Traffic	gada ikdienas kravas automašīnu satiksme
AC	Asphalt Concrete	asfaltbetons
APD	Avalanche Photodiode	lavīnfotodiode
ASE	Amplified Spontaneous Emission	pastiprināta spontānā emisija
AWG	Arbitrary Waveform Generator	patvaļīgas formas signālu ģenerators
BER	Bit-Error Rate	bitu kļūdu attiecība
BOTDA	Brillouin Optical Time Domain Analyzer	Briljuēna optiskā laika apgabala analizators
BOTDR	Brillouin Optical Time Domain Reflectometry	Briljuēna optiskā laika apgabala reflektometrs
BTB	Back-to-Back	bez pārraides vides
CDM	Code-division Multiplex	koddales multipleksēšana
CW	Continuous Wave	nepārtraukta starojuma gaismas avots
DCM	Dispersion Compensating Module	dispersiju kompensējošais modulis
DEMUX	Demultiplexer	demultipleksors
DSO	Digital Storage Oscilloscope	ciparu signālu osciloskops ar atmiņu
DSP	Digital Signal Processing	ciparu signālu apstrāde
DWDM	Dense Wavelength Division Multiplexing	blīva viļņgarumdales (spektrālā) blīvēšana
EAM	Electro-Absorption Modulator	elektro-absorbcijas modulators
EDFA	Erbium Doped Fiber Amplifier	erbija leģētas šķiedras pastiprinātājs
EF	Electrical Filter	elektriskais filtrs
FBG	Fiber Bragg Grating	šķiedras Brega režģis
FEC	Forward Error Correction	turpvērstā kļūdu labošana (kļūdu koriģējošais kods)
FWD	Falling Weight Deflectometer	krītoša svara deflektometrs
FWHM	Full Width Half Maximum	pilns platums līmenī viena puse (pilna platuma puses maksimums)
FWM	Four wave Mixing	četru viļņu mijiedarbe
GI-FMF	Graded-index Few Mode Fiber	gradienta tipa mazmodu optiskās šķiedras
HNLF	High Non-Linearity Fiber	paaugstinātas nelinearitātes (augsti nelineāra) šķiedra
IEEE	Institute of Electrical and Electronics Engineers	Elektrotehnikas un elektronikas inženieru institūts

| ITU-T	International Telecommunication Unit - Telecommunication Standardization Sector	Starptautiskā Telekomunikāciju Savienība - Telekomunikācijas Standartu Sektors
MUX	Multiplexer	multipleksors
MZM	Mach-Zehnder Modulator	Maha-Cendera optiskais modulators
NRZ	Non-Return to Zero	bez atgriešanās pie nulles līnijas kods
OBLS	Optical Broadband Light Source	optiskais platjoslas gaismas avots
OBPF	Optical Band Pass Filter	optiskais joslas filtrs
OC	Optical Circulator	optiskais cirkulators
ODN	Optical Distribution Network	optiskais sadales tīkls
OFC	Optical Frequency Comb	optiskās frekvences ķemme
OLT	Optical Line Terminal	optiskās līnijas termināls (gala iekārta)
ONU	Optical Network Unit	optiskā tīkla iekārta
OPC	Optical Power Coupler	optiskais signāla jaudas apvienotājs
OPS	Optical Power Splitter	optiskais signāla jaudas sazarotājs
OS	Optical Switch	optiskais slēdzis
OSA	Optical Spectrum Analyzer	optiskā spektra analizators
OTDR	Optical Time Domain Reflectometer	optiskā laika apgabala reflektometrs
PC	Power Coupler	jaudas apvienotājs
PD	Photodiode	fotodiode
PM	Power Meter	jaudas mērītājs
PON	Passive Optical Network	pasīvais optiskais tīkls
SBS	Stimulated Brillouin Scattering	inducētā Briljuēna izkliede
SHM	Structural Health Monitoring	tehniskā stāvokļa uzraudzība
SLED	Superluminescent Diode	superluminiscences gaismu izstarojoša diode
SLS	Side-lobe Suppression	pamatsignāla un sānjoslu jaudas attiecība
SMA	Stone Mastic Asphalt	šķembu mastikas asfalts
SMF	Single Mode Fiber	vienmodu optiskā šķiedra
SOA	Semiconductor Optical Amplifier	pusvadītāju optiskais pastiprinātājs
SS-WDM	Spectrum Sliced WDM	spektrāli sagriezta WDM sistēma
VOA	Variable Optical Attenuator	pārskaņojams optiskais vājinātājs
WDM	Wavelength Division Multiplexing	viļņgarumdales blīvēšana
WIM	Weigh in Motion	svēršana gaitā

PROMOCIJAS DARBA VISPĀRĒJS RAKSTUROJUMS

Tēmas aktualitāte

Ik gadu Latvijā un pasaulē pieaug objektu un teritoriju (autoceļu, aizsprostu, tiltu, pārvadu, dambju, dzelzceļu, ēku, u.c. objektu) skaits, kuros nepieciešams veikt dažāda veida reāla laika tehniskā stāvokļa uzraudzību. Kā arī pēdējās desmitgades laikā aizvien lielāka loma tiek piešķirta dažādu procesu un objektu uzraudzībai, publiskās infrastruktūras drošības nodrošināšanai ar dažāda tipa sensoru palīdzību[1-3]. Tā kā uzraudzība bieži jāveic lielos attālumos vairākās vietās vienlaikus, korozējošā vidē ar elektromagnētisko interferenci vai vidē bez elektrobarošanas, tad optiskie FBG sensori ir piemēroti šādai uzraudzībai[4-10].

Optiskā tīkla infrastruktūra mūsdienās netiek pilnvērtīgi izmantota un noslogota. Autors saskata augstu potenciālu šīs infrastruktūras izmantošanas klāsta papildināšanai ar šķiedru optisko sensoru risinājumiem. Ņemot vērā, ka optiskā tīkla infrastruktūra izvietota pie / tuvu autoceļiem, tiltiem, tuneļiem, dzelzceļiem, dambjiem, u.c., tad to var izmantot kā pārraides vidi, lai veiktu šo infrastruktūras objektu uzraudzību. Šādiem uzraudzības risinājumiem var izmantot "tumšās" optiskās šķiedras līnijas vai ekspluatētām līnijām, izmantojot brīvos frekvenču diapazonus. Šādu risinājumu turpmākajai attīstībai būs svarīgi izstrādāt augstvērtīgus optiskos FBG sensoru tīklus liela attāluma (40+ km) uzraudzības risinājumiem, nodrošināt sakaru un sensoru risinājumu kopdarbība, un kvalitatīvu sensoru integrācija infrastruktūras objektos (piem., ceļu segumā) uzraudzības veikšanai.

Lai labāk novērtētu tēmas aktualitāti, tika veikta analīze Scopus datu bāzē pieejamajiem zinātniskajiem rakstiem. Rakstu meklēšana tika veikta pēc raksta nosaukumiem, atslēgvārdiem un kopsavilkuma ar atslēgtas vārdiem "šķiedru optiskie sensori" un "šķiedras Brega režģa sensori". Pēdējās desmitgades laikā ar atslēgtas vārdiem "šķiedru optiskie sensori" tiek vidēji publicēti 3130 zinātniski raksti, bet ar "šķiedras Brega režģa sensori" – 1052. Detalizēta dinamika pa gadiem tiek attēlota attēlā.
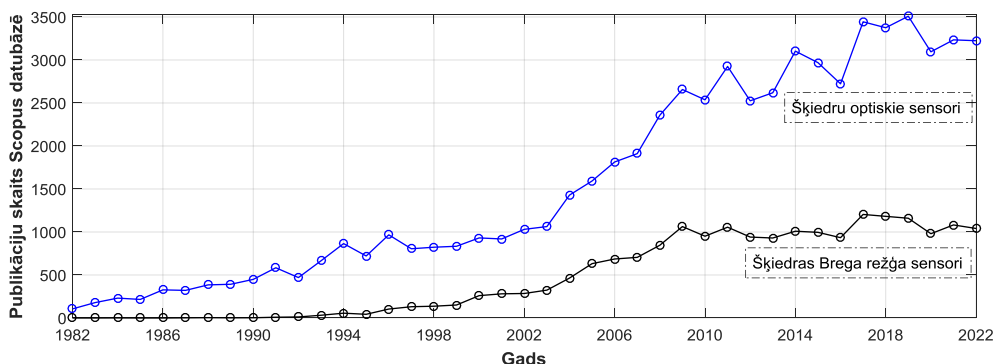
Scopus datu bāzē pieejamo zinātnisko rakstu skaits pa gadiem.

Augstais pieejamo zinātnisko rakstu skaits, raksturlīknes augošā dinamika un autora zinātnisko rakstu [9,11] augstā citējamība liecina, ka pētniecības tēma pašlaik un nākotnē būs aktuāla un veicinās tehnoloģiju attīstību.

Mērķis, uzdevumi un aizstāvamās tēzes

Promocijas darba mērķis: veikt šķiedru optisko Brega režģa sensoru tīklu integrāciju šķiedru optiskajās sakaru sistēmās, un novērtēt FBG sensoru pielietojumu autoceļa reāla laika uzraudzībai.

Darba mērķa sasniegšanai tika definēti sekojoši uzdevumi:

1. Novērtēt optisko sensoru tipus, galvenos parametrus, darbības principu un integrācijas iespējas eksistējošo optisko tīklu infrastruktūrā un to pielietojums.

2. Ar matemātiskās modelēšanas programmas palīdzību noteikt piemērotākos parametrus optisko FBG sensoru tīklu un liela attāluma uzraudzības risinājumiem.

3. Eksperimentāli un matemātiskās simulācijas vidē integrēt FBG sensorus šķiedru optiskajās sakaru sistēmās un novērtēt to kopdarbību.

4. Veikt optisko FBG deformācijas un temperatūras sensoru iestrādi (ceļa segas virskārtā, saites un stabilizētas kārtas slānī ar reciklētu asfaltbetonu) reālā autoceļa posmā.

5. Eksperimentāli novērtēt transportlīdzekļa radīto deformāciju novērtējumu reālā laikā autoceļa segumā dažādos slāņos.

Aizstāvamās tēzes:

1. Lai izveidotu FBG sensoru tīklu uzraudzības risinājumu darbībai vismaz 40 km attālumā, ir jānodrošina signāla atstarojamība vismaz 90%, SLS>20 dB un FWHM<0,2 nm.

2. Ir iespējams izveidot hibrīdu uz viena platjoslas gaismas balstītu 32 kanālu 10 Gbit/s SS-WDM PON ar integrētu piecu FBG šķiedru optisko sensoru tīklu risinājumu, nodrošinot nepieciešamo uztvertā signāla kvalitāti pie pārraides līnijas garuma 20 km.

3. FBG optiskos temperatūras un deformācijas sensorus var integrēt autoceļa stabilizētas kārtas slānī ar reciklētu asfaltbetonu, lai veiktu reāla laika transportlīdzekļu radīto deformācijas novērtējumu un tehniskā stāvokļa uzraudzību.

Zinātniskā novitāte un galvenie rezultāti

1. Izstrādāts 40 FBG sensora tīkla matemātiskais modelis, kas nodrošina uzraudzību vismaz 40 km attālumā.

2. Izstrādāta uz viena platjoslas gaismas avota balstīta 32 kanālu 10 Gbit/s spektrāli sagriezta šķiedru optiskā sakaru sistēma ar integrētu 5 FBG sensoru tīklu risinājumu.

3. Izstrādāts tehnoloģiskais risinājums optisko FBG sensoru integrēšanai autoceļa virskārtas, saites un stabilizētas kārtas slānī ar reciklētu asfaltbetonu, lai veiktu temperatūras un transportlīdzekļu radīto deformācijas novērtējumu reālā laikā.

4. Izstrādāta metode FBG deformācijas sensoru kalibrācijai, lai veiktu autotransporta radīto deformāciju novērtēšanu.

Promocijas darbā iegūtie rezultāti tika izmantoti:

1. ERAF, "RTU inovāciju granti studentiem" RTU un LMT Industriālais doktorants, 1.1.1.3/18/A/001, 01.07.2019 – 31.07.2022.

2. RTU zinātniski pētnieciskais projekts, "Šķiedru optiskie FBG sensori autoceļu tehniskā stāvokļu uzraudzībai", B4223, 02.01.2020 – 31.12.2020 (projekta zinātniskais vadītājs)

3. ERAF PIP "Pasīvi šķiedru optiskie sensori energoefektīvai transporta infrastruktūras tehniskā stāvokļa uzraudzībai" 1.1.1.1/16/A/072, 01.03.2017 – 01.03.2020.

4. RTU zinātniski pētnieciskais projekts "Kombinētas energoefektīvas šķiedru optiskās datu pārraides un sensoru sistēmas izstrāde", B4000, 07.01.2019 – 06.01.2020.

5. RTU zinātniski pētnieciskais projekts, "Eksperimentāla daudzfunkcionāla šķiedru optisko sensoru sistēmas risinājuma izveide", B3472, 15.01.2018. – 31.12.2018.

Darba struktūra un apjoms

Promocijas darbs sagatavots kā tematiski vienota zinātnisko publikāciju kopa, kas veltīta pētījumiem par šķiedru optisko FBG sensoru matemātiskā modelēšanā, integrācijā šķiedru optiskajās sakaru sistēmās un pielietojumu autoceļa reāla laika uzraudzībai. Promocijas darbs apkopo 5 oriģinālpublikācijas žurnālos, 4 zinātniskās konferences (indeksētas Scopus, IEEE vai Web of Science), vienā monogrāfijā un vienā Latvijas Republikas patentā.

Darba aprobācija un publikācijas

Promocijas darba galvenie rezultāti publicēti 5 zinātniskajos oriģinālrakstos, vienā monogrāfijā, vienā Latvijas Republikas patentā. Darba rezultāti prezentēti 4 zinātniskās konferencēs (indeksētas Scopus, IEEE vai Web of Science).

Zinātniskās publikācijas žurnālos:

1. **J. Braunfelds**, U. Senkans, P. Skels, R. Janeliukstis, J. Porins, S. Spolitis, V. Bobrovs, Road Pavement Structural Health Monitoring by Embedded Fiber Bragg Grating Based Optical Sensors, Sensors, 2022, pp.1-13. DOI: 10.3390/s22124581.

2. **J. Braunfelds**, E. Haritonovs, U. Senkans, I. Murans, J. Porins, S. Spolitis, Designing of Fiber Bragg Gratings for Long-distance Optical Fiber Sensing Networks. Modelling and Simulation in Engineering, 2022, pp.1-13. DOI: 10.1155/2022/8331485.

3. **J. Braunfelds**, U. Senkans, P. Skels, R. Janeliukstis, T. Salgals, D. Redka, I. Lyashuk, J. Porins, S. Spolitis, V. Haritonovs, V. Bobrovs, FBG-Based Sensing for Structural Health Monitoring of Road Infrastructure (2021) Journal of Sensors, 2021, art. no. 8850368. DOI: 10.1155/2021/8850368.

4. **J. Braunfelds,** K. Zvirbule, U. Senkans, R. Murnieks, I. Lyashuk, S. Spolitis and V. Bobrovs, Application of FWM-based OFC for DWDM Optical Communication System with Embedded FBG Sensor Network, Latvian Journal of Physics and Technical Sciences, 2021, pp.14. (apstiprināta publicēšanai).

5. U. Senkans, **J. Braunfelds**, I. Lyashuk, J. Porins, S. Spolitis, V. Bobrovs, Research on FBG-Based Sensor Networks and Their Coexistence with Fiber Optical Transmission Systems (2019) Journal of Sensors, 2019, art. no. 6459387. DOI: 10.1155/2019/6459387.

Zinātniskā monogrāfija:

1. **J. Braunfelds**, S. Spolitis, J. Porins, V. Bobrovs, Fiber Bragg Grating Sensors Integration in Fiber Optical Systems, IntechOpen, 2020, DOI: 10.5772/intechopen.94289.

Darba rezultāti prezentēti zinātniskajās konferencēs (indeksēti Scopus, IEEE, Web of Science):

1. **J. Braunfelds**, U. Senkans, P. Skels, I. Murans, J. Porins, S. Spolitis, V. Bobrovs, Fiber Bragg Grating Optical Sensors for Road Infrastructure Monitoring Applications, (2022) Optics InfoBase Conference Papers, Applied Industrial Optics, pp.1-2, DOI:10.1364/AIO.2022.W1A.2.

2. **J. Braunfelds,** U. Senkans, I. Lyashuk, J. Porins, S. Spolitis and V. Bobrovs, Unified Multi-channel Spectrum-sliced WDM-PON Transmission System with Embedded FBG Sensors Network, 2019 PhotonIcs & Electromagnetics Research Symposium - Spring (PIERS-Spring), 2019, pp. 3327-3333, DOI: 10.1109/PIERS-Spring46901.2019.9017809.

3. U. Senkans, **J. Braunfelds**, I. Lyashuk, J. Porins, S. Spolitis, V. Haritonovs, V. Bobrovs, FBG sensors network embedded in spectrum-sliced WDM-PON transmission system operating on single shared broadband light source, (2019) 2019 Photonics and Electromagnetics Research Symposium - Fall, PIERS - Fall 2019 - Proceedings, art. no. 9021628, pp. 1632-1639. DOI: 10.1109/PIERS-Fall48861.2019.9021628.

4. U. Senkans, **J. Braunfelds**, S. Spolitis, V. Bobrovs, Research of FBG Optical Sensors Network and Precise Peak Detection (2018) Proceedings - 2018 Advances in Wireless and Optical Communications, RTUWO 2018, art. no. 8587859, pp. 139-143. DOI: 10.1109/RTUWO.2018.8587859.

Darba rezultāti prezentēti zinātniskajās konferencēs (nav indeksēti Scopus, IEEE, Web of Science):

1. U. Senkans, **J. Braunfelds**, P. Skels, J. Porins, S. Spolitis, V. Bobrovs, Fiber Bragg Grating Sensors For Hybrid WDM-PON systems and structural health monitoring of road infrastructure, First Workshop for ERI on Telecommunication and Networks, March 14-15, 2022.

2. **J. Braunfelds**, U. Senkans, J. Porins, S. Spolitis, V. Bobrovs, Fiber Bragg Grating Sensors for structural health monitoring of road infrastructure. First Workshop of EUt+ Sustainability Lab (2021).

3. **J. Braunfelds**, J. Porins, S. Spolitis, V. Bobrovs, FBG sensors for structural health monitoring of road infrastructure. Quantum Optics and Photonics (2021).

4. E. Haritonovs, S. Spolitis, **J. Braunfelds**, Evaluation of fiber Bragg grating applications in optical sensor solutions, 63rd International scientific conference of RTU, Riga, Latvia, October 14, 2022.

5. **J. Braunfelds**, U. Senkans, I. Murans, J. Porins, S. Spolitis, V. Bobrovs, Application of FBG optical sensors in road pavement SHM, 63rd International scientific conference of RTU, Riga, Latvia, October 14, 2022.

6. I. Zalitis, **J. Braunfelds**, S. Spolitis, FBG sensor networks and their integration in fiber optical communication systems, 63rd International scientific conference of RTU, Riga, Latvia, October 14, 2022.

7. U. Senkans, **J. Braunfelds**, S. Spolitis, V. Bobrovs, Multi-channel SS-WDM-PON transmission system with embedded FBG sensors network, 60ty International scientific conference of RTU, Riga, Latvia, October 15, 2019.

8. A. Ostrovskis, **J. Braunfelds**, Research and evaluation of fiber optical sensors in FOTS solutions, 60ty International scientific conference of RTU, Riga, Latvia, October 15, 2019.

9. **J. Braunfelds**, V. Bobrovs, Development and Evaluation of Fiber Optical Sensors System, 59th International scientific conference of RTU, Riga, Latvia, October 12, 2018.

10. U. Senkans, **J. Braunfelds**, S. Spolitis, V. Bobrovs Research of FBG Optical Sensors Network and Effective Detection of Channel Spacing, 59th International scientific conference of RTU, Riga, Latvia, October 12, 2018.

11. E. Haritonovs, **J. Braunfelds,** S. Spolītis, FBG optisko sensoru režģa parametru novērtējums, RTU 62. Studentu Zinātniski tehniskā konference (2021).

12. A.Ostrovskis, **J.Braunfelds** Šķiedru optisko sensoru izpēte un novērtējums ŠOPS risinājumos, RTU 60. Studentu Zinātniski tehniskā konference (2019).

13. A. Ņikuļins, **J. Braunfelds** Optiskā intensitātes sensora izstrāde un novērtējums, RTU 60. Studentu Zinātniski tehniskā konference (2019).

IEVADS

Mūsdienās liela daļa iedzīvotāju saprot, ko nozīmē termins "optiskais internets". Lai lietotājam nodrošinātu šādu pakalpojumu, tiek izmantota optiskā šķiedra, pa kuru tiek veikta informācijas pārraide. Attīstoties tehnoloģijām optisko šķiedru pielietojumu klāsts pieaug, un viens no šādiem risinājumiem ir šķiedru optiskie sensori.

Optisko šķiedru izmantošana sensoru risinājumos tika novērota jau 1970. gadā. Tas kļuva iespējams, pateicoties lāzeru izgudrošanai 1960. gadā, un zema vājinājuma optisko šķiedru attīstībai 1966. gadā [12]. 20.gs 90. gadu sākumā sāka pielietot optiskos sensorus, ar ko varēja mērīt temperatūru, deformāciju, spiedienu u.c. parametrus. Savukārt, 21. gs. sākumā plašu pielietojumu ieguva optiskie sensori, kuri mēra temperatūru visā šķiedras garumā, un tas ļāva naftas un gāzes kompānijām novērot savus tīklus un novērst bojājumus daudz laicīgāk. Būvniecībā šķiedru optiskie sensori tika izmantoti, lai novērotu kritiskos punktus ēkās, un laicīgi veiktu remontdarbus. Laikam ejot, arvien vairāk tiek domāts par procesu efektivitāti, automatizāciju, un šķiedru optiskie sensori sāk ieņemt arvien lielāku lomu.

Kopš šī laika progress ir bijis ievērojams, un mūsdienās ar optisko šķiedru sensoru palīdzību ir iespējams veikt visdažādāko parametru izmaiņu mērīšanu, tādus kā deformācija, spiediens, temperatūra, pārvietojums, vibrācija, paātrinājums, rotācija, šķidruma līmenis, mitrums, strāvas stiprums, ķīmiskais sastāvs un daudzus citus parametrus [12]. Šo sensoru attīstībā liela nozīme bija optisko šķiedru priekšrocībām, salīdzinājumā ar citu veidu sensoriem, piemēram, augsta jūtība, imunitāte pret elektromagnētisko interferenci, pasīvi sensori, vieglums un kompaktums, noturība pret ķīmiskām vielām, multipleksēšanas iespējas, piemērotība novērot izmaiņas attālināti lielos attālumos, zems ienestais vājinājums [12], plašs mērāmo ķīmisko un fizikālo parametru spektrs [13-16]. Optisko sensoru trūkums ir salīdzinoši augstās izmaksas, bieži gala lietotāji nav informēti par šādiem risinājumiem.

Optiskās šķiedras sensorus iedala 2 lielās grupās: iekšējie un ārējie šķiedru optiskie sensori.

Ārējie šķiedru optiskie sensori

Ārējiem šķiedru optiskiem sensoriem optiskais signāls izplūst ārpus optiskās šķiedras, un tiem ir nepieciešams sensora elements šķiedras galā. Materiāls, kas maina savus optiskos parametrus, piemēram, - laušanas koeficientu, absorbēšanu, fluorescenci, atstarošanos, u.c., ļauj izveidot plašu skaitu sensoru, balstoties uz uzraugāmo parametru. Ārējie šķiedru optiskie sensori mūsdienās joprojām ieņem svarīgu vietu kopējā optiskās šķiedras sensoru klāstā. Pamatā ārējos šķiedru optiskos sensoros izmanto divu šķiedru savienojuma sensorus un Fabrī-Pero interferometrus [17].

Divu optisko šķiedru savienojuma sensors balstās uz principu, kur pārraidītais optiskā signāla stars iedarbojas uz kādu noteiktu vielu. No vielas stars tiek atstarots, un uztverošais bloks analizē vielas

iedarbību uz staru, ņemot vērā uzraugāmos parametrus. Atkarībā no uzraugāmā parametra, atstaroto signālu var pārraidīt pa to pašu vai citu optisko šķiedru. Šāda veida sensorus var izmantot temperatūras, pārvietojuma, spiediena un vibrāciju uzraudzībā [18-20].

Pateicoties zemajām ražošanas izmaksām un kompaktiem izmēriem, Fabrī-Pero interferometrs ir viens no pirmajiem un visbiežāk izmantotais ārējais optiskās šķiedras sensors. Fabrī-Pero interferometra darbības pamatā ir divas paralēlas atstarojošas virsmas ar noteiktu attālumu starp tām, kuru pārsvarā aizpilda gaisa dobums [21-23]. Sensora trūkumi ir saistīti ar savienošanas efektivitāti un to kalibrēšanu [24]. Šāda veida sensorus izmanto spiediena (piem., gāzes, betona un kompozītmateriālu konstrukciju), punktveida temperatūras, ultraskaņas uzraudzībā [25-29].

Iekšējie šķiedru optiskie sensori

Iekšējie šķiedru optiskie sensori izmanto optisko šķiedru kā sensora elementu. Iekšējie šķiedru optiskie sensori tiek iedalīti makrolocījumu un mikrolocījumu sensoros, šķiedras Brega režģa sensoros (FBG), kā arī uz Releja, Ramana un Briljona izkliedi balstītos sensoros.

Makrolocījumu un mikrolocījumu sensori ir intensitātes modulētie sensori, kas balstīti uz optisko šķiedru salocīšanu. Mikrolocījumu sensoru pamatā optiskā šķiedra tiek ievietota starp divām zobveida deformācijas plātēm. Atkarība no zobveida deformācijas plātnes, zobu izvietojumu var pielāgot sensoru dažādiem mērījumiem, piemēram, deformācijas, spiediena, ātruma, paātrinājuma, smaguma, u.c. Mikrolocījumu sensoru lielākais trūkums ir to augstais ienestais vājinājums (ap 20 dB), kas neļauj tos izmantot sensora tīkla risinājumos – vietās, kur mērījumi jāveic vairākos punktos [19, 30-32].

Makrolocījumu sensoru gadījumā locījumu rādiuss ir daudzkārt lielāks nekā mikrolocījumu sensoru gadījumā, sasniedzot 10-30 mm (atkarībā no izmantotā viļņa garuma diapazona). Makrolocījumu sensoru darbība pamatā balstīta uz vienu vai vairāku locījumu cilpu principu. Samazinot optiskās šķiedras cilpas diametru, pieaug ienestais vājinājums cilpas vietā. Šādus sensorus var izmanto kā pārvietojuma (ēku, dzelzceļa, dambju, uzbērumu u.c. objektu uzraudzībā), gaisa plūsmu, temperatūras sensorus. Ņemot vērā, ka šādu sensoru ienestais vājinājums ir daudzkārt mazāks nekā mikrolocījumu sensoru gadījumā, kas ļauj tos multipleksēt un izmantot sensoru tīklos [33-39].

Šķiedru optisko izkliedes (Releja, Ramana un Briljuēna) sensoru gadījumā optiskā šķiedra tiek izmantota gan kā pārraides vide, gan jutīga komponente. Šo sensoru gadījumā optiskā šķiedra visā garumā darbojas kā sensors. Atšķirībā no citiem sensoriem, izkliedes tipa sensoriem nav jāveic nekādas modifikācijas, lai optiskā šķiedra kalpotu par sensoru, tomēr jāizmanto augstas jutības signāla uztverošās iekārtas.

Releja izkliedes procesā atstarotā signāla jauda ir proporcionāla pārraidāmā signāla jaudai, kas ir apmēram vienāda ar λ^{-4} [40]. Releja izkliedē enerģija netiek nodota šķiedrai, turklāt gaismas izkliedes ietekmē nemainās signāla frekvence, tāpēc tā tiek uzskatīta par elastīgo izkliedi attiecībā pret

pārraidāmo signālu. Šo sensoru trūkums ir Releja izkliedes atstarotais signāls ar zemu signālu jaudu (vairāku desmitu dB vājāks nekā ievades signāls) [40]. Neatkarīgi no trūkuma, šādus sensorus izmanto temperatūras, deformācijas, vibrācijas [41], mitruma [42], radiācijas [43], u.c. uzraudzībai. Būtiski atzīmēt, ka uz Releja izkliedi ir balstīta optiskā laika apgabala (OTDR) tehnoloģija, kura tiek izmantota optisko līniju uzraudzībā (optisko līnijas ienestā vājinājuma un bojājumu vietu noteikšanai). Ja mikrolocījumu un makrolocījumu sensori tiek izmantoti tīklu risinājumos, tad uzraudzības nodrošināšanai arī tiek izmantots OTDR. Mūsdienās un nākotnē būs aktuāla vairāku optisko šķiedru sensoru tehnoloģiju un risinājumu apvienošana vienā (piemēram, OTDR un FBG [44]), tādējādi nodrošinot vēl plašāku uzraudzības klāstu.

Optisko šķiedru sensori, kas balstīti uz stimulēto Briljuēna izkliedi (SBS), tiek izmantoti temperatūras un deformācijas uzraudzībai visā šķiedras garumā. Šķiedru optiskie Briljuēna sensori ir balstīti uz neelastīga izkliedi, kur izkliedētam vilnim rodas frekvences / viļņa garuma nobīde [45-46]. SBS balstīti sensori, atkarībā no realizācijas principa un nepārtraukta (CW) lāzera novietojuma, tiek iedalīti: Briljuēna optiskā laika apgabala reflektometrs (BOTDR) un Briljuēna optiskā laika apgabala analizators (BOTDA) [40, 46, 47, 49]. BOTDA gadījumā impulsveida un CW lāzera signāls izplatās pretējos virzienos [40,49]. Šī frekvences / viļņa garuma nobīde ir atkarīga no temperatūras un deformācijas izmaiņām, kas ļauj tos izmantot sensoru risinājumos. BOTDR gadījumā sensoru uzraudzības diapazons ir 20-50 km, bet BOTDA gadījumā var sasniegt pat 200 km [40]. Telpiskā izšķirtspēja BOTDR gadījumā ir ap 1m (atkarīga no sensoru uzraudzības diapazona), bet BOTDA gadījumā – 2 cm (pie sensoru uzraudzības diapazona ir 2 km) [50], un 2 m (pie 150 km) [49, 51].

Optisko šķiedru sensori, kas balstīti uz Ramana izkliedi, tiek izmantoti temperatūras uzraudzībai visā šķiedras garumā. Konkrētajos tehnoloģiskajos risinājumos tiek plaši izmantota betona konstrukciju, gāzesvadu, ūdens apgādes sistēmu uzraudzībā [40, 52]. Sensoru uzraudzības attālums var sasniegt pat 37 km. Telpiskā izšķirtspēja cieši atkarīga no sensora uzraudzības attāluma, pie 1 km telpiskā izšķirtspēja ir 1 cm, bet pie 37 km – 17 m [49, 53, 54]. Pētījumu rāda, ka šķiedru optiskos Ramana izkliedes sensorus var izmantot temperatūras uzraudzībai pēc 26 km attālumā pa SMF ar precizitāti 3^oC un telpisko izšķirtspēju 1m [55], bet izmantojot gradienta tipa mazmodu optiskās šķiedras (GI-FMF) var veikt uzraudzību 25 km attālumā ar precizitāti 1^oC un telpisko izšķirtspēju 1,13 m [56,57].

Šķiedras Brega režģa atklāšana ievērojami veicināja optisko šķiedru sensoru un telekomunikāciju nozares attīstību. Šķiedras Brega režģis tiek izveidots, kā laušanas koeficienta izmaiņas optiskās šķiedras serdenī (gareniskās ass virzienā). FBG ir plašas pielietojuma iespējas, piemēram, dispersijas kompensēšanas, optisko filtru, šķiedru optisko pastiprinātāju, lāzeru, multipleksoru, demultipleksoru, sensoru risinājumos, u.c. [58]. Atstarotais Brega viļņa garums ir jutīgs pret dažādiem fizikāliem parametriem, tāpēc FBG var izmantot kā optisko sensoru, lai uzraudzītu, noteiktu fizikālo parametru izmaiņu laikā. FBG ir kvazi izkliedēti sensori, kas ļauj tos vienkārši multipleksēt – izmantot sensoru

tīklu risinājumos (tipiski ap 100 sensoriem, bet izmantojot CDM-WDM var sasniegt pat 1000 sensorus) [59]. FBG sensoru telpiskā izšķirtspēja ir vienāda ar režģa garumu (tipiski 2-10 mm, retākos gadījos sasniedz līdz 20 mm). Nolašu frekvence standarta signāla apstrādes iekārtām ir līdz 1 kHz, retākos gadījumos sasniedz 5 kHz. FBG sensorus var izmantot dažādas nozarēs, lai veiktu temperatūras, deformācijas, pārvietojuma, spiediena, vibrāciju, u.c. fizikālu parametru uzraudzību [48, 60-65]. FBG sensori ir visplašāk izmantotie (2/3 gadījumos) optiskie sensori objektu (piem. tiltu, dambju, ceļu, ēku, cauruļvadu, u.c.) tehniskā stāvokļa uzraudzības risinājumos [49, 66, 67].

Lai izprastu optisko sensoru lomu un radīto ietekmi uz uzraudzības un telekomunikāciju nozari, ir nozīmīgi tos klasificēt pēc darbības principa, telpiskā novietojuma un pielietojuma veida [12, 68-69].

Sensori pēc darbības principa jeb modulācijas veida tiek iedalīti[14-15,70]:
- Intensitātes modulētie sensori – parametru izmaiņu nosaka pēc signāla intensitātes;
- Fāzes modulētie, jeb interferometriskie sensori – parametru izmaiņu nosaka pēc signāla fāzes;
- Polarizācijas modulētie, jeb polarimetriskie sensori – parametru izmaiņu nosaka pēc signāla polarizācijas stāvokļa izmaiņas;
- Viļņa garuma, jeb spektrometriskie sensori – parametru izmaiņu nosaka pēc signāla viļņa garuma izmaiņas [12].

Optiskos sensorus pēc novietojuma principa iedala [14-15,70, 71]:
- Punkta tipa sensori – mērījums tiek veikts vienā punktā;
- Kvazi izkliedēti sensori – mērījumus veic vairākos punktos (sensoru tīkls);
- Izkliedēti sensori – visa optiskā šķiedra darbojas kā sensors.

Pēc konkrēta pielietojuma optiskos sensorus iedala [14-15, 70]:
- Fiziskos (temperatūra, spiediens, deformācija, ātrums, u.c.);
- Ķīmiskos (pH, gāzes analīze, spektroskopija, u.c.);
- Bio-medicīniskos (asins plūsma, glikozes saturs, u.c.).
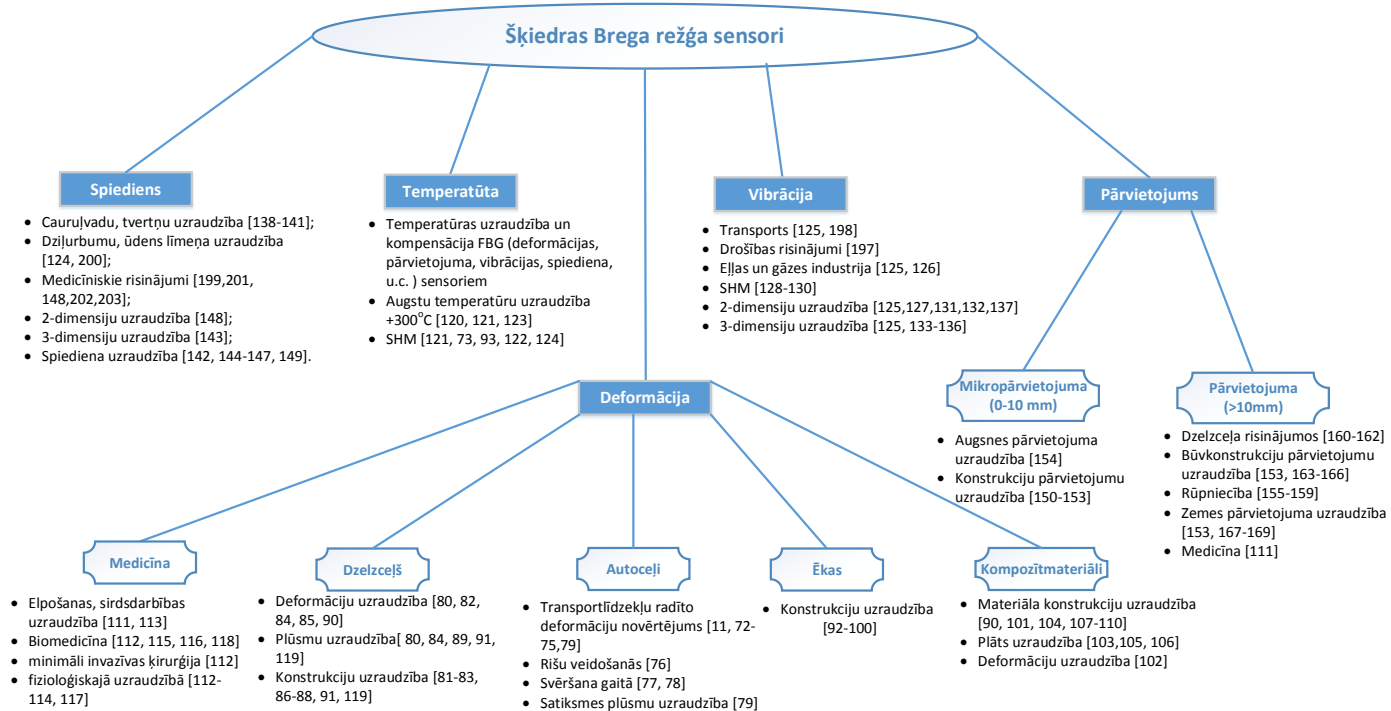
Šķiedras Brega režģa sensori

FBG sensoru pielietojuma karte, balstoties pēc sensoru uzraugāmā parametra, tiek attēlota 1. att. Visplašāk optiskie FBG sensori tiek pielietoti deformācijas un temperatūras mērījumiem dažādu autoceļu [11, 72-79], dzelzceļa [80-91], ēku [92-100], kompozītmateriālu [90, 101-110] un medicīniskos [111-118] uzraudzības risinājumos. Dzelzceļa, autoceļu, ēku un kompozītmateriālu gadījumā deformācijas sensori galvenokārt tiek izmantoti konstrukciju uzraudzībā [81-83, 86-88, 90--101, 104, 107-110, 119], savukārt medicīnā fizioloģiskā [112-114, 117], elpceļu un sirdsdarbības

18

[111, 113] uzraudzībā. Temperatūras sensori tiek izmantoti temperatūras izmaiņu kompensācijai FBG (deformācijas, pārvietojuma, vibrācijas, spiediena, u.c.) sensoriem, kā arī temperatūras [120, 121, 123] un tehniskā stāvokļa uzraudzībā [73, 93, 121, 122, 124].

FBG vibrācijas sensori galvenokārt tiek pielietoti eļļas un gāzes industrijā [125, 126], SHM [127-130], kā arī 2 un 3 dimensiju vibrācijas uzraudzības risinājumos [125, 127, 131-137].

Savukārt FBG spiediena sensori tiek pielietoti cauruļvadu [138-140], tvertņu [141], dziļurbumu [124] uzraudzībā. Pētījumos relatīvi bieži tiek prezentēti dažādi izstrādātie spiediena (t.sk. divdimensiju un trīsdimensiju) sensori [142-149] uzraudzības risinājumiem.

FBG pārvietojuma sensori pēc darbības diapazonā tiek iedalīti mikropārvietojuma ($l = 0 - 10\ mm$) un pārvietojuma ($l > 10\ mm$) sensoros. Mikropārvietojuma sensori ir retāk izplatīti, tie tiek izmantoti konstrukciju [150-153] un augsnes [154] pārvietojuma uzraudzībā. Savukārt pārvietojuma sensori tiek pielietoti rūpniecības [155-159], dzelzceļa [160-162] un medicīnas [111] risinājumos, kā arī būvkonstrukciju [153, 163-166] un zemes pārvietojuma [153, 167-169] uzraudzībā.

Šķiedras Brega režģa sensori

Spiediens
- Cauruļvadu, tvertņu uzraudzība [138-141];
- Dziļurbumu, ūdens līmeņa uzraudzība [124, 200];
- Medicīniskie risinājumi [199,201, 148,202,203];
- 2-dimensiju uzraudzība [148];
- 3-dimensiju uzraudzība [143];
- Spiediena uzraudzība [142, 144-147, 149].

Temperatūta
- Temperatūras uzraudzība un kompensācija FBG (deformācijas, pārvietojuma, vibrācijas, spiediena, u.c.) sensoriem
- Augstu temperatūru uzraudzība +300°C [120, 121, 123]
- SHM [121, 73, 93, 122, 124]

Vibrācija
- Transports [125, 198]
- Drošības risinājumi [197]
- Eļļas un gāzes industrija [125, 126]
- SHM [128-130]
- 2-dimensiju uzraudzība [125,127,131,132,137]
- 3-dimensiju uzraudzība [125, 133-136]

Pārvietojums

Mikropārvietojuma (0-10 mm)
- Augsnes pārvietojuma uzraudzība [154]
- Konstrukciju pārvietojumu uzraudzība [150-153]

Pārvietojuma (>10mm)
- Dzelzceļa risinājumos [160-162]
- Būvkonstrukciju pārvietojumu uzraudzība [153, 163-166]
- Rūpniecība [155-159]
- Zemes pārvietojuma uzraudzība [153, 167-169]
- Medicīna [111]

Deformācija

Medicīna
- Elpošanas, sirdsdarbības uzraudzība [111, 113]
- Biomedicīna [112, 115, 116, 118]
- minimāli invazīvas ķirurģija [112]
- fizioloģiskajā uzraudzībā [112-114, 117]

Dzelzceļš
- Deformāciju uzraudzība [80, 82, 84, 85, 90]
- Plūsmu uzraudzība[80, 84, 89, 91, 119]
- Konstrukciju uzraudzība [81-83, 86-88, 91, 119]

Autoceļi
- Transportlīdzekļu radīto deformāciju novērtējums [11, 72-75,79]
- Rišu veidošanās [76]
- Svēršana gaitā [77, 78]
- Satiksmes plūsmu uzraudzība [79]

Ēkas
- Konstrukciju uzraudzība [92-100]

Kompozītmateriāli
- Materiāla konstrukciju uzraudzība [90, 101, 104, 107-110]
- Plāts uzraudzība [103,105, 106]
- Deformāciju uzraudzība [102]

1.att. Šķiedras Brega režģu sensoru pielietojuma karte

PROMOCIJAS DARBA GALVENIE REZULTĀTI

Doktorantūras laikā veikti pētījumi ar mērķi noteikt piemērotākos šķiedras Brega režģa parametrus sensoru tīklu un liela attāluma uzraudzības risinājumiem, novērtēt dažāda tipa optisko sakaru sistēmu savietojamību un kopdarbību ar FBG sensoru risinājumiem un novērtēt šo sensoru pielietojumu autoceļu infrastruktūras uzraudzībā reālā laikā.

1. ŠĶIEDRAS BREGA REŽĢA PIEMĒROTĀKO PARAMETRU NOTEIKŠANA SENSORU TĪKLU UN LIELA ATTĀLUMA UZRAUDZĪBAS RISINĀJUMIEM

Lielākā daļa tirgū pieejamie optiskie FBG sensori ir ar zemu pamatsignāla un sānjoslu jaudas attiecību (SLS) (tipiski SLS <15dB [170-171]) un /vai zemu atstarojamību (tipiski 7-40% [170,172]), un aizņem plašu spektrālo joslu (FWHM>0,3 nm [171]), kas neļauj šos sensorus augstvērtīgi izmantot attālinātai uzraudzībai lielos attālumos (vismaz 40 km) un pielietot sensoru tīklu risinājumiem.

Zinātniskos rakstos [173,174] tiek veikti pētījumi, kur matemātiskās simulācijas programmās tiek modelēti FBG režģi sensoru tīklu risinājumiem. Pētījumā [173] tiek sasniegti augstvērtīgi režģa parametri pēc joslas platuma (0,13 nm) un SLS parametra (34 dB), bet atstarojamība vien 53%. Savukārt pētījumā [174] tiek sasniegti augstvērtīgi režģa parametri pēc atstarojamības (99,9%) un SLS parametra (95,6 dB), bet augsts FWHM (0,434 nm).

Lai sensorus pielietotu attālinātai uzraudzībai lielos attālumos un sensoru tīklu risinājumiem, tiem jānodrošina sekojuši parametri:

- Maksimāli augsta atstarojamība (>90%);
- Maksimāli šaura atstarotā signāla spektrālā josla (FWHM<0,2 nm);
- Maksimāli augsta SLS vērtība (SLS>20 dB).

FBG sensorus ar parametriem (atstarojamība >90% un FWHM<0,2 nm) var izstrādāt, izmantojot tradicionālos vienmērīga tipa režģus [174-175]. Lai FBG sensoram nodrošinātu SLS vismaz 20 dB, nepieciešams izmantot režģu apodizāciju. Visu trīs parametru prasības FBG sensoriem tiek nodrošinātas, pielāgojot režģa garumu, režģa laušanas koeficienta izmaiņu garenvirzienā (Δn) un apodizācijas formu. Pētījuma laikā, ar matemātiskās simulācijas programmas „OptiGrating"[176-177] palīdzību, vienmodas optiskajā šķiedrā tika modelēti režģi, nomērīti to atstarojošie spektri, un Matlab vidē tika veikta datu apstrāde un uzzīmētas raksturlīknes režģa atstarojamībai, FWHM un SLS atkarībā no režģa garuma (intervāla no 1-20 mm) pie vienmērīgas, sinusa, paceltā sinusa un Gausa formas režģa apodizācijas (pie $\Delta n = 0,5 \times 10^{-4}; 1 \times 10^{-4}; 1,5 \times 10^{-4}; 2 \times 10^{-4}$). Šķiedras serdenī tika iestrādāts režģis ar sekojošām laušanas koeficienta izmaiņām garenvirzienā:

Gausa apodizācijai:
$$\Delta n(x) = \Delta n \cdot \exp\left\{-\ln(2) \cdot \left(\frac{2 \cdot \left(x - \frac{L}{2}\right)}{s * L}\right)^2\right\} \qquad (1.1.)$$

Sinusa apodizācijai:
$$\Delta n(x) = \Delta n \cdot \sin\left(\frac{\pi \cdot x}{L}\right) \qquad (1.2.)$$

Paceltā sinusa apodizācijai:
$$\Delta n(x) = \Delta n \cdot \sin^2\left(\frac{\pi \cdot x}{L}\right) \qquad (1.3.)$$

kur: L – režģa garums, Δn – režģa laušanas koeficienta izmaiņa, s – stiepuma garums=0,5, x=(0≤x≤L).

Matemātiskā simulācijas programma režģu simulācijai un analīzei izmanto apvienoto modu teoriju. FBG režģu laušanas koeficienta izmaiņas profilu attēlojums atkarība no režģa garuma tiek attēlots 1.1. attēlā. Režģa profili tiek attēloti pie režģa garuma 10 mm, $\Delta n=1,5\times10^{-4}$ un režģa segmentu skaita 25.
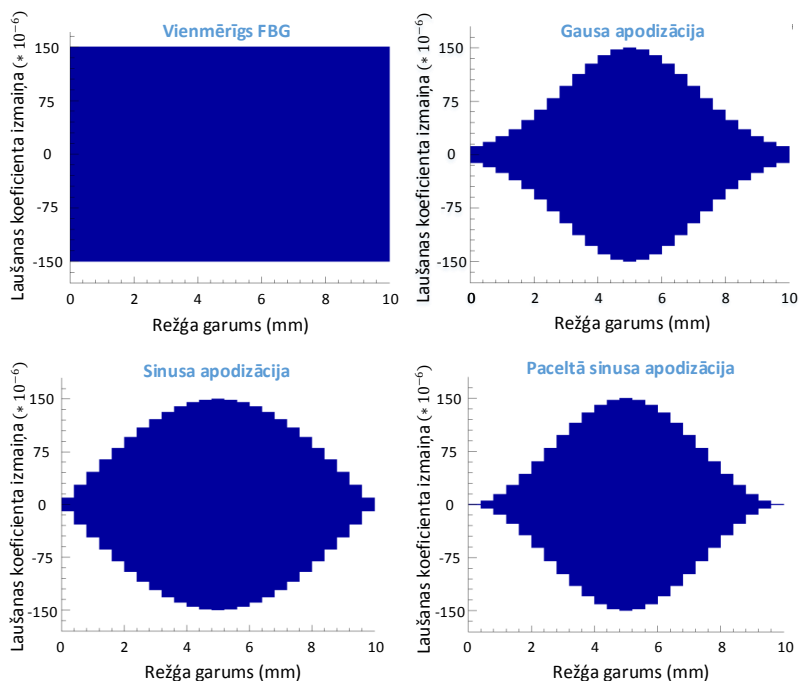
1.1. att. FBG režģu profilu attēlojums.

Iegūtie dati (atstarojamība, FWHM, SLS) no atstarotajiem FBG spektriem tika apkopoti tabulās un nodrošināti tiešsaistē atvērtā platformā Zenodo [178]. FBG ar paceltā sinusa apodizāciju atstarotā signāla spektru salīdzinājums pie režģa garumiem 4, 7, 10, 13 mm un $\Delta n = 1,5\times10^{-4}$ attēlots 1.2. attēlā. Palielinot režģa garumu no 4 līdz 13 mm, atstarojamība pieaug no 25% līdz 90%, savukārt joslas platums FWHM sašaurinās no 0,328 nm uz 0,173 nm.

1.3. attēlā tiek attēlota atstarotā signāla spektru salīdzinājums vienmērīga FBG un FBG ar Gausa, sinusa, paceltā sinusa apodizācijai pie režģa garuma 13 mm un Δn = 1,5×10⁻⁴. Spektrāli efektīvākais ir vienmērīgs FBG, pēc tam seko FBG ar sinusa apodizāciju, bet sānu joslas vislabāk nospiež jeb minimizē FBG ar paceltā sinusa apodizāciju un pēc tam seko FBG ar Gausa apodizāciju.
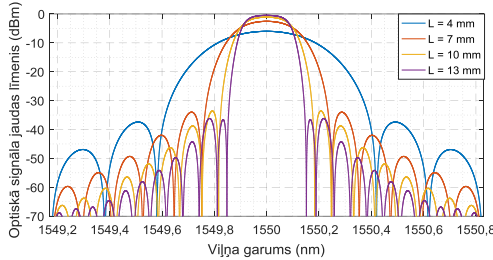
1.2.att. Atstarotais signāla spektrs FBG ar paceltā sinusa apodizāciju.
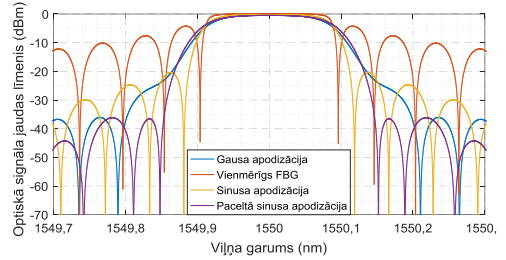
1.3.att. Atstaroto signāla spektru salīdzinājums vienmērīgam FBG un FBG ar Gausa, sinusa, paceltā sinusa apodizāciju.

Lai noteiktu piemērotākos FBG parametrus, ir būtiski noteikt atstarojamības, FWHM un SLS atkarību no režģa garuma, Δn un režģa apodizācijas, sk. 1.4. attēlos.
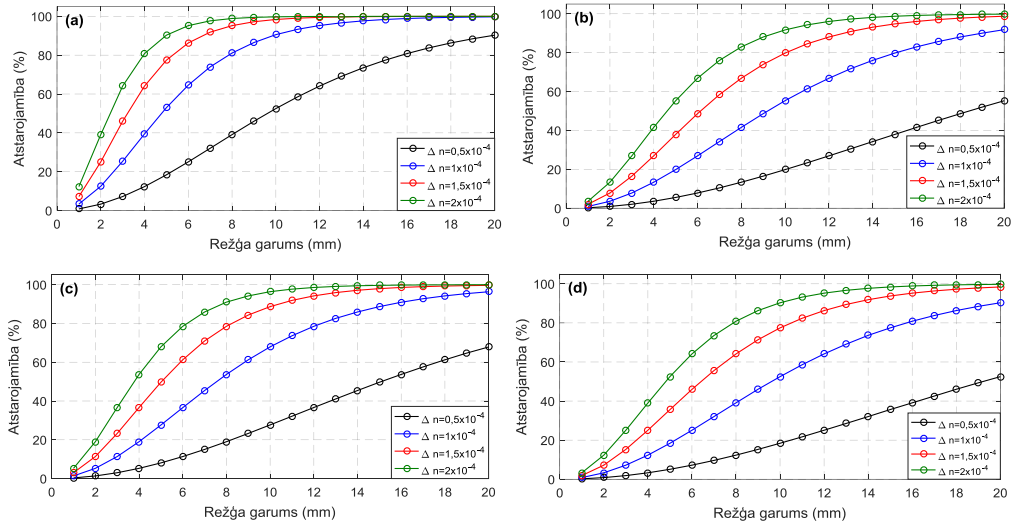
1.4. att. FBG atstarojamības atkarība režģa garuma (a) vienmērīgam FBG un FBG ar (b) Gausa, (c) sinusa un (d) paceltā sinusa apodizāciju.

Attēls 1.4. skaidri parāda atstarojamības atkarību no režģa garuma un Δn. Palielinot režģa garumu, palielinās arī atstarojamība. Augstāka atstarojamība novērojama vienmērīgam FBG (FBG bez apodizācijas), pēc tam seko FBG ar Gausa apodizāciju, taču relatīvi viszemākā atstarojamība novērojama FBG ar paceltā sinusa apodizāciju. No rezultātiem izriet, ka FBG ar Δn = 0,5×10⁻⁴ režģa

garuma intervālā (1-20 mm) nesasniedz 90% atstarojamību. Augstāku atstarojamību, iespējams, sasniedz pie augstākām Δn vērtībām ($1{,}5{\times}10^{-4}$ un $2{\times}10^{-4}$). Pie augstākām Δn vērtībām iespējams sasniegt vēlamo atstarojamību pie īsākiem režģa garumiem.

Analizējot 1.5. attēlā attēloto FBG signāla joslas platuma atkarību no režģa garuma, redzams, ka FWHM samazinās, palielinot režģa garumu. Visstraujākās FWHM izmaiņas ir novērojamas pie 1-5 mm režģa garuma. No rezultātiem var secināt, ka FBG ar režģa garumiem no 1 līdz 5 mm nav labākais risinājums sensoru tīklu risinājumiem, jo tie aizņem plašu spektrālo joslu. Ņemot vērā, ka jebkura sensora signāla apstrādes un analīzes iekārtai ir ierobežots raidītāja – platjoslas gaismas avota un uztvērēja – spektrometra joslas platums, tad, izmantojot FBG ar šaurāku spektrālo joslu, uz vienas šķiedras var izvietot lielāku sensoru skaitu. FBG ar šaurāko spektrālo joslu ir novērojami pie Δn = $0{,}5{\times}10^{-4}$. Svarīgi atzīmēt, ka visiem FBG ir noteiktas režģa garumu vērtības pie kurām režģa garumu palielināšana vairs nenodrošina būtisku FWHM samazinājumu. Vienmērīga FBG gadījumā ievērojams FWHM samazinājums ir novērojams līdz 6-8 mm režģa garumam, savukārt Gausa un sinusa apodizācijai – 8-10 mm, bet paceltā sinusa apodizācijai – 10-12 mm. Pēc šīm režģa garuma vērtībām FWHM vērtības īpaši neietekmē.
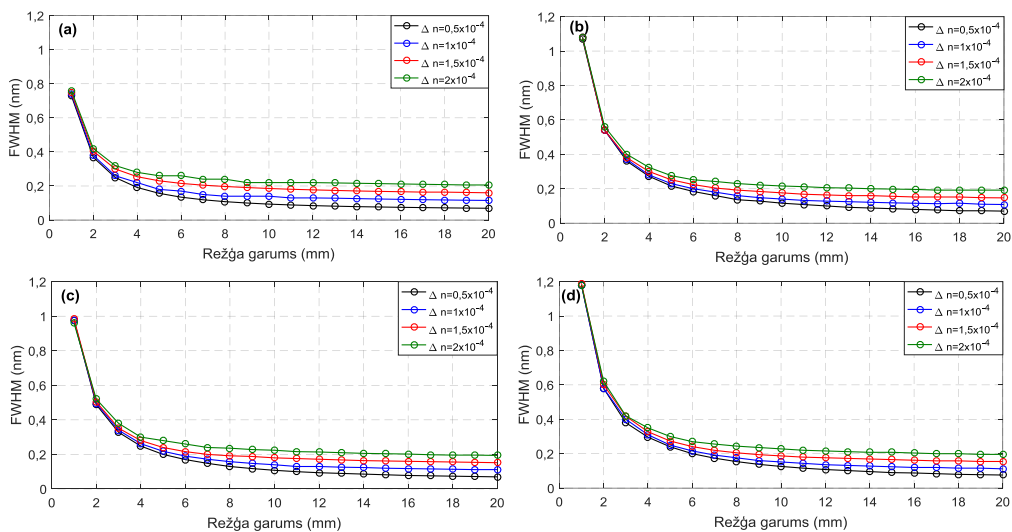
1.5. att. FBG režģa FWHM atkarība no režģa garuma (a) vienmērīgam FBG un FBG ar (b) Gausa, (c) sinusa un (d) paceltā sinusa apodizāciju.

Kā novērojams 1.6. attēla, vienmērīgam FBG un FBG ar Gausa apodizāciju SLS vērtības samazinās, palielinot režģa garumu intervāla no 1 līdz 20 mm un Δn intervālā no $0{,}5{\times}10^{-4}$ līdz $2{\times}10^{-4}$. Pielietojot FBG ar sinusa un pacelta sinusa apodizāciju, pie Δn $1{,}5{\times}10^{-4}$ un $2{\times}10^{-4}$ novērojams, ka SLS vērtības atkarībā no režģa garuma sākotnēji kritās un vēlāk sāk pieaugt. Līdzīgas tendences ir vērojamas zinātniskā rakstā [173], kur pie Δn= $4{\times}10^{-4}$ vērojams, ka SLS funkcija ir periodiska.

Zemākas SLS vērtības uzrāda vienmērīgs FBG, kas nesasniedz iepriekš definēto režģa SLS sliekšņa vērtību 20 dB, no kā izriet, ka šie FBG nav piemērotākie sensoru tīklu risinājumiem un liela attāluma uzraudzības risinājumiem. Izmantojot FBG ar Gausa, sinusa un paceltā sinusa apodizāciju, iespējams ievērojami nospiest sānjoslas.
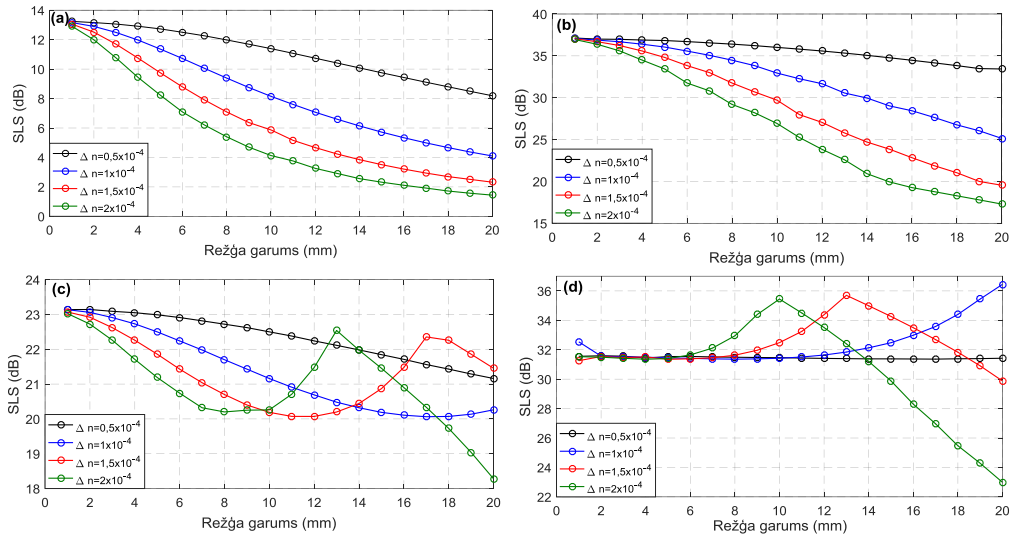
1.6. att. FBG režģa SLS atkarība no režģa garuma (a) vienmērīgam FBG un FBG ar (b) Gausa, (c) sinusa un (d) paceltā sinusa apodizāciju.

Lai labāk analizētu un salīdzinātu FBG atstarojamības (1.7. attēls), SLS (1.8. attēls), un FWHM (1.9. attēls), dažādiem apodizācijas profiliem atkarībā no režģa garuma, tie tika salīdzināti pie $\Delta n= 1{,}5\times10^{-4}$. Kā redzams 1.7. attēlā, augstāko atstarojamību režģa garuma intervālā 1-20 mm nodrošina vienmērīgs FBG, bet otro augstāko atstarojamību nodrošina FBG ar sinusa apodizāciju.
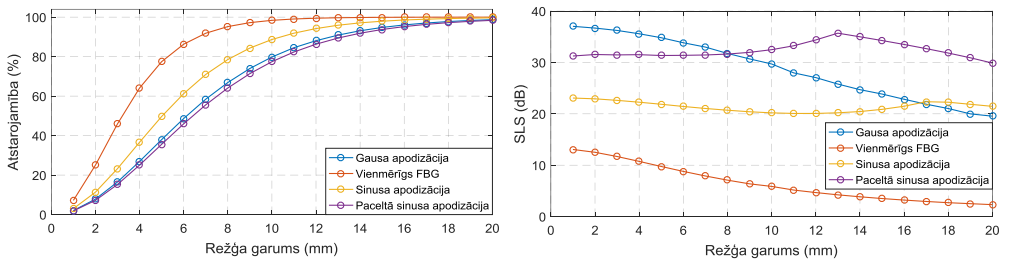
1.7. att. FBG atstarojamības salīdzinājums pie $\Delta n = 1{,}5\times10^{-4}$ vienmērīgam FBG un FBG ar Gausa, sinusa, paceltā sinusa apodizāciju.

1.8. att. FBG SLS salīdzinājums pie $\Delta n = 1{,}5\times10^{-4}$ vienmērīgam FBG un FBG ar Gausa, sinusa, paceltā sinusa apodizāciju.

Kā vērojams 1.8. attēlā, augstākās SLS vērtības (33 - 38 dB) nodrošina FBG ar Gausa apodizāciju pie režģa garuma no 1-7 mm, bet, kad režģa garums ir intervālā no 9-20 mm, tad augstāko SLS nodrošina paceltā sinusa apodizācija (30-32 dB).

Kā vērojams 1.9. attēlā, visšaurāko joslu režģa garuma intervālā 1-7 mm izmanto vienmērīgs FBG un pēc tam seko sinusa un Gausa apodizācija. Režģa garuma intervālā 8-20 mm šaurāko joslu var sasniegt, izmantojot FBG ar Gausa apodizāciju un pēc tam seko sinusa apodizācija.
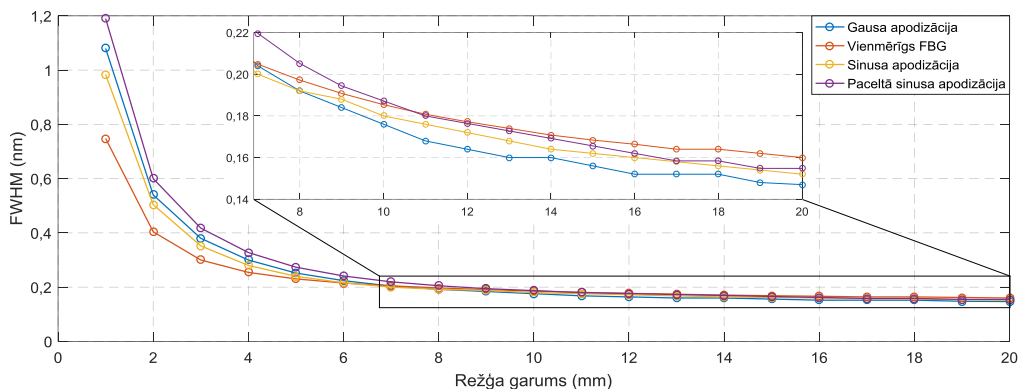
1.9. att. FBG FWHM salīdzinājums pie $\Delta n = 1{,}5 \times 10^{-4}$ vienmērīgam FBG un FBG ar Gausa, sinusa, paceltā sinusa apodizāciju.

1. tabulā tiek apkopoti vispiemērotākie, FBG režģa un apodizācijas parametri priekš FBG sensoru tīklu un liela attāluma uzraudzības risinājumiem. Minimālās prasības sensoru tīklu un liela attāluma uzraudzības risinājumiem ir: atstarojamība >90%; FWHM<0,2 nm un SLS>20 dB. Tabulā netiek apskatīts vienmērīgs FBG, jo tas nenodrošina minimālo SLS prasību.

1.tabula

Noteiktie režģa parametri FBG ar paceltā sinusa, Gausa un sinusa apodizāciju

Apodizācijas tips	Δn (×10⁻⁴)	Režģa garums (mm)	Atstarojamība (%)	FWHM (nm)	SLS (dB)
Paceltā sinusa	1,0	20	90,3	0,112	35,6
	1,5	13	90,0	0,173	35,7
	2,0	10	90,4	0,228	35,4
Gausa	1,0	19	90,0	0,110	26,0
	1,5	14	93,1	0,160	24,7
	2,0	10	91,7	0,216	26,9
Sinusa	1,0	16	90,9	0,118	20,1
	1,5	11	91,9	0,176	20,7
	2,0	13	99,0	0,210	22,5

Kā redzams no 1. tabulas datiem, paceltā sinusa apodizācija nodrošina relatīvi līdzīgu atstarojamību un FWHM kā Gausa apodizācija, taču SLS vērtības ir ievērojami labākas paceltā sinusa apodizācijai nekā Gausa apodizācijai.

Pamatojoties uz pētījuma datiem, pacelta sinusa apodizācija ir vislabākā sensoru tīklu un liela attāluma uzraudzības risinājumiem, jo ar šāda veida apodizāciju var sasniegt salīdzinoši augstās parametru vērtības FBG režīmam pie izmantotiem Δn. FBG režģa garumu var saīsināt, izmantojot augstākas režģa laušanas koeficienta izmaiņas (Δn). Taču pie augstākām Δn vērtībām palielinās spektrālās joslas platums un tādējādi FBG FWHM vērtība.

Relatīvi vislabākos rezultātus (atstarojamība = 90,3%, FWHM = 0,112 nm, SLS = 35,6 dB) uzrāda FBG ar paceltā sinusa apodizāciju pie $\Delta n=1\times10^{-4}$ un režģa garuma 20 mm. Balstoties uz šiem parametriem, tika izstrādāts sensoru tīkls ar 40 FBG sensoriem viļņa garuma diapazonā 1530 līdz 1569 nm (kanāla atstatums 1 nm). Sensora tīkla atstarotais spektrs ir attēlots 1.10. attēlā. Sensora tīklam ar 40 sensoriem ir augsta atstarojamība (>90 %) un SLS vērtība (~30 dB). Sensorus apvienojot tīklā SLS vērtība ir pasliktinājusies ~5 dB, jo pārklājas sānu joslas.
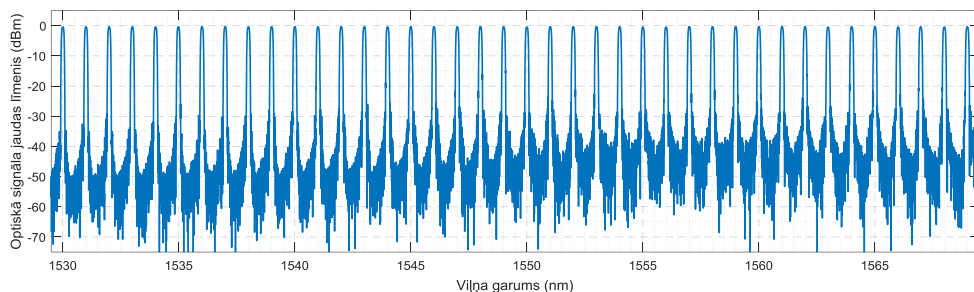
1.10. att. Atstarotais spektrs FBG sensora tīklam ar paceltā sinusa apodizāciju pie $\Delta n=1\times10^{-4}$ un režģa garuma 20 mm.

VPIphotonics matemātiskās modelēšana programmā tika izveidots modelis (1.11. att.), lai novērtētu FBG sensoru uzraudzības diapazonu.
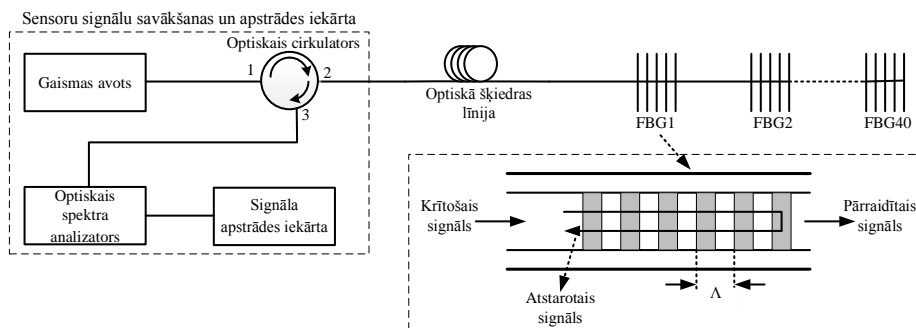
1.11. att. Matemātiskā modeļa shēma FBG sensora darbības diapazona novērtēšanai

Izstrādātais simulācijas modelis tika validēts laboratorijas vidē pret komerciālu sensoru tīklu. Modeļa raidošajā daļā tiek izmantots platjoslas gaismas avots, kas savienots ar optisko cirkulatoru, kas nodrošina signāla plūsmu atdalīšanu. Cirkulatora ports (2) tiek savienots ar vienmodas optisko šķiedras līniju. Modelī tika ieintegrēts FBG sensora nomērīta pārvades raksturlīkne FBG sensoriem. Modeļa uztverošajā daļa tika izmantots OSA un signāla apstrādes iekārta, lai varētu nomērīt signāla spektrus BTB, 20, 40, 60 km pārraides.

1.12. attēlā vērojams, ka pie pārraides līnijas garuma 60 km ir iespējams noteikt FBG centrālos viļņa garumus un SLS vērtība svārstās 9-11 dB. Tas nozīmē, ka FBG sensoru tīklu ar paceltā sinusa apodizāciju pie $\Delta n = 1 \times 10^{-4}$ un režģa garuma 20 mm var izmantot liela attāluma (60+ km) uzraudzības risinājumos.
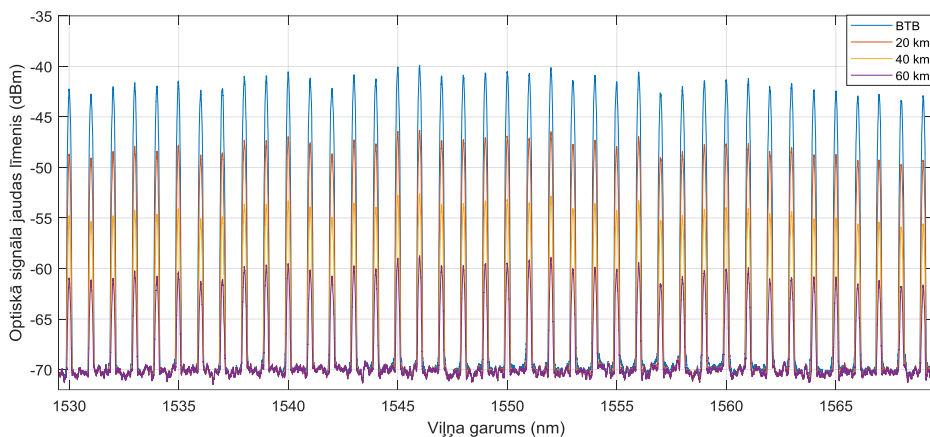
1.12.att. FBG sensora tīkla atstarotais spektrs pēc BTB, 20, 40 un 60 km pārraides

Kopsavilkums:

Lielākā daļa komerciālie optiskie FBG (visbiežāk vienmērīgs režģis – bez apodizācijas) sensori ir ar zemu SLS (tipiski SLS <15dB [170-171]) un/vai zemu atstarojamību (tipiski 7-40% [170, 172]), aizņem plašu spektrālo joslu (FWHM>0,3 nm [171]). Sensorus ar šādiem parametriem var izmantot, kā punkta veida sensorus, bet nevar augstvērtīgi izmantot attālinātai uzraudzībai lielos attālumos (vismaz 40 km) un pielietot sensoru tīklu risinājumiem.

No iegūtajiem rezultātiem var secināt, ka izvirzītas prasības (atstarojamībai>90%; FWHM<0,2 nm; SLS>20 dB) FBG sensoru tīklu uzraudzības risinājumu darbībai vismaz 40 km attālumā var izpildīt, izmantojot paceltā sinusa, Gausa, sinusa apodizāciju. Visaugstvērtīgākos rezultātus (atstarojamība = 90,3%, FWHM = 0,112 nm, SLS = 35,6 dB) uzrāda FBG ar paceltā sinusa apodizāciju pie $\Delta n = 1 \times 10^{-4}$ un L= 20 mm, kas ļauj nodrošināt FBG sensoru tīklu izmantošanu liela attāluma (60+ km) uzraudzības risinājumos.

Oriģinālpublikācija par šajā apakšnodaļā aprakstītajiem pētījumiem atrodama **pielikumā I**.

2. ŠĶIEDRU OPTISKO SAKARU SISTĒMĀS UN FBG SENSORU KOPDARBĪBAS UN RADĪTĀS IETEKMES UZ DATU KANĀLU PĀRRAIDES KVALITĀTI NOVĒRTĒJUMS

Attīstoties informācijas un komunikācijas tehnoloģiju nozarei un pieaugot lietotāju vajadzībām ikdienas dzīvē, arvien vairāk tiek izstrādātas jauni un uzlaboti esošie risinājumi un sistēmas. Ņemot vērā pateicīgo optisko tīklu novietojumu un zemo noslodzi, kā arī optisko sensoru priekšrocības un plašo sensoru pielietojumu klāstu, tad ir nepieciešams novērtēt sensoru integrācijas iespējas optiskā tīkla infrastruktūrā. Lai novērtētu nākotnes iespējas šķiedru optiskajās sakaru sistēmās integrēt optiskos FBG sensorus, ir nepieciešams novērtēt to kopdarbību un veikt radītās ietekmes analīzi.

Viena no pievilcīgākajām idejām optisko sensoru tīklu un datu pārraides sistēmu gadījumā ir to raidošās daļas balstīšana uz vienu platjoslas gaismas avotu, piemēram, pastiprinātu spontāno emisiju (ASE), superluminiscences gaismu izstarojošo diodi (SLED). Šajā gadījumā datu pārraidei tiek izmantota spektrāli sagrieztas viļņgarumdales blīvēšanas (SS-WDM) tehnoloģija, kuras galvenās priekšrocības aprakstītas zinātniskā rakstā [179], kā piemēram, izmaksu efektivitātē un raidošās daļas vienkāršošana.

2.1. Apvienotas spektrāli sagrieztas šķiedru optisko datu pārraides un sensoru sistēmas novērtējums

Uz viena platjoslas avota balstīta gaismas avota balstīta šķiedru optiskās datu pārraides sistēma ar integrētiem FBG sensoru tika realizēta gan matemātiskās simulācijas, gan eksperimentāli laboratorijas vidē. Sistēmas slēguma shēma ir attēlota 2.1. attēlā, kas sastāv no raidošās daļas, optiskā sadales tīkla un uztverošās daļas.

Raidošā daļa sastāv no optiskā platjoslas gaismas avota (OBLS) ar izejas jaudu + 7 dBm. Optiskais signāls tiek sadalīts 2 daļās ar optisko jaudas sadalītāju (PS), ar attiecību 20% (1,25 Gbit/s un 1,5 Gbit/s datu pārraides kanāliem) un 80% (sensora risinājumiem). 20% no signāla tiek pievadīti uz erbija leģētas šķiedras pastiprinātāju EDFA_1 pastiprinātāju (ieejas jauda 0 dBm, izejas jauda 18,1 dBm), bet 80% uz optisko joslas filtru, kas izfiltrē 3 nm joslu sensoru sistēmai.

EDFA_1 izeja ir savienota ar 32 kanālu sakārtotu viļņvadu režģi AWG_1 ar 54 GHz joslas platumu pie jaudas krituma 3 dB. AWG_1 16 kanāls (centrāla frekvence 193,1 THz) tika savienots ar Maha-Cendera optisko modulatoru (MZM), kam pieslēgts līdzsprieguma barošanas avots un impulsu secības ģenerators (PPG), kam pieslēgts elektriskais pastiprinātājs ar 17 dB pastiprinājumu. Optiskais datu un sensoru sistēmu signāls tiek apvienots ar optisko apvienotāju (OPC), kura izeja savienota ar EDFA_2 (izejas jauda 16 dB), kas savienots ar optiskā cirkulatora (OC) portu (1). OC komponente slēguma shēmā tiek izmantota FBG sensoru signāla plūsmu (caurejošais un atstarotais) atdalīšanai.

OC ports (2) tiek savienots ar vienmodas optisko šķiedru un FBG sensoru, bet ports (3) savienots ar optiskā spektra analizatoru (OSA), kas tiek izmantots FBG sensora atstarotā signāla mērīšanai.
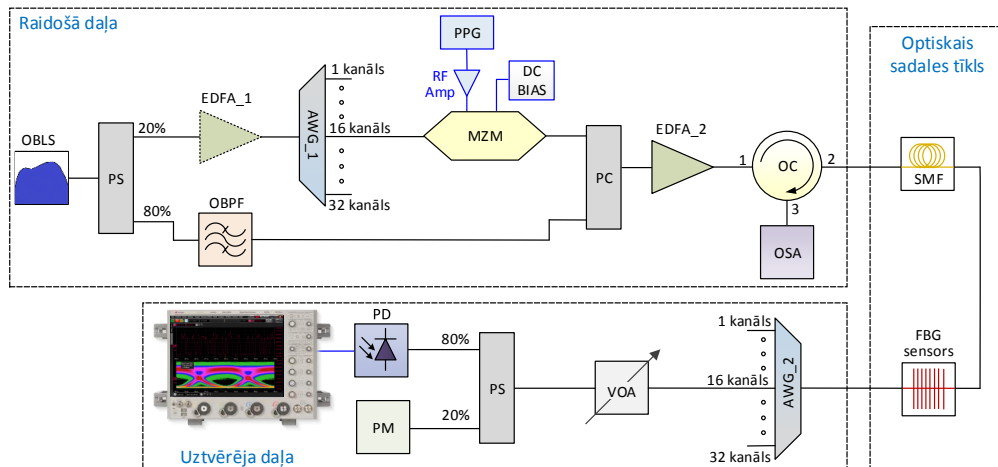
2.1. att. Uz vienu gaismas avotu balstīta šķiedru optiskās datu pārraides un FBG sensoru sistēma

Uztvērēja daļā tiek izmantots 32 kanālu AWG_2 ar 77,5 GHz joslas platumu pie jaudas krituma 3 dB, kas demultipleksē datu kanālus. AWG_2 ir savienots ar pārskaņojamo optisko vājinātāju (VOA), kas nepieciešams, lai uzņemtu bitu-kļūdas varbūtības (BER) korelācijas diagrammas. Slēguma shēmā tiek izmantots jaudas sadalītājs (ar attiecību 80:20%), lai uzraudzītu pievadīto signāla jaudas līmeni, kas pievadīts uz fotodiodi (PD) (joslas platums 10 GHz), kas pārveido optisko datu signālu elektriskajā signālā. Signāla kvalitātes novērtēšanai tika izmantots ciparu signālu osciloskops (DSO).

Datu pārraides kvalitātes novērtējums matemātiskās simulācijas programmā tika veikts 1.5 Gbit/s SS-WDM ŠOPS ar integrētu FBG sensoru un bez tā, sk. 2.2. att.
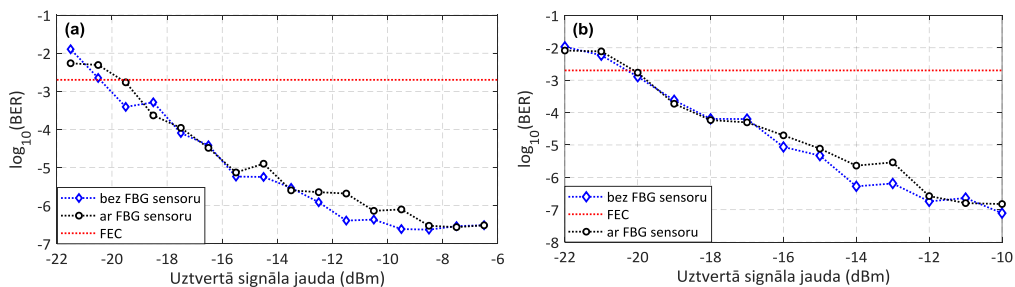
2.2. att. BER attiecība pret uztvertā signāla jaudas novērtējums SS-WDM datu pārraides un sensoru sistēmai ar un bez integrētu FBG sensoru pie līnijas garuma (a) 0 km un (b) 20 km.

No rezultātiem izriet, ka jaudas sods apvienotai optiskai datu pārraides un sensoru sistēmai (ar un bez FBG sensora) pie FEC sliekšņa $2,3 \times 10^{-3}$ bez pārraides līnijas (BTB) ir 0,5 dB, bet pie SMF garuma – 20 km 0,2 dB. Savukārt jaudas sods apvienotai optiskai datu pārraides un sensoru sistēmai (ar sensora) pie FEC sliekšņa $2,3 \times 10^{-3}$ (salīdzinājumā BTB un SMF garuma 20 km) ir 0,7 dB. Datu pārraides kvalitātes novērtējuma rezultāti eksperimentāli realizētai SS-WDM datu pārraides un sensoru sistēmai tiek attēloti 2.3.att. acs diagrammas un 2.4. att. BER korelācijas diagrammas formā.
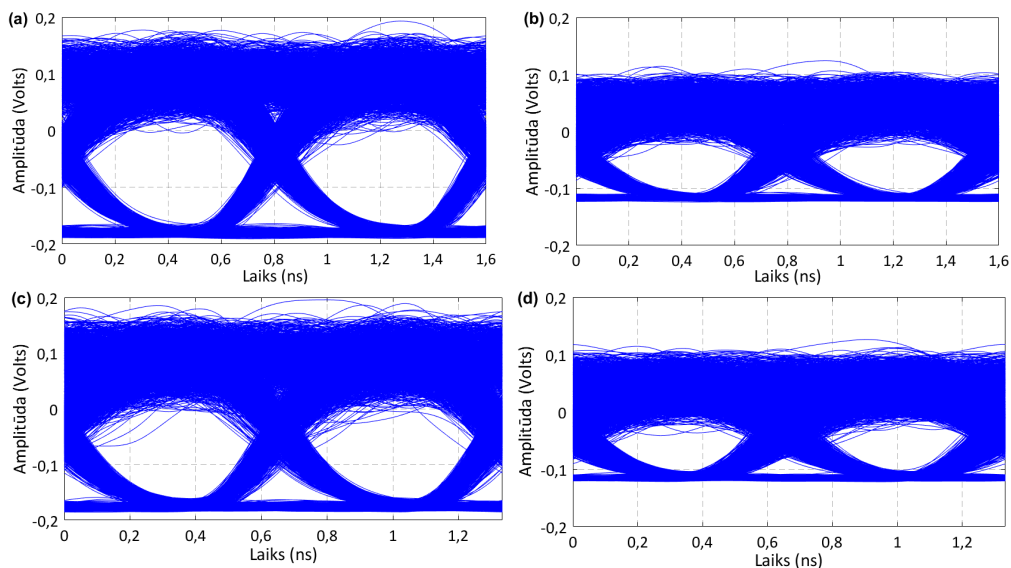
2.3. att. Acs diagrammas uztvertajam spektrāli sagrieztai šķiedru optiskajai datu pārraides un FBG sensoru sistēmas signālam pie sekojošiem parametriem (a) 1,25 Gbit/s BTB; (b) 1,25 Gbit/s pēc 20 km pārraides; (c) 1,5 Gbit/s BTB; (d) 1,5 Gbit/s pēc 20 km pārraides.

Kā redzams 2.3. attēlā (a) un (b) pie datu pārraides ātruma 1,25 Gbit/s acs diagrammas BTB gadījumā ir plaši atvērta un BER ir vienāds ar $4,6 \times 10^{-16}$, bet pēc 20 km pārraides BER vērtība samazinās un ir vienāda ar $1,3 \times 10^{-9}$. Savukārt pie pārraides ātruma 1,5 Gbit/s BTB pārraidei (2.3. attēla (c)) BER=$9,7 \times 10^{-12}$, bet pēc 20 km pārraides (2.3. attēla (d)) $6,1 \times 10^{-7}$.
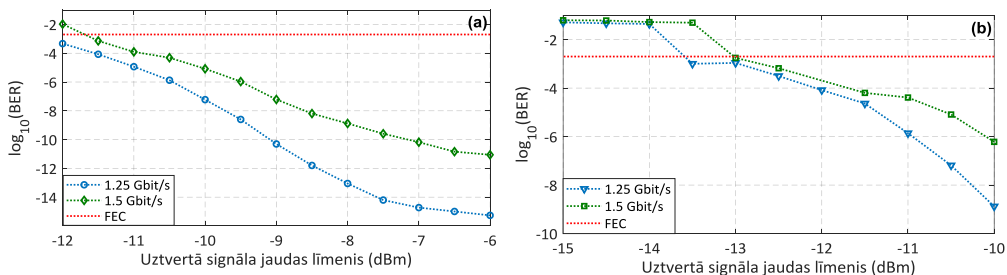
2.4. att. BER attiecības pret uztvertā signāla jaudas novērtējumu apvienotai SS-WDM datu pārraides un FBG sensoru sistēmai pie līnijas garuma (a) 0 km un (b) 20 km.

No 2.4. attēlā attēlotiem rezultātiem izriet, ka jaudas sods spektrāli sagrieztai šķiedru optiskajai 1,5 Gbit/s datu pārraides un sensoru sistēmai ar FBG, salīdzinot BTB un pēc 20 km pārraides pie FEC sliekšņa (BER = 2,3 ×10^{-3}), ir 1,5 dB. Šis jaudas sods ir novērojams galvenokārt platjoslas ASE gaismas avota trokšņainības un dispersijas dēļ. Palielinot datu pārraides ātrumu no 1,25 uz 1,5 Gbit/s, pasliktinās datu pārraides kvalitāte un BER vērtības.

Iegūtie rezultāti pierāda, ka spektrāli sagrieztai šķiedru optiskajai datu pārraides un FBG sensoru sistēmām var izmantot kopīgu platjoslas gaismas avotu un tās ir savstarpēji savienojamas, un iespējams veikt kļūdu brīvu datu pārraidi pa 20 km garu SMF pārraides līniju pie datu pārraides ātrumiem 1,25 un 1,5 Gbit/s.

2.2. Spektrāli sagrieztas daudzkanālu šķiedru optisko datu pārraides sistēmas un FBG sensoru tīkla kopdarbības novērtējums

32 kanālu 10 Gbit/s spektrāli sagrieztam viļņgarumdales blīvētam pasīvam optiskajam tīklam (SS-WDM PON) un FBG sensoru tīkla kopdarbības novērtējums tika veikts matemātikā simulācijas programmā *RSOFT OptSim*, kura slēguma shēma tiek attēlota 2.5. attēlā.
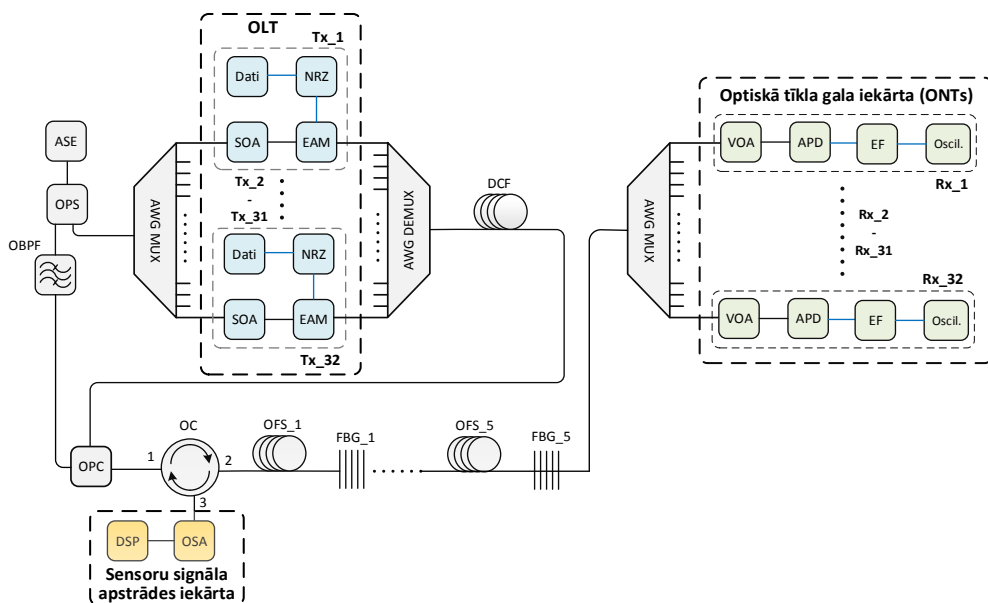
2.5. att. Slēguma shēma spektrāli sagrieztu 32 kanālu ŠOPS ar integrētu FBG sensoru tīklu.

Shēmas izveide tiek balstīta uz 2.1. attēlā shēmu, veicot sekojošus uzlabojumus:

- izmantots pusvadītāja optiskā pastiprinātājs (SOA), lai nomāktu ASE intensitātes svārstības;

- MZM modulators aizstāts ar elektro-absorbcijas modulatoru (EAM) – imūni pret signāla polarizācijas stāvokli;

- PD aizstāta ar lavīnfotodiodes (APD) – spēj darboties pie zemākām signāla jaudām.

Konkrētie uzlabojumi nodrošina sistēmas darbību pie 32 kanālu 10 Gbit/s SS-WDM PON ar integrētu 5 FBG sensoru tīklu. Sistēmas raidošā daļā tiek izmantots pastiprinātas spontānā emisijas platjoslas gaismas avots (ASE). ASE joslas platums ir no 1533,5 līdz 1565,5 nm (frekvenču joslā: 191,5 THz līdz 195,5 THz). SS-WDM PON sistēmas datu kanāliem tiek izmantota josla no 1545,7 līdz 1558,2 (192,4-194,0 THz) nm, bet FBG sensoru tīklam – no 1537,4 līdz 1545,3 nm (194 THz - 195 THz). Ar optisko jaudas sadalītāju signāls tiek sadalīts 2 daļas, kur viena daļa tiek pārraidīta uz AWG multipleksoru (SS-WDM PON sistēmas datu kanāliem), bet otra daļa uz optisko joslas filtru (sensora tīkla kanāliem).

Sistēmā AWG MUX tiek pielietots, lai izdalītu frekvenču joslu kanālus (datu kanāliem) ar fiksētu 50 GHz strapkanālu intervālu. Strapkanāla intervāls tiek izvēlēts balstoties uz ITU-T G.694.1 rekomendāciju[180]. AWG MUX kanālu platums pie -3dB jaudas krituma ir 45 GHz. Kanālu datu pārraides ātrums tiek uzstādīts uz 10,7 Gbit/s, no kuriem 7% tiek paredzēti FEC kļūdu labojošo kodu pielietošanai.

Katra kanāla raidītāja bloks sastāv no pusvadītāja optiskā pastiprinātāja, lai nomāktu ASE intensitātes svārstības. Pastiprinātās un trokšņu nospiestās spektrāli sagrieztās šķēles tiek pievadītas uz EAM, kas ir imūni pret signāla polarizācijas stāvokli (tieši pretēji MZM modulatoriem). NRZ datu bloks ģenerē datu signālu pēc NRZ līnijas koda. AWG DEMUX bloks apvieno 32 kanālus vienā, kas vēlāk tiek pārraidīts pa SMF pārraides vidi.

Optiskās pārraides līnijas dispersijas kompensēšanai (ar priekš-kompensācijas metodi) tiek izmantota dispersijas kompensējoša šķiedra. Tipiskas vienmodas optiskās šķiedras dispersija ir diapazonā D=16-18 ps/nm/km. Simulācijas vidē uzstādīts 16 ps/nm/km. Zinot pārraides līnijas garumu, var aprēķināt kopējo dispersiju, kas uzkrāsies pārraides laikā (16×20=320 ps/nm). DCF šķiedras dispersijas kompensācijas koeficients tiek uzstādīts -118,5 ps/nm/km (dati iegūti no RTU TI SSTIC laboratorijā esošās DCF šķiedras specifikācijas). DCF šķiedras garums tiek noteikts izdalot kopējo līnijas dispersiju ar DCF šķiedras dispersijas koeficientu, rezultātā tiek iegūts 2,7 km. DCF šķiedras vājinājuma koeficients tiek uzstādīts α=0,55 dB/km pie 1550 nm references viļņa garuma. Attiecīgi DCF šķiedras vājinājums ir 0,55×2,70= 1,5 dB.

DCF šķiedras izeja tiek savienota ar optisko jaudas apvienotāju (attiecība 50:50%) ar OFC ieejas portu. Pie OFC otra porta tiek pieslēgts iepriekš izdalītas OBPF izejas ports. Apvienotais signāls tiek pievadīts uz optiskos cirkulatoru (OC), kas veic signāla caurejošo un atstaroto plūsmu atdalīšanu. OC

otrais ports tiek savienots ar 5 optisko SMF pārraides līniju (katrs posms 4 km, ienestais vājinājums 0,18 dB/km) posmiem, kurā integrēts optisko FBG sensoru tīkls. Savietojamību nodrošina FBG sensoru izstrādes tehnoloģija fleksibilitāte, kas ļauj sensoru iestrādāt optiskā šķiedrā ar nepieciešamo centrālo viļņa garumu joslā 1510 – 1590 nm. Iestrādes metodoloģija ļauj definēt arī sensora atstarojamības līmeni, režģa garumu, joslas platumu, SLS u.c. parametrus. Tas ļauj sensorus maksimāli tuvu pievienot datu pārraides kanāliem, lai efektīvi izmantotu frekvenču joslu.

Optisko sensoru centrālo viļņa garuma vērtības tiek matemātiski aprēķinātas un ir attēlotas 2.1. tabulā. Definējot centrālo viļņa garumu, tiek pieņemts, ka objekta temperatūra svārstās diapazonā no -40°C līdz +80°C. Sensoru kanālu atstatums ir vienāds ar 200 GHz.

2.1. tabula.

FBG temperatūras sensoru centrālie viļņa garumi un frekvences

FBG sensora nr.	Centrālais viļņa garums (nm)	Centrālā frekvence (THz)
1	1544,53	194,1
2	1542,94	194,3
3	1541,35	194,5
4	1539,77	194,7
5	1538,19	194,9
Kanāla atstatums	1,58	0,2

FBG sensoru atstarotais signāls caur OC portu 3 tiek pārraidīts uz optiskā spektra analizatoru, kas nomēra signāla spektrālo raksturlīkni. Lai noteiktu sensoru centrālos viļņa garumus, tiek izmantots ciparu signālu procesors (DSP).

Datu signāla kvalitātes analīzei nepieciešams izdalīt 32 datu pārraides kanālus ar AWG MUX komponenti. Uztvērēja bloks (Rx) tiek izmantots datu pārraides kvalitātes analīzei. Rx bloks sastāv no optiskā pārskaņojamā vājinātāja (VOA), signāla jaudas mērītāja, lavīnfotodiodes (APD), elektriska filtra un analizatora. Optiskais pārskaņojamais vājinātājs tiek izmantots BER korelācijas diagrammas uzņemšanai. Tajā tiek uzstādīta vājinājuma vērtība decibelos (dB), par cik decibeliem nepieciešams novājināt signāla jaudas līmeni. Attiecīgi APD tiek pielietots, lai optisko signālu pārvērstu elektriskā signālā. APD priekšrocība, salīdzinājumā ar PD, ir spēja darboties pie zemākām signāla jaudām. Būtiski piezīmēt, ka signāla kvalitātes analīze pamata tiek tieši elektriskajam signālam. InGaAs APD jutība tiek uzstādīta uz -20 dBm pie references BER vērtības 10^{-12}. Elektriskā zemfrekveņču filtra josla uzstādīta uz 6 GHz -3 dB līmenī. Uztvertā signāla kvalitāte tiek vērtētā ar analizatora palīdzību. Analizators uzzīmē acs diagrammu, kurai tiek noteikta BER vērtība.
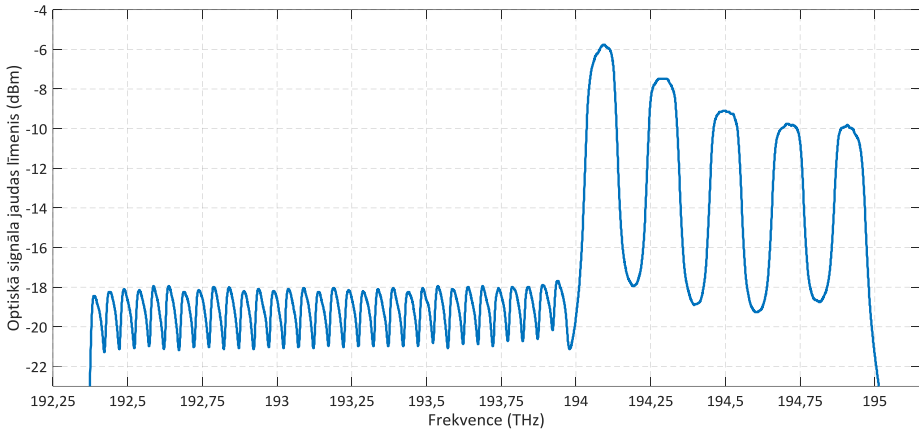
2.6. att. Atstarotais optiskais signāla spektrs sistēmai ar datu un sensoru kanāliem

Sistēmas spektrs, kas nomērīts ar sensora signāla apstrādes iekārtu, ir vērojams 2.6. attēlā, spektra kreisā puse vērojami 32 datu kanālu pīķi (ar strapkanāla intervālu 50 GHz), taču labā pusē – 5 FBG sensoru atstarotais signāls. Pilnvērtīgas savietojamības analīzei ir nepieciešams novērtēt, kādu ietekmi rada sensori uz pārraidāmo signālā kvalitāti. Ietekmi var novērtēt salīdzinot signāla kvalitāti sistēmai ar datu kanāliem, un pēc tam salīdzinot ar sistēmu, kurā ir integrēti dati un sensora kanāli. Konkrētās salīdzināšanas veikšanai tiek uzzīmēta BER korelācijas diagramma (BER atkarība no uztvertā signāla jaudas), sk. 2.7. attēlā.
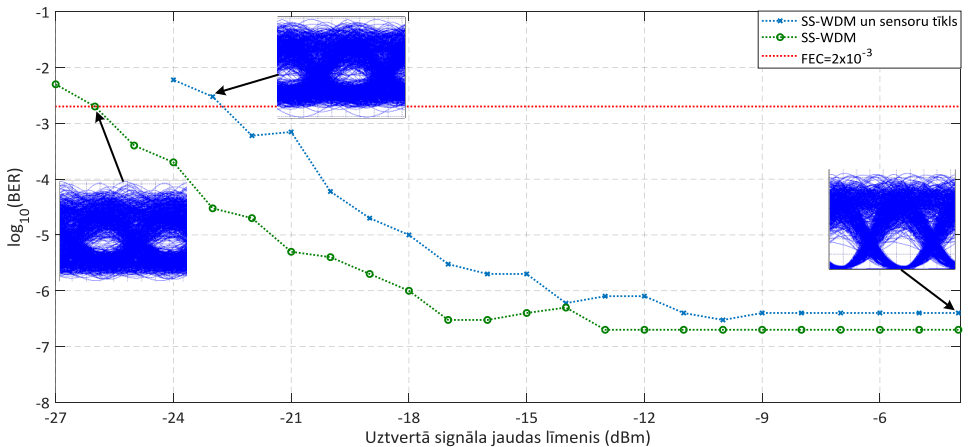
2.7. att. BER attiecības pret uztvertā signāla jaudas novērtējums spektrāli sagrieztai 32 kanālu šķiedru optiskajai datu pārraides sistēmai ar integrētu FBG sensoru tīklu pie SMF garuma 20 km.

Simulācijas modelī tiek paredzēta 7% datu pārraides ātruma rezerve (simulācijas veiktas pie 10,7 Gbit/s) FEC kļūdu labojošo kodu izmantošanai. Šādā gadījumā pieļaujamais BER slieksnis ir $2 \times 10^{-}$

35

[3], kas nozīmē, ka pie šādas vērtības datu pārraides sistēma spēs pilnvērtīgi darboties. Nomērītā BER vērtība SS-WDM PON datu kanāliem un FBG sensoru tīklam ir 4×10^{-7}, bet sistēmai ar datu kanāliem – 2×10^{-7}. Balstoties uz mērīju rezultātiem, tiek aprēķināta jaudas soda vērtība, kas ir vienāda ar 3,25 dB, salīdzinot SS-WDM-PON sistēmas datu kanāla rezultātus ar un bez FBG sensoru tīkla pie BER sliekšņa vērtības 2×10^{-3}.

2.3. Uz FWM optiskās frekvenču ķemmes balstītas DWDM optiskās sakaru sistēmas ar integrētu FBG sensoru tīklu

Simulācijas mērķis ir izstrādāt un novērtēt veiktspēju uz četru viļņu mijiedarbes balstītas optiskās frekvenču ķemmes (FWM-OFC) 8 kanālu DWDM pārraides sistēmas ar integrētu FBG sensoru tīklu. Simulācijas modelis (izstrādāts RSOFT OptSim) sastāv no optiskās līnijas termināļa (OLT), optiskās sadales tīkla (ODN) un optiskās tīkla iekārtas (ONUs), sk. 2.8. attēlu.
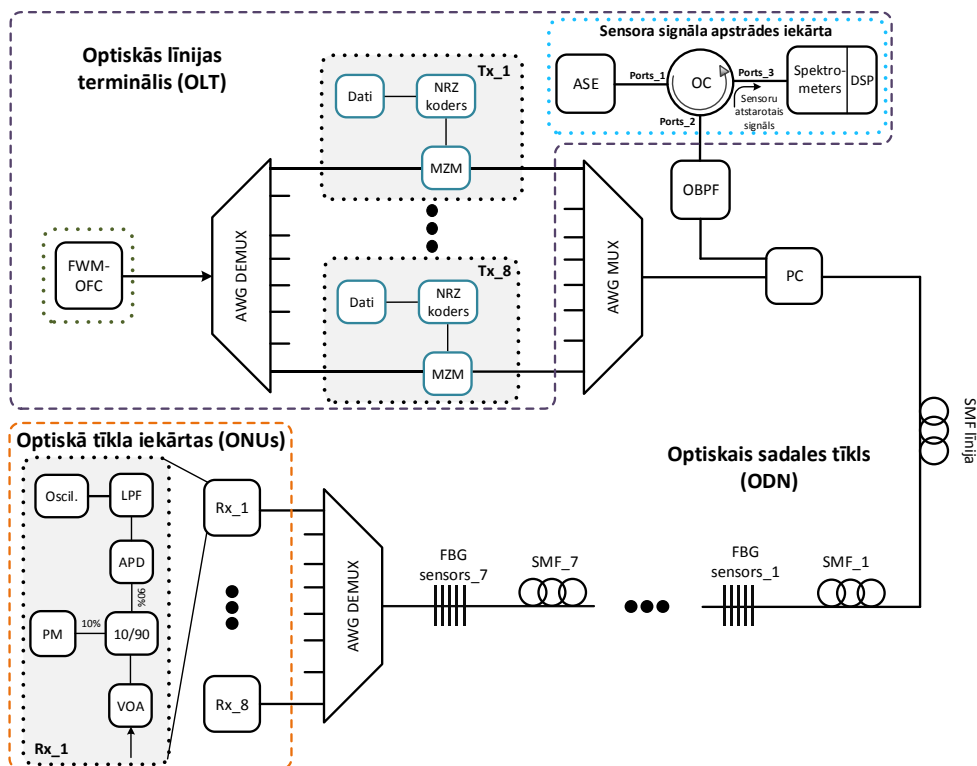
2.8. att. Matemātiskais simulācijas modelis 8 kanālu DWDM-PON sistēmai, kas balstīta uz FWM OFC ar integrētu 7 temperatūras sensoru tīklu.

FWM-OFC ģenerēšanai tika izmantoti divi nepārtraukta starojuma (CW) lāzeri, optiskais jaudas apvienotājs, paaugstinātas nelinearitātes (augsti nelineāra) šķiedra (HNLF) un ķemmes novērtēšanai tika izmantots OSA, sk. 2.9.attēlu. CW lāzera izejas jauda un HNLF garums tiek uzstādīts tāds, lai izejā tiktu iegūta frekvenču ķemme ar maksimālu ķemmju skaitu un augstu, līdzenu amplitūdu. CW lāzeriem tika uzstādīta izejas jauda 20 dBm un to centrālās frekvences uzstādītas 193,1 un 193,15 THz, lai nodrošinātu, ka starpkanālu intervāls starp tiem ir 50 GHz (atbilstoši ITU-T G.694.1 rekomendācijai [180]). HNLF šķiedras parametri (vājinājuma un dispersijas koeficients, efektīvais laukums, nelineārais indekss, u.c.) tiek uzstādīti pēc specifikācijas parametriem komerciālai šķiedrai. Noteikts, ka konkrētam risinājumam vispiemērotākais HNLF šķiedras garums ir 2 km.
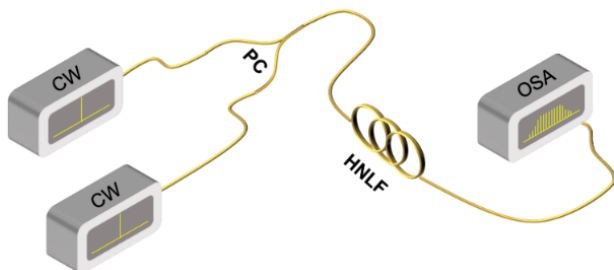
2.9. att. FWM-OFC ģenerēšanas slēguma shēma

OFC ģenerētās FWM frekvenču ķemmes toņu vidējās jaudas līmenis ir 0 dBm, fluktuācija ir zemāka par 3 dB, un 33 dB sānjoslu nospiešana frekvenču diapazonā 192,9 – 193,25 THz.

FWM-OFC bloks tiek savienots ar 8 kanālu 50GHz AWG DEMUX, kura izejas tiek savienotas ar raidītāja Tx bloku. Katrs Tx bloks sastāv no datu avota, NRZ kodera un NZM modulatora ar 20 dB ekstincijas koeficientu. Tx kanālu apvienošanai tiek izmantots AWG MUX. ODN daļā PC tiek izmantots, lai apvienotu 8 datu kanālus ar FBG sensoru tīklu. Lai nodrošinātu FBG sensoru tīklu darbību, tiek izmantota sensora signāla apstrādes iekārta. OBPF izfiltrē 800 GHz spektrālo joslu (frekvenču joslā 193,50 – 194,30 THz) sensoru tīklam pie -3dB līmeņa. ODN daļā FBG sensori tiek izvietoti starp SMF (ITU-T G.652D) līnijas posmiem (līdzīgi kā 2.5. att. shēmā).

Matemātiskās simulācijas modelī tika integrēti eksperimentāli laboratorijā nomērīti komerciāla [181] FBG sensora parametri: caurejošais un atstarotas spektrs (sk. 2.10. att.) un tehniskie parametri (centrālais viļņa garums, FWHM, atstarojamība u.c.). Eksperimentu laikā laboratorijā tika izmantots superluminiscences gaismu izstarojoša diode (SLED), 3-portu optiskais cirkulators, optiskais spektra analizators un FBG sensors. Visiem 7 FBG sensoriem tika uzstādīti vienādi parametri, izņemot to, ka katram FBG tika definēts savs centrālais viļņa garums. Konkrētā simulācijas modelī FBG temperatūras sensori var tikt vienkārši aizstājami ar FBG deformācijas, spiediena, pārvietojuma, u.c. sensoriem.
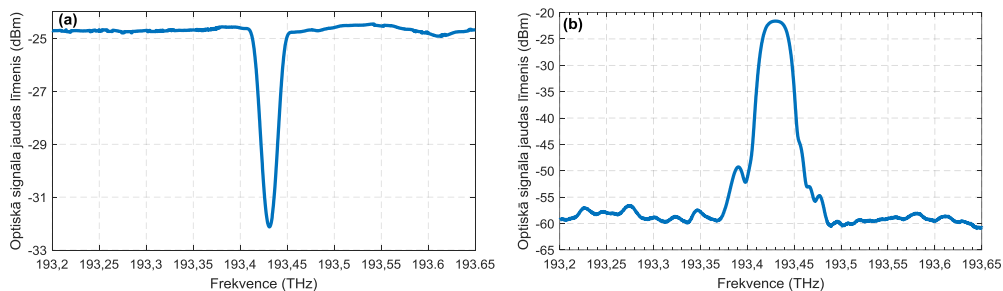
2.10. att. FBG sensora (a) caurejošais (b) atstarotais signāls pie vides temperatūras 25°C

ONUs blokā VOA, 10/90% jaudas sazarotājs, jaudas mērītājs, tiek izmantots, lai uzņemtu BER korelācijas diagrammas un uzraudzītu pievadīto jaudu uz APD fotodiodi (jutība -20 dBm pie BER≤10⁻¹²). Elektriskais Beseļa zemfrekvenču filtrs (LPF) ar 7.5 GHz joslu pie -3dB līmeni tiek izmantots, lai nofiltrētu trokšņus.

Datu pārraides kvalitātes novērtēšanai tiek izmantots ceturtais kanāls, kas uzrāda zemāko veiktspēju. 2.11. attēlā tiek attēlots osciloskopā uztvertais signāls laikā apvienotajam 10 Gbit/s sistēmas NRZ signālam pēc 50 km pārraides pa SMF šķiedru. Kā vērojams 2.11. un 2.13. (b) attēlā, NRZ signālam ir novērojama dispersijas ietekme, kā rezultātā impulsi paplašinās.
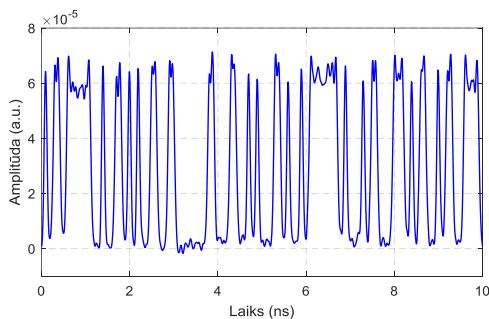
2.11. att. Uztvertais signāls 10 Gbit/s NRZ signālam pēc 50 km pārraides
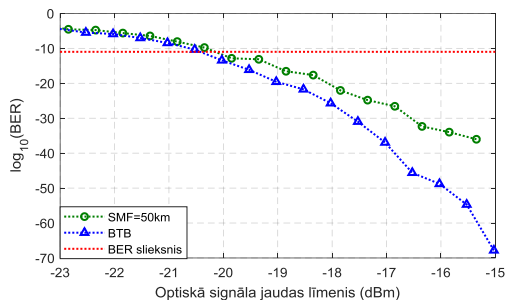
2.12. att. BER attiecības pret uztvertā signāla jaudas novērtējumu 8 kanālu ŠOPS ar integrētu FBG sensoru tīklu pēc 50 km pārraides.

BTB konfigurācijas gadījumā tiek saglabāts FBG sensoru tīkls, un līnijas garums tiek uzstādīts uz 0 km. Tipiskās BER vērtības dažādās sistēmās var atšķirties pēc konfigurācijas, komponentu, parametru u.c. atšķirību dēļ. Apskatītam sistēmas modelim, kurā ir apvienota optisko sensoru sistēma un blīvā WDM-PON sistēma, BER ir jābūt vismaz <10⁻¹², kas parasti tiek uzskatīts par BER slieksni bezkļūdu pārraidei [182-184]. Acs diagrammas apvienotai sistēmai pēc BTB un 50 km pārraides ir attēlotas 2.13. attēlā. Acs diagrammas ir plaši atvērtas, kas ļauj veikt bezkļūdu pārraidi. BTB konfigurācijā uztvertais BER ir vienāds ar 8×10⁻⁶⁷, bet pēc 50 km pārraides ir 9,4×10⁻³⁷.
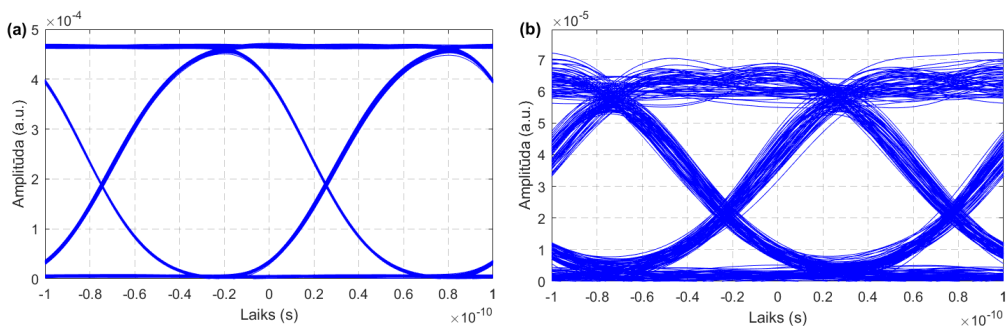
2.13. att. Acs diagramma apvienotās sistēmas sliktākam veiktspējas datu kanālam pēc (a) BTB (b) 50 km pārraides.

Kopsavilkums:

No veiktiem pētījumiem un iegūtajiem rezultātiem var secināt, ka FBG sensori var tikt integrēti DWDM, SS-WDM šķiedru optiskajās sakaru sistēmās, neradot būtiski ietekmi uz sakaru sistēmas datu pārraides kvalitāti. Hibrīdai uz viena platjoslas gaismas balstītai sistēmai ar 32 kanālu 10 Gbit/s SS-WDM PON datu kanāliem un FBG sensoru tīklu uztvertais BER ir 4×10^{-7}, bet sistēmai bez FBG tīklu – 2×10^{-7}.

Oriģinālpublikācijas un Latvijas Republikas patents par šajā apakšnodaļā aprakstītajiem pētījumiem atrodami **pielikumos II-VIII**.

3. FBG OPTISKO SENSORU PIELIETOJUMS AUTOCEĻU TEHNISKĀ STĀVOKĻU UZRAUDZĪBĀ

Lai nodrošinātu augstu publiskās infrastruktūras, ceļu, tiltu, pārvadu drošības līmeni, ir nepieciešams nepārtraukti novērtēt konstrukciju nestspēju, ko ietekmē novecošanās, nolietojums un bojājumi. Asfaltbetona segums pasliktinās pieaugošās satiksmes un sarežģītajos klimatiskajos apstākļos, t.i., mainoties temperatūrai un mitrumam atkarībā no sezonalitātes[185]. Šķiedras Brega režģa sensori ir lieliski piemēroti un ļauj momentāni reālā laikā identificēt konstrukciju deformāciju, nogurumu, nestspēju, plaisas, celtniecības defektus autoceļu konstrukcijās[11, 72-79]. Tā kā bieži mērījumi ir jāveic attālos reģionos vai arī vidēs ar elektromagnētisko iedarbību, vai vidēs kurā nav pieejama elektrobarošana, tad arvien biežāk tiek un tiks izmantoti optiskās šķiedras sensori.

Autoceļu tehniskā stāvokļu uzraudzības veikšanai tika izmantota 8 kanālu sensoru signāla apstrādes iekārta un optiskais sadales tīkls. Sensoru signāla apstrādes iekārta konkrētā risinājumā darbojas kā raiduztvērējs, kuras raidošā daļa tika izmantots SLED platjoslas avots (FWHM=55 nm), savukārt uztverošā daļā – optiskais spektrometrs un DSP bloks. Optiskais spektrometrs salīdzinājumā ar OSA nodrošina 10^3 reizes augstāku (OSA $5 \frac{nolases}{sek}$ [186], spektrometrs $5000 \frac{nolases}{sek}$) ātrdarbību, kas ir ļoti būtiski, lai precīzi novērtētu transportlīdzekļu radītās deformācijas noteikšanu kustībā. Būtiski piezīmēt, ka iekārtu ātrdarbības vērtības attiecas uz gadījumu, kad izmantots viens kanāls. Attiecīgi, ja tiek izmantoti n spektrometra kanāli, tad nolašu skaits arī samazinās n reizes. Digitālā signāla procesors (DSP) uztver spektrometra datus, detektē sensora/u centrālās frekvences un matemātiski aprēķina temperatūras un deformācijas vērtības. Matemātiski aprēķinātās parametru vērtības tiek attēlotas grafiski atkarībā no laika.
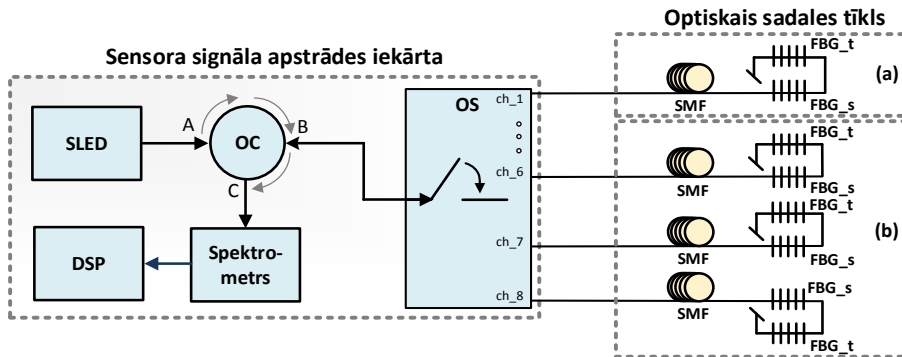
3.1. attēls Temperatūras un deformācijas uzraudzības sistēmas shēma

Optiskais slēdzis (OS) tiek izmantots, lai nodrošinātu pārslēgšanos no porta uz portu pēc iepriekš uzdota laika intervāla. Konkrētais optiskais slēdzis ir komponente, kas ļauj veikt 8 dažādu kanālu

(sensoru, sensoru tīklu) paralēlu uzraudzību reālā laikā. Sensoru signāla apstrādes iekārta tiek savienota ar ITU-T G.652 rekomendācijas SMF kabeli un FBG temperatūras un deformācijas sensoriem, kas iestrādāti autoceļā.

FBG sensoru integrācijas vietas reāla autoceļa segumā tika izvēlētas tā, lai tās atbilstu Eiropas specifikācijai transportlīdzekļu svēršanai gaitā (WIM). Pētījumu veikšanai tika izvēlēti A2 (Rīga—Sigulda—Igaunijas robeža) un A8 (Rīga—Jelgava—Lietuvas robeža) autoceļi.

3.1. Autoceļa SHM ar ceļa segas virskārtas slānī integrētiem FBG sensoriem

Komerciāli FBG deformācijas [187] un temperatūras [188] sensoru iestrāde segumā tika veikta 2019.-2020.g. sezonā 2 lokācijas vietās A2 autoceļa pārbūves projekta ietvaros (37 km, virzienā uz Rīgu) autoceļa segas virskārtas slānī. A2 autoceļā tika integrēts komerciāls pie virsmas stiprināms FBG deformācijas sensors ar režģa garumu 10 mm, kas integrēts stikls̆ķiedras kompozītmateriālā (250 × 15 mm) plāksnītē [187], un keramikas caurulē (diametrs 3mm, garums 23 mm) integrēts FBG temperatūras sensors [188]. Temperatūras sensors keramikas caurulē nodrošina izolāciju no deformācijas ietekmēm.

Lokācijā (a) 57°07′18.4″N 24°40′02.6″E FBG deformācijas un temperatūras sensori tiek integrēti ceļa segas virskārtas 30 mm akmens mastikas (SMA11) slānī. Sensoru integrācijas dziļumus ir 25 mm. Lokācijā (a) ceļa segai ir daudzslāņu konstrukcija (30 mm SMA11, 60 mm AC11, 150 mm šķembas, smilts), bet lokācijā (b) slāņu konstrukcija (70 mm AC11 un grants).


3.2. attēls FBG sensora integrācija autoceļa seguma virskārtas slānī (a) un (b) lokācijā.

Lokācijā (b) 57°07′07.4″N 24 ° 39′04.1″E FBG deformācijas un temperatūras sensori tiek integrēti pagaidu autoceļā 70 mm asfaltbetona (AC11) slānī 25 mm dziļumā.

Ņemot vērā, ka autotransporta radītā deformācija uz segumu ir atkarīga ne tikai no slodzes, bet arī no seguma temperatūras, ir būtiski izstrādāt FBG sensoru kalibrācijas metodi. FBG sensoru kalibrācijā tiek lietots krītoša svara deflektometrs (FWD), sk. 3.3. attēlā, kas nodrošina fiksētas, kalibrētas slodzes pievadīšanu uz FBG sensoru. FWD tipiski tiek plaši izmantota kā nesagraujošu seguma testēšanas un stāvokļa novērtēšanas metode [189-191]. FWD slodzes atkarība laikā pie 50 kN slodzes pievadīšanas ceļa segumam attēlota 3.4. attēlā. FWD plāts pie 50 kN slodzes ģenerē 707 kPa spiedienu (kas ir līdzvērtīgs spiediena lielumam, ko rada smagais kravas auto – līdzvērtīgs 10 tonnu ass slodzei).

3.3. attēls FWD iekārta
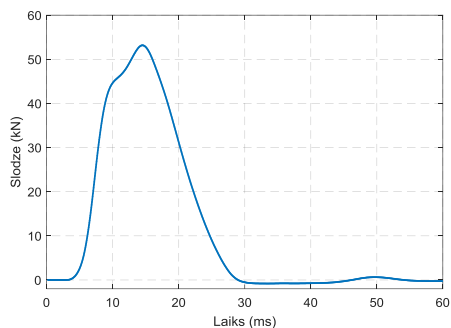
3.4. attēls FWD pievadītās slodzes atkarība laikā

Lai novērtētu FBG sensora darbību attālumu horizontāla virzienā, tika izmantota FWD iekārta. Pētījums tika veikts (a) lokācijas vietā. FWD iekārtas plāts centrs tika novietots 4 attālumos (tiešu uz sensoru un 300, 600, 900 mm attālumā), kas pievada fiksētu 48,9±0,5 kN spēku 6 reizes, sk. 3.1. tabulā. Visu mērījumu laikā tiek veikta temperatūras kompensācija ar FBG sensoru. Kā vērojams 3.1. tabulā, iegūtie rezultāti parāda, ka ar FBG sensoru var precīzi (relatīvā izkliede 4,8–12,8%) noteikt deformācijas vērtības, kas ļauj novērtēt seguma konstrukcijas reālo darbību zem slodzes.

3.1. tabula.

Deformācijas (µm/m) vērtību atkarība no horizontālā attāluma starp FWD plāts centru un sensoru

FWD pievadītās slodzes nr.	Horizontālais attālums no FWD plāts centra līdz FBG sensoram (mm)			
	0	300	600	900
1	162,5	91,5	24,6	12,5
2	145,9	77,6	27,0	13,1
3	142,7	80,5	24,2	12,2
4	149,5	73,4	28,3	12,1
5	161,6	85,8	25,7	13,2
6	148,5	71,2	25,1	13,2
Vidējā deformācijas vērtība (µm/m)	151,8±9,9	80,0±10,2	25,8±2,1	12,7±0,6

Kā redzams, lielākā deformācijas vērtība (vidēji 151,8 ± 9,9 µm/m) tiek noteikta gadījumā, kad FWD plāts centrs atrodas tieši virs iestrādātā FBG deformācijas sensora.

Augstas precizitātes rezultātus var iegūt tikai no tās puses, pie kuras FBG deformācijas sensors ir fiksēts (sāna virsmas). Konkrētā plāksnīšu tipa sensoriem ir trūkums, kas jāņem vērā integrējot sensorus objektā. Fiksētai vienvirziena satiksmei tas nerada uzraudzības ierobežojumus, bet maiņsatiksmes gadījumā nepieciešams integrēt FBG sensorus abās pusēs.

FWD pēc katra spēka pievadīšanas ("sitiena izdarīšanas") nomēra pievadīto spēku. No mērījumu datiem izriet, ka izkliede visos gadījumos ir mazāka par 1% . Mērījumi tika veikti vasarā pie seguma temperatūras 20,5ºC.

Ar FBG sensoru nomērītā deformācijas atkarība laikā, gadījumā, ka FWD plāts centrs novietots 900 mm attālumā, tiek attēlota 3.5. attēlā. Attēlā redzami 6 stabili pīķi, kuru vērtību izkliede ir 4,7%, savukārt FWD pievadītā slodze ir 48,9 ± 0,5 kN. Pīķi ar zemāku amplitūdu reprezentē FWD plāts amortizāciju, lai stabilizētu un pozicionētu iekārtu miera stāvoklī. Pie horizontālā attāluma 900 mm vidējā deformācija ir vienāda ar 12,7±0,6 µm/m.
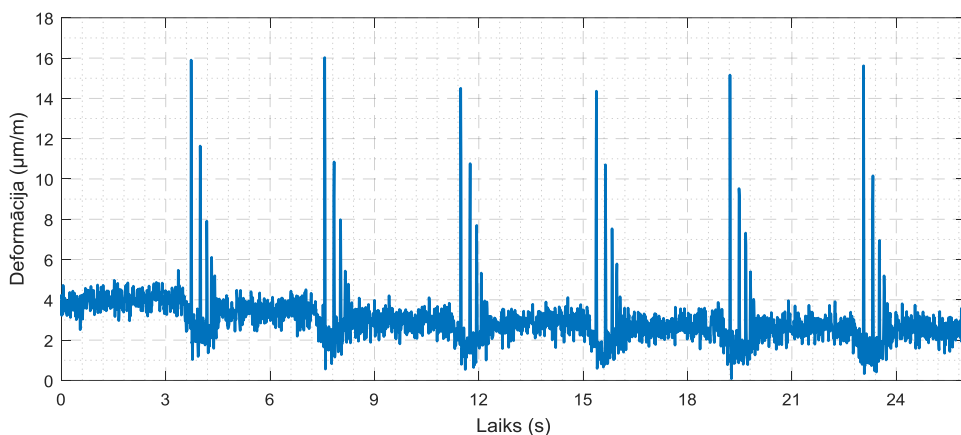

3.5. attēls Deformācijas atkarība laikā gadījumā, kad horizontālais attālums starp FWD plāts centru un FBG ir 900 mm un FWD iekārtas pievadītā slodze vienāda ar 48,9 ± 0,5 kN.

Lai novērtētu ceļa seguma temperatūras ietekmi uz izmērīto deformāciju, rudenī (seguma temperatūras 6,9ºC) tika atkārtota vēl viena mērījumu sesija. Rezultātu salīdzinājumu pie 6,9° un 20,5°C temperatūras skatīt 3.6 attēlā. Eksperimenta laikā deflektometra slodze ir 51,98 ± 0,94 kN. Kā vērojams rezultātos, tad visā mērījumu diapazonā FBG deformācijas vērtības rudenī ir zemākas nekā vasarā. Tāda pati tendence tika novērota pētījumā [76]. Siltākā laikā deformācijas vērtības bija augstākas, jo pie augstākām temperatūrām samazinās stingums un tā rezultātā deformācijas vērtības palielinās. Balstoties uz iegūtiem rezultātiem, ir būtiski, analizējot transportlīdzekļu radīto deformācijas mērījumus, ņemt vērā ceļa seguma temperatūru.
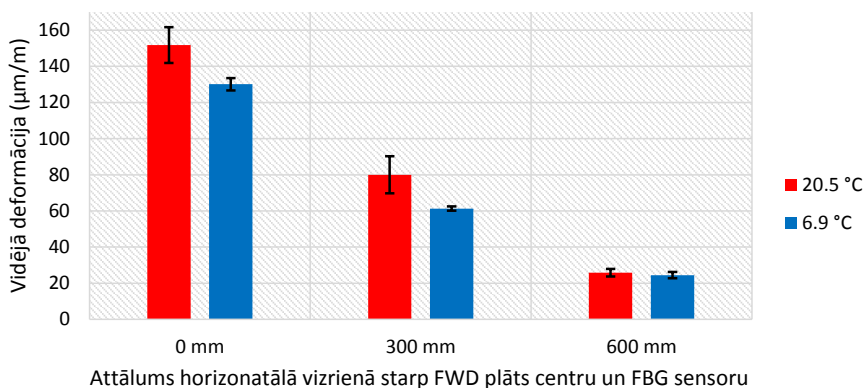
3.6. attēls Vidējās deformācijas vērtības attiecība pret attālumu horizontālā virzienā starp FWD plāts centru un FBG sensoru pie seguma temperatūras 6,9° un 20,5°C.

Transportlīdzekļu satiksmes reāllaika uzraudzība tika realizēta 2019. gada septembrī pagaidu ceļa posmā, (b) lokācijas vietā. Vidējā temperatūra ceļa segumam (mērot ar FBG temperatūras sensoru) mērījumu laikā bija +25,2 °C. Sensoru iestrādei tika izvēlēta vieta, kur ir augsta gada vidējā diennakts satiksme (AADT) un vidēji augsta gada ikdienas kravas automašīnu satiksme (AADTT). 2019. gada laikā pa konkrēto ceļu posmu pārvietojās 3,15 miljons transportlīdzekļu, no kuriem 23,3 % jeb 735 000 ir kravas automašīnas [192]. Paralēli reāla laika deformācijas uzraudzībai tika veikta video ierakstīšana, lai pārliecinātos, ka ceļu satiksmes izmaiņas korelē ar deformācijas mērījumiem, kā arī redzētu dažādu transportlīdzekļu, galvenokārt kravas automobiļu, "deformācijas rakstu".
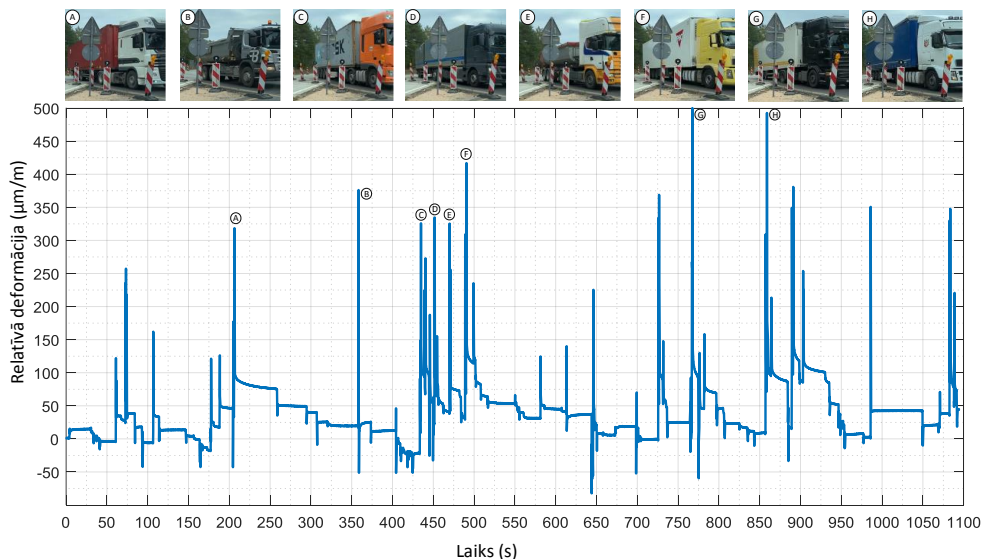

3.7. attēls Reālā laikā ar FBG sensoru nomērītās deformācijas raksturlīkne laikā

44

No FBG deformācijas sensora mērījumu datiem (3.7. att.) izriet, ka īpaši kravas automašīnas rada vislielākās deformācijas seguma konstrukcijā. Ja grafiks tiek pietuvināts, tad var noteikt transportlīdzekļa asu skaitu un katra transportlīdzekļa ass deformācijas vērtību. No mērījumu datiem izriet, ka kravas automašīnas "G" pēdējā (5.) ass rada vislielāko deformāciju (relatīvās deformācijas vērtība 375,6 μm/m). Otro lielāko deformācijas vērtību (356,4 μm/m) radīja "B" grants kravas auto ar trim asīm. Svarīgi atzīmēt, ka 3.7. attēlā augšējā daļā vizuāli nav redzamas visas kravas automašīnas, piemēram, laika brīžos 73, 728, 891, 986 un 1084 s. Izmērītās deformācijas vērtības ir salīdzināmas un līdzīgas ar pētījuma [193] datiem.

FBG deformācijas sensora mērījumu datu kopsavilkums, kas iegūts no kravas auto satiksmes uzraudzības, tiek attēlots 3.8. attēlā. Rezultātu analīzē galvenā uzmanība tiek pievērsta kravas auto, nevis vieglo automašīnu satiksmei, jo kravas automašīnas rada vislielākās deformācijas vērtības un potenciālos ceļa seguma bojājumus. Svarīgi piebilst, ka deformācijas vērtības histogramma satur visus mērījumu datus, ne tikai tos, kas parādīti 3.7. attēlā.

Kā redzams 3.8. attēla, kravas auto visbiežāk (33% gadījumos) rada 300-350 μm/m lielu deformāciju. Apkopojot un salīdzinot visus kravas auto datus, tie vidēji rada 282 μm/m deformāciju.
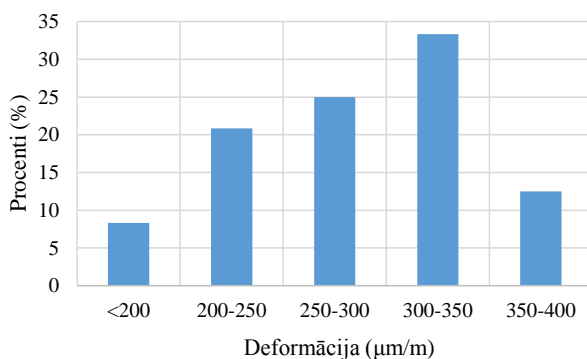

3.8. attēls Ar FBG sensoru nomērītās kravas auto radīto deformācijas vērtību histogramma

3.2. Autoceļa SHM ar ceļa segas stabilizētas kārtas slānī ar reciklētu asfaltbetonu integrētiem FBG sensoriem

2020.-2021. gada sezonā FBG sensoru iestrāde tika veikta Meitene-Jelgava-Rīga (A8) šosejas autoceļa stabilizētas kārtas slānī ar reciklētu asfaltbetonu (turpmāk reciklētā slānī) (ģeogrāfiskā lokācija). Ceļa segā tika integrēts komerciāls enkura deformācijas sensors [194] ar darbības diapazonu ±5000με, precizitāti <1μm, centrālo viļņa garumu 1544,8 nm, un temperatūras sensors [195] ar darbības diapazonu -40°C līdz 120°C, precizitāti ±0,3ºC un centrālo viļņa garumu 1554,558 nm.

Sensoru integrācija veikta ceļa segas reciklētā slānī 25 mm dziļumā (kopējais integrācijas dziļums 240 mm), skatīt 3.9. attēlā.
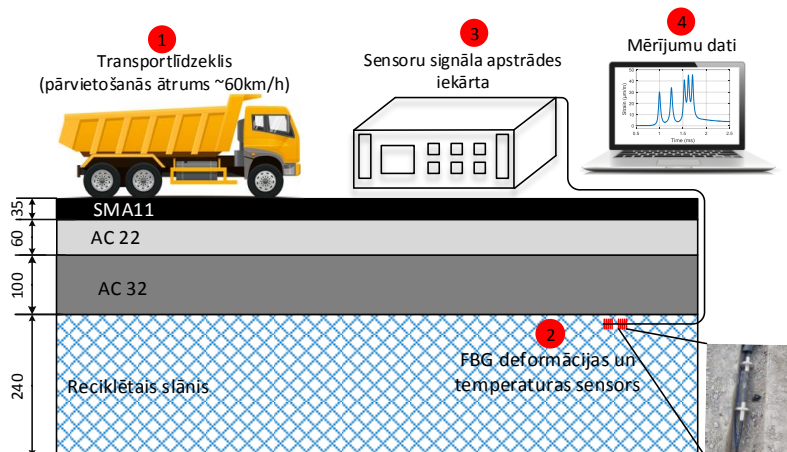

3.9. attēls Shēma FBG sensoru integrācijai ceļa segā temperatūras un deformācijas mērījumiem

Kā redzams 3.10. attēlā, pievadot slodzi ar FWD deflektometru tieši virs FBG sensoru vidējā deformācija $\Delta\varepsilon\_avg$ ir 34,63 μm/m, bet scenārijā, kad slodzes plāksne atrodas 50 cm attālumā no sensora, vidējā deformācija ir 14,03 μm/m. Mērījumi veikti pie reciklētā seguma temperatūras 1 – 1,5 ˚C. Apskatītā diapazonā deformācijas atkarību no attāluma var raksturot ar lineāru funkciju. No rezultātiem izriet, ka pētījumā būtiski nodrošināt, ka transportlīdzeklis uzbrauc uz sensoru, vai maksimāli tuvu sensoram. Gadījumos, kad iepriekš minēto prasību nav iespējams izpildīt, autors iesaka izmantot sensoru tīklu risinājumus, lai paralēlā slēgumā ar nobīdi pēc attāluma (piem. 20 cm) izvietot sensorus.
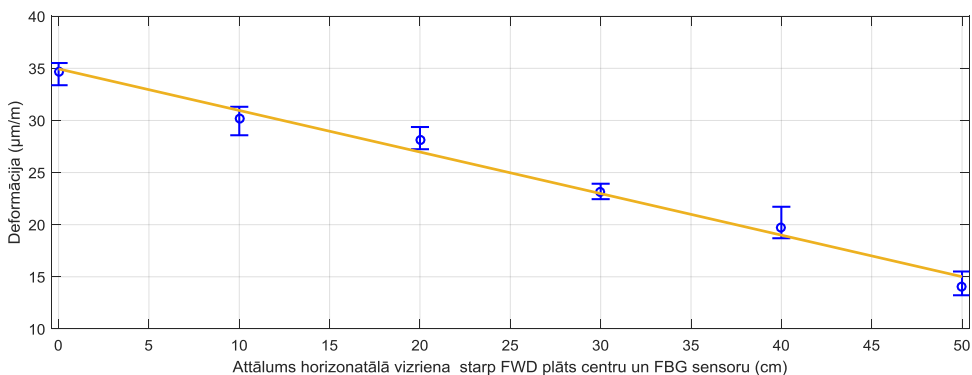
3.10. attēls Nomērītās vidējās deformācijas vērtību attiecība pret attālumu horizontālā virzienā starp FWD plāts centru un FBG sensoru

3.11. attēlā tiek attēlota FBG deformācijas sensora nomērītās vidējās deformācijas atkarība no FWD pievadītā spiediena gadījumā, kad sensori integrēti A8 autoceļa segas reciklētā slānī. Mērījumu laikā reciklētā seguma temperatūra ir 1 – 1,5 °C. Palielinot FWD pievadīto spiedienu (diapazonā no 470-1170 kPa ar soli 200 kPa), pieaug deformācijas vērtības ar lineāru raksturu. Balstoties uz iegūtās raksturlīknes datiem, iespējams veikt sensoru kalibrāciju reālā vidē. Šāda sensoru kalibrācijas metode jāizmanto transportlīdzekļu svēršanai gaitā, nosakot deformācijas vērtības atkarībā no transportlīdzekļa masas.
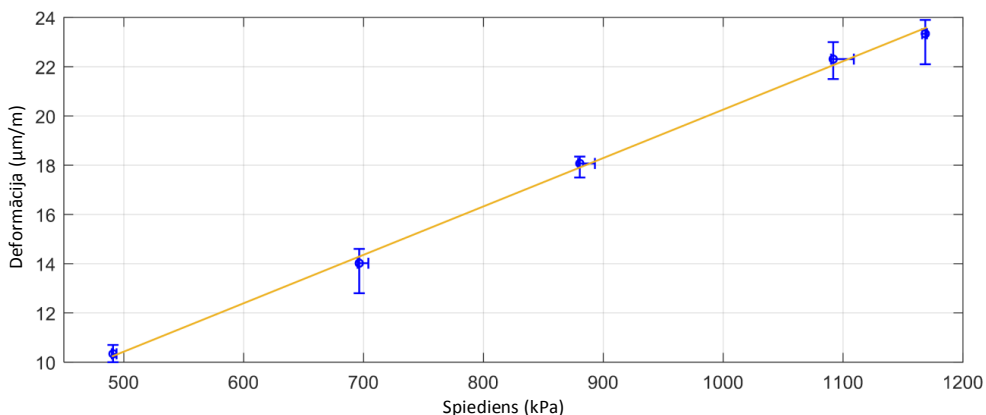
3.11. attēls FBG sensora nomērītās vidējās deformācijas atkarība no FWD pievadītā spiediena

3.2. tabula attēlotas FWD iekārtas radītās vidējās deformācijas vērtības atkarība no ceļa segas temperatūras. Pētījums tika veikts ziemā un vasarā pie attiecīgām ceļa segas temperatūrām 1 – 1,5 °C un 24,8 – 25,1 °C. Pētījumā laikā FWD iekārta atradās tieši virs sensora un pievadītā slodze ir vienāda ar 50 kN (707 kPa spiediens).

3.2. tabula

FWD iekārtas radītās deformācijas atkarība no ceļa segas temperatūras

Temperatūra ceļa segas reciklētā slānī	1 – 1,5 °C	24,8 – 25,1 °C
$\Delta\varepsilon_{avg}$ (μm/m)	34,63	13,70
Izkliede (%)	4,26	6,57

No mērījuma datiem izriet, ka pie temperatūras 1 – 1,5 °C vidējā deformācija ir 2,5 reizes augstākā nekā pie 24,8 – 25,1 °C temperatūras. Šādi rezultāti skaidrojami ar vides temperatūras ietekmi uz dažādiem ceļa konstrukcijas slāņiem. Samazinoties vides temperatūrai, samazinās arī ceļa slāņu materiālu temperatūra. Pie zemākām temperatūrām, piemēram, ziemā, augšējie asfalta slāņi kļūst

47

stingāki, līdz ar to FWD ierīces (vai jebkurš transporta līdzeklis) izraisītā slodze tiek pārnesta uz dziļākiem ceļa slāņiem – reciklēto slāni. Rezultāti parāda, ka temperatūras ietekme ir būtiska un tā jāņem vērā mērījumu laikā un sensoru kalibrācijas procesā. Rezultātā sensoru kalibrācija jāveic ne tikai atkarība no slodzes vai spiediena, bet arī no temperatūras.

Tā kā eksperimenti ar FWD ierīci apstiprināja stabilu un pareizu FBG deformācijas optisko sensoru darbību, nākamajā pētījuma posmā tika veikti reāllaika transporta satiksmes deformācijas uzraudzības eksperimenti pie seguma temperatūras 1 – 1,5 °C. Satiksmē tika analizēti visi transportlīdzekļi, sākot no 2 asu vieglajiem automobiliem līdz 6 asu kravas automobiliem. Tā kā pa ceļu pārvietojas dažādi transporta veidi, un, lai labāk izprastu deformācijas izraisītās izmaiņas un to diapazonu, tad visi transportlīdzekļi tika klasificēti 4 grupās: 2 asu vieglās automašīnas (3.12. att. (a)), 2 asu mikroautobusi (3.12. att. (b)), 2-3 asu kravas automašīnas (3.12. att. (c)) un 4-6 asu kravas automašīnas (3.12. att. (d-f)). 3.12. attēlā tiek attēlotas 6 nejauši izvēlētiem transportlīdzekļiem nomērītās deformācijas izraisītas izmaiņas laikā. Kā redzams 3.12. attēlā, rezultātos FBG optiskais deformācijas sensors ļauj precīzi noteikt deformācijas izraisītās izmaiņas laikā transportlīdzekļa katrai asij. Iegūtos rezultātus var izmantot, lai noteiktu transportlīdzekļa pārvietošanās ātrumu, piemēram, 3.12. att. (a) mērījums veikts BMW X5 automašīnai (attālums starp asīm 2,975 m), savukārt nomērītais laiks starp deformācijas maksimumiem ir 0,164 ms. Matemātiski var aprēķināt, ka transportlīdzekļa pārvietošanās ātrums ir 65,3 km/h.
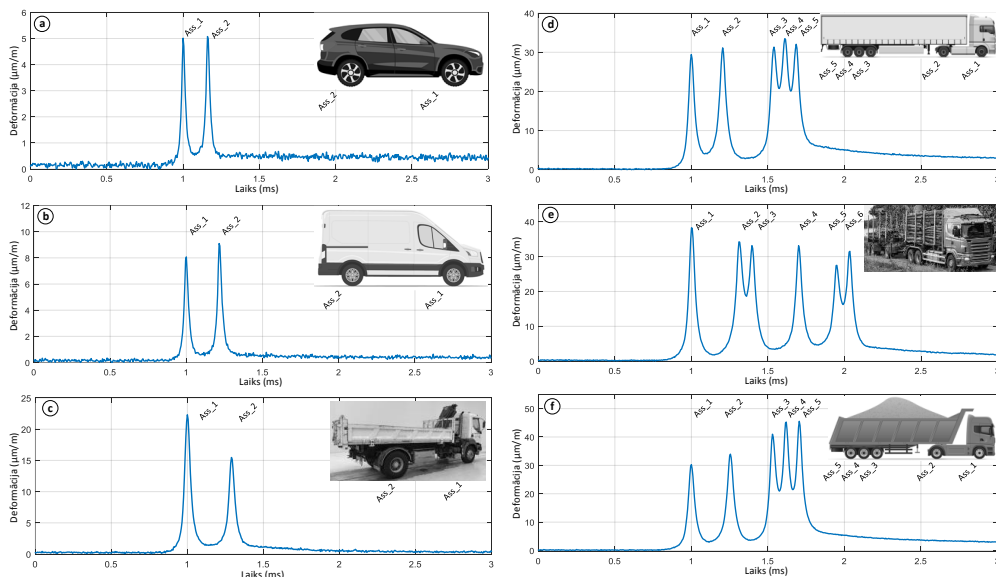
3.12. attēls Reāllaika transporta satiksmes deformācijas mērījumi dati

Svarīgi ir norādīt, ka atkarībā no transportlīdzekļa veida, masas, asu skaita, deformācijas lieluma atslābuma laiks ir dažāds. Vieglajiem transportlīdzekļiem tipiskais atslābuma laiks ir līdz 3 s, bet kravu transportlīdzekļiem līdz 5 s.

3.3.tabula tiek attēloti apkopotās deformāciju vērtību intervāli (transportlīdzekļa asij) katrai transportlīdzekļu grupai. Deformāciju vērtību intervāli tiek definēti 2 daļās: 1) pilnais vērtību diapazons; 2) tipiskais vērtību diapazona intervāls, kurā iekļaujas 90% kopējo gadījumu.

3.3. tabula

Ar FBG nomērītais deformāciju diapazons un noteiktais tipisko deformāciju diapazons reāla laika transportlīdzekļu trafikam

	 2 asu vieglās automašīnas	 2 asu mikroautobusi	 2-3 asu kravas automašīnas	 4-6 asu kravas automašīnas
Deformāciju diapazons (µm/m)	0,7-6	4,6-13	10-38	12-42
Tipiskais (90% gadījumos) deformāciju diapazons (µm/m)	0,8-4,1	5,5-8,5	11-26	14-36

No mērījumu datiem izriet, ka vieglās automašīnas ass rada tipiski 2-10 reizes mazāku deformāciju nekā 2 asu mikroautobusi un 3–45 reizes mazāku deformāciju nekā 4–6 asu kravas automašīnas ass.

Kopsavilkums:

No veiktiem pētījumiem un iegūtajiem rezultātiem var secināt, ka enkura tipa FBG sensori ir vispiemērotākie autotransporta radīto deformāciju novērtēšanai uz ceļa seguma. Veicot autoceļu uzraudzību, FBG deformācijas sensori jākalibrē ne tikai atkarībā no pievadītās slodzes, bet arī no seguma slāņa temperatūras. FBG sensoru augstā jutība ļauj noteikt katra transportlīdzekļa ass radīto deformāciju. Eksperimentu mērījumu rezultāti ir ļoti aktuāli vietējiem un starptautiskajiem ceļu seguma projektētājiem un ceļu apsaimniekošanas dienestiem, lai prognozētu iespējamo ceļa kalpošanas laiku, paliekošās deformācijas, transportlīdzekļu svaru un to asu skaitu, kā arī satiksmes un ceļu seguma temperatūras uzraudzību. Eksperimentu mērījumu datus var izmantot arī viedo ceļu risinājumos [196], piemēram, satiksmes plūsmas analīzei, transportlīdzekļu uzskaitei un brīvo autostāvvietu analīzei.

Oriģinālpublikācijas par šajā apakšnodaļā aprakstītajiem pētījumiem atrodamas **pielikumos IX - XI**.

SECINĀJUMI

1. Visaugstvērtīgākos rezultātus (atstarojamība = 90,3%, FWHM = 0,112 nm, SLS = 35,6 dB) FBG sensoru tīklu liela attāluma uzraudzības risinājumiem uzrāda FBG ar paceltā sinusa apodizāciju pie $\Delta n=1\times10^{-4}$ un L= 20 mm.

2. Sensoru tīklu, kas sastāv no 40 FBG sensoriem ar paceltā sinusa apodizāciju pie $\Delta n=1\times10^{-4}$ un režģa garuma 20 mm var izmantot vismaz 60 km un lielāka attāluma uzraudzības risinājumos.

3. Hibrīdai uz viena platjoslas gaismas avota balstītai sistēmai ar 32 kanālu 10 Gbit/s SS-WDM PON datu kanāliem un 5 FBG sensoru tīklu uztvertais BER ir 4×10^{-7}, bet sistēmai bez FBG tīkla – 2×10^{-7}. FBG sensoru tīkls nebūtiski ietekmē sakaru sistēmu.

4. Jaudas sods apvienotai SS-WDM datu pārraides un sensoru sistēmai ar un bez FBG sensora pie FEC sliekšņa $2,3\times10^{-3}$ bez pārraides līnijas ir 0,5 dB, bet pie SMF garuma – 20 km 0,2 dB.

5. Balstoties uz autoceļos veiktajiem eksperimentālajiem mērījumu rezultātiem, var secināt, ka enkura tipa FBG deformācijas sensori ir vispiemērotākie integrēšanai autoceļa segumā, lai reālā laikā novērtētu autotransporta radīto deformāciju un veiktu tehniskā stāvokļa uzraudzību.

6. Autoceļa reciklētā seguma slānī vieglās automašīnas ass tipiski rada 2-10 reizes mazāku deformāciju nekā 2 asu mikroautobusi (attiecīgi 0,7-6 μm/m un 4,6-13 μm/m) un 3–45 reizes mazāku deformāciju nekā 4–6 asu kravas automašīnas ass (12-42 μm/m).

Darba gaitā izstrādātās rekomendācijas paredzētas:

- FBG sensoru tīklu izstrādātājiem un ražotājiem;

- ekspluatācijā esošu optisko metro-piekļuves tīklu uzlabošanai, gan arī jaunu ieviešanai;

- vietējiem un starptautiskajiem ceļu seguma projektētājiem un ceļu apsaimniekošanas dienestiem, viedo ceļu risinājumos attīstītājiem un izstrādātājiem.

Promocijas darba laikā iegūtie un pētījumos attēlotie rezultāti ir prezentēti 5 zinātniskajos oriģinālrakstos un 4 zinātniskās konferencēs (indeksētas Scopus, IEEE vai Web of Science) vienā monogrāfijā, vienā Latvijas Republikas patentā. Kā arī pētījumu rezultāti tika prezentēti 13 zinātniskajās konferencēs (nav indeksēti Scopus, IEEE, Web of Science).

Publikas informēšanas pasākumi: Eiropas Zinātnieku naktis, Latvijas Radio 1 "Zināmais nezināmajā", RTU mājaslapa, Žurnāls "IR", Delfi, LMT, LETA, IZM, labsoflatvia, dienas bizness, LA.lv, u.c.

LITERATŪRAS SARAKSTS

1. A. Abdelgawad and K. Yelamarthi, Internet of Things (IoT) platform for structure health monitoring, Wireless Communications and Mobile Computing, vol. 2017, Article ID 6560797, 10 pages, 2017. DOI: doi.org/10.1155/2017/6560797.

2. Q. Jin, Z. Liu, J. Bin, and W. Ren, Predictive analytics of in-service bridge structural performance from SHM data mining perspective: a case study, Shock and Vibration, vol. 2019, Article ID 6847053, 11 pages, 2019. DOI: doi.org/10.1155/2019/6847053.

3. H. Xu, F. Li, W. Zhao, S. Wang, Y. Du, and C. Bian, A high precision fiber Bragg grating inclination sensor for slope monitoring, Journal of Sensors, vol. 2019, Article ID 1354029, 7 pages, 2019. DOI: doi.org/10.1155/2019/1354029.

4. L. Fan, Y. Bao. Review of fiber optic sensors for corrosion monitoring in reinforced concrete. Cem. Concr. Compos. 2021, 120, 104029. DOI: doi.org/10.1016/j.cemconcomp.2021.104029.

5. D. Budnicki, I. Parola, Ł. Szostkiewicz, K. Markiewicz, Z. Hołdy´nski, G. Wojcik, M. Makara, K. Poturaj, M. Kukli´nska, P. Mergo, et al. All-Fiber Vector Bending Sensor Based on a Multicore FiberWith Asymmetric Air-Hole Structure. J. Light. Technol. 2020, 38, 6685–6690. DOI: doi.org/10.1109/JLT.2020.3012769.

6. G.K. Ekechukwu, et al., Well-scale demonstration of distributed pressure sensing using fiber-optic DAS and DTS. Sci. Rep. 2021, 11, 12505. DOI: doi.org/10.1038/s41598-021-91916-7

7. F. Lu, R. Wright, P. Lu, P.C. Cvetic, P.R. Ohodnicki, Distributed fiber optic pH sensors using sol-gel silica based sensitive materials. Sens. Actuators B Chem. 2021, 340, 129853. DOI: doi.org/10.1016/j.snb.2021.129853.

8. Y. Liu, A. Zhou, L. Yuan, Multifunctional fiber-optic sensor, based on helix structure and fiber Bragg gratings, for shape sensing. Opt. Laser Technol. 2021, 143, 107327. DOI: doi.org/10.1016/j.optlastec.2021.107327.

9. U. Senkans, J. Braunfelds, I. Lyashuk, J. Porins, S. Spolitis, V. Bobrovs, Research on FBG-Based Sensor Networks and Their Coexistence with Fiber Optical Transmission Systems. J. Sens. 2019, 2019, 6459387. DOI: doi.org/10.1155/2019/6459387.

10. C. He, S. Korposh, R. Correia, L. Liu, B.R. Hayes-Gill, S.P. Morgan, Optical fibre sensor for simultaneous temperature and relative humidity measurement: Towards absolute humidity evaluation. Sens. Actuators B Chem. 2021, 344, 130154. DOI: doi.org/10.1016/j.snb.2021.130154.

11. J. Braunfelds, U. Senkans, P. Skels, R. Janeliukstis, T. Salgals, D. Redka, I. Lyashuk, J. Porins, S. Spolitis, V. Haritonovs, V. Bobrovs, FBG-Based Sensing for Structural Health Monitoring

of Road Infrastructure (2021) Journal of Sensors, 2021, art. no. 8850368. DOI: doi.org/10.1155/2021/8850368.

12. Taylor & Francis Group, Optical Fiber Sensors – Advances Techniques and Applications, CRC Press, 2015, pp. 545. DOI: doi.org/10.1201/b18074.

13. Advantages of optical sensor | Disadvantages of optical sensor. Internets: http://www.rfwireless-world.com/Terminology/Advantages-and-Disadvantages-of-Optical-Sensor.html (pieejams 2022. gada 5.decembrī).

14. J. Braunfelds, S. Spolitis, L. Gegere, D. Pikulins, V. Stepanovs and A. Supe, Demonstration of Polarization Optical-Time-Domain Reflectometer for Monitoring of Optical Fiber Lines, 2022 Workshop on Microwave Theory and Techniques in Wireless Communications (MTTW), 2022, pp. 9-12, DOI: doi.org/10.1109/MTTW56973.2022.9942583.

15. Li, X. Yang, C. Yang, S. Li, G. Fiber-Optical Sensors: Basics and Applications in Multiphase Reactors. Sensors 2012, 12, 12519-12544. DOI: doi.org/10.3390/s120912519.

16. A. D. Kersey et al., Fiber grating sensors, Journal of Lightwave Technology, vol. 15, no. 8, pp. 1442-1463, 1997, DOI: doi.org/10.1109/50.618377.

17. G. Rajan, Optical Fiber Sensors: Advanced Techniques and Applications.(2015), ISBN 9781482228250.

18. Lee, Byeong-Ha, et al. Specialty fiber coupler: fabrications and applications. Journal of the Optical Society of Korea 14.4 (2010): 326-332. DOI: doi.org/10.3807/josk.2010.14.4.326.

19. M. de Fátima F. Domingues, A. Radan, Optical Fiber Sensors for IoT and Smart Devices, Instituto de Telecomunicações - Aveiro,2017,101, ISBN: 978-3-319-47349-9.

20. U. Roland, et al. (2003). A New Fiber Optical Thermometer and Its Application for Process Control in Strong Electric, Magnetic, and Electromagnetic Fields. Sensor Letters. 1: 93–8. DOI: doi.org/10.1166/sl.2003.002.

21. M.R. Islam, et al. Chronology of Fabry-Perot interferometer fiber-optic sensors and their applications: a review. Sensors 14.4 (2014): 7451-7488. DOI: doi.org/10.3390/s140407451.

22. W-H. Tsai, C-J. Lin. A novel structure for the intrinsic Fabry-Perot fiber-optic temperature sensor. Journal of Lightwave Technology 19.5 (2001): 682. DOI: doi.org/10.1109/50.923481.

23. Y-J. Rao. Recent progress in fiber-optic extrinsic Fabry–Perot interferometric sensors. Optical Fiber Technology 12.3 (2006): 227-237. DOI: doi.org/10.1016/j.yofte.2006.03.004.

24. C. E. Lee, W. N. Gibler, R. A. Atkins, and H. F. Taylor, In-line fiber Fabry–Perot interferometer with high-reflectance internal mirrors, J. Lightwave Tech.,10, p. 1376, 1992. DOI: doi.org/10.1109/ofs.1992.762972.

25. J. H. Chow, I. C. M. Littler, D. E. McClelland, M. B. Gray, Long distance, high performance remote strain sensing with a fiber Fabry-Perot by radio-frequency laser modulation, Proc. SPIE, 6201, 620121-1, 2006. DOI: doi.org/10.1117/12.664282.

26. J. H. Chow, I. C. M. Littler, D. E. McClelland, M. B. Gray, A 100 km ultra-high performance fiber sensing system, Proceedings of Conference on Lasers and Electro-Optics, CLEO 2007, Baltimore, MD, May 6–11, 2007. DOI: doi.org/10.1109/CLEO.2007.4452840.

27. W. Habel, D. Hofmann, Determination of structural parameters concerning load capacity based on fiber Fabry-Perot interferometers, Proc. SPIE, 2361, 176–179, 1994. DOI: doi.org/10.1117/12.184819.

28. P. Chen, Y. Dai, D. Zhang, X. Wen, M. Yang, Cascaded-Cavity Fabry-Perot Interferometric Gas Pressure Sensor based on Vernier Effect. Sensors (2018). DOI: doi.org/10.3390/s18113677.

29. H. Li, D. Li, C. Xiong, W. Si, C. Fu, P. Yuan, Y. Yu, Low-Cost, High-Performance Fiber Optic Fabry–Perot Sensor for UltrasonicWave Detection, Wuhan University of Technology,(2018),11 DOI: doi.org/10.3390/s19020406.

30. J. W. Berthold, Historical review of microbend fiber-optic sensors, J. Lightwave Technol., 13, 1193–1199, 1995. DOI: doi.org/10.1117/12.185034.

31. J. N. Fields, C. K. Asawa, O. G. Ramer, M. K. Barnaski, Fiber optic pressure sensor, J. Acoust. Soc. Am., 67, 816–818, 1980. DOI: doi.org/10.1121/1.383957.

32. A. Alkina, A. Mekhtiyev, Y. Neshina, T. Serikov, P. Madi, K. Sansyzbay, A. Yurchenko, studying additional losses of standard G.652 optical fiber with protective cladding during multiple bending to develop weight control sensor, Journal of Theoretical and Applied Information Technology, Vol.100. No 7, 2022, pp.1.13.

33. Z. Zhikang, L. Yuangang, P. Jianqin, H. Chongjun, Fiber-Optic Macrobending-Based Temperature Sensor with Polyimide Coating, 2022, DOI: doi.org/10.3788/AOS202242.0706008.

34. G. Rajan, Y. Semenova, J. Mathew, et al., Experimental analysis and demonstration of a low cost temperature sensor for engineering applications, Sens. Actuat. A-Phys., 163, 88–95, 2010.

35. M. Roman, C. Zhu, R. J. O'Malley, R. E. Gerald and J. Huang, Distributed Fiber-Optic Sensing With Low Bending Loss Based on Thin-Core Fiber, iEEE Sensors Journal, vol. 21, no. 6, pp. 7672-7680, 2021, DOI: doi.org/10.1109/JSEN.2021.3050702.

36. P. Wang, Y. Semenova, Q. Wu, G. Farrell, A bend loss–based singlemode fiber microdisplacement sensor, Microw. Opt. Technol. Lett., 52, 2231–2234, 2010. DOI: doi.org/10.1002/mop.25446.

37. Y. Zheng et.al., Investigation of a quasi-distributed displacement sensor using the macro-bending loss of an optical fiber, Optical Fiber Technology, 102140, Volume 55, 2020. DOI: doi.org/10.1016/j.yofte.2020.102140.

38. X. Wang, et.al. , Vibration sensing based on macrobending loss in a standard single mode fiber loop structure, Optical Fiber Technology, Volume 48, p. 95-98, 2019. DOI: doi.org/10.1016/j.yofte.2018.12.024.

39. P. Wang, G. Brambilla, Y. Semenova, Q. Wu, G. Farrell, A simple ultrasensitive displacement sensor based on a high bend loss singlemode fibre and a ratiometric measurement system, J. Opt., 13, 075402, 2011. DOI: doi.org/10.1088/2040-8978/13/7/075402.

40. X. Bao, L. Chen, Recent progress in distributed fiber optic sensors. Sensors 2012, 12, 8601–8639.

41. F. Peng, et al. Ultra-long high-sensitivity Φ-OTDR for high spatial resolution intrusion detection of pipelines. Optics express 22.11 (2014): 13804-13810. DOI: doi.org/10.1364/oe.22.013804.

42. Lenke, Philipp, et al. Distributed humidity sensing based on Rayleigh scattering in polymer optical fibers. (EWOFS'10) Fourth European Workshop on Optical Fibre Sensors. International Society for Optics and Photonics, 2010. DOI: doi.org/10.1117/12.866279.

43. S. Rizzolo, et al. Radiation Characterization of Optical Frequency Domain Reflectometry Fiber-Based Distributed Sensors. IEEE Transactions on Nuclear Science 63.3 (2016): 1688- 1693. DOI: doi.org/10.1109/tns.2016.2527831.

44. J. Braunfelds, J. Porins, S. Spolitis, V. Bobrovs, Optisko sensoru signālu apstrādes iekārta ar integrētu optiskā laika apgabala reflektometra funkciju. Latvijas Republikas patenta pieteikums, LV15534, 11.12.2019.

45. R. Bernini, A. Minardo, and L. Zeni, Dynamic strain measurement in optical fibers by stimulated brillouin scattering, Optics Letters, vol. 34, no. 17, pp. 2613–2615, 2009. DOI: doi.org/10.1364/ol.34.002613.

46. C.A. Galindez-Jamioy, J.M. López-Higuera, Brillouin Distributed Fiber Sensors: An Overview and Applications. J. Sens. 2012, 2012. DOI: doi.org/10.1155/2012/204121.

47. K. Shimizu, T. Horiguchi, Y. Koyamada, T. Kurashima, Coherent self-heterodyne Brillouin OTDR for measurement of Brillouin frequency shift distribution in optical fibers. J. Lightwave Technol. 1994, 12, 730–736. DOI: doi.org/10.1109/50.293961.

48. I. García, J. Zubia, G. Durana, G. Aldabaldetreku, M.A. Illarramendi, J. Villatoro, Optical Fiber Sensors for Aircraft Structural Health Monitoring, Sensors, 2015, 15494.–15519.lpp. DOI: doi.org/10.3390/s150715494.

49. A. Barrias, J.R. Casas, S. Villalba, A Review of Distributed Optical Fiber Sensors for Civil Engineering Applications. Sensors 2016, 16, 748. DOI: doi.org/10.3390/s16050748.

50. Y. Dong, H. Zhang, L. Chen, X. Bao, 2 cm spatial-resolution and 2 km range Brillouin optical fiber sensor using a transient differential pulse pair. Appl. Opt. 2012, 51, 1229–1235. DOI: doi.org/10.1364/ao.51.001229.

51. Y. Dong, L. Chen, X. Bao, Extending the sensing range of Brillouin optical time-domain analysis combining frequency-division multiplexing and in-line EDFAs. J. Lightwave Technol. 2012, 30, 1161–1167. DOI: doi.org/10.1109/jlt.2011.2170813.

52. G. Bolognini, A. Hartog. Raman-based fibre sensors: Trends and applications. Optical Fiber Technology 19.6 (2013): 678-688. DOI: doi.org/10.1016/j.yofte.2013.08.003.

53. M.G. Tanner, S.D. Dyer, B. Baek, R.H. Hadfield, S. Woo Nam, High-resolution single-mode fiber-optic distributed Raman sensor for absolute temperature measurement using superconducting nanowire single-photon detectors. Appl. Phys. Lett. 2011, 99, 201110. DOI: doi.org/10.1063/1.3656702.

54. J. Park, G. Bolognini, D. Lee, Kim, P. P. Cho, F. di Pasquale, N. Park, Raman-based distributed temperature sensor with simplex coding and link optimization. IEEE Photonics Technol. Lett. 2006, 18, 1879–1881. DOI: doi.org/10.1109/lpt.2006.881239.

55. Y. Liu, L. Ma, C. Yang et al., Long-range Raman distributed temperature sensor with high spatial and temperature resolution using graded-index fewmode fiber, Opt. Express 26(16), 20562–20571, 2018.

56. M. A. Soto, T. Nannipieri, A. Signorini et al., Raman-based distributed temperature sensor with 1 m spatial resolution over 26 km SMF using low-repetition-rate cyclic pulse coding, Opt. Lett. 36(13), 2557–2559 (2011). DOI: doi.org/10.1364/ol.36.002557.

57. P. Lu, N. Lalam, M. Badar, B. Liu, B. T. Chorpening, M. P. Buric, and P. R. Ohodnicki , Distributed optical fiber sensing: Review and perspective, Applied Physics Reviews 6, 041302 (2019). DOI: doi.org/10.1063/1.5113955.

58. K. O. Hill and G. Meltz, Fiber Bragg grating technology fundamentals and overview, Journal of Lightwave Technology, vol. 15, no. 8, pp. 1263-1276, 1997, DOI: doi.org/10.1109/50.618320.

59. M. Götten, S. Lochmann, A. Ahrens, E. Lindner, J. Vlekken and J. Van Roosbroeck, A CDM-WDM Interrogation Scheme for Massive Serial FBG Sensor Networks, IEEE Sensors Journal, vol. 22, no. 12, pp. 11290-11296, 2022, DOI: doi.org/10.1109/JSEN.2021.3070446.

60. I. García, J. Zubia, G. Durana, G. Aldabaldetreku, M. A. Illarramendi, J. Villatoro "Optical Fiber Sensors for Aircraft Structural Health Monitoring", Sensors, 2015, pp.. 15494.–15519. DOI: doi.org/10.3390/s150715494.

61. F. Bortolotti, K. Morais Sousa, J.C. Cardozo da Silva, Packaging, characterization and calibration of the Bragg grating temperature sensors, Proceedings of the MOMAG 2012-15 SBMO-Brazilian Microwaves and Optoelectronics Symposium and the 10 CBMag Brazilian Conference on Electromagnetism, pp. 1-5., 2012. DOI: doi.org/10.13140/2.1.1004.0327.

62. C.E. Campanella, A. Cuccovillo, C. Campanella, A. Yurt, V.M.N. Passaro, Fibre Bragg Grating based strain sensors: Review of technology and applications, Sensors, 18 (9), 3115, 2018. DOI: doi.org/10.3390/s18093115.

63. G. Laffont, R. Cotillard, N. Roussel, R. Desmarchelier, S. Rougeault, Temperature Resistant Fiber Bragg Gratings for On-Line and Structural Health Monitoring of the Next-Generation of Nuclear Reactors, Sensors, vol. 18, no. 6, 1791, 2018. DOI: doi.org/10.3390/s18061791.

64. A. Vinagre, J. Ramos, S. Alves, A. Messias, N. Alberto, R. Nogueira, Cuspal Displacement Induced by Bulk Fill Resin Composite Polymerization: Biomechanical Evaluation Using Fiber Bragg Grating Sensors, International Journal of Biomaterials, vol. 2016, Article ID 7134283, 2016. DOI: doi.org/10.1155/2016/7134283.

65. I.S. Amiri, S.R.B. Azzuhri, M.A. Jalil, et al., Introduction to photonics: Principles and the most recent applications of microstructures, Micromachines, 9 (9), 452, 2018. DOI: doi.org/10.3390/mi9090452.

66. T. Wu, G. Liu, S. Fu, F. Xing, Recent Progress of Fiber-Optic Sensors for the Structural Health Monitoring of Civil Infrastructure. Sensors 2020, 20, 4517. DOI: doi.org/10.3390/s20164517.

67. X. W. Ye, Y. H. Su, J. P. Han, Structural Health Monitoring of Civil Infrastructure Using Optical Fiber Sensing Technology: A Comprehensive Review, The Scientific World Journal, vol. 2014, Article ID 652329, 11 pages, 2014. DOI: doi.org/10.1155/2014/652329.

68. Lecler, Sylvain & Meyrueis, Patrick. (2012). Intrinsic Optical Fiber Sensor. DOI: doi.org/10.5772/27079.

69. A. Kersey, A. Dandridge. Applications of Fiber-Optic Sensors. IEEE Transactions on Components, Hybrids, and Manufacturing Technology. 13. 472-478, 1989. DOI: doi.org/10.1109/ECC.1989.77791.

70. Fidanboylu, K. Efendioglu, H.S. Fiber Optic Sensors and Their Applications. In Proceedings of 5th International Advanced Technologies Symposium (IATS'09), Karabuk, Turkey, 13–15 May 2009.

71. A. Güemes, A. Fernández-López, P.F. Díaz-Maroto, A. Lozano, J. Sierra-Perez, Structural Health Monitoring in Composite Structures by Fiber-Optic Sensors. Sensors 2018, 18, 1094. DOI: doi.org/10.3390/s18041094.

72. J. Braunfelds, U. Senkans, P. Skels, R. Janeliukstis, J. Porins, S. Spolitis, V. Bobrovs Road Pavement Structural Health Monitoring by Embedded Fiber Bragg Grating Based Optical Sensors Sensors, 2022, pp.1-13. DOI: doi.org/10.3390/s22124581.

73. J. Braunfelds, U. Senkans, P. Skels, I. Murans, J. Porins, S. Spolitis, V. Bobrovs, Fiber Bragg Grating Optical Sensors for Road Infrastructure Monitoring Applications, (2022) Optics InfoBase Conference Papers, Applied Industrial Optics, pp.1-2, DOI: doi.org/10.1364/AIO.2022.W1A.2.

74. P. Kara De Maeijer, G. Luyckx, C. Vuye, E. Voet, W. Van den bergh, Vanlanduit, S. Braspenninckx, J. Stevens, N. De Wolf, J. Fiber Optics Sensors in Asphalt Pavement: State-of-the-Art Review. Infrastructures 2019, 4, 36. DOI: doi.org/10.3390/infrastructures4020036.

75. W. Liu, X. Liu, Z. Wang, Z. Zhi, High temperature deformation investigation of asphalt mixture with nanosized volcanic ash fillers using optical fiber sensor. Measurement 2019, 140, 171–181. DOI: doi.org/10.1016/j.measurement.2019.03.075.

76. J. Xie, H. Li, L. Gao, M. Liu, Laboratory investigation of rutting performance for multilayer pavement with fiber Bragg gratings. Constr. Build. Mater. 2017, 154, 331–339. DOI: doi.org/10.1016/j.conbuildmat.2017.07.233.

77. S.-Z. Chen, G. Wu, D.-C. Feng, L. Zhang, Development of a bridge weigh-in-motion system based on long-gauge fiber Bragg grating sensors. J. Bridge Eng. 2018, 23, 04018063. DOI: doi.org/10.1061/(asce)be.1943-5592.0001283.

78. M. Al-Tarawneh, Y. Huang, P. Lu and R. Bridgelall, Weigh-In-Motion System in Flexible Pavements Using Fiber Bragg Grating Sensors Part A: Concept, IEEE Transactions on Intelligent Transportation Systems, vol. 21, no. 12, pp. 5136-5147, 2020, doi: 10.1109/TITS.2019.2949242.

79. K. Yuksel, D. Kinet, K. Chah, C. Caucheteur, Implementation of a Mobile Platform Based on Fiber Bragg Grating Sensors for Automotive Traffic Monitoring. Sensors 2020, 20, 1567. DOI: doi.org/10.3390/s20061567.

80. B. Van Esbeen, C. Finet, R. Vandebrouck, D. Kinet, K. Boelen, C. Guyot, G. Kouroussis, C. Caucheteur, Smart Railway Traffic Monitoring Using Fiber Bragg Grating Strain Gauges. Sensors 2022, 22, 3429. DOI: doi.org/10.3390/s22093429.

81. S. Cocking, H. Alexakis, M. DeJong, (2021). Distributed dynamic fibre-optic strain monitoring of the behaviour of a skewed masonry arch railway bridge. Journal of Civil Structural Health Monitoring, 11 (4), 989-1012. DOI: doi.org/10.1007/s13349-021-00493-w.

82. E. Reynders, D.Anastasopoulos, G. De Roeck, (2021). Vibration Monitoring of a Railway Bridge Using Distributed Macro-strain Data Obtained with Fiber Bragg Gratings. In: Rainieri, C., Fabbrocino, G., Caterino, N., Ceroni, F., Notarangelo, M.A. (eds) Civil Structural Health Monitoring. CSHM 2021. Lecture Notes in Civil Engineering, vol 156. Springer, Cham. DOI: doi.org/10.1007/978-3-030-74258-4_20.

83. P. Velha et al., Monitoring Large Railways Infrastructures Using Hybrid Optical Fibers Sensor Systems, IEEE Transactions on Intelligent Transportation Systems, vol. 21, no. 12, pp. 5177-5188, 2020, DOI: doi.org/10.1109/TITS.2019.2949752.

84. Z. Xiaomei, G. Biao, P. Jianjun, H. Yong, J. Ning. Research And Realization Of Train Axle Counting System Based On Fbg. 2020 5th International Conference on Smart Grid and Electrical Automation (ICSGEA). DOI: doi.org/10.1109/icsgea51094.2020.00086.

85. Q.-A. Wang, Y.-Q. Ni, (2019). Measurement and Forecasting of High-Speed Rail Track Slab Deformation under Uncertain SHM Data Using Variational Heteroscedastic Gaussian Process. Sensors, 19(15), 3311. DOI: doi.org/10.3390/s19153311.

86. S. C. Lee, B. P. Tee, M. F. Chong, K. M. Ku Mahamud, H. Mohamad. Structural Assessment for an old Steel Railway Bridge Under Static and Dynamic Loads Using Fibre Optic Sensors. International Conference on Smart Infrastructure and Construction 2019 (ICSIC). DOI: doi.org/10.1680/icsic.64669.729.

87. B. Torres Górriz, P. Rinaudo, P. A. Calderón García. Comparison between point and long-gage FBG-based strain sensors during a railway bridge load test. Strain, 53(4), e12230, 2017. DOI: doi.org/10.1111/str.12230.

88. G. Kouroussis, D. Kinet, V. Moeyaert, J. Dupuy, C. Caucheteur, (2016). Railway structure monitoring solutions using fibre Bragg grating sensors. International Journal of Rail Transportation, 4(3), 135–150. DOI: doi.org/10.1080/23248378.2016.1184598.

89. M. L. Filograno, et al., Real-Time Monitoring of Railway Traffic Using Fiber Bragg Grating Sensors, IEEE Sensors Journal, vol. 12, no. 1, pp. 85-92, 2012, DOI: doi.org/10.1109/JSEN.2011.2135848.

90. C. Campanella, A. Cuccovillo, C. Campanella, A. Yurt, V. Passaro, (2018). Fibre Bragg Grating Based Strain Sensors: Review of Technology and Applications. Sensors, 18(9), 3115. DOI: doi.org/10.3390/s18093115.

91. S. J. Buggy, S. W. James, S. Staines, R. Carroll, P. Kitson, D. Farrington, R. P. Tatam, (2016). Railway track component condition monitoring using optical fibre Bragg grating sensors. Measurement Science and Technology, 27(5), 055201. DOI: doi.org/10.1088/0957-0233/27/5/055201.

92. S. Acikgoz, P. R. A. Fidler, M. N. Pascariello, C. Kechavarzi, E. Bilotta, M. J. DeJong, R. J. Mair, (2021). A Fibre-optic Strain Measurement System to Monitor the Impact of Tunnelling on Nearby Heritage Masonry Buildings. International Journal of Architectural Heritage, 1–19. DOI: doi.org/10.1080/15583058.2021.1884318.

93. J. Juraszek, P. Antonik-Popiołek. Fibre Optic FBG Sensors for Monitoring of the Temperature of the Building Envelope. Materials (Basel). 2021 ;14(5):1207. doi: 10.3390/ma14051207.

94. D. Li, H. Li, L Ren, D Guo, G. Song. Health Monitoring of a Tall Building during Construction with Fiber Bragg Grating Sensors. International Journal of Distributed Sensor Networks. 2012. DOI: doi.org/10.1155/2012/272190.

95. K. Čápová, L. Velebil, J. Včelák, M. Dvořák, L. Šašek, (2019). Environmental Testing of a FBG Sensor System for Structural Health Monitoring of Building and Transport Structures. Procedia Structural Integrity, 17, 726–733. DOI: doi.org/10.1016/j.prostr.2019.08.097.

96. C. Zhang, Z. Alam, L. Sun, Z. Su, B. Samali, Fibre Bragg grating sensor-based damage response monitoring of an asymmetric reinforced concrete shear wall structure subjected to progressive seismic loads. Struct Control Health Monit. 2019; 26:e2307. DOI: doi.org/10.1002/stc.2307.

97. A. Praveen Kumar, K. Kesavan, S. Balaji, 2017, Structural Health Monitoring using Fiber Bragg Grating Sensor : An Overview, International Journal of Engineering Research & Technology (IJERT) ETCEA – 2017 (Volume 5 – Issue 08), DOI : doi.org/10.17577/IJERTCONV5IS08015.

98. J. Yang, P. Hou, C. Yang, N. Yang. Study of a Long-Gauge FBG Strain Sensor with Enhanced Sensitivity and Its Application in Structural Monitoring. Sensors, 21(10), 3492, 2021. DOI: doi.org/10.3390/s21103492.

99. C. Li, J. Tang, C. Cheng, L. Cai, M. Yang. FBG Arrays for Quasi-Distributed Sensing: A Review. Photonic Sensors, 11(1), 91–108, 2021. DOI: doi.org/10.1007/s13320-021-0615-8.

100. S.-F. Jiang, Z.-H. Qiao, N.-L. Li, J.-B. Luo, S. Shen, M.-H. Wu, Y. Zhang. Structural Health Monitoring System Based on FBG Sensing Technique for Chinese Ancient Timber Buildings. Sensors, 20(1), 2019, 110. DOI: doi.org/10.3390/s20010110.

101. N. Lammens, D. Kinet, K. Chah, G. Luyckx, C. Caucheteur, J. Degrieck, P. Mégret, (2013). Residual strain monitoring of out-of-autoclave cured parts by use of polarization dependent loss

measurements in embedded optical fiber Bragg gratings. Composites Part A: Applied Science and Manufacturing, 52, 38–44. DOI: doi.org/10.1016/j.compositesa.2013.05.005.

102. U. Sampath, D. Kim, H. Kim, M. Song. Polymer-coated FBG sensor for simultaneous temperature and strain monitoring in composite materials under cryogenic conditions. Applied Optics, 57(3), 492, 2018. DOI: doi.org/10.1364/ao.57.000492.

103. A. Kefal, I. E. Tabrizi, M. Tansan, E. Kisa, M. Yildiz. An experimental implementation of inverse finite element method for real-time shape and strain sensing of composite and sandwich structures. Composite Structures, 258, 113431, 2021. DOI: doi.org/10.1016/j.compstruct.2020.1131.

104. M. Mieloszyk, K. Majewska, W. Ostachowicz. Application of embedded fibre Bragg grating sensors for structural health monitoring of complex composite structures for marine applications, Marine Structures, Volume 76, 2021, 102903, ISSN 0951-8339, DOI: doi.org/10.1016/j.marstruc.2020.102903.

105. Y. Zhan, F. Lin, Z. Song, Z. Sun, M. Yu. Applications and research progress of optical fiber grating sensing in thermoplastic composites molding and structure health monitoring. Optik, 229, 166122, 2021. DOI: doi.org/10.1016/j.ijleo.2020.166122.

106. G. Szebényi, Y. Blößl, G. Hegedüs, T. Tábi, T. Czigany, R. Schledjewski, (2020). Fatigue monitoring of flax fibre reinforced epoxy composites using integrated fibre-optical FBG sensors. Composites Science and Technology, 108317. DOI: doi.org/10.1016/j.compscitech.2020.108317.

107. B. Atli-Veltin, L.-K. Cheng, A.Vosteen, A. Jedynska, L. van der Linden. Experimental demonstration of health monitoring of composites using FBG sensor arrays. AIAA Scitech 2019 Forum, 2019. DOI: doi.org/10.2514/6.2019-0249.

108. Q. Wang, J. Huang, Q. Liu, Z. Zhou, (2016). Dynamic strain measurement of hydraulic system pipeline using fibre Bragg grating sensors. Advances in Mechanical Engineering, 8(4), 168781401664506. DOI: doi.org/10.1177/1687814016645069.

109. R. Di Sante, (2015). Fibre Optic Sensors for Structural Health Monitoring of Aircraft Composite Structures: Recent Advances and Applications. Sensors, 15(8), 18666–18713. DOI: doi.org/10.3390/s150818666.

110. F. Falcetelli, A. Martini, R. Di Sante, M. Troncossi, Strain Modal Testing with Fiber Bragg Gratings for Automotive Applications. Sensors 2022, 22, 946. DOI: doi.org/10.3390/s22030946.

111. D. Lo Presti et al., Wearable System Based on Flexible FBG for Respiratory and Cardiac Monitoring, IEEE Sensors Journal, vol. 19, no. 17, pp. 7391-7398, 2019, DOI: doi.org/10.1109/JSEN.2019.2916320.

112. D. L. Presti, et al., Smart Textile Based on 12 Fiber Bragg Gratings Array for Vital Signs Monitoring, IEEE Sensors Journal, vol. 17, no. 18, pp. 6037-6043, 2017, DOI: doi.org/10.1109/JSEN.2017.2731788.

113. D. Lo Presti, et al., Fiber Bragg Gratings for Medical Applications and Future Challenges: A Review, IEEE Access, vol. 8, pp. 156863-156888, 2020, doi: 10.1109/ACCESS.2020.3019138.

114. D. Jia, et al., A Fiber Bragg Grating Sensor for Radial Artery Pulse Waveform Measurement, IEEE Transactions on Biomedical Engineering, vol. 65, no. 4, pp. 839-846, 2018, DOI: doi.org/10.1109/TBME.2017.2722008.

115. A. Mendez, Fiber Bragg grating sensors for biomedical applications, Photonics and Fiber Technology 2016 (ACOFT, BGPP, NP), OSA Technical Digest (online) (Optica Publishing Group, 2016), paper BM4B.1. DOI: doi.org/10.1364/BGPP.2016.BM4B.1.

116. M. Ochoa, J.F. Algorri, P. Roldán-Varona, L. Rodríguez-Cobo, J.M. López-Higuera, Recent Advances in Biomedical Photonic Sensors: A Focus on Optical-Fibre-Based Sensing. Sensors 2021, 21, 6469. DOI: doi.org/10.3390/s21196469.

117. D. Lo Presti, M. Zaltieri, M. Bravi, M. Morrone, M.A. Caponero, E. Schena, S. Sterzi, C. A Massaroni. Wearable System Composed of FBG-Based Soft Sensors for Trunk Compensatory Movements Detection in Post-Stroke Hemiplegic Patients. Sensors 2022, 22, 1386. DOI: doi.org/10.3390/s22041386.

118. C. V. N. Bhaskar, S. Pal, P. K. Pattnaik. Recent advancements in fiber Bragg gratings based temperature and strain measurement. Results in Optics, 5, 100130, 2021. DOI: doi.org/10.1016/j.rio.2021.100130.

119. C. Du, S. Dutta, P. Kurup, T. Yu, X. Wang, A Review of Railway Infrastructure Monitoring Using Fiber Optic Sensors. Sens. Actuators A Phys. 2020, 303, 111728.

120. Q. Liu, Z. L. Ran, Y. J. Rao, S. C. Luo, H. Q. Yang and Y. Huang, Highly Integrated FP/FBG Sensor for Simultaneous Measurement of High Temperature and Strain, IEEE Photonics Technology Letters, vol. 26, no. 17, pp. 1715-1717, 2014, DOI: doi.org/10.1109/LPT.2014.2331359.

121. C. Dutta, J. Kumar, T. K. Das and S. P. Sagar, Recent Advancements in the Development of Sensors for the Structural Health Monitoring (SHM) at High-Temperature Environment: A

Review, IEEE Sensors Journal, vol. 21, no. 14, pp. 15904-15916, , 2021, DOI: doi.org/10.1109/JSEN.2021.3075535.

122. C. Fernando, A. Bernier, S. Banerjee, G. G. Kahandawa, J. Eppaarchchi. An Investigation of the Use of Embedded FBG Sensors to Measure Temperature and Strain Inside a Concrete Beam During the Curing Period and Strain Measurements under Operational Loading. Procedia Engineering, 188, 393–399, 2017. DOI: doi.org/10.1016/j.proeng.2017.04.500.

123. S. Ma, Y. Xu, Y. Pang, X. Zhao, Y. Li, Z. Qin, Z. Liu, P. Lu, X. Bao, Optical Fiber Sensors for High-Temperature Monitoring: A Review. Sensors 2022, 22, 5722. DOI: doi.org/10.3390/s22155722.

124. Q. Wang, L. Zhang, C. Sun and Q. Yu, Multiplexed Fiber-Optic Pressure and Temperature Sensor System for Down-Hole Measurement, IEEE Sensors Journal, vol. 8, no. 11, pp. 1879-1883, 2008, DOI: doi.org/10.1109/JSEN.2008.2006253.

125. T. Li, J. Guo, Y. Tan and Z. Zhou, Recent Advances and Tendency in Fiber Bragg Grating-Based Vibration Sensor: A Review, IEEE Sensors Journal, vol. 20, no. 20, pp. 12074-12087, 2020, DOI: doi.org/10.1109/JSEN.2020.3000257.

126. Y. Zhang, Z. Yin, B. Chen, H.-L. Cui, J. Ning, A novel fiber Bragg grating based seismic geophone for oil/gas prospecting, Proc. SPIE, vol. 5765, pp. 1112–1121, May 2005. DOI: doi.org/10.1117/12.599797.

127. P. Munendhar, S. K. Khijwania. Two dimensional fiber Bragg grating based vibration sensor for structural health monitoring, AIP Conference Proceedings 1536, 1324-1326 (2013). DOI: doi.org/10.1063/1.4810731.

128. P. Antunes, R. Travanca, H. Rodrigues, J. Melo, J. Jara, H.Varum, P. André. Dynamic Structural Health Monitoring of Slender Structures Using Optical Sensors. Sensors 2012, 12, 6629-6644. DOI: doi.org/10.3390/s120506629.

129. T. Li, C. Shi, Y. Tan, R. Li, Z. Zhou and H. Ren, A Diaphragm Type Fiber Bragg Grating Vibration Sensor Based on Transverse Property of Optical Fiber With Temperature Compensation, IEEE Sensors Journal, vol. 17, no. 4, pp. 1021-1029, 2017, DOI: doi.org/10.1109/JSEN.2016.2641931.

130. M. Sliti, N. Boudriga, Building Structural Health Monitoring: an FBG-based estimation of external vibrations, 2021 18th International Multi-Conference on Systems, Signals & Devices (SSD), 2021, pp. 1026-1031, DOI: doi.org/10.1109/SSD52085.2021.9429378.

131. Y. Zhang et al., 2-D Medium–High Frequency Fiber Bragg Gratings Accelerometer, IEEE Sensors Journal, vol. 17, no. 3, pp. 614-618, 2017, doi: 10.1109/JSEN.2016.2636453.

132. T. Li, Y. Tan, Z. Zhou, (2017). String-type based two-dimensional fiber bragg grating vibration sensing principle and structure optimization. Sensors and Actuators A: Physical, 259, 85–95. doi:10.1016/j.sna.2017.03.031.

133. G. Gagliardi, M. Salza, T. T. Lam, J. H. Chow, P. De Natale, (2009). 3-axis accelerometer based on lasers locked to π-shifted fibre Bragg gratings. 20th International Conference on Optical Fibre Sensors. DOI: doi.org/10.1117/12.835163.

134. Q. Jiang, M. Yang. Simulation and experimental study of a three-axis fiber Bragg grating accelerometer based on the pull–push mechanism. Measurement Science and Technology, 24(11), 2013, 115105. DOI: doi.org/10.1088/0957-0233/24/11/115105.

135. T. Li, Y. Tan, Y. Liu, Y. Qu, M. Liu, Z. Zhou. A Fiber Bragg Grating Sensing Based Triaxial Vibration Sensor. Sensors, 15(9), 24214–24229, 2015. DOI: doi.org/10.3390/s150924214.

136. L. Xiong, G. Jiang, Y. Guo, H. Liu, A Three-Dimensional Fiber Bragg Grating Force Sensor for Robot, IEEE Sensors Journal, vol. 18, no. 9, pp. 3632-3639, 2018, DOI: doi.org/10.1109/JSEN.2018.2812820.

137. L. Wei, L. Yu, J. Wang, D. Jiang, Q. Liu and Z. Liu, An FBG-Sensing Two-Dimensional Vibration Sensor Based on Multi-Axis Flexure Hinge, IEEE Sensors Journal, vol. 19, no. 10, pp. 3698-3710, 2019, DOI: doi.org/10.1109/JSEN.2019.2895232.

138. Z. M. Hafizi, E. Vorathin, A Temperature-Compensated FBG Pressure Sensor for Underwater Pipeline Monitoring, 2020 IEEE 8th International Conference on Photonics (ICP), 2020, pp. 66-67, DOI: doi.org/10.1109/ICP46580.2020.9206469.

139. J. Wang, L. Zhao, T. Liu, Z. Li, T. Sun, K. T. V. Grattan, Novel Negative Pressure Wave-Based Pipeline Leak Detection System Using Fiber Bragg Grating-Based Pressure Sensors, Journal of Lightwave Technology, vol. 35, no. 16, pp. 3366-3373, 2017, DOI: doi.org/10.1109/JLT.2016.2615468.

140. J. Huang, Z. Zhou, D. Zhang, Q. Wei. A Fiber Bragg Grating Pressure Sensor and Its Application to Pipeline Leakage Detection. Advances in Mechanical Engineering. 2013;5. DOI: doi.org/10.1155/2013/590451.

141. P.-L. Ko, K.-C. Chuang, C.-C. Ma, A Fiber Bragg Grating-Based Thin-Film Sensor for Measuring Dynamic Water Pressure, IEEE Sensors Journal, vol. 18, no. 18, pp. 7383-7391, 2018, DOI: doi.org/10.1109/JSEN.2018.2857561.

142. C. Hong, Y. Zhang and L. Borana, Design, Fabrication and Testing of a 3D Printed FBG Pressure Sensor, IEEE Access, vol. 7, pp. 38577-38583, 2019, DOI: doi.org/10.1109/ACCESS.2019.2905349.

143. L. Xiong, Y. Guo, W. Zhou, M. Chen and X. Zhou, Fiber Bragg Grating-Based Three-Axis Vibration Sensor, IEEE Sensors Journal, vol. 21, no. 22, pp. 25749-25757, 2021, DOI: doi.org/10.1109/JSEN.2021.3118360.

144. X. Li, et al., An FBG Pressure Sensor Based on Spring-Diaphragm Elastic Structure for Ultimate Pressure Detection, IEEE Sensors Journal, vol. 22, no. 3, pp. 2213-2220, 2022, DOI: doi.org/10.1109/JSEN.2021.3136212.

145. L. Schenato, et al., Highly Sensitive FBG Pressure Sensor Based on a 3D-Printed Transducer, Journal of Lightwave Technology, vol. 37, no. 18, pp. 4784-4790, 2019, DOI: doi.org/10.1109/JLT.2019.2919917.

146. M. Liu, Y. Wu, C. Du, D. Jiang, Z. Wang, FBG-Based Liquid Pressure Sensor for Distributed Measurement With a Single Channel in Liquid Environment, IEEE Sensors Journal, vol. 20, no. 16, pp. 9155-9161, 2020, DOI: doi.org/10.1109/JSEN.2020.2986550.

147. Y. -F. Gu, Y. Zhao, R. -Q. Lv, Y. Yang, A Practical FBG Sensor Based on a Thin-Walled Cylinder for Hydraulic Pressure Measurement, IEEE Photonics Technology Letters, vol. 28, no. 22, pp. 2569-2572, 2016, DOI: doi.org/10.1109/LPT.2016.2605696.

148. G. T. Kanellos, G. Papaioannou, D. Tsiokos, C. Mitrogiannis, G. Nianios, N. Pleros, Two dimensional polymer-embedded quasi-distributed FBG pressure sensor for biomedical applications, Opt. Express 18, 179-186 (2010). DOI: doi.org/10.1364/oe.18.000179.

149. V. S. C. S. Vaddadi, S. R. Parne, S. Afzulpurkar, S. Prabhu Desai, V. Vadakke Parambil. Design and development of pressure sensor based on Fiber Bragg Grating (FBG) for ocean applications. The European Physical Journal Applied Physics, 90(3), 30501, 2020. DOI: doi.org/10.1051/epjap/2020200036.

150. T. Li, C. Shi, H. Ren, (2017). A Novel Fiber Bragg Grating Displacement Sensor With a Sub-Micrometer Resolution. IEEE Photonics Technology Letters, 29(14), 1199–1202. DOI: doi.org/10.1109/lpt.2017.2712602.

151. L. Xiong, Y. Guo, G. Jiang, L. Jiang, X. Zhou, (2019). Fiber Bragg grating displacement sensor with high measurement accuracy for crack monitoring. IEEE Sensors Journal, 1–1. DOI: doi.org/10.1109/jsen.2019.2930761.

152. Y. Chen, J. Wu, X. Zhao, Monitoring of vertical displacement of concrete slab end at pavement joint based on FBG-dowel bar signal. J. Transp. Eng. B Pavements 2022, 148, 04022012. DOI: doi.org/10.1061/JPEODX.0000358.

153. M. Bonopera. Fiber-Bragg-Grating-Based Displacement Sensors: Review of Recent Advances. Materials (Basel). 2022; 15(16):5561. DOI: doi.org/10.3390/ma15165561.

154. C. Hong, Y. Zhang, Y. Yang, Y. Yuan, (2019). A FBG based displacement transducer for small soil deformation measurement. Sensors and Actuators A: Physical, 286, 35–42. DOI: doi.org/10.1016/j.sna.2018.12.022.

155. S. Chen, Y. Liu, X. Liu, Y. Zhang, W. Peng, (2015). Self-compensating displacement sensor based on hydramatic structured transducer and fiber Bragg grating. Photonic Sensors, 5(4), 351–356. DOI: doi.org/10.1007/s13320-015-0278-4.

156. Y.X. Guo, L. Xiong, J.Y. Kong, Z.Y. Zhang, L. Qin, Sliding type fiber Bragg grating displacement sensor. Guangxue Jingmi Gongcheng/Opt. Precis. Eng. 2017, 25, 50–58. DOI: doi.org/10.3788/OPE.20172501.0050.

157. J. Thomas, T.R. Rajanna, S. Asokan, Temperature compensated FBG displacement sensor for long-range applications. IEEE Sens. Lett. 2020, 4, 8931563. DOI: doi.org/10.1109/LSENS.2019.2959377.

158. Z. Lu, C. Hong, Y. Zhang, D. Su and Y. Fu, Development of an FBG Sensor for Measuring Large Range and Multi-Directional Settlement, IEEE Access, vol. 7, pp. 107669-107677, 2019, DOI: doi.org/10.1109/ACCESS.2019.2932774.

159. T. Li et al., A High-Sensitivity Fiber Bragg Grating Displacement Sensor Based on Transverse Property of a Tensioned Optical Fiber Configuration and Its Dynamic Performance Improvement, IEEE Sensors Journal, vol. 17, no. 18, pp. 5840-5848, 2017, DOI: doi.org/10.1109/JSEN.2017.2737556.

160. H. Li, G. Xu, X. Gui, L. Liang, Z. Li. An FBG Displacement Sensor in Deformation Monitoring of Subway Floating Slab. IEEE Sensors Journal, 21(3), 2963–2971, 2021. DOI: doi.org/10.1109/jsen.2020.3022466.

161. G. Lyu, C. Bi, Y. Zhang, C. Wang, M. Wang, X. Jiang. Large-range bridge beam-gap displacement sensors based on cantilever beam with fiber Bragg grating. Lect. Notes Electr. Eng. 2020, 567, 3–11. DOI: doi.org/10.1007/978-981-13-8595-7_1.

162. H. Xu, W. Zhang, Y. Du, F. Li, F. Li. Fiber optic displacement sensor used in railway turnout contact monitoring system. Fourth Asia Pacific Optical Sensors Conference, 2013. DOI: doi.org/10.1117/12.2031258.

163. S. Li, S. Zhongxin, Z. Chunwei, S. Yansheng, A pitman style fiber Bragg grating displacement sensor based on wedge cavity structure. Mech. Mach. Sci. 2019, 72, 313–324. DOI: doi.org/10.1007/978-3-030-17677-8_24.

164. C. Li, L. Sun, Z. Xu, X. Wu, T. Liang, W. Shi. Experimental Investigation and Error Analysis of High Precision FBG Displacement Sensor for Structural Health Monitoring. International Journal of Structural Stability and Dynamics, 2020. DOI: doi.org/10.1142/s0219455420400118.

165. S.W. Kim, D.W. Yun, D.U. Park, S.J. Chang, J.B. Park. Vehicle load estimation using the reaction force of a vertical displacement sensor based on fiber Bragg grating. Sensors 2022, 22, 1572. DOI: doi.org/10.3390/s22041572.

166. M. Bonopera, K.C. Chang, C.C. Chen, Z.K. Lee, Y.C. Sung, N. Tullini, Fiber Bragg grating–differential settlement measurement system for bridge displacement monitoring: Case study. J. Bridge Eng. 2019, 24, 05019011. DOI: doi.org/10.1061/(asce)be.1943-5592.0001470.

167. A58 M.A. Alias, M.F. Ismail, M.S.M. Sa'ad, M.K.A. Zaini, K.S. Lim, K.T.V. Grattan, G. Brambilla, B.M.A. Rahman, S.A. Reduan, H. Ahmad. A high-precision extensometer system for ground displacement measurement using fiber Bragg grating. IEEE Sens. J. 2022, 22, 8509–8521. DOI: doi.org/10.1109/jsen.2022.3159850.

168. B. Yang, S. M. Aminossadati, Z. Chen and M. S. Kizil, Fibre Optic Sensing Based Slope Crest Tension Crack Monitoring System for Surface Mines, 2017 2nd International Conference for Fibre-optic and Photonic Sensors for Industrial and Safety Applications (OFSIS), 2017, pp. 27-32, DOI: doi.org/10.1109/OFSIS.2017.21.

169. M. Maheshwari, Y. Yang, D. Upadrashta and T. Chaturvedi, A Rotation Independent In-Place Inclinometer/Tilt Sensor Based on Fiber Bragg Grating, IEEE Transactions on Instrumentation and Measurement, vol. 68, no. 8, pp. 2943-2953, Aug. 2019, DOI: doi.org/10.1109/TIM.2018.2870246.

170. HBM, Optical Fiber Sensors, Internets: https://www.hbm.com/en/4599/new-light-optical-fiber-sensors/?product_type_no=newLight (pieejams 2022. gada 11. decembrī).

171. Smart fibres, FBG sensors, Internets: https://www.smartfibres.com/products (pieejams 2022. gada 11. decembrī).

172. Sylex, ES-03 Embeddable strain sensor, pp.2. 2021.

173. K. M. Dwivedi, G. Trivedi and S. K. Khijwania, Theoretical Study and Optimization of Apodized Fiber Bragg Grating for Single and Quasi-distributed Structural Health Monitoring Applications, 2020 30th International Conference Radioelektronika (RADIOELEKTRONIKA), 2020, pp. 1-6, DOI: doi.org/10.1109/RADIOELEKTRONIKA49387.2020.9092399.

174. A. Rumadi, D. Syahriar, Astharini and A. H. Lubis, The effects of apodization profile on uniform fiber Bragg gratings, 2015 9th International Conference on Telecommunication

Systems Services and Applications (TSSA), 2015, pp. 1-6, DOI: doi.org/10.1109/TSSA.2015.7440430.

175. I. Ashry, A. Elrashidi, A. Mahros, M. Alhaddad and K. Elleithy, Investigating the performance of apodized Fiber Bragg gratings for sensing applications, Proceedings of the 2014 Zone 1 Conference of the American Society for Engineering Education, 2014, pp. 1-5, DOI: doi.org/10.1109/ASEEZone1.2014.6820640.

176. Optiwave, Photonic Software, OptiGrating, Internets: https://optiwave.com/products/component-design/optigrating/optigrating/ (pieejams 2022. gada 11. decembrī).

177. Optiwave, OptiGratingUser's Reference and Tutorials, pp. 214, 2008.

178. J. Braunfelds, E. Haritonovs, U. Senkans, I. Murans, J. Porins, S. Spolitis, Data accompanying Designing of Fiber Bragg Gratings for Long-distance Optical Fiber Sensing Networks. Zenodo: doi.org/10.5281/zenodo.6513728 (2022).

179. Z. A. El-Sahn, W. Mathlouthi, H. Fathallah, S. LaRochelle, and L. A. Rusch, Dense SS-WDM over legacy PONs: smooth upgrade of existing FTTH networks, Journal of Lightwave Technology, vol. 28, no. 10, pp. 1485–1495, 2010. DOI: doi.org/10.1109/jlt.2010.2046313.

180. ITU-T, Spectral grids for WDM applications: DWDM frequency grid (G.694.1), 2020, pp. 16.

181. Technica, T840 / Rugged In-Line Temperature Sensor, 2022, pp. 2.

182. W. Tsai et al. A 20-m/40-Gb/s 1550-nm DFB LD-Based FSO Link, IEEE Photonics J., 2015, 7, 1-7, DOI: doi.org/10.1109/JPHOT.2015.2506172.

183. Jr. N. Ledentsov, M. Agustin, L. Chorchos, J.-R. Kropp, V. A. Shchukin, V. P. Kalosha, M. Koepp, C. Caspar, J. P. Turkiewicz, N. N. Ledentsov, Energy efficient 850-nm VCSEL based optical transmitter and receiver link capable of 56 Gbit/s NRZ oper-ation, Vertical-Cavity Surface-Emitting Lasers XXIII, 109380J, 2019, pp.1-8. DOI: doi.org/10.1117/12.2509916.

184. K. Elayoubi, A. Rissons, A. Belmonte, Optical test bench experiments for 1-Tb/s satellite feeder uplinks, Laser Communica-tion and Propagation through the Atmosphere and Oceans VII, 1077006, 2018, pp. 1-11. DOI: doi.org/10.1117/12.2317728.

185. X. Ma, T. Wang, Z. Dong. Dynamic Response Monitoring and Analysis of In-Service Asphalt Pavement Based on FBG Measuring Technology. In: Chabot, A., Hornych, P., Harvey, J., Loria-Salazar, L. (eds) Accelerated Pavement Testing to Transport Infrastructure Innovation. Lecture Notes in Civil Engineering, vol 96. Springer, Cham, 2020. DOI: doi.org/10.1007/978-3-030-55236-7_55

186. Anritsu corporation, MS9740A Optical Spectrum Analyzer Operation Manual, 23rd Edition, pp. 320.

187. Safibra: Composite sensor. Internets: http://www.safibra.cz/en/composite-sensor (pieejams 2022. gada 5.decembrī).

188. Safibra: FBG temperature sensor. Internets: http://www.safibra.cz/en/fbg-temperature-sensor (pieejams 2022. gada 5.decembrī).

189. P. Ullidtz, Modelling Flexible Pavement Response and Performance, Polyteknisk Forlag, Denmark, ISBN: 8750208055, 1998.

190. L. Korkiala-Tanttu, Calculation Method for Permanent Deformation of Unbound Pavement Materials, VTT Technical Research Centre of Finland, Espoo, Finland, 2008.

191. T. Saevarsdottir and S. Erlingsson, Deformation modelling of instrumented flexible pavement structure, Procedia Engineering, vol. 143, pp. 937–944, 2016. DOI: doi.org/10.1016/j.proeng.2016.06.076.

192. SJSC Latvian State Roads, online traffic intensity at highway A2 76th km. Internets: https://lvceli.lv/traffic/ (pieejams 2020. gada 28 janvārī).

193. P. Kara De Maeijer, W. Van den Bergh and C. Vuye, Fiber Bragg Grating Sensors in Three Asphalt Pavement Layers, Infrastructures, vol. 3, 16, 2018. DOI: doi.org/10.3390/infrastructures3020016.

194. ES-01 Embeddable strain sensor. Available online: https://www.sylex.sk/wp-content/uploads/2018/09/ES-01-Embeddable-strain-sensor.pdf (24.05.2022.).

195. Xi'an Aurora Technology, Fiber Bragg Grating Embedded FBG Temperature Sensor, 2022.

196. Intel: Smart Roads Start with Smart Infrastructure, Internets: https://www.intel.com/content/www/us/en/transportation/smart-road-infrastructure.html (pieejams 2023. gada 3.janvārī).

197. Z. Yan, S. Li, & Z. Yin, K. O'Donnell, R. Pastore, M. Pellicano, D. Black, J. Kosinski. Unattended ground sensor based on fiber BRAGG grating technology. Proceedings of SPIE - The International Society for Optical Engineering. 5796. 133-140, 2005. DOI: doi.org/10.1117/12.607187.

198. M. Bocciolone, G. Bucca, A. Cigada A. Collina, L. Comolli. An application of FBG accelerometers for monitoring pantographs of underground trains. 7653, 2010. DOI: doi.org/10.1117/12.866358.

199. S. Poeggel, G. Leen, K. Bremer and E. Lewis, Miniature Optical fiber combined pressure- and temperature sensor for medical applications, SENSORS, 2012 IEEE, 2012, pp. 1-4, DOI: doi.org/10.1109/ICSENS.2012.6411305.

200. L. Schenato, J. P. Aguilar-López, A. Galtarossa, A. Pasuto, T. Bogaard and L. Palmieri, A Rugged FBG-Based Pressure Sensor for Water Level Monitoring in Dikes, IEEE Sensors Journal, vol. 21, no. 12, pp. 13263-13271, 2021, DOI: doi.org/10.1109/JSEN.2021.3067516.

201. A. F. Majeed, I. A. Murdas, Modern System for Blood Pressure and Temperature Monitoring Based on FBG Sensor, 2019 1st AL-Noor International Conference for Science and Technology (NICST), 2019, pp. 7-13, DOI: doi.org/10.1109/NICST49484.2019.9043813.

202. Z. A. Abro, C. Hong, Y. Zhang, M. Q. Siddiqui, A. M. Rehan Abbasi, Z. Abro, S. Q. Bin Tariq. Development of FBG pressure sensors using FDM technique for monitoring sleeping postures. Sensors and Actuators A: Physical, 331, 112921, 2021. DOI: doi.org/10.1016/j.sna.2021.112921.

203. S. Poeggel, D. Tosi, D. Duraibabu, G. Leen, D. McGrath, et al., Optical Fibre Pressure Sensors in Medical Applications. Sensors 2015, 15, 17115-17148. DOI: doi.org/10.3390/s150717115.

PIELIKUMI

Braunfelds J., Haritonovs E, Senkans U., Murans I., Porins J., Spolitis S. Designing of Fiber Bragg Gratings for Long-distance Optical Fiber Sensing Networks. Modelling and Simulation in Engineering, **2022**.

Research Article

Designing of Fiber Bragg Gratings for Long-Distance Optical Fiber Sensing Networks

Janis Braunfelds [1,2] **Elvis Haritonovs,** [2] **Ugis Senkans,** [2] **Inna Kurbatska,** [2] **Ints Murans,** [1] **Jurgis Porins,** [2] **and Sandis Spolitis** [1,2]

[1]*Communication Technologies Research Center, Riga Technical University, LV-1048 Riga, Latvia*
[2]*Institute of Telecommunications, Riga Technical University, LV-1048 Riga, Latvia*

Correspondence should be addressed to Janis Braunfelds; janis.braunfelds@rtu.lv

Most optical sensors on the market are optical fiber Bragg grating (FBG) sensors with low reflectivity (typically 7-40%) and low side-lobe suppression (SLS) ratio (typically SLS <15 dB), which prevents these sensors from being effectively used for long-distance remote monitoring and sensor network solutions. This research is based on designing the optimal grating structure of FBG sensors and estimating their optimal apodization parameters necessary for sensor networks and long-distance monitoring solutions. Gaussian, sine, and raised sine apodizations are studied to achieve the main requirements, which are maximally high reflectivity (at least 90%) and side-lobe suppression (at least 20 dB), as well as maximally narrow bandwidth (FWHM<0.2 nm) and FBGs with uniform (without apodization). Results gathered in this research propose high-efficiency FBG grating apodizations, which can be further physically realized for optical sensor networks and long-distance (at least 40 km) monitoring solutions.

1. Introduction

The manufacturing process of fiber Bragg grating (FBG) technology is relatively simple, and such sensors have a lot of technological advantages, for instance, the realization of passive components, resistance to electromagnetic interference (EMI) and corrosion, small size, high accuracy, and multiplexing abilities. FBG is one of the most utilized and progressing optical sensor solution technologies. Mainly, optical FBG sensors are used to detect objects or environmental temperature, induced strain, applied pressure, and vibration [1–4].

As an alternative to optical sensors, electrical sensors can be mentioned, but their performance can be negatively affected by high voltage and the presence of the electromagnetic field–electromagnetic interference. Due to the previously mentioned, depending on the measurement location, it can be difficult or even impossible to realize the use of electrical sensors. Another major disadvantage of electrical

sensor realization is that such sensors require a consistent supply of electrical energy, but it might be challenging to provide electricity to remote sensor locations if there is no available source nearby. In contrast, fiber optical sensors are passive devices that do not require electricity since optical fiber is made from a dielectric material. In these situations, the use of fiber optical sensors is a suitable solution [5].

A vital field where FBG technology has rapidly improved over the years is structural health monitoring (SHM for various constructions such as roads, bridges, railroads, dams, buildings, and aircraft) as well as in medicine, oil and gas industries, and security solutions [6, 7]. FBGs can be applied in time and wavelength multiplexing technologies and operate as optical filters, dispersion compensation modules, and sensor solutions.

Multiple FBGs can be combined on a single optical fiber, allowing FBG sensor systems to use and read many sensors simultaneously, reducing the number of fibers used and
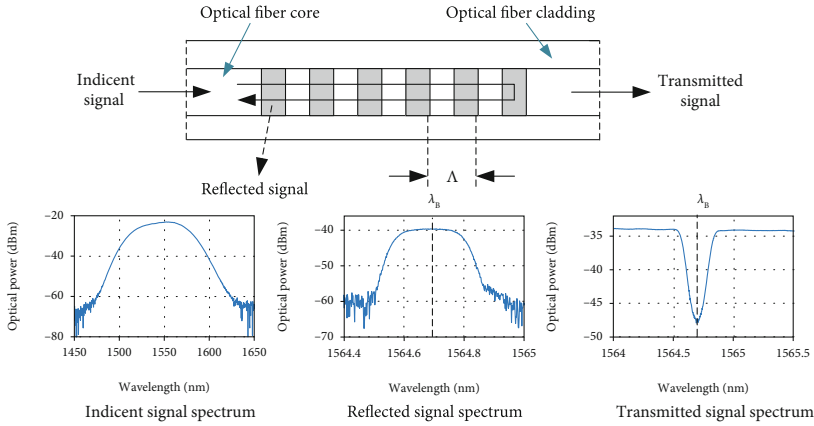
Figure 1: Structure and working principle of FBG sensors.

simplifying their installation. FBG sensors can be successfully combined with fiber optical data transmission systems [2]. An important prerequisite for the design of optical sensor networks is to choose a sufficiently efficient channel spacing to maintain the highest possible spectrum efficiency of the sensor network and to avoid overlapping of the optical signals that might be observed between adjacent optical sensors if their reference wavelengths/frequencies are configured too close to each other.

As the demand for FBG sensors in various applications grows, it is increasingly important to optimize and customize their configuration and parameters, so there are available different types of FBG sensors that vary in their structure, construction, and design techniques. Therefore, it is essential to research different FBG types and evaluate their specific advantages and disadvantages to define optimal sensor types and their parameters (especially for sensor networks) to ensure the realization of specific applications where they are utilized.

FBGs are formed by incorporating specific changes in the refractive index modulation of the optical fiber core components that are based on the diffraction grating principle. When a light signal is transmitted through such a grating structure in an optical fiber, some part of the light is reflected from each grating plane (see Figure 1). Each part of the reflected light combines to form one unified reflected beam of light, and this is possible only if the Bragg condition described by the equation is fulfilled:

$$\lambda_B = 2 \bullet \Lambda \bullet n_{\text{eff}}, \tag{1}$$

where Λ is the grating period that determines the distance between two adjacent grating planes, n_{eff} is the effective refractive index of the fiber core, and λ_B is the Bragg wavelength.

When the Bragg condition is fulfilled, the reflected light forms a backward reflected peak with a central wavelength known as λ_B. Such a grating structure, developed by the Bragg relation, acts as a mirror that reflects the wavelength
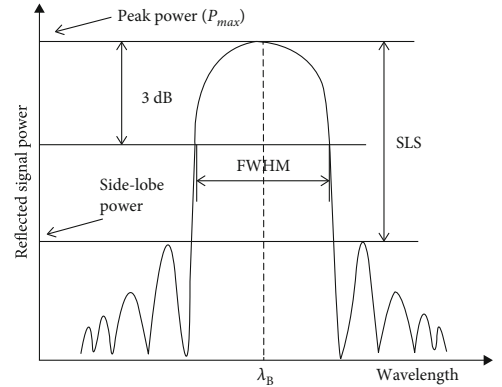

Figure 2: Typical reflected optical spectrum and main parameters of the FBG signal [5].

λ_B and transmits the rest of the optical signal further inside the optical fiber [5, 8, 9].

Two quantities determine the characteristics of the FBG, which are the grating strength (also known as the modulation depth) and the grating length. However, in general, three main parameters must be controlled while designing the fiber Bragg gratings, and these are reflectivity (%), bandwidth (nm), and SLS (dB).

The full width at half maximum (FWHM) is the bandwidth of the reflected signal at a -3 dB power level. This bandwidth depends on several parameters, especially the grating length. Most sensor applications have an average FWHM bandwidth of 0.05 nm to 0.4 nm, but for some sensors, it may even exceed 1 nm [5]. Figure 2 shows a typical peak of the reflected FBG signal spectrum, where SLS and FWHM parameters are shown. Reflected optical signal bandwidth directly depends on the grating strength; therefore, the grating strength can be used to adjust the signal's bandwidth.

The grating length can be configured to improve the reflectivity of the signal because reflectivity depends on the grating strength and the grating length. The reflectivity of the signal can be calculated by using the equation:

$$\text{Reflectivity } [\%] = 10^{P_{\max} \, [dB]/10} \bullet 100, \qquad (2)$$

where $P_{\max}$ is the maximal signal power (dB) of the reflected signal spectrum.

Apodized gratings for the FBGs' design offer a significant improvement in side-lobe reduction while maintaining reflectivity as well as the narrow bandwidth of the signal. Several apodization functions are typically used, such as Gaussian, sine, raised sine, hyperbolic tangent, Nuttall, and other types of apodizations [10–12]. However, side lobes are a type of unwanted additional distortions of the reflected signal that cannot fully be efficiently controlled with just such a simple grating optimization; thus, additional improvements for the apodization design has to be done as proposed in this research. Such side lobes can be observed in an optical spectrum when the modulation of the refractive index is constant throughout the length of the FBG and then rapidly changes to zero outside the grating range.

It is important to highlight that based on the apodization technique, the modulation of the refractive index is uniformly increased and uniformly reduced along the length of the fiber Bragg grating. However, in this configuration, an increase in total grating length may be required to reach a certain peak (reflectivity) of the reflected signal.

As explained further in this research, the specified optimal FBG parameters for sensor networks are maximally high SLS (at least 20 dB) and maximally narrow bandwidth (FWHM <0.2 nm), but for long-distance monitoring solutions, maximally high reflectivity (at least 90%) and appropriate SLS (at least 20 dB). Based on these requirements, specific FBG sensor gratings are designed and described in the following Sections 2 and 3 of this article.

2. Mathematical Modelling and Design of Fiber Bragg Gratings

The characteristics of the fiber Bragg grating were studied in the simulation environment using *Optiwave Systems* "*OptiGrating*" software [13]. This software uses the coupled mode theory to model the light and enable analysis and synthesis of gratings. A complex grating is determined by a sequence of uniform segments and analyzed by connecting the segments with the well-known transfer matrix method. This gives the designer the information needed to test and optimize grating designs for specific purposes. In simulation software, it is possible to set and change such grating parameters such as grating shape, average index modulation, period chirp, and apodization type.

Coupled mode theory method suggests that the modes of the unperturbed or uncoupled structures should be the first for defining and solving. Afterward, by realizing analytical methods, the derived coupled mode equations can be solved. The theory proposes that linear superposition of the modes

of the unperturbed structures represents the coupled structures. Such assumption provides an insightful and accurate enough mathematical description of electromagnetic wave propagation in various practical situations. This theory provides the means for analysis of near resonance guided mode interaction. In addition, transfer matrix method (TMM) can be used for coupled mode equation solving if the application (device) has multiple grating plus phase shifts. TMM can also be utilized for analysis of almost periodic gratings. TMM suggests that the whole grating structure is divided into a number of uniform grating sections (having an analytic transfer matrix). By multiplying the individual transfer matrices, the entire structure of the transfer matrix can be gathered [14].

For all *OptiGrating* simulations performed, the typical parameters of single mode optical fiber with a core diameter of 9 μm and a cladding diameter of 125 μm were set. Each grating central wavelength of the FBG is set to 1550 nm, and the number of segments (planes) is set to 25.

Various FBG reflected signal spectrums at different grating parameters were obtained. Each apodization type of the FBG was analyzed at different grating lengths from 1 mm to 20 mm at different grating modulation indexes (fiber core reflection index changes) $\Delta n = 0.5 \times 10^{-4}$, 1×10^{-4}, 1.5×10^{-4}, and 2×10^{-4} (also observable in Figure 3). Uniform (without apodization), Gaussian, sine, and raised sine apodizations are studied in this phase. These apodizations are described with the following mathematical function:

$$\text{Gaussian apodization}: \Delta n(x) = \Delta n \bullet \exp\left\{-\ln(2) \bullet \left(\frac{2 \bullet (x - (L/2))}{s * L}\right)^2\right\}, \qquad (3)$$

$$\text{Sine apodization}: \Delta n(x) = \Delta n \bullet \sin\left(\frac{\pi \bullet x}{L}\right), \qquad (4)$$

$$\text{Raised sine apodization}: \Delta n(x) = \Delta n \bullet \sin^2\left(\frac{\pi \bullet x}{L}\right), \qquad (5)$$

where L is the grating length, s is the taper length = 0.5, and x is the coordinate of light that is propagation along the length of the grating ($0 \leq x \leq L$).

Figure 3 depicts the example of our mathematically generated geometrical shapes of the FBG uniform, Gaussian, sine, and raised sine apodization profiles. Geometrical shapes are illustrated when the grating length of the FBG is 10 mm, the grating modulation index $\Delta n = 1.5 \times 10^{-4}$, and the number of segments (planes) is 25.

Several parameters (reflectivity, FWHM, and SLS) of the reflected signal spectrum were determined during the analysis of the data obtained in the simulation results and are discussed in the results section. The reflectivity, side-lobe power, and the FWHM values of the reflected signal were analyzed from all of the measured spectral data.

3. Results and Discussion

The data (reflectivity, FWHM, and SLS) from the obtained reflected signal spectra are summarized in the tables and
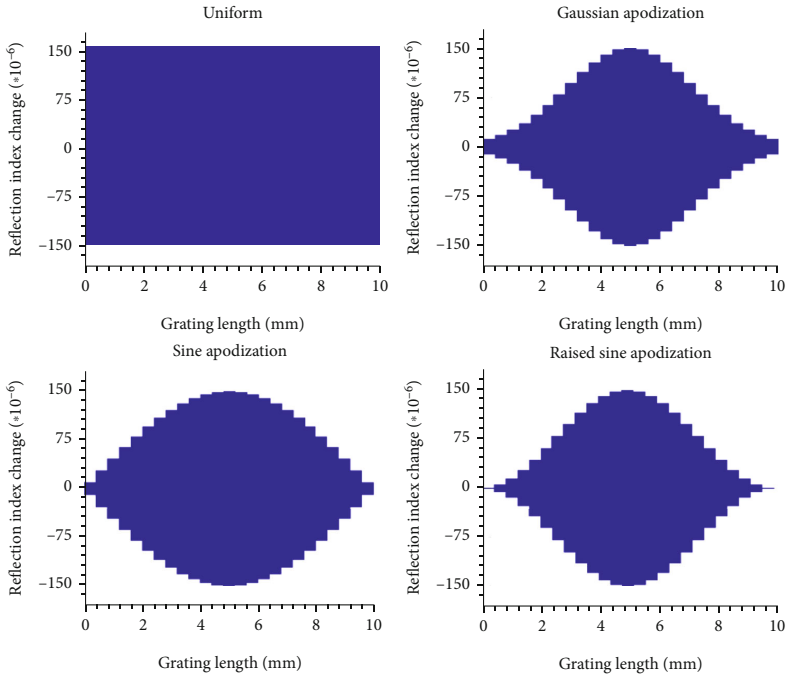
FIGURE 3: Geometrical shapes of FBG apodization profiles.
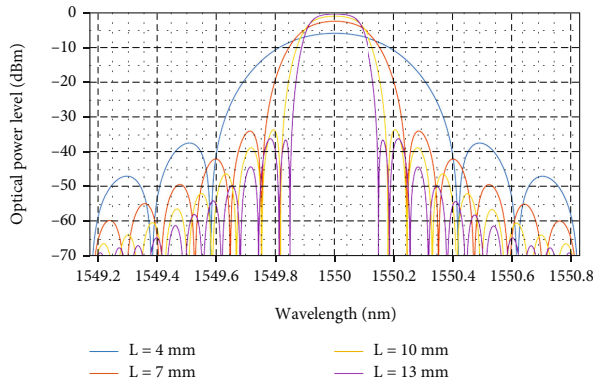

FIGURE 4: Reflected signal spectra of the FBG with raised sine apodization ($\Delta n = 1.5 \times 10^{-4}$) and various grating lengths.

provided online on the open repository platform Zenodo [15]. All of this data is included and visually presented in Figures 4–11. Figure 4, for instance, shows the reflected signal spectrum of the FBG optical sensor that uses raised sine apodization when grating lengths (in figure marked as "L") are 4, 7, 10, and 13 mm and the modulation index is $\Delta n = 1.5 \times 10^{-4}$. By increasing the grating length, reflectivity also increases (at $L = 4$ mm, $P_{max} = -6$ dB → reflectivity is 25% but for 13 mm, 90%), and spectral bandwidth becomes narrower (at $L = 4$ mm, FWHM =0.328 nm, but if $L = 13$ mm, FWHM is

0.173 nm). Figure 5 shows the reflected signal spectrum comparison between the FBGs with uniform, Gaussian, sine, and raised sine apodizations when the grating length is 13 mm and modulation index $\Delta n = 1.5 \times 10^{-4}$ is used. As we can see in Figure 5, the most efficient spectral deployment of FBG sensors is achieved if uniform FBGs are used. As for the side-lobe parameter, it is best minimized by using raised sine apodization, but after that by utilizing the Gaussian apodization.

As it can be observed, Figure 6 clearly shows the coherence between reflectivity, grating length, and grating
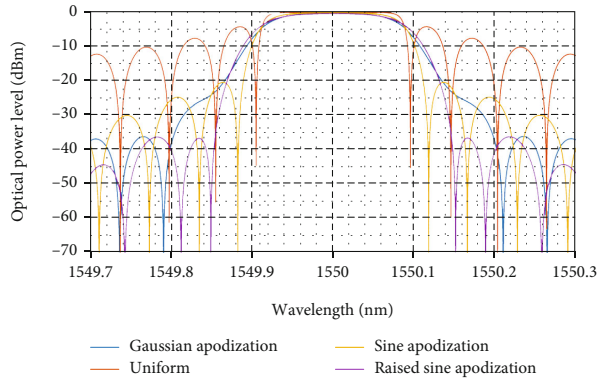
FIGURE 5: Comparison between the reflected signal spectra of FBGs with uniform, Gaussian, sine, and raised sine apodizations ($\Delta n = 1.5 \times 10^{-4}$ and fixed grating length 13 mm).

modulation index of FBG gratings. By increasing the length of the grating, also FBG reflectivity in % increases. The highest reflectivity is reached with uniform (without apodization) realization, then follows sine apodization, after that Gaussian apodization, but the relatively lowest reflectivity is by using the raised sine apodization. From the results, it can be concluded that the use of modulation index $\Delta n = 0.5 \times 10^{-4}$ provides relatively the lowest performance because the reflectivity of 90% is not reached (in the grating length range of 1-20 mm). The highest reflectivity we can observe at higher modulation index values, hence 1.5×10^{-4} and 2×10^{-4}. With higher modulation index values, it is possible to achieve preferred reflectivity while using a shorter length of the specific grating.

While analyzing the signal bandwidth, it can be seen in graphs (see Figure 7) that by increasing the grating length, the value of FWHM decreases. The most rapid changes are observed for the FBGs with 1-5-millimeter-long grating length. When the grating length of 2 mm is used, the FWHM bandwidth is reduced by half compared to the 1 mm long grating. For example, FWHM is 0.74 nm wide when 1 mm uniform grating is chosen, but the grating length of 2 mm (for the same uniform grating) leads to FWHM of 0.38 nm (at modulation index 1×10^{-4}). From the results, it can be concluded that the grating length from 1 to 5 mm is not suitable for sensor networks because it operates with relatively wide bandwidths. Hence, to save the available optical frequency spectrum and use the planned operational optical frequency range more efficiently, larger grating lengths for FGBs should be chosen, thus operating with narrower FWHMs. In Figure 7, it can be seen that the narrowest FWHMs are obtained when applying the lowest modulation index values of 0.5×10^{-4}. It is also important to highlight that for all the apodizations, there are specific values of grating lengths at which an additional increase of grating length does not provide a significant FWHM decrease anymore. For instance, as for the uniform type, significant FWHM decrement is observable until grating lengths of 6-8 mm,

while for Gaussian and sine 8-10 mm, and raised sine 10-12 mm. After those values, an increase in grating length does not highly affect FWHM values.

As shown in Figure 8, by analyzing the results obtained from simulations of FBGs with uniform and Gaussian apodization, the SLS is evenly decreased by increasing the grating length from 1 mm to 20 mm when using all four modulation index values (0.5×10^{-4} to 2×10^{-4}).

When using sine and raised sine apodization with modulation index (1.5×10^{-4} and 2×10^{-4}), graphs show the decrease of SLS when increasing the used grating length; however, at certain values (as can be seen in Figure 8(c)), the SLS also starts to increase with further increase of grating length. Yet this process can be observed for specific grating lengths, and then again, by increasing the grating length even further, SLS starts to decrease again (function is periodical). We can see similar tendencies in a scientific article [16], where a higher modulation index of 4×10^{-4} is used and well seen when the SLS function is periodical. The lowest SLS values are recorded for uniform FBG (without apodization) where they do not reach the defined threshold (20 dB); thus, we can state that it is not most suitable for FBG sensor networks and long-distance monitoring applications. When applying Gaussian, sine, and raised sine apodizations, side-lobe suppression is significantly improved compared to the uniform profile.

To better analyze and compare the FBG parameters like reflectivity (Figure 9), SLS (Figure 10), and FWHM (Figure 11) and their relation with the apodizations profiles, the comparison was performed with a modulation index of 1.5×10^{-4}. As we can see in Figure 9, while applying gratings in the range between 1 mm and 20 mm, the highest reflectivity results can be ensured by using the uniform profile. As for the second-highest – by sine apodization profile. Gratings with raised sine and Gaussian apodization provide similar results compared to each other and show relatively lower reflectivity when 1 mm to 20 mm grating lengths at modulation index 1.5×10^{-4} are chosen.
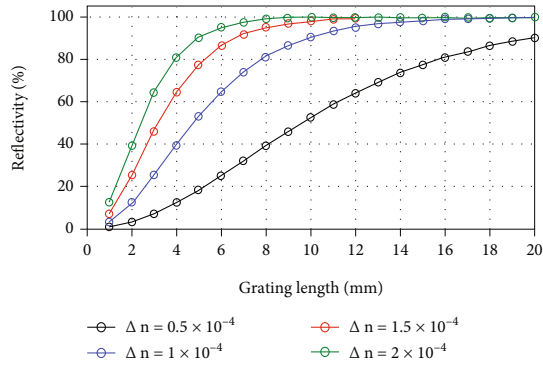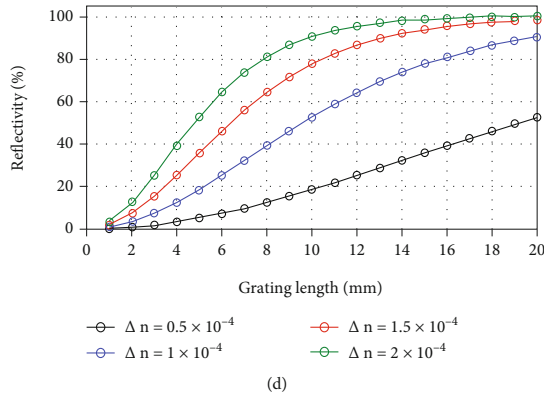
(a)
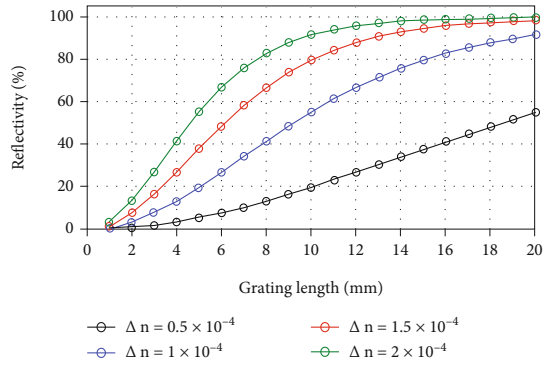
(b)
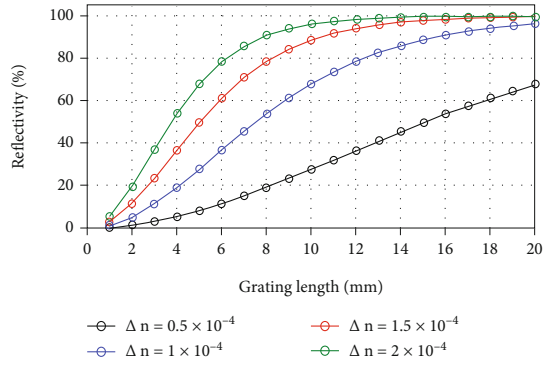
(c)

FIGURE 6: Continued.

FIGURE 6: Reflectivity versus grating length of FBG with (a) uniform, (b) Gaussian apodization, (c) sine apodization, and (d) raised sine apodization.
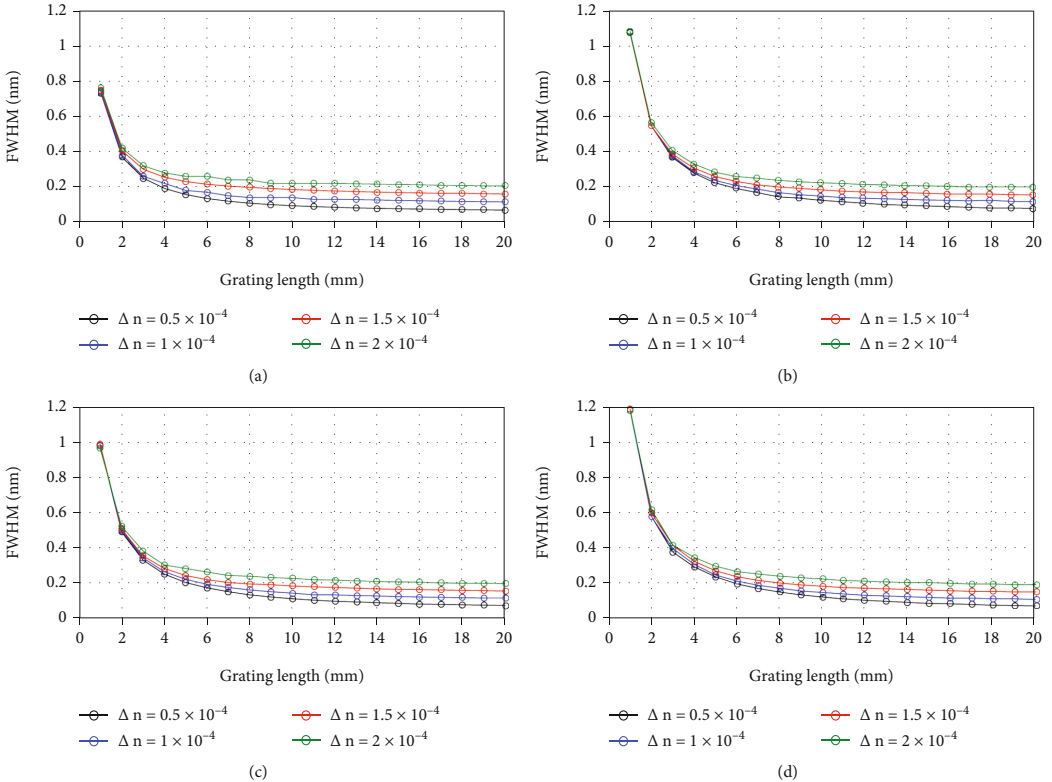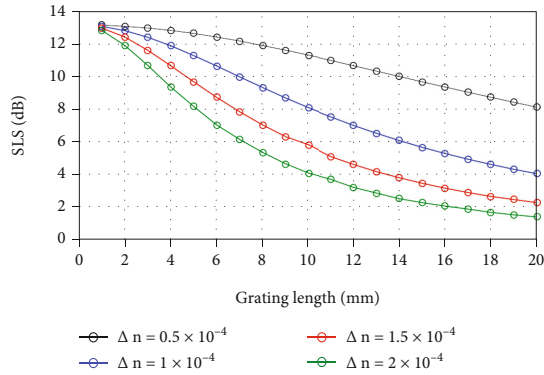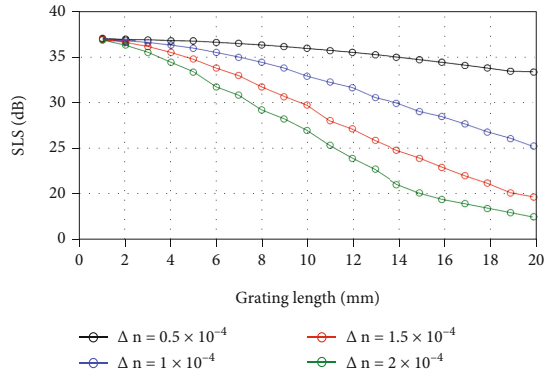

FIGURE 7: Comparison of FWHM versus grating length of FBG with (a) uniform, (b) Gaussian, (c) sine, and (d) raised sine apodization.

As we can see in Figure 10, Gaussian apodization ensures the highest SLS (33 to 38 dB) results when 1 mm to 7 mm grating lengths are chosen, but when grating lengths are between 9 mm to 20 mm, the best SLS results (30 to 32 dB) are shown by raised sine apodized FBGs. Uniform fiber Bragg grating provides the least side-lobe suppression values when grating lengths are used in the range of 1 mm to 20 mm.

(a)

(b)
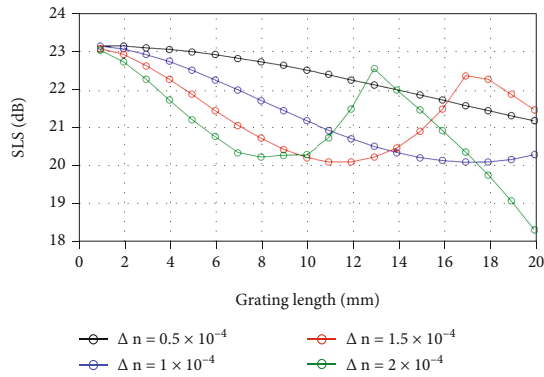
(c)
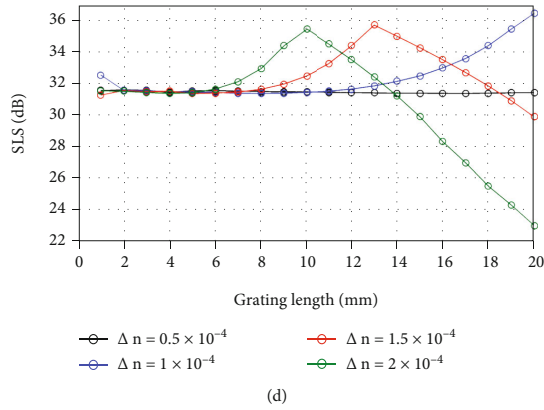
FIGURE 8: Continued.

(d)

Figure 8: FBG side-lobe suppression versus grating length of FBG with (a) uniform, (b) Gaussian, (c) sine, and (d) raised sine apodization.
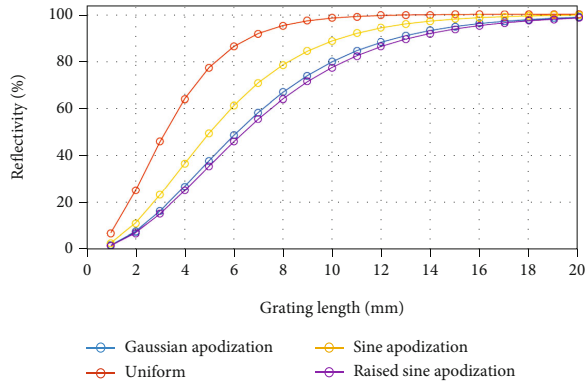

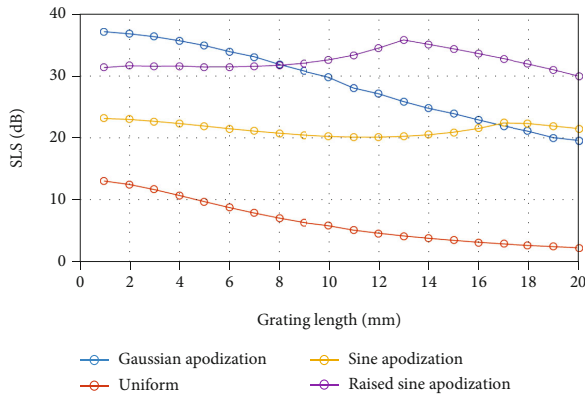Figure 9: Reflectivity versus the grating length of FBG.

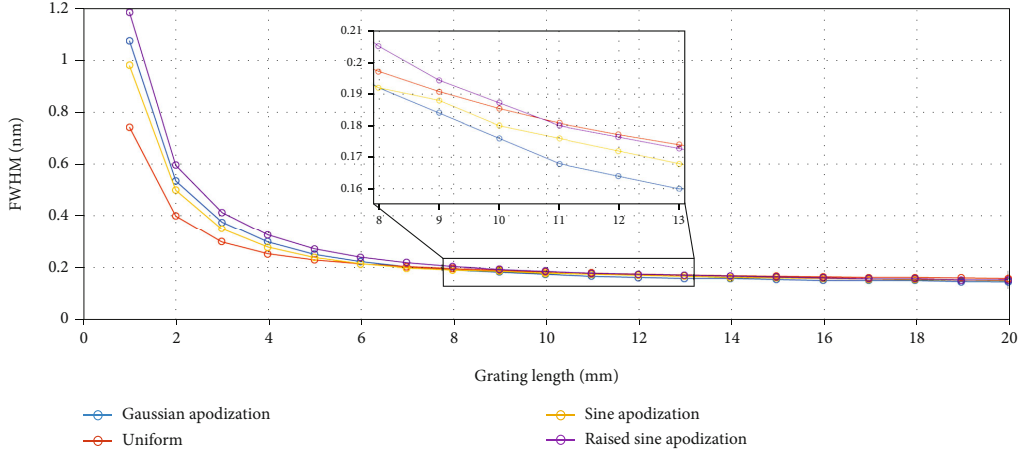Figure 10: Side-lobe suppression versus the grating length of FBG.

FIGURE 11: The full width at half maximum versus the grating length of FBG.

TABLE 1: Optimal FBG grating parameters for raised sine, Gaussian apodization, and sine apodization with modulation index 1×10^{-4}, 1.5×10^{-4}, and 2×10^{-4}.

Apodization type	Modulation index ($\times 10^{-4}$)	Grating length (mm)	Reflectivity (%)	FWHM (nm)	SLS (dB)
	1.0	20	90.3	0.112	35.6
Raised sine	1.5	13	90.0	0.173	35.7
	2.0	10	90.4	0.228	35.4
	1.0	19	90.0	0.110	26.0
Gaussian	1.5	14	93.1	0.160	24.7
	2.0	10	91.7	0.216	26.9
	1.0	16	90.9	0.118	20.1
Sine	1.5	11	91.9	0.176	20.7
	2.0	13	99.0	0.210	22.5

While analyzing the signal spectral bandwidth, it can be seen in graphs (see Figure 11) that by increasing the grating length, the value of FWHM decreases. The most rapid changes are observed for the FBGs with 1-6 mm long grating length. To save the optical frequency spectrum band, larger grating lengths (at least 6 mm) for FGBs should be chosen, thus operating with narrower FWHMs. The narrowest bandwidth when grating lengths are chosen between 1 mm and 7 mm is provided by uniform FBGs and then by sine and Gaussian apodizations. As for the gratings between 8 mm and 20 mm in length, the narrowest bandwidth can be reached by applying the Gaussian and then sine apodizations.

To provide FBG with narrower bandwidth (FWHM<0.2 nm) and high reflectivity (at least 90%), larger grating lengths for FGBs should be chosen. However, long FBG gratings do not always guarantee higher SLS parameter values. Due to that, it is vital to estimate optimal FBG parameters for every grating type as it is shown in the next paragraph.

Table 1 summarizes the most optimal FBG grating and apodization parameters evaluated from the previously men-tioned data and graphs. This table does not include previously mentioned uniform type FBG data because results gained by uniform FBGs do not comply with the SLS threshold (at least 20 dB) requirements. As we can see from the Table 1 data, the raised sine apodization provides relatively similar reflectivity and FWHM as does Gaussian apodization, but SLS values are significantly better for raised sine apodization than they can be observed from Gaussian apodization. Based on the research data, raised sine apodization is most optimal for the usage of sensors networks and long-distance monitoring, because overall, the relatively highest quality parameters for the grating can be reached with this type of apodization when mentioned modulation indexes are used. The length of the grating can be reduced when applying higher modulation indexes. However, a higher modulation index increases the spectral band and thus the FWHM value of an FBG.

The relatively best FBG results (reflectivity =90.3%, FWHM =0.112 nm, and SLS =35.6 dB) are observed for raised sine apodization with a modulation index 1×10^{-4} and grating length of 20 mm.
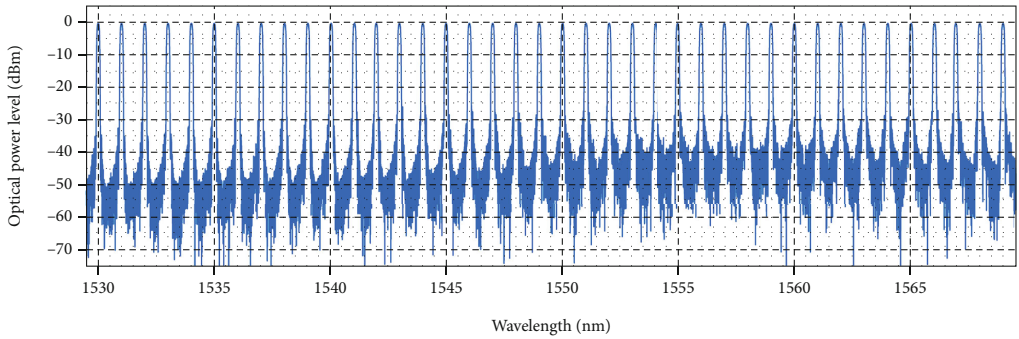
FIGURE 12: Reflected optical signal spectrum of the developed 40 FBG sensor network, where optimal grating parameters are used.
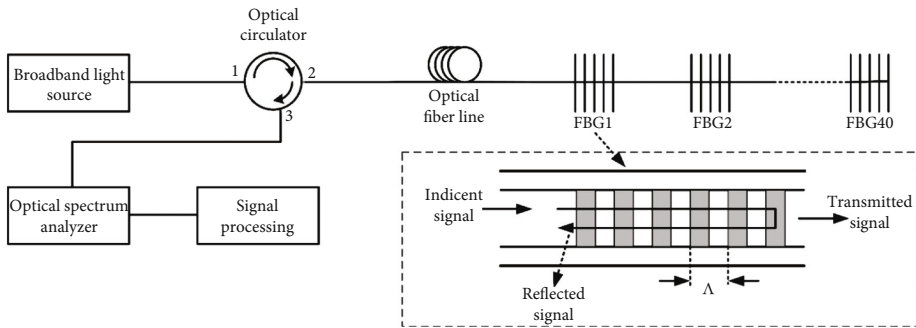

FIGURE 13: Simulation setup for testing FBG sensors' operation distance.

The sensor network with 40 FBG sensors in the wavelength band of 1,530 to 1,659 nm (spacing between the sensors is 1 nm) is developed ("OptiGrating" software) based on these FBG parameters to validate the found optimal parameters (raised sine apodization with modulation index 1×10^{-4} and grating length of 20 mm). The reflected optical signal spectrum is shown in Figure 12.

Figure 12. indicates that the developed 40 FBG sensor network has high reflectivity (>90%) and SLS value (~30 dB). SLS values have slightly deteriorated for the sensor network as the adjacent side lobes overlap.

For testing of FBG operation distance, we have firstly developed an additional simulation setup (see in Figure 13) by using *VPIphotonics* mathematical modelling software. In this model, FBG sensors operation distance (SMF fiber distance between optical circulator and FBG sensor network) is measured and tested.

In this simulation setup, the parameters of components are set based on the real parameters of commercial components. The transmitter part of the setup includes an optical broadband light source (BLS) which has full width at half maximum (FWHM) =80 nm in wavelength band of 1510-1590 nm. BLS component's output spectrum is experimentally measured with S-line Scan 800 interrogator and uploaded into this simulation setup. Here, BLS output is connected to the 3-port optical circulator (OC), which is

used for the separation of the optical light flows—transmitted and reflected FBG signals. Insertion loss for OC of direction $1 \rightarrow 2$ and $2 \rightarrow 3$ is 1 dB, but isolation 50 dB. OC port (2) is connected to SMF-28 single mode optical fiber (SMF) line. For SMF, such parameters are set as follows: attenuation: 0.18 dB/km; dispersion: 16 ps/(nm·km); dispersion slope: 0.092 ps/(nm²·km); PMD: 0.04 ps/√km; effective area: 85 μm²; and nonlinear index: 1.27 (W × km)⁻¹. SMF is connected with FBG sensor network, in which amplitude-frequency response (FBG transmitted and reflected spectrums) and technical parameters such as reflectivity, FWHM, and central frequency are uploaded. FBG sensors' reflected signals are transmitted from OC port $2 \rightarrow 3$ to the optical spectrum analyzer and signal processing unit, in order to analyze the received optical spectrums of the FBG sensors.

Afterward, for testing and validation purposes, such FBG sensor network's setup is then developed in laboratory environment where the architecture of the scheme is the same (see in Figure 14).

However, the specific 40 FBG sensor network with the estimated optimal parameters (that were investigated, developed, and described in the article, see Figure 12) was not physically available in our laboratory. Therefore for the testing and validation purposes, we have here used the FBG setup available for us in the laboratory, FBG sensor network
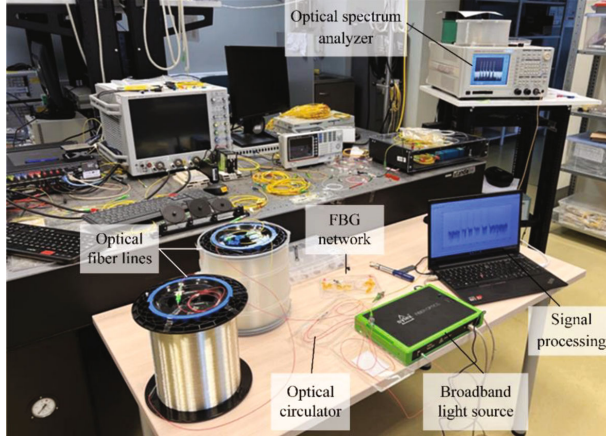
FIGURE 14: Experimental validation of the developed simulation model in laboratory environment.
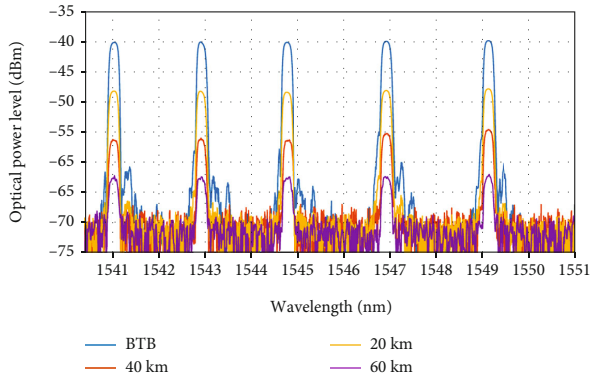

FIGURE 15: Experimentally measured reflected signal spectrum of FBG sensors after BTB, 20, 40 and 60 km transmissions.
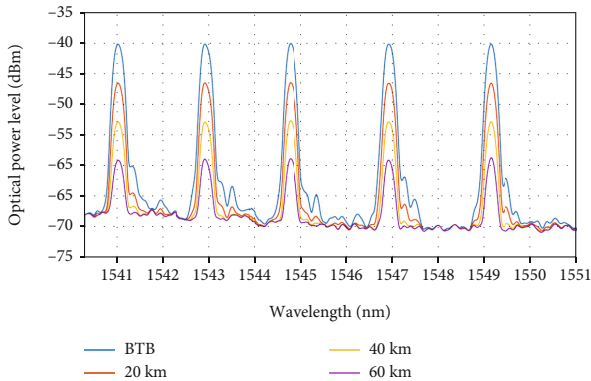

FIGURE 16: Mathematical simulation's measured reflected signal spectrum of FBG sensor after BTB, 20, 40, and 60 km transmission.
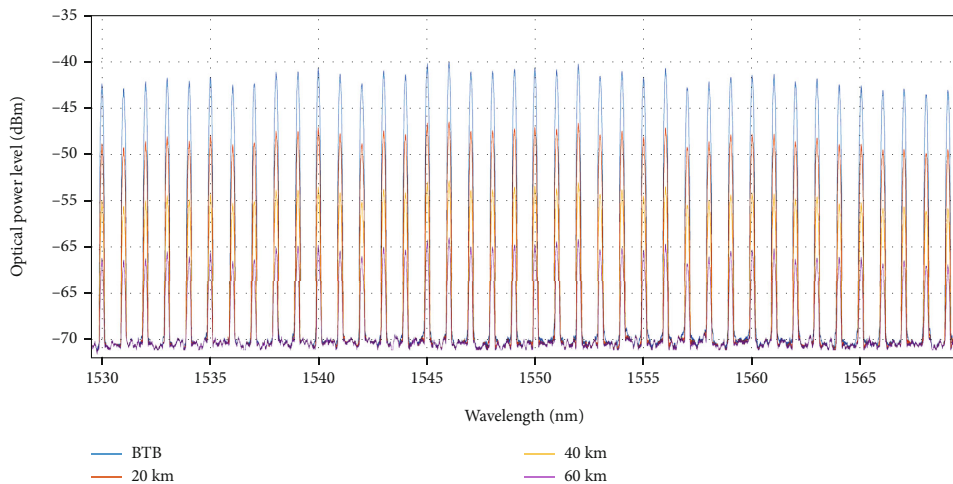
FIGURE 17: Reflected optical signal spectrum of the developed 40 FBG sensor network after BTB, 20, 40, and 60 km transmission.

with 5 FBGs (with central wavelengths of 1541, 1543, 1545, 1547, and 1549 nm).

As we can see in Figures 15 and 16, reflected signal spectrums of FBG sensor networks after BTB, 20, 40, and 60 km transmissions experimentally measured and measured by mathematical simulation are closely similar to each other. In mathematical simulation software, optical spectrum analyzer (OSA) uses extra signal processing function; therefore, at the noise level (~70 dB), the lines are smoother (less amount of noise) than in the experimental setup results. The obtained similar simulation and experimental results prove that the mathematical simulation model has been created correctly.

FBG sensor network with optimal parameters (developed and described in the article, see Figure 12) is then integrated into the developed and experimentally validated simulation model and tested after BTB, 20, 40, and 60 km long transmissions. As we can see in Figure 17, after 60 km transmission, it is possible to detect the received signals of FBGs central wavelengths, and side-lobe suppression ratio (SLSR) values are 9-11 dB. This means that the developed FBG sensors network can be used for long-distance (60+ km) monitoring solutions.

4. Conclusions

In this research, we have analyzed and defined optimal grating and apodization parameters that provide maximally high reflectivity (at least 90%) and acceptable SLS (at least 20 dB), and maximally narrow bandwidth (FWHM <0.2 nm) for FBG sensor networks and long-distance monitoring applications. In the article, we have estimated optimal FBG parameters for Gaussian apodization, sine apodization, and raised sine apodization when modulation indexes 1×10^{-4}, 1.5×10^{-4}, and 2×10^{-4} are used. From the apodizations used in this research, raised sine apodization was found to be the most optimal for the application in FBG sensor networks and long-distance (60+ km) monitoring if the binding parameters (as described in this work) are used.

Data Availability

The data generated in this study have been deposited in the open repository, Zenodo [15].

Conflicts of Interest

The authors declare that there is no conflict of interest regarding the publication of this paper.

Acknowledgments

References

[1] C. E. Campanella, A. Cuccovillo, C. Campanella, A. Yurt, and V. M. N. Passaro, "Fibre Bragg grating based strain sensors: review of technology and applications," *Sensors*, vol. 18, no. 9, p. 3115, 2018.

[2] U. Senkans, J. Braunfelds, I. Lyashuk, J. Porins, S. Spolitis, and V. Bobrovs, "Research on FBG-based sensor networks and their coexistence with fiber optical transmission systems," *Journal of Sensors*, vol. 2019, Article ID 6459387, 13 pages, 2019.

[3] I. S. Amiri, S. Azzuhri, M. Jalil et al., "Introduction to photonics: principles and the most recent applications of microstructures," *Micromachines*, vol. 9, no. 9, p. 452, 2018.

[4] A. Vinagre, J. Ramos, S. Alves, A. Messias, N. Alberto, and R. Nogueira, "Cuspal displacement induced by bulk fill resin composite polymerization: biomechanical evaluation using fiber Bragg grating sensors," *International Journal of Biomaterials*, vol. 2016, Article ID 7134283, 9 pages, 2016.

[5] M. M. Werneck, R. C. S. B. Allil, B. A. Ribeiro, and F. V. B. de Nazaré, "A guide to fiber Bragg grating sensors," in *Current Trends in Short- and Long-period Fiber Gratings*, IntechOpen, 2013.

[6] J. Braunfelds, U. Senkans, P. Skels et al., "FBG-based sensing for structural health monitoring of road infrastructure," *Journal of Sensors*, vol. 2021, Article ID 8850368, 11 pages, 2021.

[7] T. Li, C. Shi, Y. Tan, and Z. Zhou, "Fiber Bragg grating sensing-based online torque detection on coupled bending and torsional vibration of rotating shaft," *IEEE Sensors Journal*, vol. 17, no. 7, pp. 1999–2007, 2017.

[8] K. Sahota, N. Gupta, and D. Dhawan, "Fiber Bragg grating sensors for monitoring of physical parameters: a comprehensive review," *Optical Engineering*, vol. 59, no. 6, 2020.

[9] B. Van Esbeen, C. Finet, R. Vandebrouck et al., "Smart railway traffic monitoring using fiber Bragg grating strain gauges," *Sensors*, vol. 22, no. 9, p. 3429, 2022.

[10] R. Paschotta, "Fiber Bragg gratings," in *Encyclopedia of laser physics and technology*, Wiley-VCH, 1 edition, 2008.

[11] I. Ashry, A. Elrashidi, A. Mahros, M. Alhaddad, and K. Elleithy, "Investigating the performance of apodized fiber Bragg gratings for sensing applications," in *Proceedings of the 2014 Zone 1 Conference of the American Society for Engineering Education – "Engineering Education: Industry Involvement and Interdisciplinary Trends"*, Bridgeport, CT, USA, 2014.

[12] F. Chaoui, O. Aghzout, M. Chakkour, and M. El Yakhloufi, "Apodization optimization of FBG strain sensor for quasi-distributed sensing measurement applications," *Active and Passive Electronic Components*, vol. 2016, Article ID 6523046, 8 pages, 2016.

[13] Optiwave, Photonic Software, OptiGratinghttps://optiwave .com/products/component-design/optigrating/optigrating/.

[14] Optiwave, *OptiGratingUser's Reference and Tutorials*, p. 214, 2008.

[15] J. Braunfelds, E. Haritonovs, U. Senkans, I. Murans, J. Porins, and S. Spolitis, *Data accompanying "Designing of Fiber Bragg Gratings for Long-distance Optical Fiber Sensing Networks"*, Zenodo, 2022.

[16] K. M. Dwivedi, G. Trivedi, and S. K. Khijwania, "Theoretical study and optimization of apodized fiber Bragg grating for single and quasi-distributed structural health monitoring applications," in *Proceedings of the 2020 30th International Conference Radioelektronika, RADIOELEKTRONIKA 2020*, Bratislava, Slovakia, 2020.

Senkans U., **Braunfelds J.**, Lyashuk, I., Porins, J., Spolitis, S., Bobrovs, V. Research on FBG Based Sensor Networks and Their Coexistence with Fiber Optical Transmission Systems. Journal of Sensors, **2019**, pp.1-19.

Research Article

Research on FBG-Based Sensor Networks and Their Coexistence with Fiber Optical Transmission Systems

Ugis Senkans ⓘ**, Janis Braunfelds** ⓘ**, Ilya Lyashuk, Jurgis Porins, Sandis Spolitis** ⓘ**, and Vjaceslavs Bobrovs** ⓘ

Institute of Telecommunications, Riga Technical University, Azenes St. 12, LV-1048 Riga, Latvia

Correspondence should be addressed to Janis Braunfelds; janis.braunfelds@rtu.lv

Market forecasts and trends for the usage of fiber optical sensors confirm that demand for them will continue to increase in the near future. This article focuses on the research of fiber Bragg grating (FBG) sensor network, their applications in IoT and structural health monitoring (SHM), and especially their coexistence with existing fiber optical communication system infrastructure. Firstly, the spectrum of available commercial optical FBG temperature sensor was experimentally measured and amplitude-frequency response data was acquired to further develop the simulation model in the environment of RSoft OptSim software. The simulation model included optical sensor network, which is combined with 8-channel intensity-modulated wavelength division multiplexed (WDM) fiber optical data transmission system, where one shared 20 km long ITU-TG.652 single-mode optical fiber was used for transmission of both sensor and data signals. Secondly, research on a minimal allowable channel spacing between sensors' channels was investigated by using MathWorks MATLAB software, and a new effective and more precise determination algorithm of the exact center of the sensor signal's peak was proposed. Finally, we experimentally show successfully operating coexistence concept of the spectrum-sliced fiber optical transmission system with embedded scalable FBG sensor network over one shared optical fiber, where the whole system is feed by only one broadband light source.

1. Introduction

As it is observed in [1], fiber optical sensors are commonly used to measure a wide range of physical parameters, for example, temperature, strain, vibration, mechanical deformation, and pressure. Sensors that are based on a fiber Bragg grating (FBG) technology are one of the most promising and are widely used mainly due to their significant advantages like small size, high sensitivity, remote sensing capabilities and provided immunity to electromagnetic (EM) interference, etc.

From a physical point of view, the FBG is small (typically few centimeters in length) optical fiber span that is created by introducing a modulation of its core effective refractive index. To develop such grating, few methods can be used, as shown, for instance, in [2]—direct point-by-point method, continuous core-scanning method, or inter-

ferometric method. As a result, the FBG will reflect signals with specific central frequency or wavelength, called Bragg wavelength. Another aspect of fiber optical sensors is their adaptability as it is confirmed in [3] that glass optical fibers are more suitable for data transmission than polymer optical fibers. That is due to their smaller attenuation and higher bandwidth capabilities.

However, besides the important advantages, according to the article [1], FBG optical sensors have some disadvantages that can be triggered by crossed sensitivity providing inaccurate measurements of strain or temperature. Parallel to that, as it is discussed in the article [4], a risk factor can also be areas with high temperatures and places where vibration or trembling is observed near the optical fiber sensors.

For a couple of years until now, the need for fiber optical sensors globally is continuously rising. From the analysis of current trends of fiber optical sensor market

shown in an article [1], especially highlighting the FBG, it is clear that there are three main segments leading to the demand for fiber optical sensors. One of them is sensing devices—optical sensors as a technology for different sensing applications. Another one is instrumentation, for example, software, acquisition systems, interrogation devices, and graphical interfaces. The third segment is system integration and installment services, for example, engineering projects.

Nowadays, lots of different fields, for example, structural health monitoring (SHM), have a wide variety of possible optical sensor installation and deployment methods. For instance, there are applications evaluated [5] where FBG optical sensors are embedded in concrete to measure strain and monitor tracks. According to [6], topical research theme in a matter of SHM is also an underground coal mine monitoring due to the occurring construction accidents. Furthermore, studies have shown [7] implementation of optical sensors in different surfaces and materials, like 3D-printed structures, where 3D printing technology can serve as a link to connect FBG optical sensors and robotic devices. Last but not least, in the latest studies [8], particular interest is in sensing applications for supertall buildings that might be in a risk of different types of deformations, hence a threat for civil security.

Considering a wide variety of reports that are based on a fiber optical market research [9], the newest statistics predict average annual growth of the sensor market in the range between 4.41% and 10.5%. These numbers are acquired by combing a different kind of optical sensor types such as [10] point, distributed, quasidistributed, intensity, phase, polarization, frequency, physical, chemical biomedical ones, and different categories that are based on sensing location, operating principle, and applications.

Due to the growth in the number of devices using available transmission spectrum for communications and data transmission as well as enhancement of optical networks infrastructure, literature in [11, 12] has shown an indication that there is increased attention on effective spectrum utilization. One of the key elements in the deployment of sensor networks is an effective choice of their minimal channel spacing to keep spectral efficiency of sensor network high as possible and to avoid overlapping of adjacent optical sensor signals that leads to the need for developing algorithms for precise determination of the exact center of the sensor signal's peaks (also called as central frequency or wavelength). Changes in measured central frequency or wavelength of the sensor's reflected signal are representing the variation of physical parameters such as temperature and strain. Another key element, which is as important as the first one, is ensuring resource-effective architectures of data transmission and sensing systems, maximizing their compatibility. Therefore, our experimental fiber optical transmission system with embedded FBG sensor network, as shown in Section 4 of this paper, operating over one shared optical distribution network (single-mode optical fiber), while using unified broadband light source for both systems, serves as a good example of the coexistence of these systems. To the best of our knowledge, such experiments for the implementation of unified light source have not been conducted yet.

2. Fiber Optical Sensors in IoT and SHM Applications

Internet of Things (IoT) is an area of potential growth and different kinds of innovations which agrees the majority of the world's governments in Europe, America, and Asia. As indicated in [13], public safety, environmental protection, and Smart Industries, e.g., smart homes, are only a few of the potential IoT application areas. As mentioned in studies like [14, 15], SHM applications can be an important field of fiber optical sensor usage as well as for the domain of IoT in cases of optical sensor implementation for operational safety of structure (e.g., buildings, roofs, bridges) observations. The authors can suggest one of the many ways of the possible scenarios, which links the IoT with SMH. From a wide variety of modern technology research, one of them, for instance, which is carried out in IoT direction, is smart cars and traffic control. In this case, one of the scenarios includes IoT smart car combination together with fiber optical sensing for SHM needs. In the scenario when there are roads with embedded FBG optical sensors, providing strain measurements for road SHM, this information can be provided through the nearly deployed single-mode optical fiber cable to the service provider central office for further processing. All the strain measurements can be processed to detect the streets which at that particular moment have traffic jams and by knowing that, a traffic control optimization could be initiated. Such information, for example, traffic jam situation and traffic safety information, could be as well wirelessly transmitted to IoT smart cars, which then could take alternative routes.

By taking a closer look on a sensing layer, [16] presents that it can be seen that a layer is made of different types of control modules, for instance, sensor networks that include particular kind of sensors needed for monitoring of vibration, strain, temperature, humidity, etc. As for the main information, it is collected in the perception level and sensing layer comprises a data acquisition as well as a short-distance transmission where data and information is aggregated via sensing devices and later handed over to the particular gateway by bus or short-distance wireless transmission technology applications.

To ensure high safety of civil infrastructures, such as buildings, bridges, roads, and even road embankments, assessment of structural integrity in relation to the load-carrying capacity, which decreases due to aging, damage, or deterioration, must be carried out continuously. Studies [17] have previously shown that traditionally this structural health monitoring is carried out by periodic visual investigations, or by using discrete electrical or mechanical sensors. However, such sensor deployment is time-consuming and they are difficult to install during construction and repairs. They require a large number of electrical connections and complex cabling and have a high susceptibility to electromagnetic interference (EMI), humidity, and relatively short lifetime.

As an example, currently, in Latvia, SHM of bridges, roads, railways, and surrounding embankments is mostly done through visual inspections. Latvia is a good example
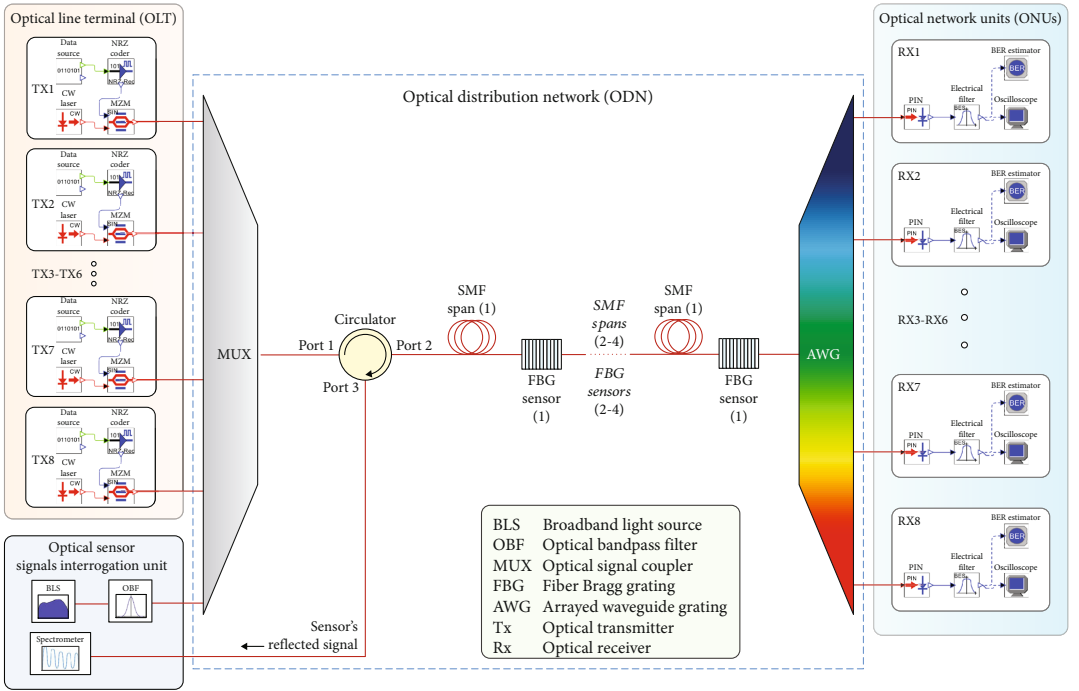
Figure 1: Developed simulation model of combined 5 FBG temperature sensor networks integrated into 8-channel 10 Gbit/s NRZ-OOK WDM-PON transmission system.

in successful fiber optical network rollout and holds the leadership position in the European fiber to the home (FTTH) ranking, with fiber coverage of 45.2%. Therefore, due to the availability of fiber optical infrastructure, fiber optical sensors are paying large attention from Latvian companies like the national road administration—State Joint Stock Company "Latvian State Roads" [18], which are interested in using the existing fiber optical infrastructure and FBG sensors for remote monitoring of their objects. For example, with passive FBG sensor solution, where multiple sensors are embedded in different layers of the road pavement, it is possible to monitor road condition during its lifetime. In addition, research of [19] also support the FBG technology topicality in relation to fiber optical sensors in SHM applications and especially highlighting different algorithm tests for detection of tiny wavelength shifts, hence pointing out the importance of an efficient available frequency spectrum and FBG application improvements. Considering that IoT and SHM field develops a closer connection with fiber optical sensors' field [20], therefore it is important to research FBG sensor coexistence with typical fiber optical transmission network infrastructure, starting from combined network architecture and ending with spectrum allocation and minimal spacing between sensors and data transmission channels. In our research, the aim for correct measurement acquisition of physical parameters like temperature and strain and precise detection of FBG sensor central wavelengths or peaks is crucial and can

be complicated due to the amplitude fluctuations of FBG's reflected signal peak, as shown in Section 3 of this paper.

3. Modeling of Combined FBG Sensors and WDM-PON Transmission System Network

Our simulation setup was developed by using RSOFT OptSim software, where we used measured amplitude-frequency response data of commercial optical temperature sensor, which is a sensitive, ruggedized temperature sensor based on uniform FBG technology (Figure 1). The goal of this modelling is to develop an operating simulation model that provides successful FBG optical temperature sensor network collaboration with 8-channel wavelength division multiplexed passive optical network (WDM-PON). The developed model was further used for observation of temperature effect on sensors' signals (optical signal reflected from deployed FBG sensors) as well as observation and calculation of minimal channel spacing, which led to our proposed peak detection algorithm (Section 3.2). As for the data transmission system, our created model uses a non-return-to-zero on-off keying (NRZ-OOK) modulation scheme. Optical line terminal (OLT) with 10 Gbit/s transmitters is located in the service provider's side. From structural point of view, we integrated few element configurations based upon our previous research shown in the article [21], where every transmitter includes 10 Gbit/s pseudorandom binary sequence

(PRBS) data source, NRZ driver, optical Mach-Zehnder modulator (MZM) with 20 dB extinction ration and 3 dB insertion loss, and continuous wave (CW) laser with output power of +3 dBm. For those eight data channels, central frequencies are set as follows: 192.90, 192.95, 193, 193.05, 193.1, 193.15, 193.2, 193.25 THz. According to the ITU-TG694.1 recommendation [22], data channel spacing is set to 50 GHz. Afterwards, all eight of the data transmission channels are then coupled by the optical coupler (MUX) for further transmission in an optical distribution network.

As for the light source, for the sensor network, the broadband light source (BLS) represented by super-luminescent light-emitting diode (SLED) was chosen. The BLS source's optical band from 193.7 THz to 195.3 THz was used for deployment of FBG optical sensors. We experimentally measured the spectrum of SLED source in RTU Fiber Optical Transmission Systems Laboratory and then loaded its amplitude-frequency response data into our simulation model. If we look at the spectral intensity fluctuations in this specific frequency region, we can observe that they are relatively small—less than 0.37 dB and output power is set to -9 dBm. Our SLED signal, which will be further used as a seed light for optical FBG sensors, is then filtered by an optical bandpass filter and sent to the optical signal coupler (MUX), where it is coupled with 8 data channels from OLT (see Figure 1). In this setup, we use optical circulator for separation of signal transmission directions to separate sensors' (FBGs) reflected signals from transmitted data signals and light source. Influence of the transmission spectrum of a circulator is negligible as circulators' bandwidth is wide enough (1525–1610 nm in wavelength or 186.206–196.585 THz in frequency) and the directivity was >50 dB, and isolation was >40 dB. In the middle part of the transmission scheme, there is an optical distribution network containing 5 optical FBG temperature sensors and 5 single-mode optical fiber (SMF) spans forming 5 sections with 4 km distance between each and every sensor. Therefore, the total optical line length is 20 km. The length of the spans was selected to present 4 km, based on the data that such distance is commonly used in Latvia between fiber optical cable cabinets or manholes, where fiber optical closures are placed. In addition, the fact that each sensor is located in the different distances from optical signal interrogation unit allows evaluating the combined system under different scenarios.

As shown in Figure 1, after the last FBG sensor, there is located demultiplexer for separation of data transmission channels, represented by an arrayed waveguide (AWG) and optical network units (ONUs). The received optical sensing signal quality is monitored by a spectrometer, which is connected to a circulator. As an optical receiver, we use PIN photodiodes with a sensitivity of -17 dBm at reference bit error ratio (BER) 10^{-10}. PIN output is connected to electrical Bessel low-pass filter with 7.5 GHz 3 dB cutoff frequency and afterwards to the electrical scope or BER estimator. This combined scheme provides coexistence of two previously mentioned systems. As we observed in the investigated optical sensor network model, the influence of WDM data transmission channels on sensor signals was negligible, causing only a slight decrease in optical signal to noise ratio of
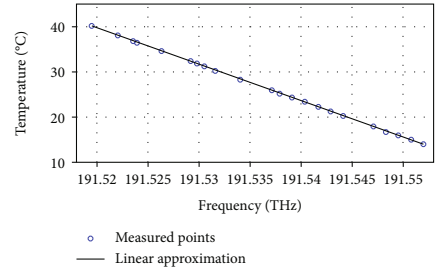

FIGURE 2: Measured experimental data and their linear approximation representing the correlation between temperature and frequency for commercial FBG optical temperature sensor.

received data signals. In other words, by making the overall system more complex (combining both systems by including more devices and elements in total) results in a power loss for optical sensor network. It is also important to remember that with the collaboration of both systems, crosstalk is inevitable, respectively, mutual interference can be observed. Adding to that, signal noise in this situation can be expected, mainly due to each and every simulation schemes' element. However, to make this combined system more resource and spectrum efficient, it is necessary to assess and calculate minimal channel spacing or frequency band between FBG sensor central frequencies (channels) as well as to create an algorithm for precise signal peak detection. Such aspects are further investigated in this article.

3.1. Research of Minimal Allowable Channel Spacing between Sensors' Signals.
For this research, the precise determination of minimal channel spacing, as well as peak detection using different methods, was important. According to the datasheet of the commercial optical FBG temperature sensor, its calibrated frequency at +26°C is 191.53713 THz or 1565.191 nm in wavelength and frequency response to temperature change is 1.279 GHz per 1 degree Celsius. The reflectivity of the used FBG temperature sensor is higher than 15%.

In our research, we also compared the theoretical temperature sensor's response from datasheet with our measured one. To perform this, we firstly heated FBG optical sensor to measure a wide variety of FBG's reflected signal central frequencies in the temperature range between +14°C and +40°C. The temperature response of the peak frequency of the FBG was measured to be −1.231 GHz per 1 degree Celsius. The acquired linear equation describing temperature and frequency correlation (response) for the FBG optical temperature sensor is represented in Figure 2.

As one can see, the difference between our experimentally measured FBG response data and manufacturer's provided data is only 3.9%. Therefore, we used the experimentally measured temperature response of the peak frequency of the FBG further in our research. This response value was a decisive factor for the evaluation and analysis of minimal channel spacing between sensor channels.

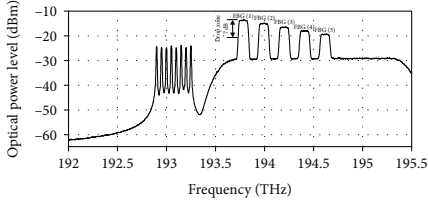In Figure 3, you can see the spectrum of the simulated combined system at 0°C environment temperature, which

Figure 3: Spectrum of simulated combined system with 5 FBG optical sensor reflected peaks and 8 data channels (spectrum obtained by spectrometer located in optical sensor interrogation unit) at 0°C environment temperature.

Table 1: Calculated frequency channel plan of optical FBG temperature sensors.

FBG sensor's no.	Frequency (THz)
1	193.800
2	194.008
3	194.217
4	194.425
5	194.633

includes 5 optical FBG sensor channels (FBGs' reflected signals) and 8 data channels, measured by a spectrometer with resolution bandwidth set to 0.07 nm and located in optical sensor signal interrogation unit. Please pay attention that this is a spectrum of the reflected signal, not the spectrum of transmitted signal; therefore, the 8 data channels are visible and significantly attenuated.

Further, the next FBG parameter was to be estimated, in this case of 5 FBG optical sensors, the average spectral width of sensor signals in the optical power drop zone of 7 dB (see Figure 3). Here, 7 dB optical power drop zone applies not only to the first sensor but also to each and every reflected sensor signals' own maximal amplitude.

Power drop zone value was calculated by creating an equation, which is based upon our previous research [23] for the detection of channel spacing between sensor signals in the specific spectrum region:

$$P_{\text{drop zone}} = 10 \cdot \log (n) = 10 \cdot \log (5) = 7 \text{ dB}, \qquad (1)$$

in which $P_{\text{drop zone}}$ (dB) is the optical power drop zone and n is the number of sensors. An equation was created by analysing the optical sensor reflected signals' overlapping in case of different temperature changes for fiber optical sensors that are located close to each other, as well as by evaluating [23] proposed minimal power drop zone diapason value in which the nearby reflected sensor signals should be maintained. With this information, we were able to propose the formula that describes such calculations. This formula was chosen to calculate the worst case scenario—when creating overlapping to one of FBG sensors from all other sensors. According to our measurement results, the average spectral width of sensor peaks in the optical power drop zone of 7 dB is 109.8278 GHz. This value is further used for the determina-

tion of minimal frequency channel spacing between adjacent FBG sensors.

We expect that the operating temperature for FBG sensor network will be in the range of 80°C (from -20°C to +60°C, typical to structural health monitoring applications). By knowing frequency to temperature response as well as spectral width of FBG sensor peaks, we were able to develop our equation to determine theoretical minimal channel spacing (CS) between every FBG optical sensor that was integrated into our system:

$$\text{CS} = \text{bw}_{\text{avg}} + (T_{\text{tot}} \cdot f_{\text{var}}), \qquad (2)$$

in which CS (GHz) is the channel spacing, bw_{avg} (GHz) is the average spectral width of FBG's reflected signal peak at the optical power drop zone level of 7 dB, T_{tot} (°C) is the total expected temperature variation range, and f_{var} (GHz) is the temperature response of the peak frequency of the FBG for one degree Celsius. After inserting all known variables, the result of minimal channel spacing calculation is as follows:

$$\begin{aligned} \text{CS} &= \text{bw}_{\text{avg}} + (T_{\text{tot}} \cdot f_{\text{var}}) \\ &= 109.8278 + (80.1.231) \\ &= 208.285 \text{ GHz}. \end{aligned} \qquad (3)$$

The channel plan, based on the abovementioned calculations of FBG sensors, is shown in Table 1.

Accordingly, central frequencies of optical FBG temperature sensors were set in the simulation model as in the table above, starting from the first to the fifth sensor, as it is also seen in Figure 3. We chose such frequencies while considering occupied spectrum by the 10 Gbit/s downstream data transmission channels to provide stable operation of combined FBG sensors and WDM-PON transmission system network. By stable operation, we mean the case where no overlapping between optical sensors and data transmission channels is observed and it is possible to measure and interrogate both sensor channels and data transmission channels with BER not higher than, for example, 10^{-9}. These frequencies (Table 1) represent the FBG signal peak frequencies, where peaks have maximal amplitude. However, due to the irregularity of reflected spectra of the FBG sensor, not always the peak point with the highest amplitude is the exact center or central frequency of the peak. Therefore, it is important to develop an algorithm allowing to precisely detecting FBG central frequency, thus reducing the sensor measurement error.

3.2. Development of an Algorithm for Precise FBG Signal Interrogation. If all FBG signals are equally attenuated (e.g., located in one physical place), deployed relatively apart from each other in the spectrum and FBG has smooth amplitude-frequency response curve, then interrogation of FBG signals is not a hard task. Nevertheless, there are some difficulties in real applications, where FBG optical sensors are located in different physical locations; therefore, each FBG peak experiences different amounts of attenuation. For example, in situations when there are multiple FBG sensors connected
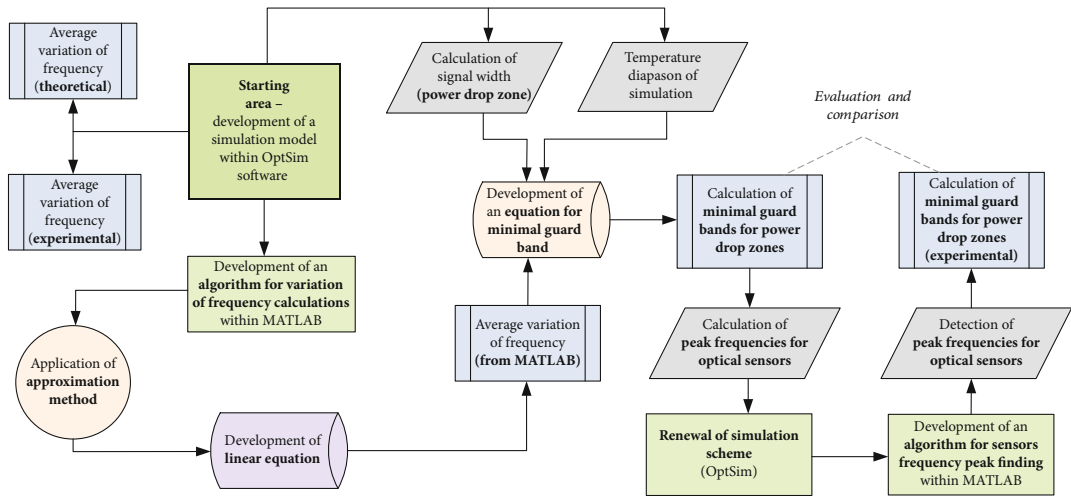
FIGURE 4: Flowchart of the algorithm development for precise detection of the exact center of the signal's peak (central frequency).

in series on one optical fiber and they are located in different distances between each other, a different amount of attenuation (decrease in optical power) on each reflected sensor peak can be observed. It generally leads to the situations where some reflected sensor signal peaks can be very attenuated if compared to the signal peaks of the sensors, which are physically connected closer to the interrogator. Not to forget that light is passing through optical fiber twice—first through optical sensors and then reflected back through the circulator. In that case, it is important to detect the precise center of the reflected sensor signal peaks for systems' optimization, as well as efficient preservation of the available frequency spectrum. Accordingly, if the sensor is located farther away from the interrogation unit, then its signal is more attenuated, as it can be seen in Figure 3.

Thereby, authors offer a precise peak detection solution created within MATLAB software. Our work structure and sensors' signal processing order is visualized in the flowchart (see Figure 3). This figure represents our research process starting from the creation of a simulation model and ending with the creation of an algorithm (MATLAB code) for the finding of precise sensors' peak central frequencies.

As shown in Figure 4, based on the measured temperature response of the peak frequency of the FBG and creation of minimal channel spacing equation, it is possible to evaluate minimal FBG channel spacing what was also one of the main objectives during this research. Subsequently, we investigated peak central frequency calculations for sensor signals, and by updating our OptSim simulation model with new adjustments, we were able to create a new algorithm (written as MATLAB code) for determination of the exact center of the sensor signal's peak that was yet another objective of this research. Once that it was completed, it was possible to compare traditional approach, where the peak central frequency is the peak's point with the highest intensity (standard automatic peak detection) against our pro-

posed algorithm, where the peak central frequency is the exact center of the peak.

In order to determine precise channel spacing between FBG signals, it is important to locate an exact center of each signal peak and vice versa. It needs to be made clear that not always the highest value in a peak region is its center. In this case, all the commonly used standard algorithms (represented as "x" in Figure 5) of automatic peak finding, regardless of the MATLAB algorithm typically used, do not achieve the needed result, as shown in Figure 5.

As it is shown in Figure 5, it is not an easy task to detect the exact center of the FBG's reflected signal's peak due to its irregularity. To solve this problem, we created an algorithm within MATLAB software where we imported data about sensor signals from OptSim simulation scheme discussed in this article. Our method and approach are similar to the one widely used for measurement of pulse width—well-known full width at half maximum (FWHM) method. To detect the exact center of each FBG sensors' peak, we based our calculations upon relative peak power level that was equal to 90% from its maximum. When the algorithm had detected 90% power level, it started locating spectrum values on both sides—left and right. Once it had acquired such values, it mathematically summarized both values and divided by two. Then, from this point at the 90% power level, algorithm started finding a spectrum point that is located upwards till it reached the exact point, which was our desired exact signals' peak middle point. With such a method being used, we improved our FBG signal interrogator accuracy and excluded the wrong detection of signal peaks due to power fluctuations and irregularity of the frequency spectrum.

Once we composed this algorithm, it provided us the ability to process spectrum data of each sensor and detect the exact center frequency of each sensor's reflected signal (see Figure 6 and Table 2).
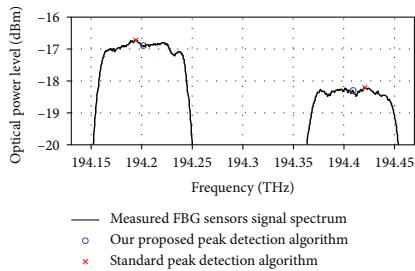
FIGURE 5: Comparison between standard automatic peak detection algorithm, based on the highest value in the peak region, and our proposed algorithm, which detects the exact center of the peak for 3rd and 4th FBG sensors.
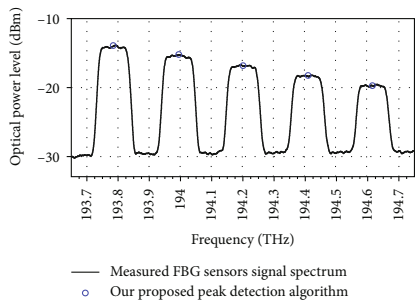

FIGURE 6: Reflected signal spectrum of 5 simulated FBG sensors with precisely detected center peak frequencies by using the proposed algorithm.

TABLE 2: Calculated and detected FBG optical sensor central signal frequencies using both methods.

| FBG sensor's no. | Central peak frequency (THz) obtained by | | Difference (GHz) |
	Calculated central frequencies	Measured with our proposed peak detection algorithm	
1	193.800	193.785	15.166
2	194.008	193.994	14.084
3	194.217	194.201	15.385
4	194.425	194.409	15.642
5	194.633	194.616	17.322
Channel spacing (GHz)	**208.285**	**207.746**	**0.539**

Knowing that FBG channel spacing is estimated as a difference between two adjacent FBG signal peak centers and that our newly acquired peak center frequency values differ from values obtained by calculated FBG's central frequencies (as shown in Table 1), it was understandable that the channel spacing will differ as well. Therefore, we summarized the newly detected central frequencies of FBGs's

peaks in Table 2, as well as compared them to previously obtained values by calculated central FBG's frequencies. From these results, channel spacing values can also be determined and compared to each other.

As it is possible to observe from Table 2, there is a difference between frequency values (GHz). This number is representing the difference in error between both used algorithms.

From our results, it is clear that such a peak detection algorithm can be integrated into FBG optical sensor interrogation units to precisely detect the exact center of each FBG signal's peak.

4. Research of Concept for the Coexistence of Single Light Source Fed Fiber Optical Data Transmission System with Embedded FBG Sensor Network over Shared Optical Fiber

One of the appealing ideas in the matter of optical sensor networks and data transmission systems is by unifying their input light sources. In this case, the spectrum-sliced wavelength division multiplexing (SS-WDM) technology that is realized with amplified spontaneous emission (ASE) source might be considered to achieve such a goal. SS-WDM was chosen for our further study due to its advantages also discussed in the article [24], for instance, cost-efficient solution that can be acquired by its ability to compose optical elements and electronics in one central office allowing network architecture simplification specifically for optical transmitter side.

We developed a simulation model and an experimental model of a spectrum-sliced WDM transmission system, where one broadband ASE source was shared by the optical transmission system and sensor network at the same time (see Figures 7 and 8). Differently, from other related studies in this field, we focused our goal on achieving error-free transmission system model that provides reliable output for both data transmission and optical sensor channels. Adding to that, our initial research in this matter uses the data transmission rate of maximum 1.5 Gbit/s per channel, which was limited by the characteristics of the light source, as described further.

4.1. Description of Realized Spectrum-Sliced Transmission System Simulation Model with Embedded FBG Sensor. Another one simulation carried out within OptSim software was aimed for a better understanding of the influence of the FBG optical sensor system on the data transmission system which was unified together with the optical sensor system. Figure 7 shows the created simulation model that has 3 main parts—central office (CO), optical distribution network (ODN), and optical network terminal (ONT). In central CO part, here for the BLS source, we chose amplified spontaneous emission (ASE) source. The ASE source's optical band from 191.75 THz to 195.8 THz was used to provide operation of FBG optical sensor. We experimentally measured the spectrum of the ASE source and then loaded its spectral characteristics into our simulation model. Please see the measured spectrum of ASE source in Figure 9.
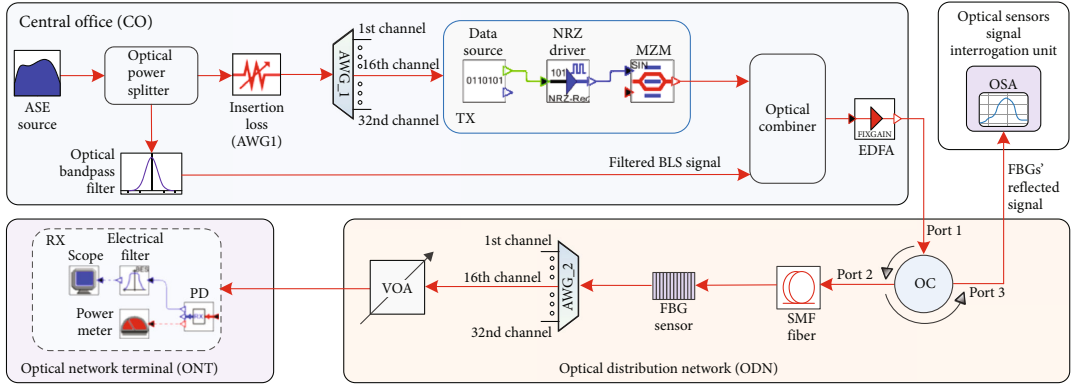
FIGURE 7: The simulation model of 1.5 Gbit/s spectrum-sliced transmission system with embedded FBG sensor.
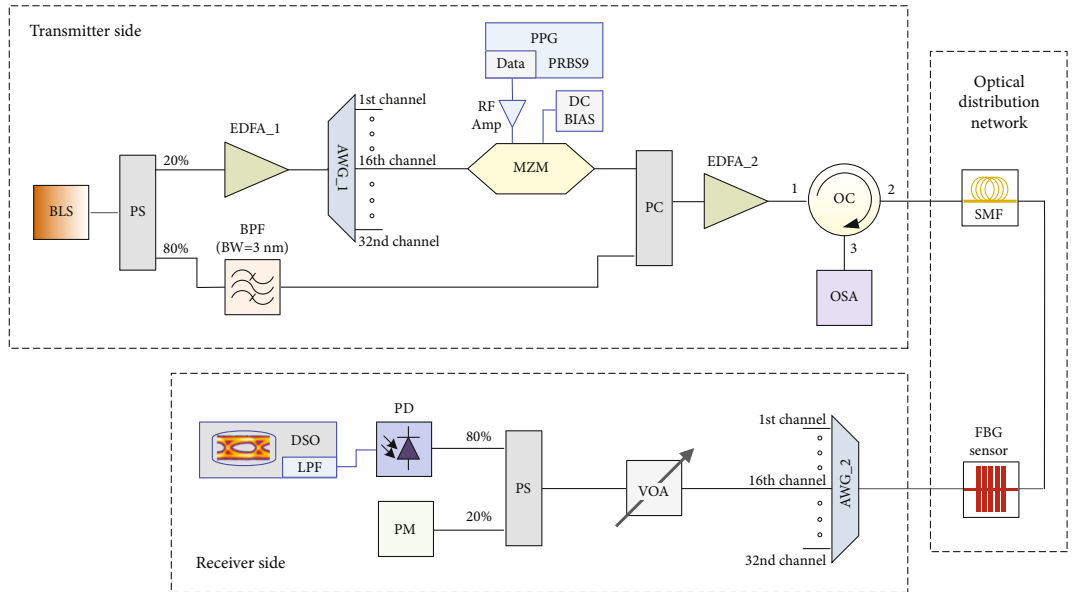

FIGURE 8: Experimental system of spectrum-sliced WDM fiber optical transmission system with embedded FBG sensing system fed by a single shared broadband light source.

Further, optical power splitter was used for dividing the optical signal into two parts (with 50 : 50 power division ratio). One of the signal parts was used for data transmission channel needs and the other one for FBG optical sensors' spectrum allocation. 32-channel AWG was chosen for the separation of data transmission channels. The central frequency for data transmission channel is set to 193.1 THz or 1552.52 nm, according to ITU-TG.694.1 frequency grid. From Figure 7, it is possible to observe the structure of every transmitter (Tx), where they consist of data source, non-return-to-zero (NRZ) driver, and Mach-Zehnder modulator (MZM) with an extinction ratio of 26 dB. The other part of

the signal (50%) is filtered through an optical bandpass filter (OBF). Here, the OBF with 1 THz 3 dB bandwidth is used to avoid overlapping of modulated data channels and the BLS source spectrum intended for the operation of FBG sensors. Then, both signals are coupled by using optical Y type (50% : 50%) coupler. Afterwards, coupled optical signal is amplified by EDFA with 20.5 dB fixed gain (output power up to 22 dBm).

Next, in the optical distribution network (ODN), to provide the ability to observe FBG optical sensor (with optical spectrum analyzer (OSA)), the optical circulator is chosen for the optical sensor to separate combined transmitted
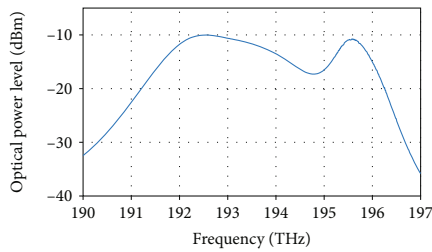
Figure 9: Measured optical spectrum of broadband ASE light source.

signal from FBGs' sensor reflected signals. Furthermore, the data transmission channel signal is carried by 20 km long SMF fiber line through FBG sensor and variable 3 dB optical attenuator (VOA) to AWG 2, where 16th data transmission channel is observed in optical network terminal (ONT).

ONT here consists of receiver part—high-speed pin photodiode with -18 dBm sensitivity (10^{-10} BER), electrical Bessel low-pass filter with 1.25 GHz 3 dB bandwidth, electrical scope, and optical power meter.

Here, multiple scenarios for one channel were tested. Data transmission speed is set to 1.5 Gbit/s. Then, signal quality—BER difference (BER correlation diagrams) with and without FBG optical sensor—is measured while the data transmission line is 20 km long. In Figure 10(b), it is possible to observe BER versus average received optical power of 1.5 Gbit/s signals after transmission over 20 km long SMF fiber. Afterwards, the same configuration is applied, yet 20 km long data transmission line is changed to back-to-back (B2B) condition (without data transmission line). Figure 10(a) shows the BER correlation diagrams for B2B transmission.

From measured results (see Figure 10), we calculated that for system with B2B and 20 km long SMF fiber, the power penalty, in case of both system collaborations, is approximately 0.5 and 0.2 dB at the forward error correction (FEC) level of 2.3×10^{-3}, if compared to the optical transmission system without embedded FBG sensor. The power penalty (system with FBG sensor) for 20 km optical signal transmission compared to B2B measurement at FEC level of BER = 2.3×10^{-3} is approximately 0.7 dB, which can be characterized as negligible.

4.2. Description of Developed Experimental Combined Network Setup.

To prove the concept of the coexistence of fiber optical transmission system with embedded FBG sensor network over one shared optical fiber, we realized the experimental fiber optical system setup as shown in Figure 8.

The key point in this system is that only one shared broadband light source (BLS) is used for data transmission and sensing channels. It is important to highlight that for simulation (Section 3) and experimental (Section 4) purposes, the same FBG optical sensor's spectral response curve has been used.

Realized WDM data transmission system is based on the spectrum slicing approach of BLS light source, namely,

broadband ASE light source. As an alternative to ASE, the light-emitting diodes (LED) or super-luminescent emitting diodes (SLED), which typically have higher output power, also can be used for the realization of spectrum-sliced multichannel transmission system. However, in our setup, we used ASE due to its higher average optical output power (+7 dBm), if compared to available SLED (+4 dBm). Please see the measured spectrum of ASE source in Figure 9.

The bitrate of the investigated data transmission system is chosen to be 1.5 Gbit/s per channel and also 1.25 Gbit/s to test lower transmission speeds. Transmission bitrate in such a type spectrum-sliced optical communication systems is limited by the excess intensity noise (EIN) evaluated in the articles [25, 26], where it is discussed that particular noise is created by the spontaneous-spontaneous beating between different wavelength components of the spectrum-sliced light. Moreover, articles [27, 28] propose that the intensity noise can be suppressed by gain saturated semiconductor optical amplifier (SOA), which amplifies incoming carrier spectral slice, as well as suppresses EIN, which rises from the spontaneous-spontaneous beating between different wavelength components of the spectrally sliced incoherent broadband ASE light source. However, it adds extra complexity to the optical transmission system.

The capacity of experimental system setup is up to 32 spectrum-sliced channels for data transmission, which are limited by the bandwidth of BLS source, optical signal power, and the number of output channels of arrayed waveguide grating (AWG) used for slicing operation. However, for the proof of principle, we set-up and investigated only one separate data channel (only one AWG slice for further data transmission was used) and one FBG sensing channel in the same model, where all system is feed by one shared BLS source.

In transmitter side, an optical signal from BLS source is split into two arms by a 20/80 power splitter, where the 20% output port was connected to the input of erbium-doped fiber amplifier (EDFA) and 80% output port to an optical band pass (OBP) filter. This splitting ratio of power splitter (PS) is chosen intentionally to provide sufficient optical signal power for FBG sensing purposes. OBP was used to provide dedicated ASE spectrum region for experimentally used fiber Bragg grating (FBG) temperature sensor and to ensure that this signal will not overlap with data channels. The 20% PS output port with 0 dBm average optical signal power is fed to first EDFA (EDFA_1) and amplified up to 18.1 dBm. This was done to compensate relatively high insertion loss (loss was 8.6 dB) of 10 GHz Mach-Zehnder modulator (MZM) and AWG. The high loss in MZM is explained in [29] where it is stated that MZM is polarization-sensitive and ASE by its nature is randomly polarized chaotic light, therefore introducing excess loss.

For slicing of BLS light source and demultiplexing of data transmission channels, we used two AWGs with 100 GHz channel spacing each. The first AWG (in the setup shown as AWG_1) is flat-top type with 54 GHz 3 dB and 132 GHz 20 dB bandwidth. Second AWG (AWG_2), which is used for demultiplexing of data channels, is Gaussian-type with 77.5 GHz 3 dB and 145 GHz 20 dB bandwidth. First AWG (AWG_1) introduced optical signal loss equal

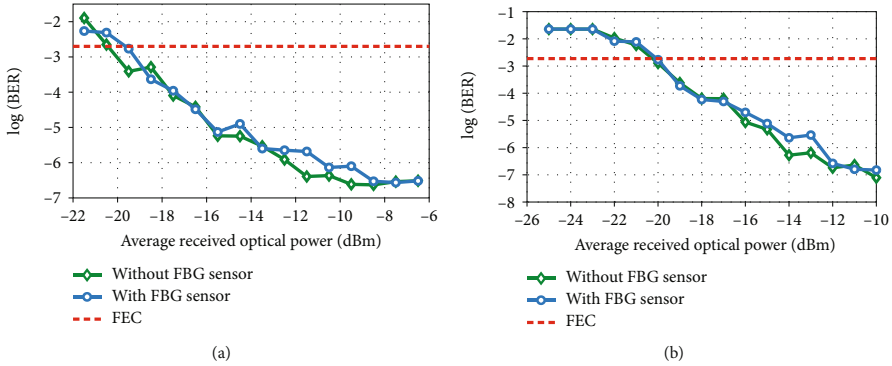(a)   (b)

FIGURE 10: BER versus average received optical power of 1.5 Gbit/s spectrum-sliced data signals for (a) B2B transmission and (b) after transmission over 20 km long SMF fiber.
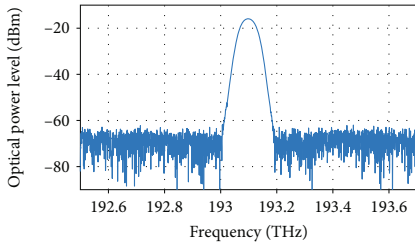

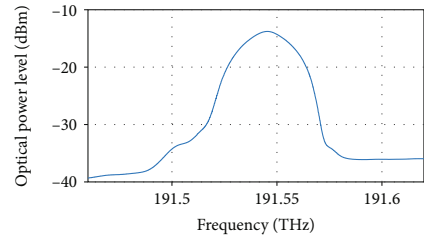FIGURE 11: Optical spectrum of modulated 1.5 Gbit/s NRZ-OOK spectral slice.

FIGURE 12: Measured spectrum of FBG temperature sensor's reflected signal.

FIGURE 13: Captured waveform of the received 1.5 Gbit/s signal after 20 km SMF transmission.

to 23.2 dB that is formed from insertion loss of AWG unit (4 dB at 1552.52 nm wavelength) and loss due to the slicing operation, where the relatively narrow carrier spectral slice is spectrally cut out from wide BLS source spectrum. For further modulation of the carrier, we used 16th output channel of AWG unit with a central frequency of 193.1 THz or 1552.52 nm, according to ITU-TG.694.1 frequency plan. The 16th output channel of AWG produces optical spectral slice with an average power of -5.1 dBm, which is further launched into 10 GHz LiNbO$_3$ intensity modulator biased at the quadrature point of DC$_{bias}$ = 6.6 V. Optical spectrum of the second AWG filtered and 1.5 Gbit/s NRZ-OOK-modulated spectral slice is shown in Figure 11.

Up to 12.5 GHz pulse pattern generator (PPG) is used to generate 2^9-1 long pseudorandom bit sequence (PRBS) with bitrates of 1.25 Gbit/s and 1.5 Gbit/s, respectively. Electrical signal adopted non-return-to-zero (NRZ) coding scheme with peak-to-peak voltage (V$_{pp}$) of 0.7 volts. The output signal of the PPG is amplified by 25 GHz broadband RF amplifier with 17 dB gain, forming electrical NRZ signal with 5 V$_{pp}$ swing to drive the MZM modulator and obtain the maximum extension ratio of a modulated optical signal evaluated in [30].

Afterwards, MZM-modulated signal and BPF's filtered ASE signal are coupled by Y-type (50/50) power coupler (PC). Afterwards, combined optical signal is amplified up
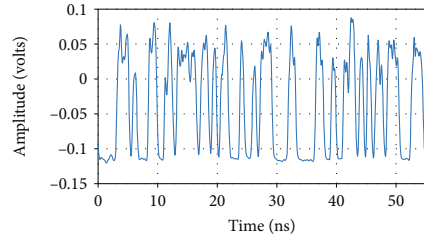
to 16 dBm by second EDFA (EDFA_2). The output of the second EDFA is connected to optical circulator (OC), which is used for separation of the data transmission signal (ports 1 to 2) and FBG reflected signal (ports 2 to 3). Here, the high precision optical spectrum analyzer (OSA) is used for interrogation of FBG reflected the optical signal. The OC's output optical signal is launched into the optical distribution network (ODN) represented by an ITU G.652 single-mode optical fiber (SMF) and FBG temperature sensor with a central wavelength of λ = 1565.124 nm (191.5455 THz) corresponding to the temperature of +19.44 degrees Celsius. The central wavelength of the FBG sensor was measured from a reflected signal spectrum shown in Figure 12. The FBG sensor,
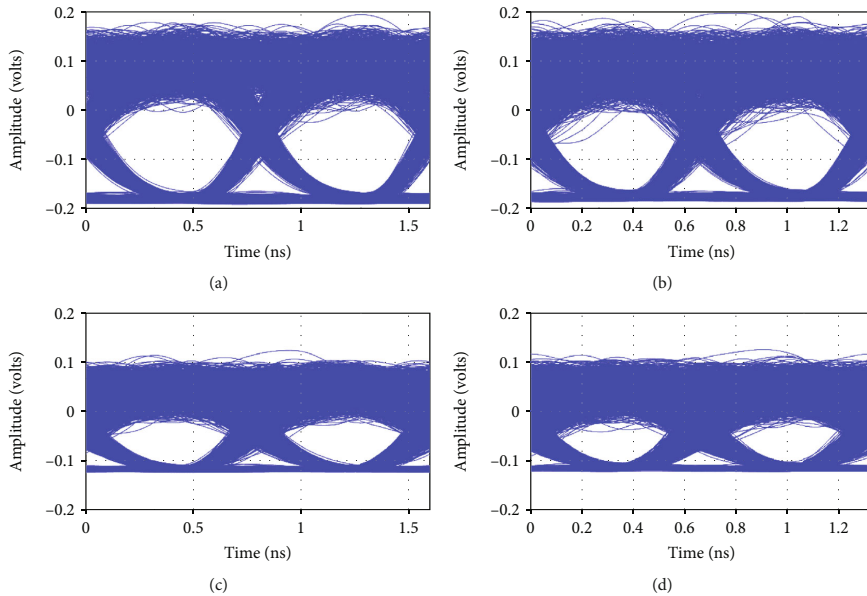
(a)

(b)

(c)

(d)

FIGURE 14: Eye diagrams of received (a) 1.25 Gbit/s B2B signal, (b) 1.5 Gbit/s B2B signal, (c) 1.25 Gbit/s signal after 20 km transmission, and (d) 1.5 Gbit/s signal after 20 km transmission over SMF fiber.

according to its data sheet, was calibrated to $\lambda = 1565.191$ nm (191.537 THz) corresponding to +26 degrees Celsius.

In receiver side, the second AWG (AWG_2) is performing demultiplexing operation of data channels. Here, the 16th output channel of AWG is connected to a linear variable optical attenuator (VOA) with 1.5 dB insertion loss at the used wavelength. The VOA is used to emulate different loss budgets in the ODN, therefore enabling measurement of BER versus received average optical power. The output of the VOA is connected to 20/80 power splitter, where the 20% output port is connected to the monitoring power meter (PM) and 80% output port to a photodiode (PD) with 10 GHz bandwidth. The PD converts the optical signal into an electrical signal, which is captured by a digital storage oscilloscope (DSO) with 33 GHz bandwidth and 80 GSa/s sampling rate. The bandwidth of DSO is limited down to 0.9 GHz (for 1.25 Gbit/s bitrate) and 1.05 GHz (for 1.5 Gbit/s) by applying 4th order Bessel-Thomson low-pass filter response for noise reduction purpose. The waveform of received 1.5 Gbit/s NRZ-OOK-modulated signal after 20 km transmission is shown in Figure 13. The amplitude fluctuations in the logical "1" level are well observed due to the noise-like nature of ASE source.

4.3. Performance Analysis of Experimental Setup. As one can see in Figures 14(a) and 14(c), after 1.25 Gbit/s B2B transmission, the eye diagram of the received optical signal is wide open and measured BER = 4.6×10^{-16} but after transmission over 20 km long ITU-TG.652 SMF fiber span, the BER increases up to BER = 1.3×10^{-9}.

As one can see in Figures 14(b) and 14(d), an increase of bitrate from 1.25 to 1.5 Gbit/s leads to the decrease of received signal quality. Numerically, the BER value in the case without transmission optical fiber (B2B) with a bitrate of 1.5 Gbit/s received optical signals' BER was 9.7×10^{-12}. However, after 20 km transmission over 20 km long SMF fiber span, it increased up to BER = 6.1×10^{-7}. It must be taken into account that during the data transmission, the transmitted signal has been affected by parallel transmitted FBG sensor seed signal (coming from BPF). We observed that the impact of this sensor's seed light on the received signal quality was negligible, as the spectrum regions of FBG sensor and data channels do not overlap and there is provided sufficient spectral spacing between them.

From obtained results (see Figure 15), we calculated that for the bitrate of 1.5 Gbit/s, the power penalty for 20 km signal transmission compared to back-to-back (B2B) measurement at forward error correction (FEC) level of BER = 2.3×10^{-3} is approximately 1.5 dB.

This power penalty is introduced mainly due to the noise-like nature of broadband ASE light source and dispersion. As one can see in Figures 15(a) and 15(b), BER performance below the 7% overhead FEC limit of 2×10^{-3} is achieved in all transmission cases with 1.25 and 1.5 Gbit/s bitrates. Consequently, an error-free transmission is possible and the coexistence of data and sensor network in one system is experimentally demonstrated.

As it is shown, due to sensor system prevalence in modern days and with successful system integration, the overall benefit can be obtained, mainly highlighting the reduction
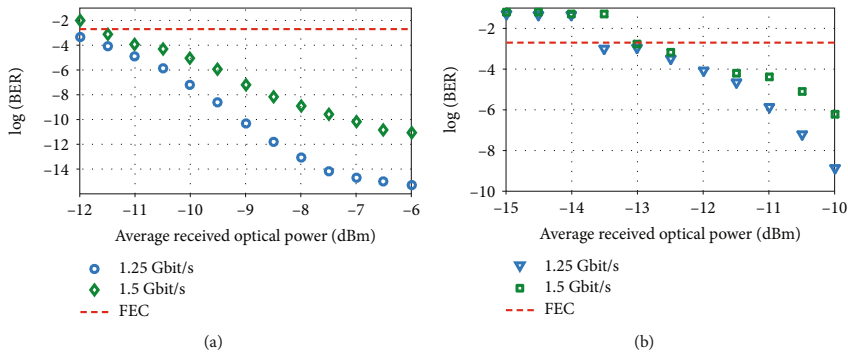
FIGURE 15: BER versus average received optical power of 1.25 Gbit/s and 1.5 Gbit/s signals for (a) B2B transmission and (b) after transmission over 20 km long SMF fiber span.

of network structure complexity and their coexistence with deployed fiber optical infrastructure. From this, it is clear that even further studies can be planned in order to test higher transmission speeds as well as integrating more system elements, e.g., optical sensors and data channels.

5. Conclusions

Market trends show that industry is in constant demand for fiber optical sensors in a wide variety of applications. Looking from a financial point of view, the annual growth in the market for such technology is increasing steadily every year. As one of the fields, where fiber optical sensors are needed and so will be in the future, is the Internet of Things (IoT) and especially structural health monitoring (SHM) applications, e.g., monitoring of the technical condition of buildings, bridges, and roads.

In this paper, we show a successful combination of 5 FBG optical sensor networks with 8-channel NRZ-OOK-modulated 10 Gbit/s fiber optical data transmission system. During this research, we offered the equation for calculation of minimal channel spacing, which allows calculating the minimal frequency band between adjacent optical FBG sensors to provide that their reflected signals will not overlap in spectrum region. Obtained results showed that, in our case, the frequency channel spacing between two adjacent deployed FBG temperature sensors should be at least around 208 GHz. Traditionally used peak detection algorithms define that the peak central frequency is the peak's point with the highest intensity. However, not always, the highest point is the peak center due to power fluctuations and irregularity of FBG's reflected signal frequency spectrum. Therefore, in this paper, we proposed and validated the algorithm for precise detection of signal peak's central frequency. This algorithm has direct application in FBG signal interrogation solutions as well as in other applications in a wide variety of fields.

We have experimentally demonstrated the coexistence of fiber optical transmission system with an FBG sensor network over one shared optical fiber and unified broadband light source for both systems. Error-free transmission has

been demonstrated over different bitrates (1.25 Gbit/s and 1.5 Gbit/s) over 20 km long ITU G.652 single-mode optical fiber (SMF), in the same time providing successful operation of FBG temperature sensor. Therefore, the successful operation of multifunctional fiber optical data transmission and optical sensing solution has been demonstrated. Authors believe that the more FBG sensor technologies will develop, the bigger will be the need for research on the coexistence of data transmission and sensing systems in a unified system operating over one shared optical fiber.

Data Availability

The data used to support the findings of this study are available from the second author upon request.

Conflicts of Interest

The authors declare that there is no conflict of interest regarding the publication of this paper.

References

[1] F. Bortolotti, K. Morais Sousa, and J. C. Cardozo da Silva, "Packaging, characterization and calibration of the Bragg grating temperature sensors," in *Proceedings of the MOMAG 2012-15 SBMO-Brazilian Microwaves and Optoelectronics Symposium and the 10 CBMag Brazilian Conference on Electromagnetism*, pp. 1–5, João Pessoa, Paraíba, Brasil, August 2012.

[2] C. E. Campanella, A. Cuccovillo, C. Campanella, A. Yurt, and V. M. N. Passaro, "Fibre Bragg grating based strain sensors: review of technology and applications," *Sensors*, vol. 18, no. 9, p. 3115, 2018.

[3] T. Becker, O. Ziemann, R. Engelbrecht, and B. Schmauss, "Optical strain measurement with step-index polymer optical

fiber based on the phase measurement of an intensity-modulated signal," *Sensors*, vol. 18, no. 7, p. 2319, 2018.

[4] G. Laffont, R. Cotillard, N. Roussel, R. Desmarchelier, and S. Rougeault, "Temperature resistant fiber Bragg gratings for on-line and structural health monitoring of the next-generation of nuclear reactors," *Sensors*, vol. 18, no. 6, p. 2018, 1791.

[5] K. Bremer, L. S. M. Alwis, F. Weigand et al., "Evaluating the performance of functionalized carbon structures with integrated optical fiber sensors under practical conditions," *Sensors*, vol. 18, no. 11, p. 3923, 2018.

[6] B. W. Jo, R. M. A. Khan, Y. S. Lee, J. H. Jo, and N. Saleem, "A fiber Bragg grating-based condition monitoring and early damage detection system for the structural safety of underground coal mines using the Internet of things," *Journal of Sensors*, vol. 2018, Article ID 9301873, 16 pages, 2018.

[7] A. Leal-Junior, J. Casas, C. Marques, M. J. Pontes, and A. Frizera, "Application of additive layer manufacturing technique on the development of high sensitive fiber Bragg grating temperature sensors," *Sensors*, vol. 18, no. 12, p. 4120, 2018.

[8] D. Qiu, T. Wang, Q. Ye et al., "A deformation prediction approach for supertall building using sensor monitoring system," *Journal of Sensors*, vol. 2019, Article ID 9283584, 12 pages, 2019.

[9] G. Allwood, G. Wild, and S. Hinckley, "Fiber Bragg grating sensors for mainstream industrial processes," *Electronics*, vol. 6, no. 4, p. 92, 2017.

[10] X. Li, C. Yang, S. Yang, and G. Li, "Fiber-optical sensors: basics and applications in multiphase reactors," *Sensors*, vol. 12, no. 9, pp. 12519–12544, 2012.

[11] G. B. Rajan, *Optical Fiber Sensors – Advanced Techniques and Applications*, CRC Press, Boca Raton, Florida, 2015, 91-93.

[12] A. Alsarhan and A. Agarwal, "Optimizing spectrum trading in cognitive mesh network using machine learning," *Journal of Electrical and Computer Engineering*, vol. 2012, Article ID 562615, 12 pages, 2012.

[13] O. Vermesan and P. Friess, "Internet of things strategic research and innovation agenda," in *Internet of Things: Converging Technologies for Smart Environments and Integrated Ecosystems*, pp. 15–26, River Publishers, Aalborg, Denmark, 2013.

[14] B. W. Jo, R. M. A. Khan, and Y.-S. Lee, "Hybrid blockchain and Internet-of-things network for underground structure health monitoring," *Sensors*, vol. 18, no. 12, p. 4268, 2018.

[15] A. Abdelgawad and K. Yelamarthi, "Internet of things (IoT) platform for structure health monitoring," *Wireless Communications and Mobile Computing*, vol. 2017, Article ID 6560797, 10 pages, 2017.

[16] W. Zeng and H. Gao, "Optic fiber sensing IOT technology and application research," *Sensors & Transducers Journal*, vol. 180, no. 10, pp. 16–21, 2014.

[17] Y. M. Gebremichael, W. Li, B. T. Meggitt et al., "A field deployable, multiplexed Bragg grating sensor system used in an extensive highway bridge monitoring evaluation tests," *IEEE Sensors Journal*, vol. 5, no. 3, pp. 510–519, 2005.

[18] "Latvian State Roads homepage – traffic speed sensors network," https://lvceli.lv/en/.

[19] D. Tosi, "Improved KLT algorithm for high-precision wavelength tracking of optical fiber Bragg grating sensors," *Journal of Sensors*, vol. 2017, Article ID 5412825, 10 pages, 2017.

[20] Y. Wang, "Application of optical fiber sensor technology in building Internet of things," *Journal of Chemical and Pharmaceutical Research*, vol. 6, no. 6, pp. 1151–1155, 2014.

[21] S. Spolitis, V. Bobrovs, and G. Ivanovs, "Investigation of high-speed AWG filtered spectrum-sliced WDM PON system," in *8th International Symposium on Communication Systems, Networks & Digital Signal Processing (CSNDSP)*, pp. 1–4, Poznan, Poland, July 2012.

[22] ITU-T Recommendation G 694.1, "Spectral grids for WDM applications: DWDM frequency grid," in *International Telecommunication Union, Telecommunication standardization sector of ITU*, pp. 1–7, Geneva, Switzerland, 2002.

[23] S. Spolitis, I. Lyashuk, and V. Bobrovs, "Design and performance evaluation of FBG-based temperature sensors network," in *2017 Progress in Electromagnetics Research Symposium - Fall (PIERS - FALL): Conference Proceedings 2017*, pp. 2673–2678, Singapore, Singapore, Nov. 2017.

[24] Z. A. El-Sahn, W. Mathlouthi, H. Fathallah, S. LaRochelle, and L. A. Rusch, "Dense SS-WDM over legacy PONs: smooth upgrade of existing FTTH networks," *Journal of Lightwave Technology*, vol. 28, no. 10, pp. 1485–1495, 2010.

[25] M. S. Leeson and S. Sun, "Spectrum slicing for low cost wavelength division multiplexing," in *2nd ICTON Mediterranean Winter: Conference Proceedings 2008*, pp. 1–4, Marrakech, Morocco, Dec 2008.

[26] A. Ghazisaeidi, F. Vacondio, and L. A. Rusch, "Filter design for SOA-assisted SS-WDM systems using parallel multicanonical Monte Carlo," *Journal of Lightwave Technology*, vol. 28, no. 1, pp. 79–90, 2010.

[27] Z. Al-Qazwini and H. Kim, "Ultranarrow spectrum-sliced incoherent light source for 10-Gb/s WDM PON," *Journal of Lightwave Technology*, vol. 30, no. 19, pp. 3157–3163, 2012.

[28] T. Yamatoya and F. Koyama, "Noise suppression of spectrum-sliced light using semiconductor optical amplifiers," *Electronics and Communications in Japan (Part II: Electronics)*, vol. 86, no. 2, pp. 28–35, 2003.

[29] C. C. K. Chan, *Optical Performance Monitoring: Advanced Techniques for Next-Generation Photonic Networks*, ELSEVIER Inc., The Chinese University of Hong Kong, 2010.

[30] Measuring extinction ratio of optical transmitters application note 1550-8, Available online: January 2019, http://literature.cdn.keysight.com/litweb/pdf/5966-4316E.pdf.

Braunfelds J., Senkans, U., Lyashuk, I., Porins, J., Spolitis, S., Bobrovs, V. Unified Multi-channel Spectrum-sliced WDM-PON Transmission System with Embedded FBG Sensors Network. No: Proceedings of Photonics & Electromagnetics Research Symposium (PIERS 2019), Itālija, Roma, 17.-20. jūnijs, 2019. Piscataway: IEEE, **2019**, pp. 1.-7.

Unified Multi-channel Spectrum-sliced WDM-PON Transmission System with Embedded FBG Sensors Network

Janis Braunfelds, Ugis Senkans, Ilya Lyashuk, Jurgis Porins,
Sandis Spolitis, and Vjaceslavs Bobrovs

Institute of Telecommunications, Riga Technical University, Riga, Latvia

Abstract— Fiber Bragg grating (FBG) sensors are passive components with high immunity to electromagnetic interference (EMI) and radio frequency interference (RFI). Optical FBG sensors are typically used for remote monitoring purposes of physical parameters (e.g., strain, temperature, acceleration, pressure, load, vibration, etc.) over large optical fiber distances — 20 km. As the number of end-user equipment (smartphones, computers and other devices) is generating a large amount of data needed to be transmitted, it is necessary to look for new efficient solutions on how to fulfill the worldwide rising requirement for transmission capacity. In the same time, it is important to maintain openness for transmission systems and networks, to combine them with sensing networks, therefore making them more resource and cost-efficient. In this paper, we successfully demonstrate the realization and coexistence of multi-channel (32 channels) spectrum-sliced wavelength-division-multiplexed passive optical network (SS-WDM PON) with FBG sensors network containing at least 5 optical sensors. The investigated system was designed in RSOFT OptSim mathematical simulation software based on the ITU-T G.694.1 DWDM frequency grid to maintain maximum compatibility of the system. The system with spectrum-sliced WDM-PON data and optical FBG sensors channels is cost and energy efficient solution in optical transmission part because it is realized by using one broadband light source (BLS), for example, light-emitting diode (LED), superluminescent light-emitting diodes (SLED) or amplified spontaneous emission (ASE) sources. SS-WDM PON system with embedded FBG sensors network showed successful data transmission over 20 km of transmission distance with bitrates 10 Gbit/s per channel and non-return-to-zero on-off-keying (NRZ-OOK) coding scheme. The key strength of the proposed system is that the unified SS-WDM PON system and embedded FBG sensor network is operating based on just one broadband light source, shared by data and sensor channels.

1. INTRODUCTION

The requirement for the faster and higher amount of data transmission and communication between people and technical systems through times has led scientists to experiment with different methods and materials to provide customer needs. From staring with laser invention back in the 1960s and first low-loss optical fibers to the massive replacement of coaxial cable systems for fiber optical ones, modern society now is capable to exchange gigabits per data within vast fiber optical networks. With developments that lead to decreasing material inserted signal loss as well as reduction of price, fiber optical sensors keep on replacing traditional electronic and mechanical sensors [1].

Fiber optical sensors have a wide range of advantages compared to its predecessors, for instance, immunity to electromagnetic interference, small size and weight, robustness, multiplexing and remote sensing capabilities among other ones. These advantages make them suitable for the different fields of applications, for example, to measure temperature, vibration, strain, pressure and other parameters typical for monitoring purposes [1, 2].

Fiber Bragg grating (FBG) technology for optical sensor applications in recent years has stabilized its place as one of the prominent technologies for satisfying both customer and manufacturer's needs. There are loads of possible engineering spheres were FBG optical sensor technology can and is implemented, for instance, civil engineering, public security, structural health monitoring applications (SHM, for instance, bridges, roofs and pylons), chemical and medical fields, transportation (railway, road, tunnel monitoring), cabinet security, oil and gas production industry, as well as in nuclear systems and other [3–5].

FBG, from a technical point of view, works somewhat similar to a narrow-band optical filter that provides reflective narrow spectrum according to Bragg wavelength or frequency and principle is described as an equation:

$$\lambda = 2 \cdot n_{eff} \cdot \Lambda \tag{1}$$

where λ is equal to spectral reflectance, n_{eff} is fiber cores' refractive index and Λ is grating period [6]. In other words, FBG is made as a structure that is resonating at one specific frequency

or wavelength. When light is traveling through the optical fiber, FBG pass part of it through and part of it is reflected back. For sensing purposes, a key element is the way how Bragg wavelength changes in a linear nature according to the changes in the environment, for example, with changes of temperature or strain. To establish optical sensor systems or provide data transmission systems, commonly, in such cases, wavelength-division-multiplexing configuration model is integrated over passive optical network (WDM-PON), which will also be used in a form of spectrum-sliced wavelength-division-multiplexing passive optical network (SS-WDM PON) [3, 7].

2. INTEGRATION OF FBG OPTICAL SENSORS NETWORK INTO DATA TRANSMISSION NETWORK FOR SHM APPLICATIONS

In modern days, FBG interrogation mechanisms provide real-time measurements of used spectrum, where sampling ratio is chosen differently for dynamic systems, where frequency range is within 1–5 kHz, or as for static systems — 1–10 Hz. One of the most eligible methods to ensure signal input for FBG in commercial industries is white-light setup [4]. In this, broadband source (BLS) — asynchronous spontaneous emission (ASE) is considered as a light source. In our research, where we combine the fiber optical sensor system with data transmission system over one optical fiber. We use ASE as a unified input light source for both of them.

ASEs broadband spectrum can be effectively used in SS-WDM PON systems to provide multiple data transmission channels within fiber optical access networks. There are several advantages while considering SS-WDM PON, for instance, its capability to position optical elements and devices in one, unified central office (CO). By doing so not only it is possible to simplify but as well reduce the costs for network architecture. Knowing that nowadays even more and more applications and devices for customers relates to available frequency/wavelength spectrum region, the WDM-PON system can be mean to solve situations where bottleneck' principle problem may apply. Spectrum slicing provides the ability to divide equal spaced wavelengths for numerous amounts of channels. In this way, for example, ASE's spectrum can be spectrally sliced by an optical filter, and after the slicing process, these slices can be modulated and used for data transmission [8].

In recent years fiber optical sensors, especially FBG ones, have stabilized its positions amongst sensor applications for various monitoring needs [9]. Structural health monitoring (SHM) has been one of them. The time may come for every different kind of material, device or infrastructure, where its original status, structure or function abilities decreases or changes. By knowing this, it is necessary to do regular inspections and maintenance to ensure public safety and avoid systems or devices malfunctions. As previously mentioned, all of the fiber optical sensor advantages over common mechanical or electrical sensors makes this technology a suitable choice for SHM purposes. Optical fiber sensors in SHM applications are typically embedded in three main ways. Firstly — by single point sensors, which are commonly used for most of the temperature sensors. Secondly, with distribution optical sensing, where measurements can be carried out at any point of the located sensors within an optical fiber. Thirdly, quasi-distributed systems where various single point sensors are located, providing sensing ability over large structures and crucial measurement points [10]. Our research was based on distributed optical sensor network, and this approach might be valuable in cases where optical network systems provide both — sensing and monitoring needs as well as data transmission over the same network.

Although there has been a previous research on data transmission channel unification with one single broadband source where this source was used as a seed light source for all of the data transmission channels [8], yet we investigate this research further to combine such a data transmission system with a fiber optical FBG sensor network on one, shared fiber and one shared ASE light source. It is necessary due to the growth of overall coverage for fiber optical networks worldwide. There, for instance, Latvia holds a leading position amongst European fiber to the home (FTTH) rankings, with total fiber coverage of 45.2%. Although, until now, SHM of railways, bridges, dams, and roads, in Latvia, are performed through visual inspections, yet due to high availability of fiber optical infrastructure, different companies, for example, nationa road administration — State Joint Stock Company "Latvian State Road", are interested in potentially using existing fiber optical systems infrastructure and FBG optical sensors for remote sensing purposes of objects that are under their ownership [11]. For instance, in situations, where FBG optical sensors are positioned as a distributed network throughout whole dam or road construction, sensors can provide infrastructure' manager with information about different measurements (strain, pressure, temperature, and others) and conditions of the specific infrastructure throughout its lifetime.

3. SIMULATION SETUP OF COMBINED OPTICAL SENSOR NETWORK AND 32-CHANNEL SSWDM PON SYSTEM

The simulation setup of the combined system was developed within RSOFT OptSim software. Here, the main aim for this research was to successfully create an operating simulation model that consists of 32 non-return-to-zero on-off-keying (NRZ-OOK) modulated 10 Gbit/s spectrum-sliced WDM-PON data transmission channels and 5 fiber optical FBG temperature sensors while using only one broadband light source (BLS). As for the spectral band of BLS source we used a spectral range from 192.15 THz to 195 THz, which is shared by the combined system — data transmission and sensor channels. For these purposes we established our WDM frequency grid setup according to ITU-T G.694.1 to maintain maximum compatibility of the system. Frequency band from 192.4 till 193.95 THz is used for data channels and spacing between these data channels is fixed — 50 GHz. However, for the sensor channels the frequency band from 194 to 195 THz is used. As for the overall information transmission medium according to ITUT G.652 we were using standard single mode optical fiber (SMF) [12, 13].

For the data transmission part, we set our goal to establish the quality of our data signals that would provide pre-forward error correction (pre-FEC) bit error ratio (BER)of no more than 2×10^{-3}. Particular value was chosen considering the requirements enough for ensuring errorfree output signal detection. Such a model applies in the case of FEC encoding scheme application with 7% overhead. Figure 1 displays our created systems' model where SS-WDM PON system is combined together with an optical sensor network on one shared BLS light source for all of the optical network terminals (ONT), which in this case depicts end-users of our proposed system network.

As it is shown in Figure 1, the BLS output signal is split with 1 : 2 optical power splitter equally assuring 50% of its optical power for both systems. Such a 50 : 50 ratio was chosen, considering simulative results, where stable system operation can be maintained. Here, by a stable operation, we mean three following things. Firstly, we mean the situation where both — optical sensor channels can be interrogated and data transmission channels — received for gained results. Secondly, there is no visual spectral interference between both systems. Last but not least, our main set goal for this research is proven and the results do not affect the goal negatively.
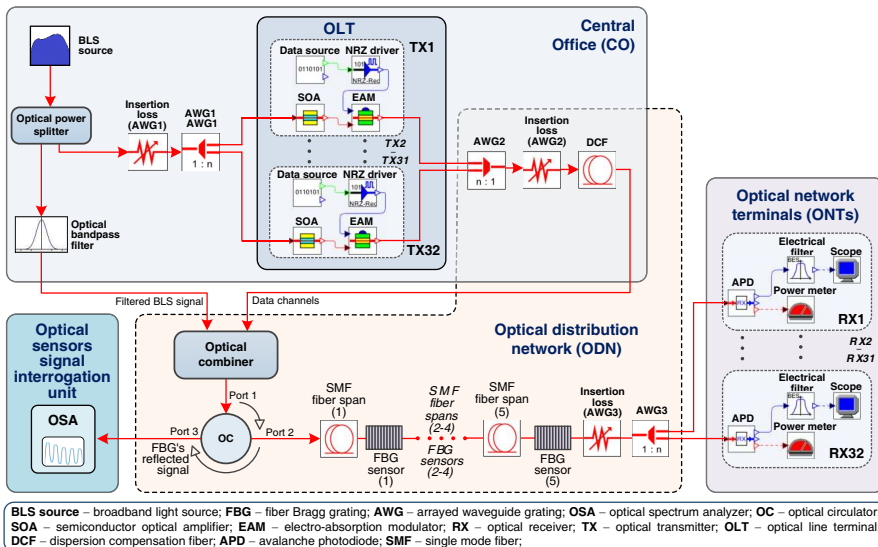

Figure 1: The simulation model of combined 10 Gbit/s 32-channel SS-WDM PON transmission system and 5 FBG optical sensors system with one shared optical fiber and optical light source.

As for the data transmission system optical signals' input part of 50% optical power that was transmitted from optical splitter is spectrally sliced into 32 channels by arrayed waveguide grating

(AWG) operating as an array of filters. Channel spacing, according to ITU-T G.694.1, is chosen as 50 GHz [12]. 3-dB bandwidth of each AWG's channel is chosen as 45 GHz, which is the threshold in between data channel crosstalk and received optical power in order to maintain BER seemingly low as it is possible in particular conditions. This specific model, where AWG device is being used, can lead to acquiring of 32 data transmission channels with 50 GHz intervals between each and every one of them. In addition, insertion loss blocks are being implemented to resemble insertion loss generated by the AWG unit. Once the spectrum-slicing procedure has been applied by the first AWG unit, slices of an optical signal are then fed into the data transmitters (TX) that are positioned within the optical line terminal (OLT), what, on the other hand, is inside the central office (CO). From Figure 1, it is possible to observe the structure of every TX in our OLT, where they consist of gain-saturated semiconductor optical amplifier (SOA), data source, NRZ driver and polarization insensitive electro-absorption modulator (EAM). Then 10.7 Gbit/s generated data stream represented by 2^9-1 pseudo-random bit sequence (PRBS) pattern which consists of 7% FEC overhead plus 10 Gbit/s payload is sent from our NRZ driver towards RF input of EAM modulator [14]. We used EAM due to its immunity to signal polarization (which is the opposite to MZM). Adding to that, SOA was chosen to suppress intensity fluctuation noise, which was generated because of the ASE source.

Accordingly every EAM modulates SOA's beforehand amplified and noise-suppressed spectral slices and forms optical pulses representing data. These optical pulses in all 32 channels (starting from TX1 to TX32) are being coupled by the second AWG multiplexer device. Afterward, right before channels are being launched into SMF, they are pre-compensated by the dispersion compensating fiber (DCF) to decrease the negative effect of chromatic dispersion. DCF dispersion coefficient is $D = -118.5$ ps/nm/km and attenuation coefficient is $\alpha = 0.55$ dB/km at 1550 nm reference wavelength. During our research, we were using SMF fiber to relate to ITU-T G.652.D recommendation to preserve compliance and full backward compatibility with standard single-mode optical fibers. For SMF we chose often used parameters based for 1550 nm wavelength region — dispersion coefficient $D = 16$ ps/nm/km and attenuation coefficient $\alpha = 0.18$ dB. Next, the dispersion pre-compensated data signals are transmitted over SMF to the optical coupler and combined together with another half (other 50% optical power) of BLS input optical signal Here the optical band-pass filter with 1 THz 3-dB bandwidth is used to avoid overlapping of modulated data channels and the BLS source spectrum intended for operation of FBG sensors. Then, as it is shown in the lower part of Figure 1 the combined signal is passing through 5 optical sensors, which are connected by SMF optical fiber spans and fed into optical receivers marked as optical network terminals (ONTs).

For an optical sensor network, initially, the signal of the BLS source, as mentioned before, is divided into two equal parts. Here, another half of 50% optical power, which was transmitted through optical power splitter is further carried on through optical bandpass filter into other input of optical signal coupler as shown in Figure 1. In our simulation setup, we use an optical circulator for the optical sensor network to separate optical signal transmission directions. In other words, to separate combined transmitted signal from FBGs' reflected signals. In Figure 1 is shown 5 FBG optical temperature sensors that are located between 5 SMF fiber spans, with a distance of 4 km between each of them. Accordingly, the total length of all spans within the optical sensor network part is 20 km. We based the length of our spans according to our previous research [9] where we mentioned that such distance values are typically used in Latvia between fiber optical manholes or cabinets — places where optical closures are positioned. Adding to that, by knowing that every optical sensor is positioned in different physical point apart from the optical signals interrogation device, it allows for observing wider perspectives and operation conditions of our created combined system model.

Once the optical signals have passed through OLT and optical sensor network, they are then sent to the receiver section part — optical network terminal (ONT) starting from RX1 to RX32. For this purpose, we refer the transmission section as an optical distribution network (ODN). Here the ODN includes AWG multiplexers and demultiplexers, as well — optical attenuators for simulation purposes to maintain insertion loss that would be acquired from optical devices within systems' architecture and, as previously mentioned, 2.7 km long DCF and 20 km long SMF fiber line. Last but not least, optical signal is passing true fiber optical line and containing all of the 32 data transmission channels that are divided to relevant ONTs by AWG demultiplexer. Each and every ONT, starting from RX1 to RX32, includes optical receiver with InGaAs avalanche photodiode (APD) with sensitivity of -20 dBm at reference BER of 10^{-12}, electrical Bessel low pass filter with

6 GHz 3-dB bandwidth, electrical scope and optical power meter in order to evaluate the overall quality of received signals. In this way, it is possible to observe bit pattern, eye diagrams and measure BER as well as to make sure that no interference has been made between both systems — optical sensors network and data transmission system.

4. RESULTS AND DISCUSSION

During our research process within the simulation environment, we achieved our set goal for providing SS-WDM PON system model that has unified 32 data transmission channel system and 5 FBG optical sensor network over one shared optical transmission line and single broadband light source. The FBGs' reflected signal spectrum from circulator's 3rd port is analyzed with optical spectrum analyzer (OSA) in optical sensors signal interrogation unit. On the left side of the reflected signal spectrum are shown suppressed and attenuated 32 spectrum-sliced WDM-PON transmission system channels, as well as, on the right side, 5 reflected FBG temperature sensor channels (peaks) that are further used for interrogation.

As it is shown in the captured spectrum (Figure 2), the temperature of each sensor is +26°C, which is also the calibrated temperature. The experimentally measured temperature variation of each FBG sensor per one Celsius degree is 1.24498 GHz. On the right side of the measured spectrum it can be seen, that peak frequencies of sensor network signals are 194.1, 194.3, 194.5, 194.7, and 194.9 THz, providing stable sensor's network operation in a temperature range from −20 to +60°C, typical for SHM applications.

To evaluate the collaboration of two systems, it is necessary to analyze sensors' network influence on SSWDM PON data channels. To analyze the influence, a simulation model is developed, and the results are shown in Figures 3 and 4. In Figure 3, BER of the combined system with 32-channel SS-WDM PON and 5 FBG sensor network is shown. As one can see in Figure 3, average BER of the combined system is equal to 9.6×10^{-8}. The lowest performance of the combined system was provided by the 3rd channel, where BER was 4×10^{-7}.
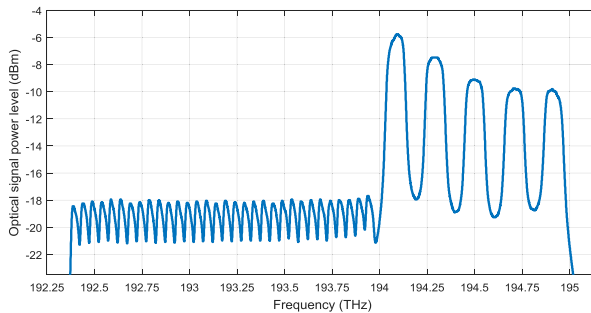

Figure 2: Reflected signal spectrum of 5 FBG temperature sensors network captured by OSA, located in optical sensor signals interrogator.
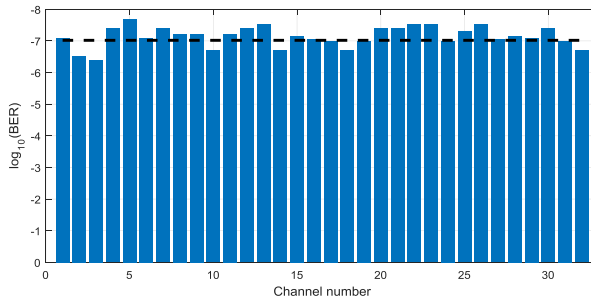

Figure 3: Measured BER value per channel of the SS-WDM PON data transmission channels combined with sensors network (dotted line represents the average value of measured BER $−9.6 \times 10^{-8}$).
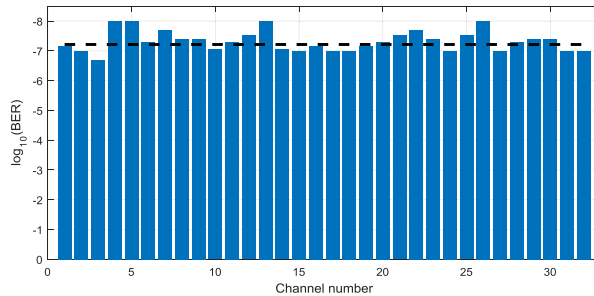
Figure 4: Measured BER value per channel of SS-WDM PON data transmission system without FBG sensors network (dotted line represents the average value of measured BER -6.1×10^{-8}).
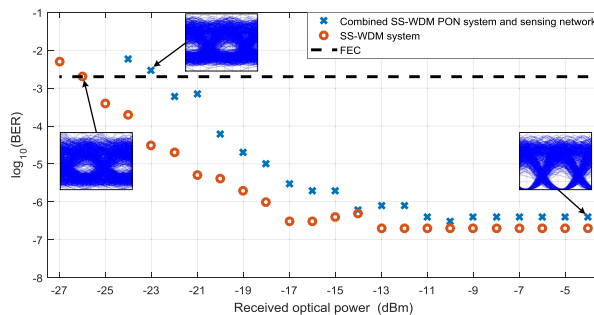

Figure 5: BER versus received optical power for 32-channel 10 Gbit/s SS-WDM PON system and combined system with embedded FBG sensing network.

In Figure 4, the BER of every SS-WDM PON data transmission channel can be seen. Please pay attention that this is the data transmission system performance without embedded FBG sensors network.

As one can see in Figure 4, the average BER of the received optical signal is 6.1×10^{-8}. As one can see in Figures 3 and 4, embedding of the sensor network leads to a slight decrease in received signal quality (estimated by the measured BER) of SS-WDM PON system.

To compare the performance of SS-WDM PON system versus SS-WDM PON system with embedded 5 FBG sensors network, we measured the BER curves of both systems, as shown in Figure 5. From obtained results (see Figure 5), we calculated that the power penalty, in case of both system collaboration, is approximately 3.25 dB at the pre-FEC BER level of 2.3×10^{-3}, if compared to the transmission system without embedded FBG sensors network.

5. CONCLUSIONS

In this research we successfully realized simulation model of combined 10 Gbit/s 32-channel SS-WDM PON transmission system and 5 FBG optical sensors system with one shared optical fiber and broadband light source. Afterwards it was possible to evaluate optical sensors' network impact to the data transmission system by observing the changes of output signal quality. It was observed as a eye diagrams and their BER values. In case of single simulation model (only data transmission system), the average value for all of the 32 data transmission channels of measured BER was 6.1×10^{-8}. On the other hand, while observing collaborated system model (data transmission system together with fiber optical sensor network) the average acquired BER was 9.6×10^{-8}. From these results we concluded that it possible to unify both systems with only slight influence on the received data transmission signal quality. We calculated that the power penalty, in case of both system collaboration, is approximately 3.25 dB at the pre-FEC BER level of 2.3×10^{-3}, if compared to the transmission system without embedded FBG sensors network.

ACKNOWLEDGMENT

REFERENCES

1. Fidanboylu, K. and H. S. Efendioglu, "Fiber optic sensors and their applications," *5th International Advanced Technologies Symposium (IATS'09)*, 1–6, 2009.
2. Senkans, U., J. Braunfelds, S. Spolitis, and V. Bobrovs, "Research of FBG optical sensors network and precise peak detection," *Wireless and Optical Communications (RTUWO) 2018 Advances in Wireless and Optical Communications (RTUWO)*, 139–143, Riga, 2018.
3. Spolitis, S., I. Lyashuk, and V. Bobrovs, "Design and performance evaluation of FBG-based temperature sensors networ," *2017 Progress in Electromagnetics Research Symposium — Fall (PIERS — FALL)*, 2673–2678, Singapore, Nov. 19-22, 2017.
4. Tosi, D., "Review and analysis of peak tracking techniques for fiber bragg grating sensors," *Sensors*, Vol. 17, No. 2368, 1–30, 2017.
5. Taylor & Francis Group, *Optical Fiber Sensors — Advances Techniques and Applications*, 545, CRC Press, 2015.
6. He, W., L. Zhu, W. Zhang, F. Liu, and M. Dong, "Point-by-point femtosecond-laser inscription of 2-µm-wavelength-band FBG through fiber coating," *IEEE Photonics Journal*, Vol. 11, No. 1, 1–8, Art No. 7100108, Feb. 2019.
7. Tosi, D., "Review of chirped fiber bragg grating (CFBG) fiber-optic sensors and their applications," *Sensors*, Vol. 18, No. 7, 2147, 1–32, 2018.
8. Spolitis, S., V. Bobrovs, and G. Ivanovs, "Investigation of high-speed AWG filtered spectrum-sliced WDM PON system," *8th International Symposium on Communication Systems, Networks & Digital Signal Processing (CSNDSP)*, 1–4, Poznan, 2012.
9. Senkans, U., S. Spolitis, and V. Bobrovs, "Evaluation and research of FBG optical temperature sensors network," *Advances in Wireless and Optical Communications (RTUWO)*, 79–89, Riga, 2017.
10. García, I., J. Zubia, G. Durana, G. Aldabaldetreku, M. A. Illarramendi, and J. Villatoro, "Optical fiber sensors for aircraft structural health monitoring," *Sensors*, Vol. 15, 15494–15519, 2015.
11. Latvian State Roads homepage — traffic speed sensors network, Available online: https://lvceli.lv/en/.
12. ITU-T Recommendation G.694.1, "Spectral grids for WDM applications: DWDM frequency grid, International Telecommunication Union, Telecommunication standardization sector of ITU," 1–7, 2012.
13. ITU-T Recommendation G.652, "Characteristics of a single-mode optical fibre and cable, International Telecommunication Union, Telecommunication standardization sector of ITU," 1–17, 2016.
14. Spolitis, S., V. Bobrovs, R. Parts, and G. Ivanovs, "Extended reach 32-channel dense spectrum-sliced optical access system," *2016 Progress in Electromagnetic Research Symposium (PIERS)*, 3764–3767, Shanghai, China, Aug. 8–11, 2016.

Braunfelds J., Zvirbule K., Senkans U., Murnieks R., Lyashuk I., Porins J., Spolitis S., Bobrovs V. Application of FWM-based OFC for DWDM Optical Communication System with Embedded FBG Sensor Network. The Latvian Journal of Physics and Technical Sciences, **2021**, pp.1-9. (apstiprināta publicēšanai).

APPLICATION OF FWM-BASED OFC FOR DWDM OPTICAL COMMUNICATION SYSTEM WITH EMBEDDED FBG SENSOR NETWORK

J. Braunfelds[1,2*], K. Zvirbule[1], U. Senkans[1], R. Murnieks[1,2], I. Lyashuk[1], J. Porins[1], S. Spolitis[1,2] and V. Bobrovs[1]

[1]Institute of Telecommunications, Riga Technical University, 12 Azenes Str., LV-1048, Riga, Latvia
[2]Communication Technologies Research Center, Riga Technical University, 12 Azenes Str., LV-1048, Riga, Latvia
*e-mail: janis.braunfelds@rtu.lv

Four-wave mixing optical frequency comb fiber-based setups (FWM-OFCs) have the potential to improve the combined dense wavelength division multiplexed passive optical network (DWDM-PON) and fiber Bragg grating (FBG) temperature sensors network providing easier application, broader technological opportunities for network development, and energy efficiency by substituting a power-demanding laser array. Application where OFCs are generated for the DWDM-PON and FBG optical sensors combined network and investigates its compatibility with such a system. The mathematical simulation model has been developed and the performance of FWM-OFC based 8-channel 50 GHz spaced non-return-to-zero on-off keying (NRZ-OOK) modulated DWDM-PON transmission system, operating at 50 km single-mode fiber (SMF) with a bit rate of at least 10 Gbps embedded with 7 FBG optical temperature sensors has been studied. As it is shown, FWM application results in OFC source that has fluctuations of the individual comb tones of less than 3 dB in power, and with an extinction ratio of about 33 dB for operation range of 192.9 – 193.25 THz, acting as a unified light source for all the data transmission channels. Embedded FBG optical sensors network causes negligible 0.3 dB power penalty.

Keywords: four-wave mixing (FWM), optical frequency combs (OFC), fiber Bragg grating (FBG) optical sensors, highly nonlinear optical fiber (HNLF), dense wavelength division multiplexed passive optical network (DWDM-PON), non-return-to-zero on-off keying (NRZ-OOK).

1. INTRODUCTION

Nowadays, multichannel fiber optical data transmission systems have become the standard of the Internet, e-commerce, multimedia, and data operation. Systems of this type encounter channel crosstalk and their performance degrades by the effect of four-wave mixing (FWM), where non-linear interactions between channels are observed [1-4]. FWM is an effect when two or more different signals with different frequencies propagate next to each other, and due to this reason, new carriers are generated. However, solutions for the useful application of the FWM effect are being studied, for instance, the generation of optical frequency combs [1, 5, 6].

OFC generators based on FWM have the potential to improve the energy efficiency of wavelength division multiplexed (WDM) fiber optical transmission systems. One of the main reasons for this is that one OFC light source can provide multiple data transmission carriers substituting a power-demanding laser array that also requires synchronization among the lasers. OFC generators can also be used in spectroscopy [7-9], radio-frequency photonics [7, 10], quantum optics [7, 11], optical clocks, and microwave systems [12, 13]. Spatial microresonators (crystalline, microsphere, microrod, micro-bubble), microresonators on a chip (toroidal, disk, ring, etc.) [14-16], and fiber-based setups [17-19] might be used to generate OFC. Even though spatial microresonators and integrated

microresonators have been widely studied as WDM-PON light source, fiber-based setups (e.g. our demonstrated FWM-based OFC) have the advantage to provide spectrally flat comb and narrow channel spacings or so-called free spectral range (FSR) [20] (based on 10-100 GHz corresponding to ITU-T G.694.1 dense WDM passive optical network (DWDM-PON) frequency grid [21]), which is more difficult to obtain, for example, with microspherical resonators.

Fiber Bragg grating (FBG) sensors are one of the most promising fiber optical sensors for different environmental measurements. FBG sensors have multiple advantages that can be applied in different areas. Some of these advantages are small size and weight [22], corrosion resistance [23], immunity to electromagnetic interference (EMI) [23, 24], the pos-sibility to withstand direct embedment into the composite material, together with rein-forced fibers, as well as the potential to multiplex several optical sensors within the same optical fiber [23, 25, 26]. FBGs are applied for vast solutions, for instance, in offshore plat-forms - to monitor ship collisions and ocean wave loads, while providing lasting perfor-mance without significant reduction, as do conventional strain gauges [27, 28]. Also, for structural health monitoring (SHM) applications in civil (e.g., roads [29], bridges [30], dams, tunnels and roads [31]), aerospace, energy applications [25, 27, 32, 33], oil and gas industry [34], biomedicine [35, 36], and so on. Fiber optic sensors can be used to measure, for example, temperature [37-39], strain [37, 40, 41], pressure [41,42], vibration velocity [43], and displacement [43]. Single-mode fiber (SMF) and multimode fiber (MMF) can be used for fiber optic sensor construction. Yet single-mode fibers have a smaller core (ap-proximately 10 μm in diameter) and they are more strain sensitive than multimode opti-cal fibers [25].

FBG working principle can be described with a mathematical equation:

$$\lambda_B = 2 \times n_{eff} \times \Lambda \qquad (1)$$

where λ_B is Bragg wavelength, neff is effective refractive index of the optical fiber in the region of the Bragg grating and Λ is grating period [28].

FBG optical sensors are typically used when strain, pressure and temperature sensing is necessary, for instance, in hostile environments with temperatures exceeding 250°C (thermal well applications). Bragg grating-based sensing systems are typically used in WDM transmission systems, when wavelength multiplexing of various sensors on single optical line might be required [34, 36, 37]. All of the information mentioned above shows the topicality of the FBG optical sensors and their integration with WDM data transmission systems.

Considering that fiber optical data transmission system like DWDM-PON interconnection with optical sensor system is topical [26, 44, 45] and the search for new improvements and solutions continues, authors propose the application of FWM-OFC [1, 5, 6] as a light source to provide power efficiency to such a system. To the best of authors knowledge, studies on FWM-OFC implementation as a light source in collaboration with FBG optical sensor network and DWDM-PON system have not been performed. This article shows that such realization can provide more straightforward application, broader technological opportunities for network development, and greater energy efficiency with a reduced light source amount required.

The remainder of the manuscript is structured as follows: Section II describes the construction and analysis of the simulation model where FWC-OFC is developed and integrated into the DWDM-PON system in collaboration with the FBG optical sensor network. Section III discusses the simulation results of the OFC application in fiber optical communication systems, showing received signal waveforms, reflected signal of the FBG optical sensors, eye diagrams and BER versus received optical power chart. More specifically, this section shows negligible power penalty at the BER threshold level of 1×10^{-12} (only 0.3 dB) between B2B and 50 km long transmission line on the received optical power and BER comparison. Finally, section IV gives a brief summary of the simulative

results and concludes the article, stating that the BER of the worst-performing channel in the 8-channel DWDM-PON system is 9.4×10^{-37}.

2. CONSTRUCTION AND ANALYSIS OF THE SIMULATION MODEL

The simulation model aims to evaluate the developed comb source and the performance of the FWM-OFC based DWDM transmission system with an integrated FBG sensor network. The proposed system includes the following main blocks – optical line terminal (OLT), optical distribution network (ODN), optical network units (ONUs).

2.1. FWM-OFC generation for the requirements of the DWDM-PON data transmission channels

We have created the simulation setup of the combined system using Synopsys OptSim optical system design tool. Application framework allows to generate coherent optical communication systems (Polarization multiplexed-quadrature phase shift keying, Polarization multiplexed-binary phase-shift keying, etc.), use advanced modulation for-mats (Differential Quadrature Phase-Shift Keying, Doubinary, etc.), ensure optical amplification (Erbium Doped Fiber Amplifier, Raman, Semiconductor Optical Amplifier, etc.), different passive optical network configurations and so on. Time and frequency domain split-step configurations with an extensive library of predefined as well as authors defined components are necessary to develop and generate complex optical systems as described in the following paragraphs [46]. From the simulation perspective, the time domain split-step (TDSS) algorithm was used to simulate the signal propagation in optical elements, especially fiber. The principle of this algorithm has been already well explained in our previous research [50].

Two continuous-wave (CW) pump laser sources with +20 dBm output power and 50 GHz channel spacing according to the ITU-T G.694.1 recommendation [21], optical power coupler (PC), and 2 km long highly nonlinear optical fiber (HNLF) are used to develop an OFC source (see Fig. 1).
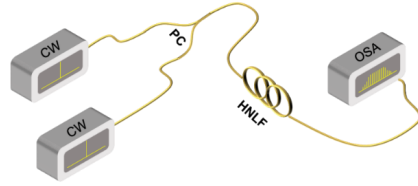

Fig. 1. FWM-OFC generation setup.

We have set HNLF fiber parameters like the attenuation coefficient, dispersion coefficient, effective area, nonlinear index and others based on the datasheet from real commercial OFS HNLF Standard fiber (please see Table 1).

Table 1. The main parameters of the chosen fiber types at 1550 nm reference wavelength.

Parameters	Fiber types	
	OFS Standard HNLF	**Corning SMF-28 (ITU-T G.652D)**
Attenuation (dB/km)	0.8	0.18
Dispersion (ps/(nm·km))	-0.027	16
Dispersion slope (ps/(nm²·km))	0.019	0.092
PMD (ps/√km)	0.20	0.04
Effective area (μm²)	11.6	85
Nonlinear index (W×km)⁻¹	11.5	1.27

The first and second pump laser source (depicted in Figure 1 as CW_1 and CW_2) are anchored to central frequencies of 193.1 and 193.15 THz, respectively. Pump laser parameters that can affect the generation of OFC carriers are signal phase, which was set to random, and realistic noise parameters as relaxation oscillation peak frequency and peak overshoot. The number of comb carriers and their peak power are varying depending on the output power of CW pump lasers and the length of HNLF fiber. For instance, as it was observed, if the output power of pump CW lasers is too low (e.g., 0 dBm) and HNLF fiber length is too short (e.g., 0.5 km), the number of newly generated optical carriers is limited. However, if the output power of the CW is too high (e.g., 25 dBm) and

HNLF fiber is too long (e.g., 2.5 km), the carriers are not formed evenly. HNLF fiber length has an important role in OFC generation based on the FWM effect. The nonlinear length of the fiber is smaller than the dispersion length by orders of magnitude, and this fact is important from the FWM point of view – for smaller fiber lengths nonlinear effects dominate over the dispersion effects, which is an advantage for FWM. It is an advantage in terms of dispersion –more dispersion means less efficiency of the FWM effect. Additionally, high CW pump power leads to unwanted broadband noise via Raman scattering and parametric vacuum noise amplification [17-19]. Therefore, it is vital to determine and evaluate the optimal parameters for the FWM-based OFC comb light source to ensure the stable operation of the system. Optimal parameters (pump laser output power and HNLF length) are those, which provide the smallest power variation range among peaks of OFC carriers. It is essential to have the lowest possible OFC fluctuation value for a couple of

reasons. The fluctuations of the OFC source directly affect the performance of separate data channels, for instance, if the peak power of a particular channel is lower, then the resulting performance indicator as BER can have higher values compared to neighboring channels and ultimately be higher than the chosen BER threshold. On the other hand, looking at the WDM-PON network as a whole, then channels with higher power may induce more crosstalk into neighboring channels. However, for the data transmission, we have chosen eight optical carriers in that frequency range, where the average optical power of the peaks is the highest, also having the smallest fluctuations of optical peak power. It is important to have a peak power of OFC carriers as high as possible to achieve better performance of individual channels and the network as whole. As shown in Figure 2, optical power fluctuations between all OFC peaks are observed, and extinction ratios are depending on the CWs lasers' output power as well as the length of the HNLF.
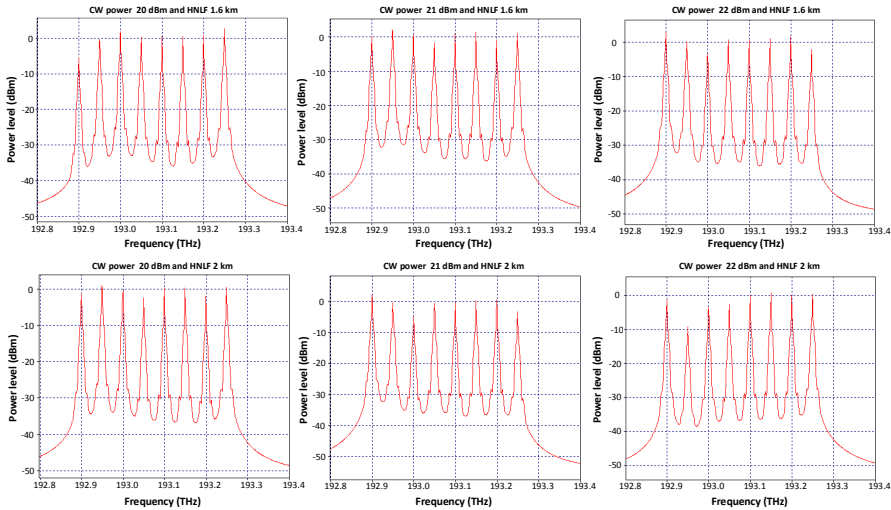

Fig. 2. Measured optical spectrum on the AWG MUX output of FWM-based OFC for different CW pump powers and HNLF fiber lengths.

For HNLF fiber with a length of 1.6 km, the fluctuations of optical frequency comb peaks are in the range of -4.5 to 3 dBm, -2 to 2 dBm, and -4 to 3 dBm, where CW power is 20, 21, and 22 dBm, respectively.

For fiber length of 2 km, the fluctuations of optical frequency comb peaks are in the range of -1.5 to 2 dBm, -5 to 2 dBm, and -8.5 to 1 dBm for CW power of 20, 21, and 22 dBm, respectively. All OFCs have the same extinction ratio of 33 dB, the

same number of optical carriers, and a free spectral range (FSR) of 50 GHz.

By comparing the scale of fluctuations and average comb peak power, the optimal pumping lasers (CW1 and CW2) output power was chosen as +20 dBm and HNLF fiber length - 2 km, to generate the OFC with the lowest fluctuations of -1.5 dBm and highest average peak power of 2 dBm.

2.2. Development of DWDM-PON system with integrated FBG optical sensors network

Output of the OFC source is connected to the input of a 50 GHz spaced arrayed waveguide grating multiplexer (depicted in Figure 3 as AWG MUX). AWG MUX and AWG demultiplexer (DEMUX) with the same optical parameters are used in this setup to separate and combine 8 channels in the frequency band from 192.9 THz to 193.25 THz. The 3-dB bandwidth of each AWG channel is 50 GHz.
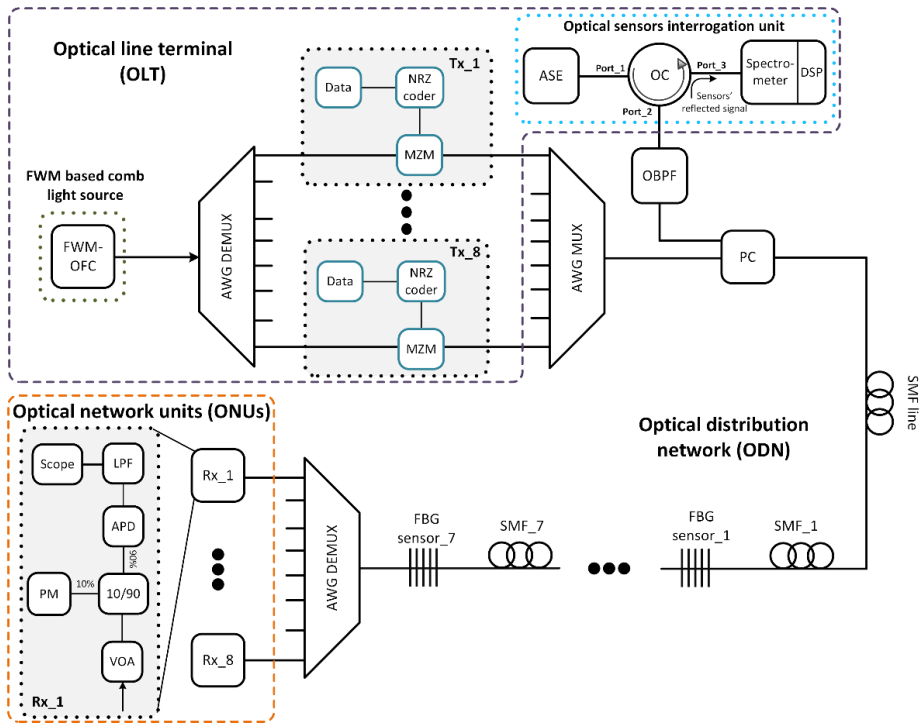
FWM-OFC – Four-wave mixing optical frequency comb; AWG MUX/DEMUX – Arrayed waveguide grating multiplexer/demultiplexer; Tx – Transmitter; NRZ – Non-return-to-zero; MZM – Mach-Zehnder Modulator; OC – Optical circulator; OBPF – Optical band-pass filter; PC – Optical power coupler; ASE – Amplified spontaneous emission source; DSP – Digital signal processor; SMF – Single mode fiber; FBG – Fiber Bragg grating; VOA – Variable optical attenuator; 10/90 - Optical power splitter with ratio 10/90%; APD – Avalanche photodiode; LPF– Low-pass filter; PM – Power meter; Rx – Receiver.

Fig. 3. The simulation model of 8-channel DWDM-PON system based on FWM OFC source, integrated 7 FBG temperature sensors' network and FWM multi-wavelength light source.

OLT also includes transmitter blocks (depicted in Figure 2 as Tx_1 to Tx_8) where each has data generator, non-return-to-zero (NRZ) coder, and Mach-Zehnder modulator (MZM) with 20 dB extinction ratio and insertion loss of 4 dB. An optical power coupler (PC) is used to combine all 8 data transmission channels and the signal for the FBG sensor network. The optical sensors' interrogation unit block transmission part consists of broadband amplified spontaneous emission (ASE) light source which has an optical output power of +23 dBm and 20-dB bandwidth is 48.1 nm (5.607 THz). From our test results, this configuration for the ASE source enables acceptable received optical power level from the reflected signal of the FBG sensors network where quasi-distributed optical sensor scheme is applied in 50 km optical fiber line.

This is discussed more detailed in next paragraphs of this article. 3-port optical circulator (OC) is used to separate the optical transmission directions – FBGs' reflected signal from the transmitted data and ASE signal. The optical signal of the ASE broadband light source is transmitted from the OC input port (Port_1) to the common port (Port_2) and then a tunable optical band-pass filter (OBPF) with 800 GHz 3-dB bandwidth (in frequency band 193.50 - 194.30 THz). OBPF is used to filter the necessary spectral band for the operation of the FBG sensor network, where such parameters for the OBPF were chosen according to the spectral bandwidth of the ASE light source and FBGs position within the available optical spectrum.

The reflected optical signal from all FBG sensors is sent back through the circulator's common port (Port_2) and forwarded to the output port (Port_3). FBG sensors' reflected signal is received at the optical sensors interrogation unit, where optical spectrometer block and digital signal processor (DSP) are used to detect the central frequency of the reflected signal and by knowing the temperature coefficient (frequency or wavelength shift for 1°C) calculate the temperature variations.

PC coupled signal is transmitted to the 15 km SMF having an attenuation coefficient of 0.18 dB/km and dispersion coefficient of 16 ps/nm/km, etc set based on the datasheet parameters from real commercial Corning SMF-28 fiber corresponding to ITU-T G.652D requirements. The next main part of the transmission scheme is an optical distribution network (ODN) with 7 optical FBG temperature sensors.

These FBG sensors contain the experimentally measured optical and response parameters. Amplitude-frequency response (see Figures 4 and 5.) and technical parameters (central frequency, full-width half-maximum (FWHM)), etc.) of commercial FBG sensors reflected and transmitted signals were measured in the laboratory and have been implemented within simulation setup. SLED broadband light source, 3-port optical circulator, spectrometer, and FBG sensor components were used for laboratory measurements of these parameters. As for reflected spectrum measurements - the components are connected the same as shown in fig.3 (in optical sensor interrogator unit part), but for the transmitted signal spectrum measurements - the spectrometer is connected with the FBG sensors' output. Central frequencies and FWHM values of FBG sensor were determined based on the measured spectrum of the FBG reflected signals.
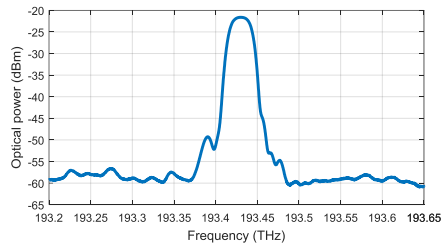

Fig. 4. Reflected signal spectrum of the FBG optical sensor (laboratory temperature 25 °C).

These spectral measurements of the used FBG sensor are shown in Table 2. All 7 implemented FBG sensors have the same (except reference wavelength) optical parameters.
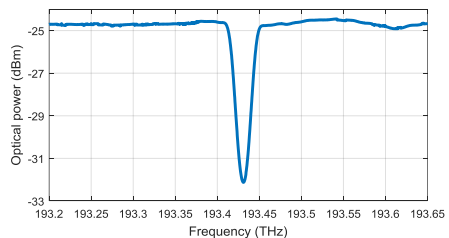

Fig. 5. Transmitted signal spectrum of the FBG optical sensor (laboratory temperature 25 °C).

The developed simulation model can be widely used and particular FBG optical temperature sensors can be substituted with different ones (for example, strain, pressure, displacement, etc. sensors) in a situation where it is necessary. However, the maximum available number of optical sensors available for implementation in such a combined system is limited to the bandwidth of the optical light source – its optical power level, channel spacing between optical sensors as well as the optical bandwidth for each and every sensor's channel and the distance from the optical sensors interrogation unit. Also, the WDM-PON system and its configuration – number of data channels, their positioning in the optical spectrum, etc. limits the integration of the optical sensors. All these parameters have to be calculated and adjusted in order to sustain the proper performance of both systems while providing the necessary application of each one of them.

Table 2. The main parameters of the used FBG temperature sensor.

Parameters	Value	
	Wavelength	Frequency
Operation temperature range	-40 to +150 °C	
Reflectivity	88.73 %	
FWHM	0.22 nm	27.448 GHz
Temperature coefficient (frequency or wavelength shift for 1°C)	9.6 pm/1°C	1.198 GHz/1°C
Reference wavelength or frequency used in the simulation setup	1548.52; 1547.72; 1546.92; 1546.12; 1545.32; 1544.53; 1543.73 nm	193.60; 193.70; 193.80; 193.90; 194.00; 194.10; 194.20 THz

Figure 6 shows the relevance between temperature and frequency curve for the implemented FBG sensor, in order to understand the correlation between the temperature and frequency shift. The curve is based on the commercial (Technica T840) FBG sensor's calibrated datasheet data. Then a linear approximation method is used for a more precise evaluation of the acquired data. Authors developed the mathematical linear function for this optical FBG temperature sensor, where the correlation of the temperature and frequency can be expressed as follows:

$$T = -764.57 \times F + 1.4791 \cdot 10^{-5} \qquad (2)$$

where: T-measured temperature (°C) and F – measured frequency of the FBG sensor (THz).
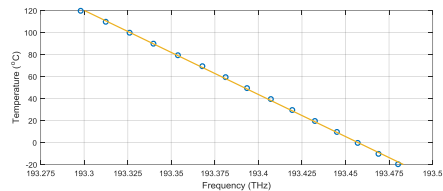

Fig. 6. The correlation of the temperature and frequency shift of the commercial FBG temperature sensor.

The length of 7 SMF spans between each FBG optical sensor is 5 km, whereas FBG sensors are located at 20th, 25th, 30th, 35th, 40th, 45th, and 50th km of the optical distribution network. Such positioning provides quasi-distributed FBG optical sensing applications, where optical sensors are implemented with a certain distance or evenly in the whole transmission media [47-49]. It is also important to note that the optical signal necessary for the operation of FBG optical sensors is transmitted twice through the ODN – firstly together with dense WDM-PON data transmission channels and then reflected back, being received at the optical sensors' interrogation unit. Knowing this, all the related parameters for the acceptable system setup development can be adjusted and are mentioned in this article. FBG temperature sensors were set in the frequency band between 193.60 THz and 194.20 THz having channel spacing of 100 GHz between each and every one of them. Such channel spacing was chosen considering the measured spectral bandwidth of each FBG (0.22 nm at FWHM) and the potential temperature range variation to avoid spectral overlapping. The output of FBG sensor_7 is connected with the AWG demultiplexer.

The optical network units (ONUs) section is realized as receiver blocks (Rx_1 to Rx_8). The

AWG demultiplexed signal is transmitted to a variable optical attenuator (VOA) and optical power splitter with a 10/90 splitting ratio for optical power level monitoring, enabling data transmission system BER curve measurements. The 10% port of the power splitter is connected with an optical power meter, and 90% port is connected with an avalanche photodiode (APD), which has a sensitivity of -20 dBm at reference BER≤10⁻¹². On the output of APD, the received electrical signal is filtered by Bessel low-pass filter (LPF) having a 7.5 GHz 3-dB bandwidth to reduce the noise. The filtered signal is then sent to the electrical scope to evaluate the waveform quality, e.g. to show eye diagrams, electrical spectrum, and estimate BER. Here the BER of the received signal is estimated analytically based on the eye quality.

3. RESULTS

The spectrum of the reflected signal of the 7 FBG sensor network is measured with an optical sensor interrogator unit's spectrometer, see Figure 7. As one can see in the measured spectrum, the central reflected frequencies of the sensors' network are 193.60, 193.70, 193.80, 193.90, 194.00, 194.10, and 194.20 THz. The central frequencies are the same as previously mentioned, considering that all sensors of the simulation model are configured to the reference temperature +25 °C. The main reason for the slanted reflected signal spectrum of the FBG sensor network (Fig.6) is the attenuation of optical fiber. As we are measuring the reflected FBG signal, it experiences double the attenuation of optical fiber (100 km in total).
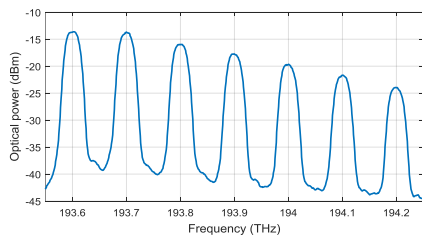

Fig. 7. The reflected signal spectrum of the FBG sensor network.

The optical signal spectrum (measured at the input of AWG DEMUX) of the simulated model where 8 data channels of the DWDM-PON transmission system (left side) are collaborated with 7 FBG temperature sensors' network transmitted signal (right side) is shown in Figure 8. AWG DEMUX acts as a filter and blocks the signal of the ASE, therefore it is not received by the ONUs. There is no visual interference, overlapping, and signal degradation between both systems (8-channel DWDM-PON and 7 FBG sensors), see Figure 8.
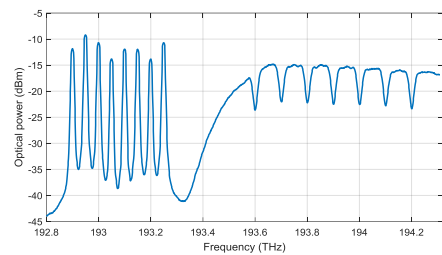

Fig. 8. The optical spectrum at AWG DEMUX input.

We chose the worst-performing data transmission channel (4th) in terms of the BER of an 8-channel DWDM-PON transmission system to analyze the performance of the overall DWDM system. Figure 9 shows a signal waveform of the received 10 Gbps signal after 50 km SMF transmission. As one can see in Figures 9 and 11, the bit pattern is clearly visible with the impact of chromatic dispersion, leading to a pulse broadening. The time window of 10 ns is chosen to represent the bit sequence in a way understandable to the reader. This signal has passed not only the 50 km of SMF fiber but also 8 FBG sensors, from which no significant signal degradation effects can be observed.
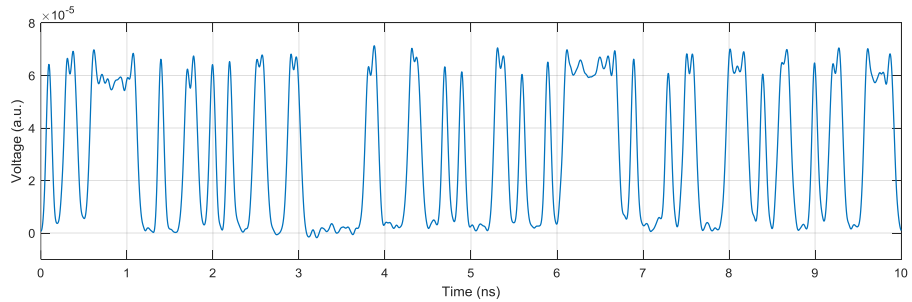
Fig. 9. The received signal 10 Gbps NRZ waveform of the 4th channel after 50 km long SMF transmission.

As shown in Figures 10 and 11, the eye diagrams of the 4th data transmission channel in the back-to-back (B2B) configuration (Figure 10) and after 50 km long SMF transmission (Figure 11) are widely open, and error-free transmission is calculated. The B2B configuration also includes the optical sensors' network, but the SMF line and SMF_1-SMF_7 are set to 0 km.
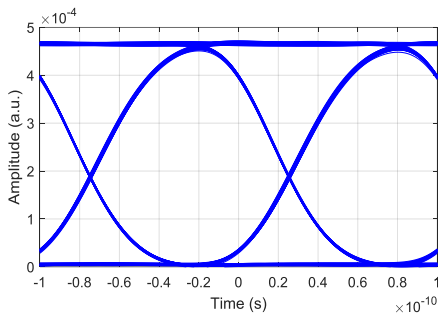

Fig. 10. The eye diagram of the worst-performing data channel in B2B configuration.

For B2B transmission the obtained BER for the worst-performing channel is 8×10^{-67}, and after 50 km long SMF line the obtained BER is 9.4×10^{-37}.

The eye diagrams are wide open and therefore the transmission of 10 Gbps NRZ-OOK signal can be considered as error-free.
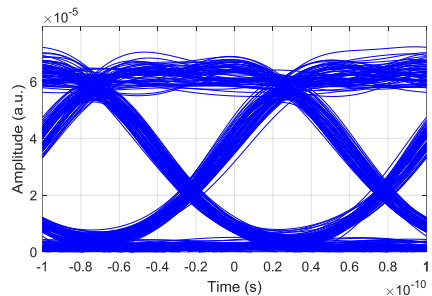
Fig.11. The eye diagram of the worst-performing data channel after 50 km long transmission line.

We measured the BER versus received optical signal power (see Figure 12) to understand the impact of a 50 km long SMF transmission line on the created mathematical simulation model.

Typical BER values would vary between the systems due to the differences in configuration, components, parameters, and so on. For such a collaborated system model, where the optical sensor system and dense WDM-PON system are merged, allowed BER should be at least $<10^{-9}$, which is typically to be considered as a BER threshold for error-free transmission [51-53]. In our research this goal is accomplished and even lower BER values are estimated (for example, 10^{-37}) yet it is not an easy task to calculate precisely such small BER values, thus the eye diagrams (which are wide open and even in our results) also have to be inspected.
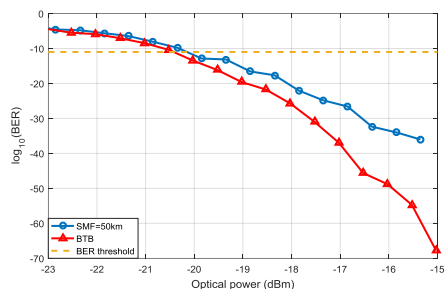
Fig. 12. BER versus the received optical signal power of 10 Gbps 8-channel DWDM PON data transmission system and 7 FBG sensors network, in the case of B2B and 50 km SMF configurations.

Here a strong correlation between B2B and a 50 km long transmission line is observed. The power penalty at the BER threshold level of 1×10^{-12} is negligible (only 0.3 dB). This power penalty introduced is mainly due to the fiber chromatic dispersion.

4. CONCLUSIONS

FWM-OFC can reduce the overall expenses of the proposed combined fiber optical DWDM transmission system and FBG temperature sensors' network. The FWM-based OFC source provides an energy-efficient solution due to the fewer light sources required to ensure multiple data transmission channels. Only two CW pump light sources and one NHLF fiber is necessary to power the 8-channel DWDM-PON data transmission system. The OFC generated through FWM exhibits fluctuations of individual comb tones of less than 3 dB in power, the average peak power of 0 dBm, and an extinction ratio of about 33 dB for an operating range of 192.9 – 193.25 THz. The created shared light source powers all data transmission channels. Supplementing to that, a spectrally efficient configuration has been applied and calculated, as the minimum channel spacing between the DWDM channels, optical sensor channels, as well as between both systems (DWDM-PON and FBG sensors) has been presented. Thereby, allowing other critical applications (for example, applications in Structural Health Monitoring (SHM)) to be positioned in the available frequency spectrum. This research approved a successful realization of the FWM-based OFC source in the simulation model and its implementation in a 10 Gbps 8-channel DWDM-PON optical transmission system with an integrated 7 FBG temperature sensors network. Successful integration of FWM-based OFC source is confirmed by the fact that interference between DWDM-PON and FBG sensor networks is still negligible. The measured BER value of the worst-performing channel in this 8-channel DWDM-PON system is 9.4×10^{-37}, thus demonstrating the stable operation of the system. From the acquired results and all the significant parameters and components provided for such collaborated net-work, authors can state that such configuration and fundamental information can be applied and used to provide easier application, broader technological opportunities for the optical network development, and greater energy efficiency with reduced light source amount required and to ensure collaboration between optical sensing applications and data transmission solutions, as well as used for further research in the field of the OFC based WDM/DWDM-PON and optical sensor collaborated networks.

References

[1] Bhatia, R.; Bhatia, S. Responsiveness of FWM with Fraction of Planck HOD Parameters in Presence of Intensity Dependent Phase Matching Factor in Optical Transmission. 2020 International Conference on Intelligent Engineering and Management (ICIEM), London, United Kingdom, 2020, pp. 142-147. https://doi.org/10.1109/ICIEM48762.2020.9160075

[2] Olonkins, S.; Spolitis, S.; Lyashuk, I.; Bobrovs, V. Cost Effective WDM-AON with Multicarrier Source Based on Dual-Pump FOPA. 6th International Congress on Ultra Modern Telecommunications and Control Systems and

Workshops (ICUMT), Russia, October 2014, pp. 23-28. https://doi.org/10.1109/ICUMT.2014.7002073.

[3] Ivaniga, P.; Ivaniga, T. Mitigation of non-linear four-wave mixing phenomenon in a fully optical communication system. Telkomnika, 2020, 18, 2878-2885. http://dx.doi.org/10.12928/telkomnika.v18i6.16136.

[4] Keiser, G. Optical Fiber Communications. 4th ed., Tata McGrawHill Publishing Co. Ltd., 2008.

[5] Sharma, N.; Singh, H.; Singh, P. Mitigation of FWM in the Fiber Optic DWDM System by using Different Modulation Tech-niques and Optical Filters. 5th International Conference on Communication and Electronics Systems (ICCES), Coimbatore, India, 2020, pp. 343-348. https://doi.org/10.1109/ICCES48766.2020.9138080.

[6] Selvamani, A.; Sabapathi, T. Suppression of four wave mixing by optical phase conjugation in DWDM fiber optic link. In-ternational Conference on Recent Advancements in Electrical, Electronics and Control Engineering, India, December 2011, pp. 95-99. 10.1109/ICONRAEeCE.2011.6129821.

[7] Anashkina, E.A.; Marisova, M.P.; Andrianov, A.V.; Akhmedzhanov, R.A.; Murnieks, R.; Tokman, M.D.; Skladova, L.; Olady-shkin, I.V.; Salgals, T.; Lyashuk, I.; Sorokin, A.; Spolitis, S.; Leuchs, G.; Bobrovs, V. Microsphere-based optical frequency comb generator for 200 GHz spaced WDM data transmission system. Photonics, 2020, 7, 72, 1-16. https://doi.org/10.3390/photonics7030072.

[8] Lin, G.; Diallo, S.; Chembo Y. K. Optical Kerr frequency combs: Towards versatile spectral ranges and applications. 2015 17th International Conference on Transparent Optical Networks (ICTON), Budapest, 2015, pp. 1-4. DOI: 10.1109/ICTON.2015.7193612.

[9] Del'Haye, P.; Schliesser, A.; Arcizet, O.; Wilken, T.; Holzwarth, R.; Kippenberg, T. J. Optical Frequency Comb generation from a monolithic microresonator. Nature, 2007, 450, 1214-1217. https://doi.org/10.1038/nature06401.

[10] Liopis, O.; Merrer, P. H.; Bouchier, A.; Saleh, K.; Cibiel, G. High-Q optical resonators: characterization and application to stabilization of lasers and high spectral purity oscillators.

Proceeding of SPIE, San Francisco, 2010, pp. 10. https://doi.org/10.1117/12.847164.

[11] Liang W.; Savchenkov A. A.; Matsko A. B.; Ilchenko V. S.; Seidel D.; Maleki L. Generation of near-infrared frequency combs from a MgF2 whispering gallery mode resonator. Opt. Lett., 2011, 36. https://doi.org/10.1364/OL.36.002290.

[12] Savchenkov, A. A.; Matsko, A. B.; Ilchenko, V. S.; Solomatine, I.; Seidel, D.; Maleki, L. Optical combs with a crystalline whispering gallery mode resonator. Phys. Rev. Lett., 2008, 101, 093902. https://doi.org/10.1103/PhysRevLett.101.093902.

[13] Savchenkov, A. A.; Matsko, A. B.; Maleki, L. On Frequency Combs in Monolithic Resonators. Nanophotonics, 2016, 5, 363-391. https://doi.org/10.1515/nanoph-2016-0031.

[14] Braunfelds, J.; Murnieks, R.; Salgals, T.; Brice, I.; Sharashidze, T.; Lyashuk, I.; Ostrovskis, A.; Spolitis, S.; Alnis, J.; Porins, J.; Bobrovs, V. Frequency comb generation in WGM microsphere based generators for telecommunication applications. Quantum Electronics, 2020, 50, 1043. https://doi.org/10.1070/QEL17409.

[15] Anashkina, E.A.; Andrianov, A.V. Kerr-Raman Optical Frequency Combs In Silica Microsphere Pumped near Zero Disper-sion Wavelength. IEEE Access, 2021, 9, 6729-6734. https://doi.org/10.1109/ACCESS.2021.3049183.

[16] Andrianov, A.V.; Anashkina, E.A. Single-mode silica microsphere Raman laser tunable in the U-band and beyond, Results Phys., 17, 103084, 2020, 1-5. https://doi.org/10.1016/j.rinp.2020.103084.

[17] Antikainen, A.; Agrawal, G. P. Dual-pump frequency comb generation in normally dispersive optical fibers. J. Opt. Soc. Am. B, 2015, 32, 1705–1711. https://doi.org/10.1364/JOSAB.32.001705.

[18] Myslivets, E.; Kuo, B. P.; Alic, N.; Radic, S. Generation of wideband frequency combs by continuous-wave seeding of multi-stage mixers with synthesized dispersion. Opt. Express, 2012, 20, 3331–3344. https://doi.org/10.1364/OE.20.003331.

[19] Hänsel, W.; Hoogland, H.; Giunta, M.; Schmid S.; Steinmetz T.; Doubek R.; Mayer P.; Dobner S.; Cleff C.; Fischer M.; Holzwarth R. All polarization-maintaining fiber laser architecture for robust femtosecond pulse generation. Appl.

Phys. B, 2017, 123, 1-6. https://doi.org/10.1007/s00340-016-6598-2.

[20] Ataie, V.; Myslivets, E.; Kuo, B. P.-P.; Alic, N.; Radic, S. Spectrally Equalized Frequency Comb Generation in Multistage Parametric Mixer With Nonlinear Pulse Shaping. J. Light. Technol., 2014, 32, 840–846. https://doi.org/10.1109/JLT.2013.2287852.

[21] ITU-T Recommendation G 694.1, "Spectral grids for WDM applications: DWDM frequency grid," in International Telecom-munication Union, Telecommunication standardization sector of ITU, pp. 1–7, Geneva, Switzerland, 2002.

[22] Bohnert, K.; Frank, A.; Yang, L.; Gu, X.; Müller, G. M. Polarimetric Fiber-Optic Current Sensor With Integrated-Optic Polar-ization Splitter. J. Light. Technol., 2019, 37, 3672-3678. https://doi.org/10.1109/JLT.2019.2919387.

[23] Giurgiutiu, V. Comprehensive Composite Materials II Elsevier, 2018, ISBN 9780081005347.

[24] McKnight, M.; Agcayazi, T.; Ghosh, T.; Bozkurt, A. Wearable Technology in Medicine and Health Care, Academic Press, 2018, ISBN 9780128118108.

[25] Giurgiutiu, V. Composites Science and Engineering, Polymer Composites in the Aerospace Industry (Second Edition), In Woodhead Publishing Series in, Woodhead Publishing, 2020, ISBN 9780081026793.

[26] Senkans, U.; Braunfelds, J.; Lyashuk, I.; Porins, J.; Spolitis, S.; Bobrovs, V. Research on FBG-Based Sensor Networks and Their Coexistence with Fiber Optical Transmission Systems. Journal of Sensors, 2019, 2019, 1-13. https://doi.org/10.1155/2019/6459387.

[27] Kim, M.H.; Lee, J.M. Woodhead Publishing Series in Electronic and Optical Materials, Sensor Technologies for Civil Infrastructures, Woodhead Publishing, Vol. 56, 2014, ISBN 9781782422426.

[28] Hayes, S.A.; Swait, T.J., Lafferty, A.D. Composites Science and Engineering, Recent Advances in Smart Self-healing Polymers and Composites. In Woodhead Publishing Series in, Woodhead Publishing, 2015, ISBN 9781782422808.

[29] Braunfelds, J.; Senkans, U.; Skels, P.; Janeliukstis, R.; Salgals, T.; Redka, D.; Lyashuk, I.; Porins, J.; Spolitis, S.; Haritonovs, V.; Bobrovs, V. FBG-Based Sensing for Structural Health Monitoring of Road Infrastructure. Journal of Sensors, 2021, 2021, 1-11. https://doi.org/10.1155/2021/8850368.

[30] Alamandala, S.; Sai Prasad, R.L.N.; Pancharathi, R.; Pavan, V.D.R.; Kishore, P. Study on bridge weigh in motion (BWIM) system for measuring the vehicle parameters based on strain measurement using FBG sensors. Opt. Fiber Technol., 2021, 61, 102440, 1-9. https://doi.org/10.1016/j.yofte.2020.102440.

[31] Taheri, S. A review on five key sensors for monitoring of concrete structures. Construction and Building Materials, 2019, 204, 492-509. https://doi.org/10.1016/j.conbuildmat.2019.01.172.

[32] Peters, K.J.; Inaudi, D. Electronic and Optical Materials, Sensor Technologies for Civil Infrastructures, Woodhead Publishing, Vol. 55, 2014, ISBN 9780857094322.

[33] Ansari, F. Civil and Structural Engineering, Structural Health Monitoring of Civil Infrastructure Systems, Woodhead Publishing, 2009, ISBN 9781845693923.

[34] Baldwin, C. 8 - Fiber Optic Sensors in the Oil and Gas Industry: Current and Future Applications, Editor(s): Alemohammad, H. Opto-Mechanical Fiber Optic Sensors, Butterworth-Heinemann, 2018, ISBN 9780128031315.

[35] Vadgama, P. Biomedical Sensors: Materials, Editor(s): Buschow, J.; Robert, K.H., Cahn, W.; Flemings, M.C.; Ilschner, B.; Kramer, E.J. Subhash, S.; Veyssière, P.; Encyclopedia of Materials: Science and Technology, Elsevier, 2001, ISBN 9780080431529.

[36] Tosi D., Poeggel S., Iordachita I., Schena E. 11 - Fiber Optic Sensors for Biomedical Applications, Editor(s): Alemohammad, H. Opto-Mechanical Fiber Optic Sensors, Butterworth-Heinemann, 2018, ISBN 9780128031315.

[37] Broughton W. Welding and Other Joining Technologies, Adhesives in Marine Engineering, Woodhead Publishing, 2012, ISBN 9781845694524.

[38] Subramanian, R.; Zhu, C.L.; Zhao, H.; Li, H.P. Torsion, strain, and temperature sensor based on helical long-period fiber gratings. IEEE Photonics Technol. Lett., 2018, 30, 327-330. https://doi.org/10.1109/LPT.2017.2787157.

[39] Velazquez-Gonzalez, J.S.; Monzon-Hernandez, D.; Martinez-Pinon, F.; Hernandez-Romano, I. Simultaneous measurement of refractive index and temperature using a SPR-

based fiber optic sensor. Sens. Actuat. B-Chem., 2017, 242, 912-920. https://doi.org/10.1016/j.snb.2016.09.164.

[40] Gu, J.; Kwon, D.; Ahn, J.; Park, I. Strain Sensor Based on Optical Intensity Change Through the Carbon Nanotube Embedded Elastomer. 2019 20th International Conference on Solid-State Sensors, Actuators and Microsystems & Eurosensors XXXIII (TRANSDUCERS & EUROSENSORS XXXIII), Berlin, Germany, 2019, pp. 1716-1719. https://doi.org/10.1109/TRANSDUCERS.2019.8 808701.

[41] Madan, A.; Liu, O.; Jiang, W.; Wang, Y.; Shum, P. P.; Hao, J. Carbon-steel tube surface mounted FBG sensors under high-temperature environment, part I: Polyimide coated and femtosecond laser written. 2020 IEEE 5th Optoelectronics Global Conference (OGC), Shenzhen, China, 2020, pp. 125-129. https://doi.org/10.1109/OGC50007.2020.926046 2.

[42] Ran, Z.; Liu, S.; Liu, Q.; Wang, Y.; Bao, H.; Rao, Y. Novel High-Temperature Fiber-Optic Pressure Sensor Based on Etched PCF F-P Interferometer Micromachined by a 157-nm Laser. IEEE Sens. J., 2015, 15, 3955-3958,. https://doi.org/10.1109/JSEN.2014.2371243.

[43] Khadour, A.; Waeytens, J. Civil and Structural Engineering, Eco-Efficient Repair and Rehabilitation of Concrete Infrastructures, Woodhead Publishing, 2018, ISBN 9780081021811.

[44] Mahawar, N.; Khunteta, A. Design and performance analysis of WDM optical Communication system with EDFA-DCF and FBG for dispersion compensation using 8x5 Gbps data rate. 2019 International Conference on Communication and Elec-tronics Systems (ICCES), Coimbatore, India, 2019, pp. 431-435, https://doi.org/10.1109/ICCES45898.2019.90022 36.

[45] Götten, M.; Lochmann, S.; Ahrens, A.; Lindner, E.; Vlekken, J.; Van Roosbroeck, J. 4000 Serial FBG Sensors Interrogated with a Hybrid CDM-WDM System. IEEE Sens. J., 2020, 1-4, https://doi.org/10.1109/SENSORS47125.2020.9 278764.

[46] Synopsys OptSim Product Overview. Available online: https://www.synopsys.com/photonic-solutions/rsoft-system-design-tools/system-network-optsim.html (accessed on 18.02.2021).

[47] Xia, L.; Cheng, R.; Li, W.; Liu, D. Identical FBG-Based Quasi-Distributed Sensing by Monitoring the Microwave Responses. IEEE Photon. Technol. Lett., 2015, 27, 323-325. https://doi.org/10.1109/LPT.2014.2370650.

[48] Dwivedi, K. M.; Trivedi, G.; Khijwania, S. K. Theoretical Study and Optimization of Apodized Fiber Bragg Grating for Sin-gle and Quasi-distributed Structural Health Monitoring Applications. 2020 30th International Conference Radioelektronika (RADIOELEKTRONIKA), Bratislava, Slovakia, 2020, pp. 1-6, https://doi.org/10.1109/RADIOELEKTRONIKA 49387.2020.9092399.

[49] Moon, H.; Kwak, S.; Im, K.; Kim, J.; Kim, S. Wavelength Interrogation System for Quasi-Distributed Fiber Bragg Grating Temperature Sensors Based on a 50-GHz Array Waveguide Grating. IEEE Sens. J., 2019, 19, 2598-2604. https://doi.org/10.1109/JSEN.2018.2889853.

[50] Bobrovs V., Spolitis S., Ivanovs G. Extended Reach Spectrum-Sliced Passive Optical Access Network. International Journal of Physical Sciences, 2013, 8 (13), pp. 537.-548. https://doi.org/10.5897/IJPS2013.3868

[51] Tsai W. et al. A 20-m/40-Gb/s 1550-nm DFB LD-Based FSO Link, IEEE Photonics J., 2015, 7, 1-7, doi: 10.1109/JPHOT.2015.2506172.

[52] Ledentsov Jr. N., Agustin M., Chorchos L., Kropp J.-R., Shchukin V. A., Kalosha V. P., Koepp M., Caspar C., Turkiewicz J. P., Ledentsov N. N. Energy efficient 850-nm VCSEL based optical transmitter and receiver link capable of 56 Gbit/s NRZ oper-ation, Vertical-Cavity Surface-Emitting Lasers XXIII, 109380J, 2019, pp.1-8. https://doi.org/10.1117/12.2509916.

[53] Elayoubi K., Rissons A., Belmonte, A. Optical test bench experiments for 1-Tb/s satellite feeder uplinks, Laser Communica-tion and Propagation through the Atmosphere and Oceans VII, 1077006, 2018, pp. 1-11. https://doi.org/10.1117/12.2317728.

Senkans U., **Braunfelds J.**, Lyashuk I., Porins J., Spolitis S., Haritonovs V., and Bobrovs V. FBG Sensors Network Embedded in Spectrum-sliced WDM-PON Transmission System Operating on Single Shared Broadband Light Source. No: Proceedings of Photonics & Electromagnetics Research Symposium (PIERS 2019), China, Xiamen, 17 - 20 December, **2019**, pp.1.-9.

FBG Sensors Network Embedded in Spectrum-sliced WDM-PON Transmission System Operating on Single Shared Broadband Light Source

Ugis Senkans, Janis Braunfelds, Ilya Lyashuk, Jurgis Porins,
Sandis Spolitis, Viktors Haritonovs, and Vjaceslavs Bobrovs

Institute of Telecommunications, Riga Technical University, Azenes Street 12, LV-1048, Riga, Latvia

Abstract— With the development of modern communication technology industry and expansion of user needs in daily life, more and more applications, as well as systems, are being created and upgraded. Part of them, for example, sensor and data transmission systems, in a lot of scenarios are based upon the use of available frequency spectrum. Given that the overall amount of information that needs to be collected or exchanged is growing exponentially, there is a constant need to develop new system models that provide faster data transmission rates, increased capacities, simplified architecture, and resource optimization. In line with previously mentioned, it is important not to forget providing the availability to ensure interaction between systems and their models in scenarios where that could be required. For instance, merging data transmission systems with optical sensor ones, therefore establishing resource and finance optimization. Fiber Bragg grating (FBG) technology is one of the appealing ways for fiber optical sensor systems that provide immunity to radio frequency interference (RFI) and electromagnetic interference (EMI) as well as operate passively, provide multiplexing applications and remote real-time monitoring within large distances. In this research, we demonstrate a successful realization of a unified 7 FBG sensors network with the 32-channel spectrum sliced wavelength-division-multiplexed passive optical network (SS-WDM PON) data transmission system. As the length of standard single mode (SMF) optical fiber span between each sensor on the 7-sensor network is 4 km, we show the sustainable remote operation of this embedded sensor network over a distance of 28 km. We provide a resource and cost-efficient solution in an optical part of the developed system by unifying input light sources as we implemented the single broadband light source (BLS) shared between both merged systems, instead of using different light sources for each of them. For the development of this merged system model, its characterization and performance evaluation the mathematical modeling and simulation software was used. Performance evaluation was made for 4 different scenarios — with and without collaboration between both systems and at bit rates of 2.5 Gbit/s and 10 Gbit/s per each and every data transmission channel, confirming that the successful operation of data transmission and sensing network in one merged system is achievable.

1. INTRODUCTION

Due to the rapid growth of a wide range of different applications and high-speed fiber optical communication and data transmission systems, a lot of concerns are already discussed by the modern community. For instance, security issues, huge continuous increase in transmitted data amount and so on. There is research carried out where by using fiber optical sensor systems, it can be a great assist in the matter of solving such difficulties. Although, there are traditional transmission line monitoring and warning methods that in lots of scenarios are costly and human-resource oriented not to mention result difference compared to actual results [1].

However, fiber optical sensor technology dismisses such problems, providing real-time monitoring applications for a wide range of parameters and needs, for example, starting from detecting small chemical substance concentration parameters [2] to monitoring large buildings — Structural health monitoring (SHM) application [1]. One of the examples of fiber optical sensor implementation in SHM applications is within concrete structures in order to monitor deformation and strain of the reinforced concrete as well as corrosion of the reinforcing steel [3]. There, they can be used as either as a single point optical sensor or distributed within a network in order to ensure multiple region monitoring [4]. Fiber optical sensors nowadays are used in a wide variety of applications, even in harsh environments, where, for instance, fiber optical temperature sensors (which we will be integrating into our system model) are situated. For example, in cases of extremely high temperatures (approximately 1000°C) for monitoring of modern nuclear reactors [5].

Due to their characteristic advantages — lightweight, tiny size, immunity to electromagnetic interference, fact that they do not require active power supply, high precision ratio, multiplexing abilities, as well as great long-term monitoring possibilities and so on, they provide probability

to measure and monetarize parameters along the whole length of the optical fiber [6, 7]. Sensor measurement principle wise, Fiber Bragg grating (FBG) is an appealing way for fiber optical sensors. Multiple FBG optical sensors can be positioned along a single unified fiber while providing simplicity in use, cost-friendly application and high accuracy in measurements [8, 9]. They can be integrated into different compounds of materials to provide measurements of not only parameters like temperature and strain, but as well as humidity, liquid elevation, force and so on [10].

With the advancement of fiber optical systems and their collaboration with data transmission systems, so are developed new solutions for providing fast transmission over passive optical access networks (PONs) which maintains also as an environment for placement of fiber optical sensor systems. The United States has been working on "Connecting America: The National Broadband plan" in order to provide 1 Gbit/s connections to local communities by the year 2020. PONs are considered as the best solution while providing a cost-efficient way for providing deployment of Fiber-To-The-Home (FTTH) networks [11].

Technology-wise PONs have been upgraded and defined by different standards. Starting from Broadband PON (BPON) standardization by International Telecommunication Union (ITU-T) G.983.1–G.983.5 in the year of 2000 and providing up to 1.25 Gbit/s downstream bit rate and 0.625 Gbit/s — upstream, to nowadays, when Next Generation Ethernet PONs (NG-EPON), standardized by ITU-T and Institute of Electrical and Electronics Engineers (IEEE) 802.3ca working group (where rates of 25 Gbit/s, 50 Gbit/s and even high ones by the year of 2020) are being discussed. Research shows that worldwide FTTH revenue by technology will switch away from 2.5 Gbit/s GPON even more towards XGS-PON and NGPON-2 in the years between 2020 to 2022 [11, 12].

From the analysis of European commission documents and guidelines [13], until 2026, more than 50 billion objects, including cars, homes, and watches are predicted to be connected all around the world. Transformative solutions are needed in a matter of internet connectivity that includes the Internet of Things, huge data analytics, cloud computing, high-performance computing and different kind of systems and applications. Fiber optical application is a recommended medium that would provide a link between core networks and final sub-networks. This shows a clear indication that fiber optical sensor systems and data transmission systems will more and more incorporate as well as be even easier available for end-users in order to satisfy their needs.

Evaluating [13] document even further, it shows clear expectations for the QoS — the quality of service of fixed internet connectivity to be improved by the time of 2025, highlighting downlink speed — above 1 Gbps (responsiveness — less than 10 miliseconds). For Europe's development, very high-capacity networks are evolving as a requirement, where the strategic aim is to build a Gigabit society, relying on high-speed capacity networks.

2. TRENDS OF MODERN SOCIETY IN A MATTER OF CONSUMPTION OF TRANSMISSION DATA

Every year, in modern days, continues the raise of fiber optical technology deployment over communication systems not only in business and public sphere but as well in the private sector. From the FTTH deployment statistics, United States, for instance, has reached its highest point. By the year 2017, the United States had increased the number of households having access to fiber broadband over 4.4 million. Overall, approximately 28% of all the United States households, which is 35 million, now are able to access fiber provided communications [14].

AT&T, one of the leading telecommunication companies in the United States are planning to reach around 14 million homes located in small rural towns with fiber communication technology by the end of the second quarter in the year of 2019. In order to achieve their set goals — providing virtualization of access functions in the last-mile network, 10 Gbit/s XGS-PON virtualized network has been already tested in Dallas and Atlanta. Not only is it the needs of the users and households progressing, but the industry as a whole is expanding drastically. A large number of companies are competing for the place in Top 100 in the global industrial market, with that they are trying to find new and improved solutions for communication capacity, speed and quality markings [14].

From the research and reports done from the telecommunication engineering industry of India, it is shown, that consumption ratio in telecommunication consists of over 2,360 Petabytes of data, which could be aligned to a data amount that is stored within 526 million DVDs. Alongside — India, the USA, China, and Japan are contributing large amounts of data transmission as well. The United Kingdom has stated, that modern internet is a utility as a right to have reliable and fast connections. Canada, for example, declared that high-speed internet access is needed in order

to provide for "quality of life" [15].

Not only does the transmitted data amount is increasing, but also the way and form of this data changes and becomes more complex, mainly due to different styles of systems that need to be integrated. Internet-of-things is already switching beyond smartphones and gadgets in order to connect billions of devices, monitoring systems, household applications, vehicles, and sensor systems. Intelligent, fast, robust and smart automation will provide in redefining modern life in this hyper-connected world [15].

With all of the previously mentioned, it is clears that with time even more and more users will demand the availability of access to communications in different places all around the world. With that, the increase of transmitted data from both — users and different kinds of systems, like optical sensor ones, will continue to grow exponentially. This will genuinely lead to a need for bandwidth optimization, the larger capacity of data processing, storing and higher rates of data transmission.

3. SIMULATION SETUP OF DIFFERENT SCENARIOS FOR 32-CHANNEL SS-WDM PON SYSTEM AND OPTICAL SENSOR NETWORK COMBINATIONS

During our research, we realized few different scenarios for evaluating successful realization of a collaborated FBG sensor network in 28 km long SMF line (according to ITU-T G.652 [16]) that had 7 optical sensors with 4 km fiber spans together with data transmission system with 32-channel spectrum sliced wavelength-division-multiplexed passive optical network (SS-WDM-PON). The particular length of fiber spans was chosen based upon our previous research [17], where it was explained that 4 km long fiber spans are commonly used in Latvia between two cabinets or fiber optical manholes (are where optical closures are placed). Such simulations were created within RSOFT OptSim mathematical simulation software. To prove the successful operation of both systems — fiber optical sensor and data transmission one, we created two simulation setups (Figure 1). In first simulation setup data transmission system was observed without interference from the fiber optical sensor system. On the other hand, simulation setup No. 2 is a more complex solution, where both systems (optical sensor channels and data transmission channels) are combined together while using one unified light source and one unified fiber as a transmission media. In both simulation setups, pseudo-random bit sequence (PRBS) modulation was chosen and Amplified spontaneous emission (ASE) as a broadband light source (BLS) was chosen. The whole spectrum was allocated in the spectral range between 191.5 THz and 195.5 THz. For data transmission channels, 191.65 THz to 193.20 THz spectrum was selected, whereas 193.6 THz to 194.9 THz spectrum was saved for optical sensors.

To evaluate the impact on the overall system, for both simulation setups, as well to see the impact of transmission speed, two different data transmission rates were chosen, hence 2.5 Gbit/s and 10 Gbit/s per each and every data channel. Particular values nowadays are typical and interesting to ensure the developing needs of customers in order to maintain the progress of data transmission collaboration with other system models that are demanded by our modern society. The objective was to acquire results that prove enough quality of the proposed system model, meaning that the data signals would provide pre-forward error correction or pre-FEC bit error ratio of not higher than 2×10^{-3}. With this value, an error-free output signal observation could be monitored. A configuration like this is applicable to the FEC encoding scheme application with 7% overhead.

For Figure 1, abbreviations were used, where: BLS — broadband light source, AWG — arrayed waveguide grating, OLT — optical line terminal, TX — optical transmitter, SOA — semiconductor optical amplifier, EAM — electro-absorption modulator, DCF — dispersion compensation fiber, FBG — Fiber Bragg grating, OC — optical circulator, RX — optical receiver, SMF — single mode fiber, PD — photodiode.

In simulation setup No. 2 we divided BLS output optical signal into 2 identical optical radiation streams with 1 : 2 optical power splitter, ensuring that 50% of whole optical power would be generated to the unified system — optical sensor and data transmission. During our tests, such a particular division was chosen because it provided an acceptable operation of the overall system. This means that such a model provided results where the output of optical sensors and data channels could be received and evaluated. This ratio also provided that no visual interference takes place during simulations.

For both simulation setups arrayed waveguide grating (AWG) was used to spectrally slice 32 channels. Here the channel spacing according to the ITU-T G.694.1 was chosen as 50 GHz [18]. Adding to that, we used 3 dB insertion loss blocks in order to resemble the insertion loss generated by the AWG unit. In both simulation setups (100% optical power in the first one and 50% optical
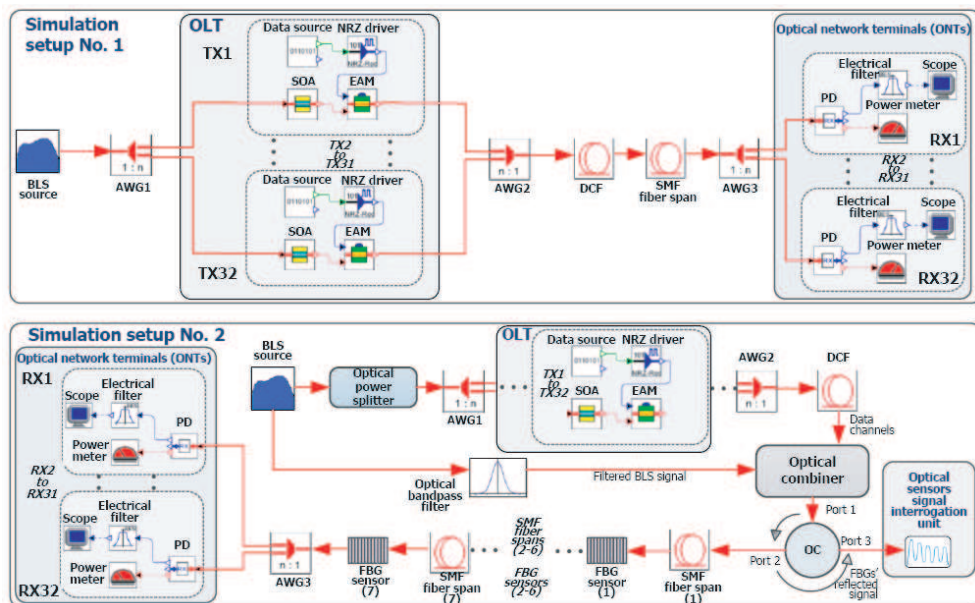
Figure 1: Simulation models for both setups where one shared optical fiber and the optical light source are used for 32-channel SS-WDM PON transmission system (operating at 2.5 Gbit/s and 10 Gbit/sbitrate) with and without an embedded 7 fiber optical FBG sensors system.

power in the second one(saving another half of 50% for fiber optical sensor system)) are spectrally sliced and then fed into the data transmitters (TX) which are located in optical line terminal or OLT. Each of 32 data transmitters in both simulations consists of data source, NRZ driver, gain saturated semiconductor optical amplifier or SOA and polarization insensitive electro-absorption modulator (EAM). EAM, in this scenario, was used mainly due to their immunity to signal polarization. SOA on the other hand — was chosen in order to provide intensity fluctuation noise suppressing that was introduced because of the BLS-ASE source nature. Afterward, both simulation setups run twice. Firstly with 2.675 Gbit/s generated data stream which is represented by pseudo-random bit sequence (PRBS) pattern and consists of 7% FEC overhead plus 2.5 Gbit/s payload sent from our NRZ driver towards RF input of EAM modulator. Secondly, a 10.7 Gbit/s data stream was generated that consisted of 7% FEC overhead plus 10 Gbit/s payload.

Once all of the EAMs have modulated and formed optical pulses as representing data, these pulses, from TX 1 to TX 32 are then coupled back together by the second AWG multiplexer device. After that, channels, prior to being launched into SMF (in first simulation setup) or optical combiner (second simulation setup), are pre-compensated by the dispersion compensating fiber (DCF) to limit the negative effect of chromatic dispersion. DCF length is set to 3.73 km dispersion coefficient is $D = -120$ ps/nm/km and the attenuation coefficient is $\alpha = 0.55$ dB/km at 1550 nm reference wavelength. After this part, there is a slight difference between simulation setups.

For the first simulation setup, at this point signal is carried through SMF for which we chose commonly used parameters that were based for 1550 nm wavelength spectrum, with dispersion coefficient $D = 16$ ps/nm/km, while attenuation coefficient α was set to 0.18 dB/km. At the end of the first simulation setup scheme, the signal is divided with another arrayed waveguide grating (AWG) and sent to the receiver section, where optical network terminals (ONTs) are stored. The receiver part, as it the same for the simulation setup No. 2, will be discussed in further paragraphs.

The previously mentioned difference between both simulation setups after DCF part is that, in simulation setup No. 2, after the signal is carried through DCF, it is then coupled together with another half of the BLS spectrum. This was done with an optical band-pass filter with 1.65 THz 3-dB bandwidth to ensure that 50% of the optical power from the source is reserved for data

channels and the other 50% — for optical sensors network (excluding the possibility of both signals overlapping). After optical combiner, in simulation No. 2, the combined signal is passing through 7 FBG optical sensors that are positioned within SMF and fed into optical receivers in ONTs or optical network terminals.

Further on, in the simulation setup No. 2, an optical circulator is used for the optical sensor network in order to divide optical signal transmission directions. Figure 1 depicts 7 FBG optical temperature sensors that are separated from each other with 7 SMF 4 km long fiber spans. That makes a total of 28 km long transmission line. The same length for SMF was chosen in simulation setup No. 1 as well to ensure the maximum similarities between both setups thereby excluding any other factors that might make difference on the output results except only the optical sensor network.

Afterwards, when the optical signal has been carried through optical sensor network (as in simulation setup No. 2) or straight through 28 km long SMF span (as in simulation setup No. 1), it is then sent to the receiver part (RX1 to RX32) which are positioned in optical network terminal (ONT). Every ONT, from RX1 to RX32 includes optical receiver with InGaAs avalanche photodiode (APD) that has sensitivity of -20 dBm at the reference BER of 10^{-12}, electrical Bessel low pass filter with 6 GHz 3-dB bandwidth, electrical scope and last but not least — optical power meter for the observation of overall quality of the average received signal power. Here we were able to evaluate optical signals eye diagrams, bit patterns, and BER values as well as check that no visual and numeric interference has been created between data transmission and optical sensor network systems. On the other hand, as for the FBG optical sensors, their reflected signals are observed in the optical sensors interrogation unit which includes spectrometer and digital signal processing unit for overall sensor signal processing.

As previously mentioned, this was done two times for both simulation models at different data transmission rates (2.5 Gbit/s and 10 Gbit/s) to see the correlation of how precisely transmission rates affect combined simulation scheme where data transmission and optical sensor networks are connected via one unified light source and optical fiber. Adding to that, this also allows examining broader perspectives for such created system setups.

4. RESULTS AND DISCUSSIONS

We reached our set goals for the research of simulation setups. Firstly an SS-WDM PON system model was successfully created that had a unified system where one was 32 data transmission channel system and the other one — 7 FBG optical sensor system (with peak central frequencies set to 193.6, 193.8, 194.0, 194.2, 194.4, 194.6 and 194.8 THz). Both systems shared one unified transmission media — optical line and had a single BLS source. Secondly, we were also able to numerically and visually determine the impact on the data transmission system when there was an FBG optical sensor system integrated within the setup. This evaluation was done with two different bit rates in order to see what the effects on the data transmission system are. The reflected optical signal spectrum of simulated 32-channel SS-WDM PON transmission system (operating at
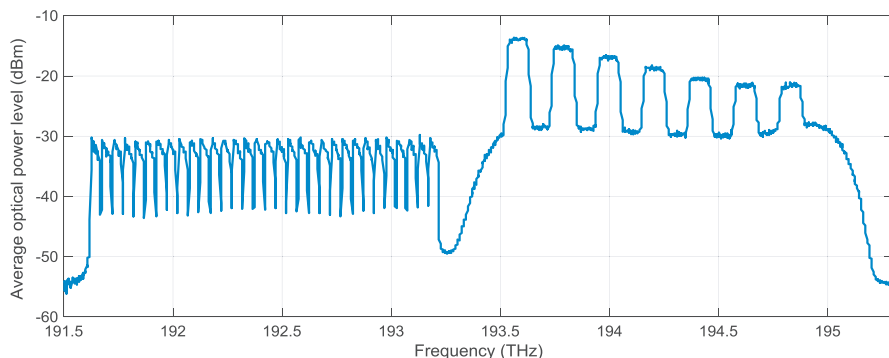

Figure 2: Reflected optical signal spectrum of simulated 32-channel SS-WDM PON transmission system (operating at 2.5 Gbit/s bit rate) with embedded 7 FBG sensors network.

2.5 Gbit/s bit rate) with embedded 7 FBG sensors network is shown in Figure 2.

For evaluation of the collaboration process for both systems, it was important to investigate FBG optical sensors' network impact on the SS-WDM PON data transmission system.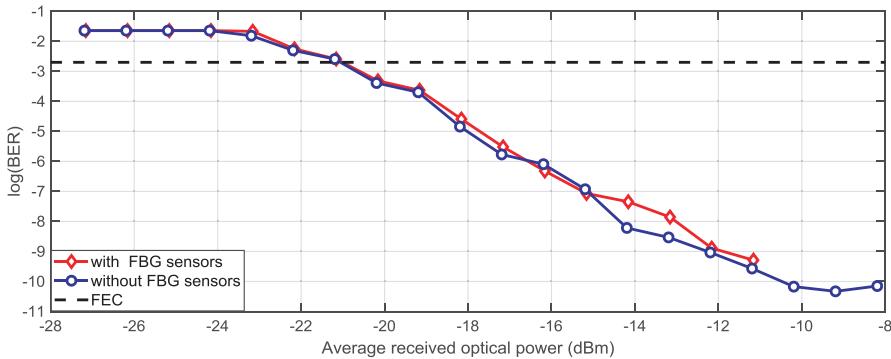 Acquired results are shown in Figure 3 and Figure 4. Figure 3 shows a BER versus received optical power for 32-channel 2.5 Gbit/s SS-WDM PON system with and without an integrated FBG optical sensor network for one of the data transmission channels.

From Figure 3 it possible to observe a few important things. Firstly, there is a strong correlation between both simulation setup output results. Meaning that the overall FBG optical sensor system does not negatively affect the SS-WDM PON data transmission system at a bit rate of 2.5 Gbit/s. Only a small difference in BER for a channel can be observed if both simulation setups are measured at the same received average optical power. Secondly, calculations show that the power penalty for simulation setup No. 2 is close to the value of zero dB at the pre-FEC BER level of 2.3×10^{-3}, if the comparison is made to the simulation No. 1 result data.

Figure 3: BER versus received optical power for 32-channel 2.5 Gbit/s SS-WDM PON system with and without integrated FBG optical sensor network.
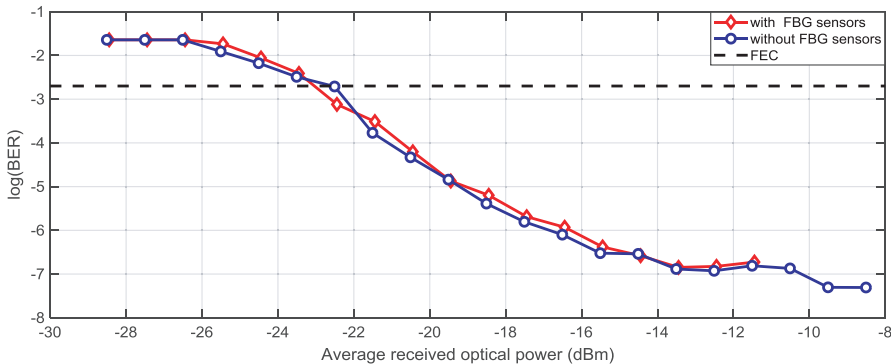
Figure 4: BER versus received optical power for 32-channel 10 Gbit/s SS-WDM PON system with and without integrated FBG optical sensor network.

In Figure 4, a BER versus received optical power for 32-channel 10 Gbit/s SS-WDM PON system with and without an integrated FBG optical sensor network for one of the data transmission channels is shown. Although there is some slight deviation from the theoretical aspect at some received optical power points. However, this might be due to some negligible errors in measurement and here as well a strong correlation can be seen between both simulation setup results. Here the results also prove that even an increase of the bit rate (in this scenario 10 Gbit/s) for the particular system does not affect negatively the output result. The only downside of such a model is that it

becomes more complex — more additional devices and components are needed, thus the insertion loss of the overall system generally increases.

5. CONCLUSIONS

This research approved a successful realization of simulation models where a 32-channel SS-WDM PON transmission system was combined with a 7 FBG optical sensor system with one shared BLS source over one optical fiber. We were also able to confirm that it is possible to combine an optical sensor system with 2.5 Gbit/s and 10 Gbit/s data transmission system considering the output results of both simulation setups. Although there were some slight differences between the results for both simulation setups discussed in previous sections, however from the output results (Figure 3, Figure 4 and Table 1) it was clear, that even by increasing data transmission speed 4 times, we would still acquire readable data with average BER for 32 channels as 2.6×10^{-7}. Last but not least, power penalty in simulation setup No. 2, where both systems were collaborated was close to the value of zero dB at the pre-FEC BER level of 2.3×10^{-3} and therefore can be neglected. With that being said, we can conclude that FBG optical sensors network does not negatively affect the SS-WDM PON data transmission system and such collaboration between both technologies.

REFERENCES

1. Tang, B. and Z. Zhou, "The design of communication network optical fiber cable condition monitoring system based on distributed optical fiber sensor," *2018 International Conference on Electronics Technology (ICET)*, 97–101, Chengdu, 2018, doi: 10.1109/ELTECH.2018.8401433.

2. Memon, S. F., M. M. Ali, J. T. Pembroke, B. S. Chowdhry, and E. Lewis, "Measurement of ultralow level bioethanol concentration for production using evanescent wave based optical fiber sensor," *IEEE Transactions on Instrumentation and Measurement*, Vol. 67, No. 4, 780–788, April 2018, doi: 10.1109/TIM.2017.2761618.

3. Bremer, K., L. Alwis, F. Weigand, et al., "Evaluating the performance of functionalized carbon structures with integrated optical fiber sensors under practical conditions," *Sensors*, Vol. 18, No. 11, 3923, 2018.

4. Zhang, Q. and Z. Xiong, "Crack detection of reinforced concrete structures based on BOFDA and FBG sensors," *Shock and Vibration*, Vol. 2018, Article ID 6563537, 1–10, 2018.

5. Laffont, G., R. Cotillard, N. Roussel, R. Desmarchelier, and S. Rougeault, "Temperature resistant fiber Bragg gratings for on-line and structural health monitoring of the next-generation of nuclear reactors," *Sensors*, Vol. 18, No. 6, 1791, 2018.

6. Morana, A., et al., "Steady-state radiation-induced effects on the performances of BOTDA and BOTDR optical fiber sensors," *IEEE Transactions on Nuclear Science*, Vol. 65, No. 1, 111–118, Jan. 2018, doi: 10.1109/TNS.2017.2772333.

7. Zhang, L., B. Shi, L. Zeni, A. Minardo, H. Zhu, and L. Jia, "An fiber Bragg grating-based monitoring system for slope deformation studies in geotechnical centrifuges," *Sensors*, Vol. 19, No. 7, 1591, 2019.

8. Bekmurzayeva, A., M. Shaimerdenova, Y. Abukhanov, M. Sypabekova, and D. Tosi, "Detection of tilted fiber Bragg grating fiber-optic sensors with short-term KLT: Towards low-cost biosensors," *2018 IEEE Sensors*, 1–4, New Delhi, 2018, doi: 10.1109/ICSENS.2018.8630292.

9. Guo, H.-Y., Z.-B. Wang, and H.-Y. Li, "Development and commissioning of high temperature FBG solid pressure sensors," *Journal of Sensors*, Vol. 2018, Article ID 2056452, 1–8, 2018.

10. Leal-Junior, A. G., C. Díaz, C. Marques, A. Frizera, and M. J. Pontes, "3D-printing techniques on the development of multiparameter sensors using one FBG," *Sensors*, Vol. 19, No. 16, 3514, 2019.

11. Muciaccia, T., F. Gargano, and V. M. N. Passaro, "Passive optical access networks: State of the art and future evolution," *Photonics 2014*, Vol. 1, 323–346, 2014.

12. International Telecommunication Union (ITU), ITU-T PON standards — progress and recent activities, Q2/SG15.

13. Communication from The Commission to The European Parliament, The Council, The European Economic and Social Committee and The Committee of The Regions, Connectivity for a Competitive Digital Single Market — Towards a European Gigabit Society, (SWD(2016)300 final), European Commission, Brussels, Vol. 14, 9, 2016.

14. Fiber-To-The-Home TOP 100 Broadband Communities Magazine, Fiber-to-the-home leaders and innovators for 2018, A BBC Staff Report, Jul. 2018.

15. #Broadband2022 — Unlocking a trillion dollar digital economy, Confederation of Indian Industry, Ernst & Young LLP Report, 2018.

16. ITU-T Recommendation G.652, Characteristics of a single-mode optical fibre and cable, International Telecommunication Union, Telecommunication standardization sector of ITU, 1–17, 2016.

17. Senkans, U., S. Spolitis, and V. Bobrovs, "Evaluation and research of FBG optical temperature sensors network," *Advances in Wireless and Optical Communications (RTUWO)*, 79–89, Riga, 2017.

18. ITU-T Recommendation G.694.1, Spectral grids for WDM applications: DWDM frequency grid, International Telecommunication Union, Telecommunication standardization sector of ITU, 1–7, 2012.

Senkans U., **Braunfelds J.**, Spolitis S., Bobrovs V. Research of FBG Optical Sensors Network and Precise Peak Detection. 2018 Advances in Wireless and Optical Communications (RTUWO), Riga, **2018,** pp.1-5.

Research of FBG Optical Sensors Network and Precise Peak Detection

Ugis Senkans, Janis Braunfelds, Sandis Spolitis and Vjaceslavs Bobrovs

Institute of Telecommunications
Riga Technical University, Riga, Latvia
ugis.senkans@edu.rtu.lv, janis.braunfelds@rtu.lv, sandis.spolitis@rtu.lv, vjaceslavs.bobrovs@rtu.lv

Abstract—**In this paper research of optical fiber Bragg grating (FBG) temperature sensors network is made and new effective sensors' signal peak detection algorithm is proposed. Primary research was carried out at the Fiber Optical Transmission Systems laboratory of Riga Technical University. First, the parameters of available commercial optical FBG temperature sensor was experimentally measured and by using RSoft OptSim simulation software, the acquired data was further examined in developed simulation model of fiber optical transmission system. Secondary, Mathworks Matlab software was used, where research on minimal allowable spacing (guard band) of sensors' signals was investigated and new precise peak detection algorithm was created. The optical sensors network created in simulation environment was combined with 8-channel intensity modulated wavelength division multiplexed (WDM) data transmission system, where one shared 20 km long ITU-T G.652 single mode optical fiber was used for both – transmission of data and sensors signals. As market forecasts implies steady growing need for different kind of fiber optical sensors in the near future, brief analysis was made evaluating these trends and forecast for FBG sensors usage in the given field. Connection between fiber optical sensors and internet of things (IoT) concept was also evaluated.**

Keywords— fiber Bragg grating (FBG), fiber optical sensors, peak detection, internet of things (IoT), guard band, wavelength division multiplexing (WDM), passive optical network (PON), digital signal processing.

I. INTRODUCTION

Fiber optical sensors are widely used for different kinds of measurements, for example, to measure temperature, pressure, strain, vibration and mechanical deformation. Optical sensors based on Fiber Bragg grating (FBG) technology is one of the most promising sensors type, and is commonly used mainly due to its significant advantages that provides immunity to electromagnetic interference and RF interference, small size, high sensitivity, remote sensing capabilities, etc. [1].

Although important advantages, FBG optical sensors have some disadvantages that can be caused by crossed sensitivity providing incorrect measurements of temperature or strain. Risk factor can also be areas with high temperatures as well as places with increased characteristics of trembling or vibration near the optical sensors [1]. More detailed look about FBG optical sensors structure and working principles are evaluated in our previous publication [2].

From recent years till now the world's demand for fiber optical sensors is continuously rising and it is complicated to evaluate and predict precise market forecast. One of the main factors for such phenomena is the diversity of the market which consists of wide variety of applications, technology and new industrial inventions. Analyzing current trends of fiber optical sensors market, specifically highlighting FBG, it is shown that three main segments lead the supply and demand in fiber optical sensors. Firstly, sensing devices – FBG as technology for sensing applications. Secondly – instrumentation, for example, software, graphical interfaces, acquisition systems and interrogation devices. Thirdly comes systems integration and installment services, for instance, engineering projects [1]. From variety of reports related to fiber optical market, newest statistics shows average annual growth or sensors market in range of 4.41% to 10.5%. Present calculations provides that global consumption value of fiber optical sensors by 2020 will consist of 1.3 billion US dollars for discrete optical sensors (discrete sensors work as a specific part of fiber) and 3.2 billion US dollars for distributed sensors, where the entire fiber can be used as sensors [3].

With enhancement of optical networks infrastructure and growth of devices using available bandwidth spectrum for data transmission and communications, there is a significant increase in need for bandwidth effective optimization [4]. Therefore, one of the key elements in sensor networks is effective choice of minimal channel spacing to keep spectral efficiency of sensor network high as possible, in the same time ensuring precise detection of sensors' signal peaks, which are representing the changes in measured physical value, e.g. temperature, strain, etc.

II. IMPLEMENTATION OF FIBER OPTICAL SENSORS IN IoT

Nowadays majority of world's governments in Asia, Europe and America agree that Internet of Things (IoT) is an area of potential growth and different kinds of innovations. Possible IoT application areas consists of Smart Industries, environmental protection and public safety. Creating connection between Internet Protocol and devices such as sensors to communicate with each other as well as provide control mechanism, makes the way for intersection of IT-oriented networks applications more perspective. Forecast shows that by 2020, more than 30 billion connected devices or applications will be intermittent with 200 billion connections worldwide [5]. At a given moment, architecture of IoT is described in five and three layer levels, such as application platforms, middleware platforms, backbone network, access network and sensor network. Sensing level or layer is made of different types of control modules, for example, sensor networks that consist of particular temperature, vibration, strain and other kind of sensors. The main information is collected in the perception level and sensing layer comprises a data acquisition as well as short-distance transmission where data and information is collected via sensing devices and later passed to the particular gateway by bus or short-distance wireless transmission technology [6].

IoT industry mostly includes a network of information sensing equipment that is combined with Internet and its content. Moreover IoT is associated with radio frequency identification (RFID), GPS, sensors and information sensing devices, as well as laser scanners. This is performed according to the accepted protocol that provides connection to the internet for communication and information exchange in order to establish tracking, location, monitoring, identification and management. Given the fact that IoT sphere grows a closer connection with fiber optical sensors, it is necessary to evaluate and research different kind of aspects in fiber optical sensing applications. To do so, it would be required to research minimal guard band effective optimization as well as more precise signal peak finding detection appropriately to the needs of IoT applications and devices [7].

III. SIMULATION SETUP

Main simulation setup was created in OptSim software while using the measured parameters from commercial FBG optical sensors (Fig 1). One of the main goals was to create operating simulation model that provides successful FBG optical temperature sensors network collaboration with 8-channel data transmission system to observe temperature effect on sensors' signals (signals reflected from deployed FBG sensors) as well as, to observe and calculate minimal channel spacing (guard band) and propose peak detection algorithm. Our data transmission system use non-return-to-zero on-off keying (NRZ-OOK) modulation scheme. In the service provider's side optical line terminal (OLTs) is located, where eight 10 Gbit/s transmitters are implemented. Every transmitter's structure includes continuous wave (CW) laser with output power +3 dBm, 10 Gbit/s Pseudorandom binary sequence (PRBS) data source, NRZ driver and optical Mach-Zehnder modulator (MZM) with 20 dB extinction ratio and 3 dB insertion loss [8]. Central frequencies for these eight data channels are set as following: 192.90, 192.95, 193, 193.05, 193.1, 193.15, 193.2, 193.25 THz. Here the channel spacing is set to 50 GHz, according to the ITU-T G.694.1
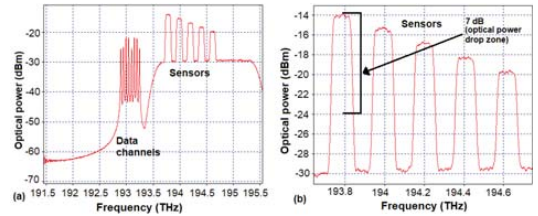
Fig. 2. (a) Simulated spectrum of 5 FBG optical sensors central reflected signals and 8 data channels (OSA spectrum located in optical sensors interrogation unit) at 0°C environment temperature, and (b) zoomed spectrum of 5 FBG optical sensors central reflected signals.

recommendation. All 8 of these data transmission channels are then combined by optical coupler (MUX(1)) for further transmission[2,9,10].

In sensors network, on the other, hand light emitting diode (LED) was used as a light source. Its spectrum region is within range of 193.7 THz to 195.3 THz where FBG optical will be deployed. The spectrum of LED source was acquired by firstly measuring it within RTU Fiber Optical Laboratory and then importing the experimental data into our simulation model. Spectral intensity fluctuations in this frequency region are relatively small – less than 0.37 dB and output power is set to -9 dBm. This LED signal is then filtered by optical bandpass filter (it will be further used as a seed light for optical FBG sensors) and sent to the optical signal coupler (MUX(2), where it is coupled with 8 data signals from OLT, see Fig. 1. Optical circulator is used for separation of signals transmission directions - separate sensors' (FBGs) reflected signals from transmitted data signals and seed light. On the bottom part of the transmission scheme there is optical distribution network (ODN) with 5 deployed optical FBG temperature sensors. All single mode optical fiber (SMF) line is divided into five fiber sections with 4 km distance between every sensor. Such distance is commonly used in Latvia between fiber optical cable cabinets or manholes, where fiber optical closures are located [2].
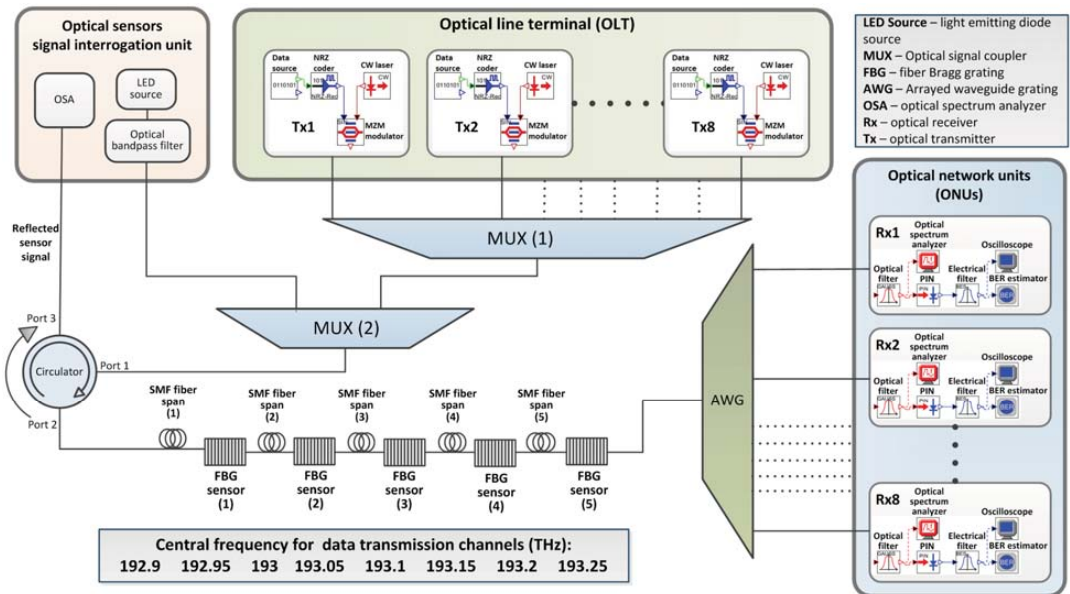

Fig.1. Realized combined 5 FBG temperature sensors network integrated into 8-channel 10 Gbit/s NRZ-OOK dense WDM-PON transmission system.

Initial central frequencies of FBG optical sensors were set as following: 193.8, 194, 194.2, 194.4, 194.6 THz starting from the first till last sensor. Such frequencies were chosen taking into consideration the ITU-T recommendations (as in case of data signals) and occupied spectrum of implemented 10 Gbit/s downstream data transmission channels to ensure stable operation of combined sensor and data channel system. Last part of the simulation model consists of the arrayed waveguide grating (AWG) model including Gaussian bandpass optical filters with Gaussian shape frequency response to filter out data channels and 10 Gbit/s optical network units (receivers) with electrical 7.5 GHz Bessel low-pass filters and scopes [2]. Such combined scheme provides coexistence of two previously mentioned systems. As we observed in investigated optical sensor network model, influence of WDM data channels on sensor signals was negligible, causing only a slight increase in noise. However to make it more resource effective it is vital to observe and calculate minimal channel spacing or frequency guard band between FBGs' signals or channels. This aspect is investigated further in this paper.

IV DEVELOPMENT OF ALGORITHM FOR PRECISE FBG SIGNAL INTERROGATION

When one's sensor optical power level is similar to another one's, and they are located relatively apart from each other in the spectrum, then it is possible to use different kind of methods to achieve the needed results for guard band acquisition. However there are complications in real cases where every next FBG optical sensors' reflected signal weakens with time and distance (due to fiber attenuation and insertion loss of optical elements) within given system model (Fig 2). Therefore, authors propose a solution created within Matlab software. Full flowchart of our work structure and sensors' signal processing is shown in Fig. 3. In this figure it is possible to see our research process from the starting point with creation of our Optsim simulation scheme as well as acquisition of variation of frequencies. Then a customized Matlab code for such parameter calculations is created. While
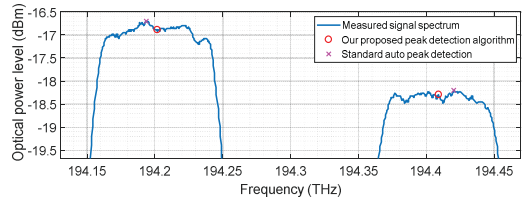

Fig. 4. Comparison between our acquired average peak and auto peak detection for 3rd and 4th FBG optical sensors.

using approximation method we created linear equation and calculate yet more appropriate variation of frequency. With this, a creation of minimal guard band equation is made from where it is next possible to calculate minimal guard bands for power drop zones what was also one of the main goals during this research. Furthermore we investigated peak frequency calculations for sensors and by updating Optsim simulation scheme with new adjustments we were able to create Matlab code for precise sensors average peak finding algorithm what was another goal that needed to be achieved. With that it was possible to compare peak frequencies with different algorithms thereby compare minimal guard bands for power drop zones. More detailed look is discussed in further paragraphs.

To determine precise guard band between FBG signals, it is necessary to detect an exact signals peak center and vice versa, which is not always the highest value in a peak region. In this case, every commonly used algorithms of peak finding does not achieve the needed result, see Fig. 4. Due to irregularity of reflected spectra of FBG sensors, it is not an easy task to detect exact center of reflected peak. For this matter we created algorithm within Matlab software where we imported data about sensors signals from OptSim simulation scheme discussed in this paper. This algorithm allowed us to process spectrum data of each sensor and detects exact average center frequency of each sensor's reflected signal, please see Fig. 4.
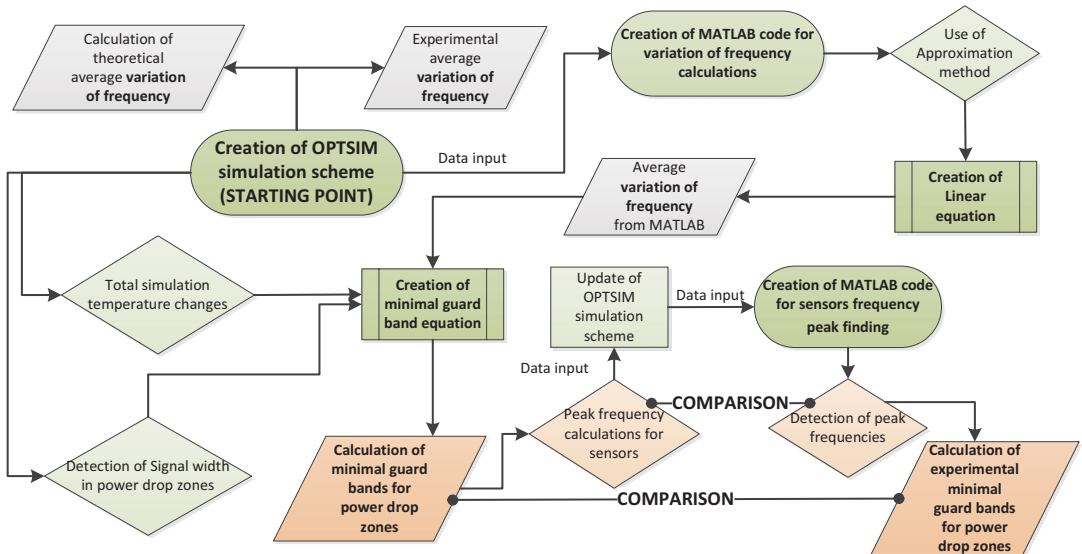

Fig. 3. Flowchart of our process through creation of simulations and experiments, as well as development of equations, calculations and comparison analysis.

141

Reflected FBG signal peaks were detected at relative peak power level equal to 0.9. Our approach is similar to the one widely used for measurement of pulse width – well known full width at half maximum (FWHM) method. By using our method, we improved our FBG signals interrogator accuracy and excluded wrong detection of signals peaks due to power fluctuations.

V. SIMULATION AND EXPERIMENT RESULTS

Precise minimal channel spacing (guard band) evaluation and calculation as well as peak detection using different methods was important part of this research. Manufacturer of experimentally used FBG fiber optical temperature sensor stated that the calibrated frequency of this sensor at +26°C is 191.537130 THz and basis on manufacturer data (temperature to wavelength response) it was calculated that variation of frequency for one degree Celsius is 1.279 GHz.
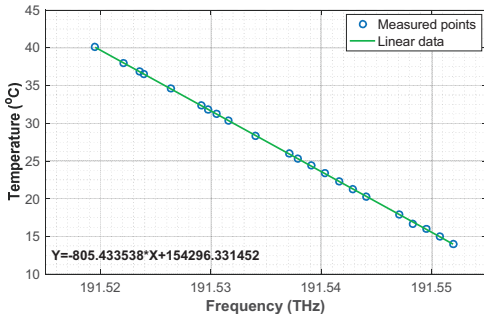
Fig. 5. Acquired data about correlation between temperature and frequency by using approximation method and calculated linear equation for commercial fiber optical temperature sensor.

To compare theoretical temperature sensor's response with experimental, firstly in laboratory we heated it, then measured wide variety of reflected signal central frequencies in the temperature range between +14°C till +40°C. By comparing each and every reflected FBG's central frequency with manufacturer's calibration data, we achieved that the experimental average variation of frequency for one degree, relative to calibrated, and is 1.232 GHz. For the further analysis we used Matlab software and through signal approximation method we acquired linear equation that defines temperature and frequency correlation (response) for the optical fiber temperature sensor, please see Fig.5.

From the acquired linear equation we specified average variation of frequency for one degree which was 1.231 GHz. Given that, it is clear that this is the precise variation of frequency for one degree due to gained similar results of each method using data provided by manufacturer and our measured experimental temperature/frequency response data. For detection of guard band or minimal channel spacing between sensor signals this value was a crucial factor.

Afterwards, the next value needed, in this case of 5 optical sensors was the average spectral width of sensors signal in the optical power drop zone of 7 dB, please see Fig. 2. Such values were acquired by solving equation that was introduced in our previous research [11] for detection of guard bands between sensor signals in spectrum. From our calculation the average sensors reflected signal spectral width in the optical power drop zone of 7 dB is 109.8278 GHz. Knowing that total temperature change range in this case is planned over

80°C (from -20°C to +60°C, typical to structural health monitoring (SHM) applications) and acquiring frequency change per one degree as well as signal spectral width, it was possible to compose our equation to determine theoretical minimal channel spacing or guard band between each and every optical sensor in our system:

$$GB = bw_{avg} + (T_{tot} * f_{var}), \qquad (1)$$

where GB (GHz) is the guard band, bw_{avg} (GHz) is the average sensors reflected signal spectral width in the optical power drop zone level, T_{tot} (°C) is the total temperature variation range and f_{var} (GHz) is variation of frequency for one degree (temperature response). After calculating guard band, it was possible to define, by this first method, acquired FBG optical sensors central reflected signal frequencies with the minimal guard band or channel spacing. The acquired results are shown in table I that is also visible as *Method 1* in table II.

TABLE I CALCULATED FBG OPTICAL SENSORS CENTRAL PEAKS' FREQUENCIES AND GUARD BAND FOR BOTH OPTICAL POWER DROP ZONES

Values in **THz**	Power drop zone: **7 dB**
Sensor 1	193.800000
Sensor 2	194.008285
Sensor 3	194.216570
Sensor 4	194.424854
Sensor 5	194.633139
Guard band:	**0.208285**

Knowing these peak frequencies, we estimated yet another guard band. For this instance we based our comparison on optical power drop zone of 7 dB. The acquired results are shown in table II. Where *Method 1* contains data of estimated peak frequencies and guard band using previously discussed equation. On the other hand, *Method 2* includes estimated peak frequencies that are also visible in Fig 6, as well as their guard band.
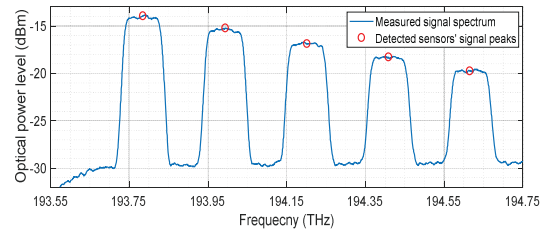

Fig. 6. Guard band detection using MATLABs algorithm for precise sensors reflected signal peak middle finding.

TABLE II CALCULATED FBG OPTICAL SENSORS CENTRAL REFLECTED SIGNAL FREQUENCIES AND GUARD BANDS USING BOTH METHODS

Values in **THz**	**Method 1**	**Method 2**	**Difference**
Sensor 1	193.800000	193.784834	0.015166
Sensor 2	194.008285	193.994201	0.014084
Sensor 3	194.216570	194.201185	0.015385
Sensor 4	194.424854	194.409212	0.015642
Sensor 5	194.633139	194.615817	0.017322
Guard band:	**0.208285**	**0.207746**	**0.000539**

142

Compared to Method 1 the Method 2 data consists of our calculated optical sensors average signal peaks that are detected by adjusted algorithm that we created specifically to achieve average signal peaks despite the spectrum fluctuations. From this guard band values can also we estimated and compared.

From our calculations it is clear that such Matlab algorithms can be implemented in real optical FBG sensors interrogation units to detect the location of signal peak central frequency, as seen in table II, *Method 2*.

VI. CONCLUSIONS

Studies have shown that world is in constant demand for fiber optical sensors in wide variety of applications. The annual growth in market for such technology is increasing steadily with every year. One of the sections where fiber optical sensors are needed and will be further on, is IoT. From the authors' point of view, with time, even more applications that require Internet will be associated with fiber optical sensor technology due to the needs of consistent monitoring of different kind of systems that uses fiber optical sensors, for example, security and structural health monitoring (e.g. roads, their embankments, bridges, etc.) applications

Our research showed that it is possible to successfully integrate at least 5 FBG optical sensor network into 8-channel NRZ-OOK modulated 10 Gbit/s fiber optical data transmission system. In our research we used different kind of methods to acquire temperature/frequency response of available investigated commercial FBG sensor, which was used further in our mathematical simulation model. In this paper we developed guard band calculation equation, which allow calculating recommended frequency band between adjacent FBG sensors, to be sure that signals of deployed sensors will not overlap in spectrum. The data that we achieved shows consistency, as for example, guard band that we calculated by first method was 208.285 GHz while from our research within Matlab - a strong correlation can be seen, where guard band is detected as 207.746 GHz. That makes a total difference of only 0.539 GHz. We also showed different ways of estimating variation of temperature / frequency response. From our research it was 1.279 GHz, 1.232 GHz and 1.231 GHz, depending on the method or algorithm used.

We proved that with collaboration of two mathematical modeling and calculation software it is possible to find minimal allowable sensors guard-band and precise signal spectrum peak center. Although there are some signal peak finding solutions, nevertheless we created algorithm in Matlab by using Optsim input data to create solution that not only targets highest peak values but finds the exact middle of the peak.

Such possibility can be needed for different kind of signal processing applications in wide variety of fields. It is important that our developed FBG signal peak frequency detection algorithm can be implemented further in real FBG sensors signal interrogation solutions.

However, there is still opportunity for further research to test even smaller guard-bands and very attenuated sensors' signals in FBG optical sensor systems. This kind of research is vital for effective available spectrum usage in future. As with development of FBG sensor technologies, there will be need for further research on coexistence of sensing and data transmission systems in one shared optical network.

REFERENCES

[1] F.Bortolotti, K.Morais Sousa, J.Carlos Cardozo da Silva, "Packaging, characterization and calibration of the Bragg grating temperature sensors", pp. 1-5, 2012.

[2] U.Senkans, S.Spolitis. V.Bobrovs, "Evaluation and research of FBG optical temperature sensors network," pp. 1-4, 2017

[3] G.Allwod, G.Wild, S.Hinckley, "Fiber Bragg Grating Sensors for Mainstream Industrial Processes", pp. 1-14, 2017.

[4] Taylor & Francis Group, Optical Fiber Sensors – Advances Techniques and Applications, CRC Press, pp. 1-19, 91-93, 2015.

[5] O.Vermesan, P.Friess, "Internet of Things: Converging Technologies for Smart Environments and Integrated Ecosystems", pp. 15-26 ,2013

[6] W.Zeng, H.Gao, "Optic Fiber Sensing IOT Technology and Apllication Research" pp. 16-21, 2014.

[7] Y.Wang, "Application of optical fiber sensor technology in building Interner of things", pp. 1-5, 2014.

[8] S. Spolitis, V. Bobrovs, G. Ivanovs, "Investigation of high-speed AWG filtered spectrum-sliced WDM PON system," 8th International Symposium on Communication Systems, Networks & Digital Signal Processing (CSNDSP), pp.1-4, 2012.

[9] ITU-T Recommendation G.694.1, Spectral grids for WDM applications: DWDM frequency grid, International Telecommunication Union, Telecommunication standardization sector of ITU, pp. 1-7, 2002.

[10] S. Spolitis, V. Bobrovs, S. Berezins, G. Ivanovs, "Optimal Design of Spectrally Sliced ASE Seeded WDM-PON System," *15th International Telecommunications Network Strategy and Planning Symposium*: Conference Proceedings 2012, Italy, Rome, 15.-18. October, pp. 1-5, 2012.

[11] S.Spolitis, I.Lyashuk, V.Bobrovs, "Design and Performance Evaluation of FBG-based Temperature Sensors Network," pp. 1-6, 2017.

Braunfelds J., Spolitis S., Porins J., Bobrovs V. Fiber Bragg Grating Sensors Integration in Fiber Optical Systems, IntechOpen, **2020,** pp. 1-13.

Chapter

Fiber Bragg Grating Sensors Integration in Fiber Optical Systems

Janis Braunfelds, Sandis Spolitis, Jurgis Porins and Vjaceslavs Bobrovs

Abstract

Fiber Bragg grating (FBG) sensors are a progressive passive optical components, and used for temperature, strain, water level, humidity, etc. monitoring. FBG sensors network can be integrated into existing optical fiber network infrastructure and realized structural health monitoring of roads, bridges, buildings, etc. In this chapter, the FBG sensor network integration in a single-channel and multi-channel spectrum sliced wavelength division multiplexed passive optical network (SS-WDM-PON) is presented and assessed. The operation of both the sensors and data transmission system, over a shared optical distribution network (ODN), is a challenging task and should be evaluated to provide stable, high-performance mixed systems in the future. Therefore, we have investigated the influence of FBG temperature sensors on 10 Gbit/s non-return-to-zero on–off keying (NRZ-OOK) modulated data channels optical transmission system. Results show that the crosstalk between both systems is negligible. The successful operation of both systems (with BER < 2×10^{-3} for communication system) can be achieved over ODN distances up to 40 km.

Keywords: fiber Bragg grating (FBG) sensors, sensor network, WDM-PON, SS-WDM-PON

1. Introduction

Optical fiber sensors are classified as intensity, phase, polarization, and wavelength modulated sensors based on their operating principles [1]. Fiber Bragg grating (FBG) sensors are wavelength modulated sensors or sensors which detect physical parameter (strain, temperature, and others) based on wavelength changes. Fiber Bragg grating (FBG) technology typically is used in optical filters, dispersion compensation modules, and sensors solutions. FBG sensors are passive optical components with high sensitivity and immune to electromagnetic interference and radio frequency interference, which can be integrated into existing optical fiber network infrastructure for structural health monitoring (SHM) applications [2–4]. FBG sensors can be used for roads, tunnels, bridges, rails, aircrafts SHM, as well as civil engineering, security, oil, and gas solutions monitoring [5]. With FBG sensors, it is possible to monitor various physical parameters such as temperature, strain, vibration, pressure, humidity, etc. [6–8].

It is necessary to analyze sensor influence on deployed and operating fiber optical communications systems data channels before FBG sensors integration in this fiber optical network infrastructure. Optical sensors signal interrogation (OSSI) units maximal monitoring distance between monitoring equipment and FBG sensors can be longer than 40 km.

First, in this paper optical sensor and single–channel 10 Gbit/s transmission system compatibility and co-operation were experimentally evaluated in the fiber-optical transmission system (FOTS) laboratory of Riga Technical University, Communication Technologies Research Center (RTU SSTIC), as described in Section 2 of this article.

Further, we have also demonstrated the collaboration with 32-channel spectrum-sliced wavelength-division-multiplexing passive optical network (SS-WDM PON) data channels and FBG sensor network in the simulation environment, as described in Section 3 of this article. Results showed that the optical transmission system with SS-WDM PON data and FBG sensor channels is an energy and cost-efficient solution, because its transmitter part is realized using a single amplified spontaneous emission (ASE) light source.

2. Evaluation of compatibility and co-operation on fiber-optic FBG sensor and single channel 10 Gbit/s NRZ-OOK transmission system

In this section, FBG temperature sensor integration and co-operation with operating fiber-optical transmission system are experimentally evaluated in the laboratory environment. The transmitter part of the experimental setup (see **Figure 1**) includes a broadband light source - ASE source, which is necessary to provide the operation of the deployed FBG sensor.

The measured output spectrum of the ASE light source is shown in **Figure 2**. The maximal peak power of around −10 dBm is located in wavelength bands of 1532–1534 and 1550–1560 nm. The high output power of the ASE light source and FBG sensor reflectivity is essential when monitoring distance (between the OSSI unit and FBG sensor) is long. Broad spectral band and fixed output power of the light source spectrum are crucial for multiplexing many sensors.

The output of the ASE light source is connected with an optical bandpass filter (OBPF). An OBPF (wavelength range: 1530 to 1610 nm (C&L Band), crosstalk >50 dB, bandwidth: 0.2 to 10.0 nm) is used to filtered spectral band for FBG temperature sensor. The spectral band is calculated based on FBG sensor defined operating
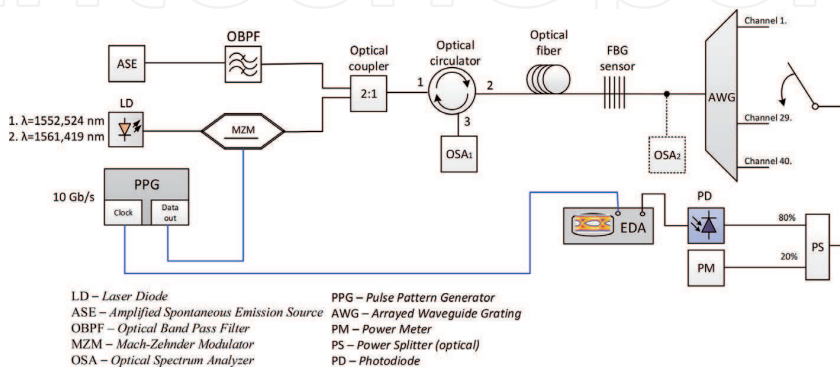
Figure 1.
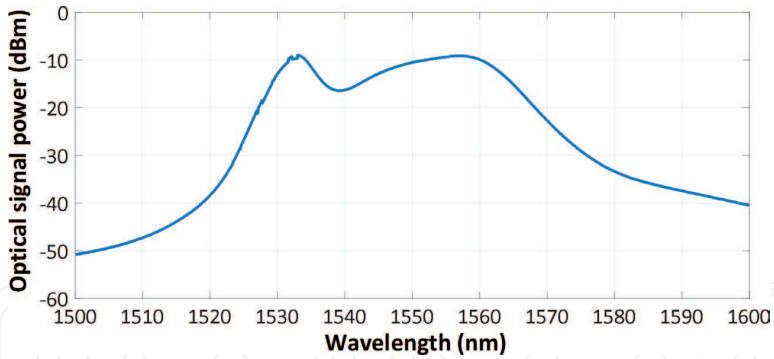*Experimental setup of single–channel 10 Gbit/s transmission system with integrated optical FBG sensor.*

Figure 2.
Measured ASE output spectrum.

temperature band (−20 to +40°C). Temperature change by one degree causes a wavelength shift of 10.174 pm, taking into account the FBG reference temperature of 26°C ($\lambda_{ref} = 1565.191\,nm$). Wavelength shift depends on thermal-expansion coefficient and the thermal-optic coefficient of common single-mode fiber.

Central wavelength and frequency values for FBG temperature sensors are shown in **Table 1**. The wavelength band from 1565.05 to 1565.66 nm are set as a bandwidth of OBPF. The measured spectral curve of the OBPF passband is shown in **Figure 3**. The output of OBPF is connected to one of the optical coupler ports.

For the generation of FOTS data channel signal, the tunable laser diode (LD) with +9 (fiber length 20 km) and 12 dBm (fiber length 40 km) output power, 100 kHz linewidth, 50 dB sidemode suppression ratio (SMSR) is used. LD output is connected with Mach-Zehnder modulator (MZM) with polarization-maintaining PANDA type

Temperature	Wavelength [nm]	Frequency [THz]
−20 °C	1565.66	191.48
26°C	1565.19	191.54
40°C	1565.05	191.55

Table 1.
FBG temperature sensor central wavelength and frequency values.
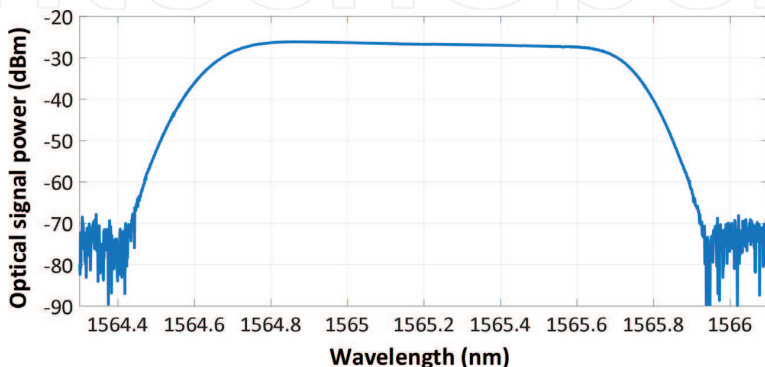
Figure 3.
Measured spectral curve of the OBPF filter passband.

fiber. Electrical data signals are generated by the pattern generator (PPG) (Anritsu, operating bitrate 10 Gbit/s, PRBS 2^{15}–1, signal purity –75 dBc/Hz). PPG data output and electrical RF input of the MZM is connected with proper RF cable. MZM optical output is connected with one of the optical power coupler (OPC) ports. OPC couples signals for FBG sensor and FOTS data channels.

OPC output is connected with the optical circulator (OC) port (1), necessary for separation of the sensor systems optical signal flows (transmitted and reflected). Please see the measured optical circulator insertion loss values in **Table 2**.

The optical circulator port (2) is connected with the optical fiber line and FBG sensor. 20 and 40 km long single-mode optical fiber (SMF-28) spools with insertion loss 4.3 and 8.3 dB are used in these experiments. The optical fiber output is connected with the FBG temperature sensor. FBG sensor structure and operation principle are shown in **Figure 4**.

FBG sensor technology is based on periodical reflection index changes in the fiber core [9–12]. FBG sensor reflects one part of the signal, but another part is transmitted further through the optical fiber. If the object's temperature changes, it shifts transmitted and reflected Bragg wavelength (λ_B), also known as signal central wavelength (see in **Figure 5**). OSA_1 and OSA_2 are used for the analysis of the FBG temperature sensor reflected and transmitted signals.

Bragg wavelength (λ_B) can be described by the following formula (1):

$$\lambda_B = 2 \cdot n_{eff} \cdot \wedge \tag{1}$$

Where:

$\wedge$ – grating period, nm;

n_{eff} – effective group reflection index;

λ_B – Bragg wavelength, nm [10].

FBG sensor temperature is calculated, based on the formula (2):

$$t = t_{ref} + \left(\frac{-\lambda_{ref} + \lambda_{mea}}{\Delta\lambda_{coe}} \right) \tag{2}$$

Where:

t_{ref} - reference temperature (defined in the sensor specification), $^{\circ}$C

λ_{ref} – reference wavelength (defined in the sensor specification), nm

λ_{mea} - measured wavelength value, nm

$\Delta\lambda_{coe}$ – wavelength coefficient, describing wavelength shift, when temperature is changed per 1°C (defined in sensor specification), nm

Temperature sensor parameters used in experiments are listed in **Table 3**.

Direction	Measured insertion loss (dB)
1→2	2
2→3	1
1→3	60

Table 2.
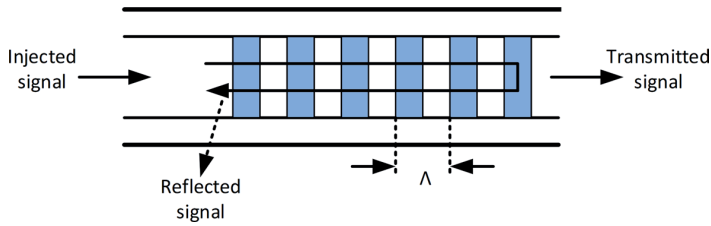*The insertion loss of experimentally used optical circulator.*
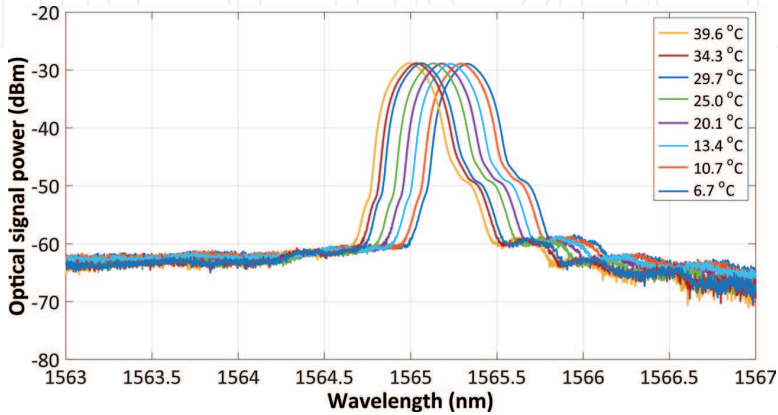
Figure 4.
FBG structure and operation principle.

Figure 5.
Measured reflected FBG sensor signal spectrum at different temperatures.

FBG sensor parameter	Value
Reference temperature (t_{ref})	26°C
Reference wavelength (λ_{ref})	1565.191 nm
Wavelength coefficient ($\Delta\lambda_{coe}$)	10.174 pm
Sensor size	3 × 3 × 23 mm
Operation temperature band	−40 °C to +80°C

Table 3.
Parameters of experimentally used FBG temperature sensor.

As we can see in formula 2, and the measured graph (**Figure 6**), the temperature versus wavelength relationship has linear nature.

FBG output is connected with 40-channel (100 GHz channel spacing) arrayed waveguide grating (AWG) flat-top filter with operating wavelength band 1530.334–1561.419 nm (192–195.9 THz). The AWG is used to test the system with different spacing between data and sensor channels. The AWG (with 54 GHz 3-dB and 132 GHz 20-dB bandwidth) 29th and 40th channels are used in experiments, and its parameters are listed in **Table 4**.

AWG output is connected with optical power splitter (20:80%), where 20% are used for signal power monitoring, but 80% are transmitted to photodiode (PD) (with sensitivity (1e-10 BER) = −20 dBm, operation wavelength range = 1280 nm–1580 nm and maximum output voltage = 350 mVp-p) that
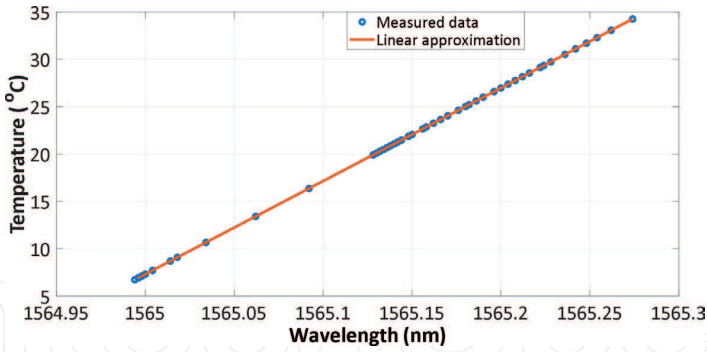
Figure 6.
Temperature versus wavelength relationship for experimentally used FBG temperature sensor.

No. of AWG Channel	Central wavelength [nm]	Frequency [THz]	Attenuation [dB]	
			min	max
29	1552.524	193.1	3.91	4.05
40	1561.419	192.0	4.28	4.41

Table 4.
AWG filter parameters 29th and 40th channel.

converts optical signal to electrical signal. PD output is fed through an RF cable to the eye diagram analyzer (EDA) for data signal quality analysis. For synchronization, the PPG clock signal is transmitted with RF cable to EDA.

Please see the measured FOTS data channel and FBG temperature sensor reflected spectrum in **Figures 7** and **8**, respectively. FBG temperature sensor reflected signal central wavelength is 1565.1279 nm, and the temperature (calculated with formula (2)) is 19.7°C.
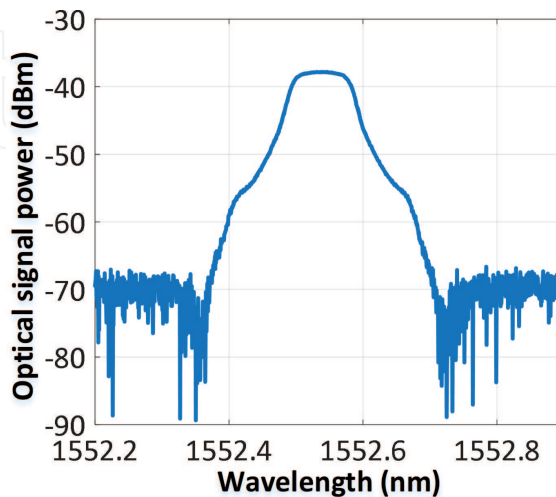
Figure 7.
Measured spectrum of transmission data channel.
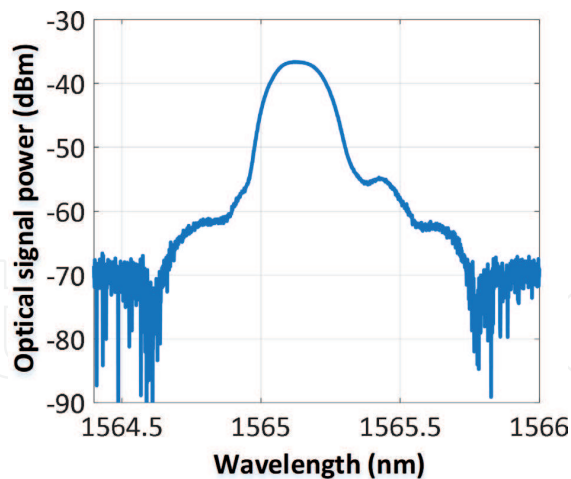
Figure 8.
Measured reflected spectrum of FBG temperature sensor.

Experimentally measured eye diagrams for NRZ-OOK modulated 10 Gbit/s FOTS (after 20 and 40 km long transmission) with and without integrated FBG temperature sensor are shown in **Figure 9**. As we can see in **Figure 9**, the data channel eye diagrams' quality is not degraded by the FBG sensor. Dispersion influence can be observed in eye diagrams (c, d) after 40 km signal transmission, which

(a) 20 km FOTS

(b) 20 km FOTS with integrated FBG temperature sensor

(c) 40 km FOTS

(d) 40 km FOTS with integrated FBG temperature sensor
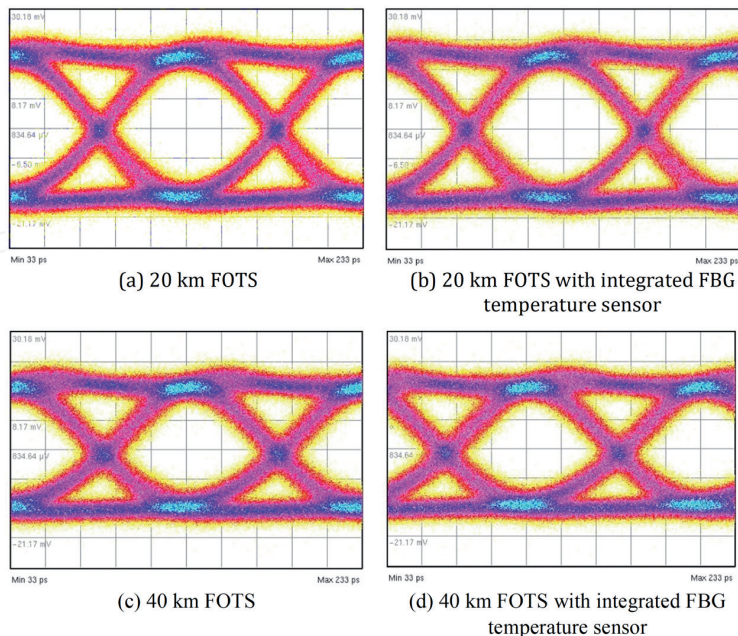
Figure 9.
Comparison of NRZ-OOK modulated 10 Gbit/s FOTS experimental eye diagrams. (a) 20 km FOTS. (b) 20 km FOTS with integrated FBG temperature sensor. (c) 40 km FOTS. (d) 40 km FOTS with integrated FBG temperature sensor.

can be prevented with chromatic dispersion (CD) compensation, such as dispersion compensation fiber (DCF).

3. Evaluation of combined FBG optical sensor network and 32-channel spectrum-sliced wavelength-division-multiplexing passive optical network system in simulation environment

The combined system's simulation setup with the FBG sensor network and SS-WDM PON data channels was developed within RSOFT OptSim software. The simulation setup is shown in **Figure 10**. In this system, only one shared broadband ASE light source is used. ASE spectrum was allocated in the spectral band between from 1533.47 to 1565.50 nm (in frequency band 191.5 THz and 195.5 THz). For SS-WDM PON systems, data transmission channels 1545.7 to 1558.2 nm.

(192.4 THz - 193.95 THz) spectrum was used, whereas 1537.4 to 1545.3 nm (194 THz - 195 THz) spectrum was used for optical FBG sensors network.

ASE light source is connected with an optical power splitter (50%:50%). One of the signal parts is transmitted to AWG MUX for data channel generation, but the second part to OBPF for sensor network. OBPF filtered spectral band from 1537.4 to 1545.3 nm (194 THz - 195 THz) for optical FBG sensor network. 32-channel AWG MUX is used in the setup, that filtered optical signal in the frequency band from 192.4 to 193.95 THz with 50-GHz channel spacing (according to ITU-T G.694.1 recommendation [13]) for 10 Gbit/s NRZ-OOK data channels transmitters. 3-dB bandwidth of each AWG's channel is set to 45 GHz. The data channels bitrate is set to 10 Gbit/s, considering 7% overhead for FEC encoding scheme application resulting in the total bitrate of 10.7 Gbit/s.

Each transmitter block consists of a semiconductor optical amplifier (SOA) to suppress intensity fluctuation noise coming from ASE and electro-absorption modulator (EAM) having immunity to signal polarization state (contrary to MZM). NRZ data signal is generated by data and NRZ component in simulation setup. 32 data channels are coupled with the AWG DEMUX block.

Additionally, DCF is used for dispersion pre-compensation. The transmission line dispersion coefficient is D = 16 ps/nm/km, but the total accumulated dispersion
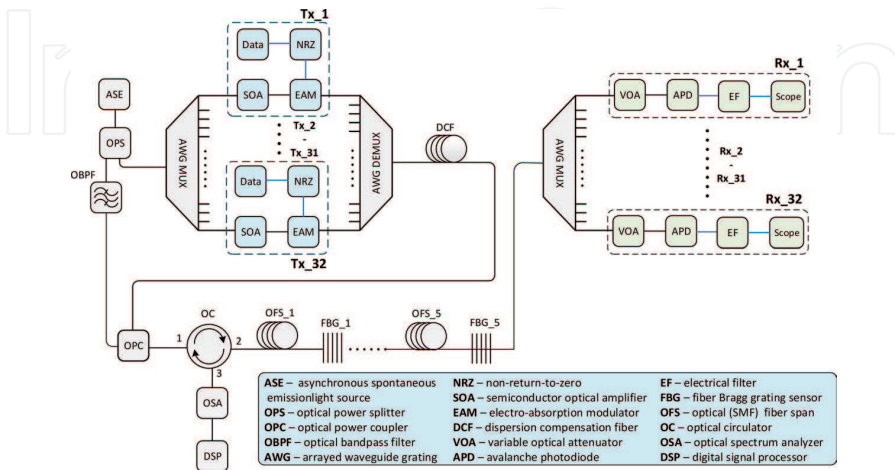

Figure 10.
Simulation setup of combined 32-channel 10 Gbit/s NRZ-OOK modulated SS-WDM-PON system with FBG temperature sensor network.

is 320 ps/nm. DCF fiber dispersion coefficient is −118.5 ps/nm/km, and the attenuation coefficient is α = 0.55 dB/km at 1550 nm reference wavelength. For total dispersion compensation, 2.7 km long DCF is used.

DCF fiber output is connected with one of the OPC input ports, but the second input port is connected with the OBPF output port. The coupled signal is transmitted to OC for separation of the sensor systems signal flows. OC port (2) is connected with 5 optical standard single-mode fiber (ITU-T G.652 recommendation [14]) spans (the length of each span is 4 km, insertion loss is 0.18 dB/km) and 5 FBG temperature sensors network (sensors central wavelength and frequency see in **Table 5**). The spectral band for operation in temperature band −40°C to +80°C (sensor parameters are listed in **Table 3**) is calculated for each sensor. FBG temperature sensor channel spacing is 200 GHz.

The FBG reflected signal from OC port (3) is transmitted to OSA for signal spectrum measurements. Central wavelength or frequency detection, and temperature value calculation are realized in a digital signal processor (DSP).

AWG MUX filtered signal of 32 channels is transmitted to the receiver block. Each receiver block consists of a variable optical attenuator (VOA), avalanche photodiode (APD), electrical filter (EF), and scope components. In this setup, VOA is used for SS-WDM-PON data channels' BER correlation diagram measurements. InGaAs APD (sensitivity set to −20 dBm at the reference BER of 10^{12}) converts optical signal to digital signal. Electrical Bessel low-pass filter 3-dB bandwidth is set to 6 GHz. The received signal quality is analyzed with the scope component, which measures signal eye diagrams and BER value.

FBG sensor's No.	Central wavelength (nm)	Central frequency (THz)
1	1544.53	194.1
2	1542.94	194.3
3	1541.35	194.5
4	1539.77	194.7
5	1538.19	194.9
Channel spacing	1.58	0.2

Table 5.
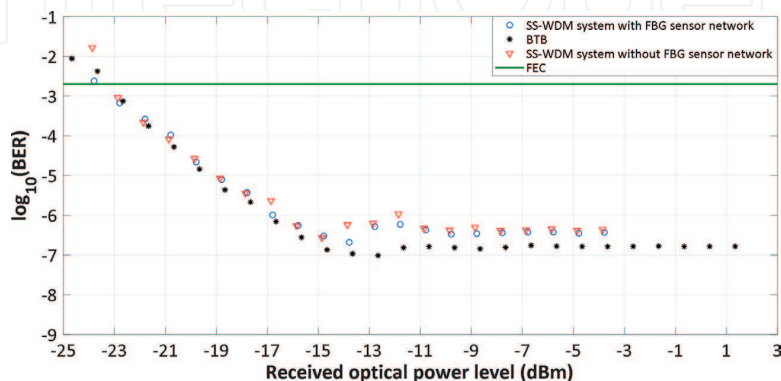*FBG temperature sensors central wavelength and frequency.*

Figure 11.
BER versus received signal power (BER correlation diagrams) for SS-WDM PON system with and without an integrated FBG temperature sensing network.

The 3rd data channel provided the lowest performance of the combined system (SS-WDM-PON data channels and FBG sensor network). Measured BER versus received signal power, known as BER correlation diagram, for SS-WDM-PON system with and without integrated FBG temperature sensing network is shown in **Figure 11**. BER correlation diagram is measured for the worst-performing (in terms of BER) channel of the SS-WDM PON data transmission system.

As we can see in the measured BER versus received signal power (**Figure 11**) graph, the FBG influence on SS-WDM-PON transmission data channels is minimal. FOTS system power reserve is 19.5 dB at the pre-FEC BER level of 2×10^{-3} [15]. The measured BER value of back-to-back (BTB) systems with SS-WDM PON data channels and FBG sensor network is 3.72×10^{-7}, but for back-to-back (BTB) system 1.65×10^{-7}.

Based on the measured results, the calculated power penalty value (compared SS-WDM-PON system with and without integrated FBG temperature sensors network) is 0.5 dB at the pre-FEC BER level 2×10^{-3}.

4. Conclusion

In this research, we successfully demonstrated FBG temperature sensor integration in FOTS experimentally, but the combined system with FBG temperature sensor network and 32-channel spectrum-sliced wavelength-division-multiplexing passive optical network were realized in the simulation environment. The simulation model is based on one shared amplified spontaneous emission source. As shown in **Figures 9** and **11**, FBG sensors do not degrade data channel signal quality.

The measured BER value for the worst channel of a back-to-back (BTB) systems with SS-WDM-PON data channels and FBG sensor network is 3.72×10^{-7}, but for BTB system 1.65×10^{-7}. The FOTS systems power reserve is 19.5 dB at the pre-FEC BER level of 2×10^{-3}.

Acknowledgements

Conflict of interest

The authors declare no conflict of interest.

Data availability

The data used to support the findings of this study are available from the first author upon request.

Author details

Janis Braunfelds[1*], Sandis Spolitis[1], Jurgis Porins[2] and Vjaceslavs Bobrovs[2]

1 Riga Technical University, Communication Technologies Research Center, Riga, Latvia

2 Riga Technical University, Institute of Telecommunications, Riga, Latvia

*Address all correspondence to: janis.braunfelds@rtu.lv

IntechOpen

References

[1] Taylor & Francis Group. Optical Fiber Sensors – Advances Techniques and Applications. CRC Press. 2015. pp. 545. DOI: 10.1201/b18074.

[2] Fidanboylu K., Efendioğlu H. S.b. Fiber optic sensors and their applications. In: 5th International Advanced Technologies Symposium (IATS'09); 13-15 May 2009; Karabuk, Turkey. pp. 7.

[3] Senkans U., Braunfelds J., Lyashuk I., Porins J., Spolitis S., Bobrovs V. "Research on FBG-Based Sensor Networks and Their Coexistence with Fiber Optical Transmission Systems". Hindawi. Journal of Sensors. 2019. 6459387.DOI: 10.1155/2019/6459387.

[4] Marcelo M. Werneck, Regina C. S. B. Allil, Bessie A. Ribeiro and Fábio V. B. de Nazaré. A guide to Fiber Bragg Grating Sensors. In: Christian Cuadrado-Laborde editors. Current Trends in Short- and Long-period Fiber Gratings. IntechOpen. 2013, pp. 24. DOI: DOI: 10.5772/54682.

[5] Braunfelds J., Senkans U., Lyashuk I., Porins J., Spolitis S., Bobrovs V. Unified Multi-channel Spectrum-sliced WDM-PON Transmission System with Embedded FBG Sensors Network. In: (2019) Progress in Electromagnetics Research Symposium; 17-20 June 2019; Rome, Italy; 2019. pp. 3327-3333.

[6] Senkans U., Braunfelds J., Lyashuk I., Porins J., Spolitis S., Haritonovs V., Bobrovs V. FBG sensors network embedded in spectrum-sliced WDM-PON transmission system operating on single shared broadband light source. In: 2019 Photonics and Electromagnetics Research Symposium - Fall, PIERS - Fall 2019 – Proceedings; 17-20 Dec. 2019; Xiamen, China; 2019. pp. 1632-1639.

[7] Campanella C.E., Cuccovillo A., Campanella C., Yurt A., Passaro V.M.N. "Fibre Bragg Grating based strain sensors: Review of technology and applications". MDPI. Sensors. 2018. 18 (9). 3115. DOI: 10.3390/s18093115.

[8] Laffont G., Cotillard R., Roussel N., Desmarchelier R., Rougeault S. "Temperature resistant fiber bragg gratings for on-line and structural health monitoring of the next-generation of nuclear reactors". MDPI. Sensors. 2018. 18 (6). 1791. DOI: 10.3390/s18061791.

[9] Laferrière J., Lietaert G., Taws R., Wolszczak S., "Reference Guide fo Fiber Optic Testing" JDSU. pp. 172. 2012.

[10] Qiao X., Shao Z., Bao W., Rong Q., "Fiber Bragg Grating Sensors for the Oil Industry". MDPI. Sensors. 2017. 17 (3). 429. DOI: 10.3390/s17030429.

[11] Zhang M., Xing Y., Zhang Z., Chen Q. "Design and Experiment of FBG-Based Icing Monitoring on Overhead Transmission Lines with an Improvement Trial for Windy Weather". MDPI. Sensors. vol. 14, no. 12. DOI: 10.3390/s141223954.

[12] Qiao X., Shao Z., Bao W., Rong Q. "Fiber Bragg Grating Sensors for the Oil Industry". MDPI. Sensors. 2017. 17. DOI: 10.3390/s17030429.

[13] ITU-T Recommendation G.694.1, Spectral grids for WDM applications: DWDM frequency grid, International Telecommunication Union, Telecommunication standardization sector of ITU, 2012, pp. 1-7.

[14] ITU-T Recommendation G.652, Characteristics of a single-mode optical fibre and cable, Telecommunication Union, Telecommunication standardization sector of ITU, 2017, pp. 1-28.

[15] Spolitis S., Bobrovs V., Parts R.,
Ivanovs G. Extended reach 32-channel
dense spectrum-sliced optical access
system, In: Progress in Electromagnetic
Research Symposium (PIERS); 8-11
Aug. 2016. Shanghai, China; 2016. pp.
3764-3767.

Braunfelds J., Porins J., Spolitis S., Bobrovs V. Optisko sensoru signālu apstrādes iekārta ar integrētu optiskā laika apgabala reflektometra funkciju. Latvijas Republikas patents, LV15534, 11.12.2019.

(57) **Kopsavilkums:**

Izgudrojums attiecas uz telekomunikācijas nozari, konkrētāk uz optiskajiem sensoriem. Izgudrojuma mērķis ir izstrādāt sensoru signālu apstrādes iekārtu ar integrētu optiskā laika apgabala reflektometru, lai veiktu objekta tehniskā stāvokļa uzraudzību. Piedāvātā iekārta satur signāla apstrādes un analīzes bloku un optiskās pārraides līniju ar integrētu optisko FBG un intensitātes sensora tīklu. Izgudrojums atšķiras ar to, ka signāla apstrādes un analīzes bloks satur optiskā laika apgabala rekflektometru (1), superluminiscējošo diodi SLED (2) un optisko cirkulatoru (3), kā arī šķiedras Brega režģa FBG sensora atstarotā signāla centrālo frekvenču noteikšanai tika izmantots signāla centrālo frekvenču detektors (13). Izgudrojums spēj nodrošināt sensoru tīkla uzraudzību un ir savietojams ar viļņgarumdales blīvētām pasīvām optiskām piekļuves sistēmām.

1. zīm.
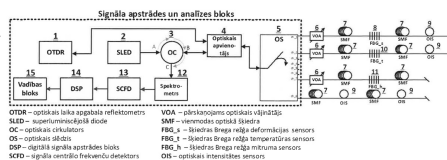
IZGUDROJUMA APRAKSTS

Tehnikas nozare

[001] Izgudrojums attiecas uz telekomunikāciju nozari, konkrēti uz šķiedru optisko sensoru risinājumiem. Izgudrojums var tikt lietots telekomunikāciju jomā, objektu tehniskā stāvokļa uzraudzībā (no angļu valodas *Structural Health Monitoring*, SHM), kā arī drošības risinājumos, t.sk. objekta perimetra uzraudzībā. Šķiedras Brega režģa (no angļu valodas *Fiber Bragg Grating*, FBG) sensori ļauj veikt ceļu, uzbērumu, aizsprostu, tiltu, dzelzceļa, ēku tehniskā stāvokļa uzraudzību, kā piemēram, momentāni identificēt plaisas un celtniecības defektus konstrukcijās, kamēr tie vēl ir nelieli, tādā veidā samazinot remonta izmaksas un būtiski veicinot autoceļu un ar tiem saistīto konstrukciju drošību. FBG sensori, atšķirībā no elektriskajiem sensoriem, kuriem ir nepieciešama elektrobarošana, ir pilnībā pasīvi, un šādi dažāda veida sensori (piemēram, deformācijas, temperatūras, mitruma, u.c.) var tikt izvietoti uz vienas optiskās šķiedras.

Zināmā tehnikas līmeņa analīze

[002] Par izgudrojuma prototipu izvēlēta FBG sensoru sistēma, kurā izmantots lineāra rezonatora šķiedras lāzers un optiskās šķiedras cilpas spogulis, lai nodrošinātu augstas jutības un relatīvi lētu sensoru sistēmu temperatūras un deformācijas uzraudzībai [1]. Sensoru sistēmas prototipa shēmā elektro-optiskā slēdza, optiskā apvienotāja, vadības iekārtas un šķiedras Brega režģa sensora komponentes ir kopīgas ar izgudrojuma iekārtu. Prototipa raidošā daļa sastāv no pumpējošā avota, Y tipa apvienotāja un ierosinošās erbiju leģētās šķiedras (no angļu valodas *Erbium Doped Fiber*, EDF) – optiskā platjoslas gaismas avota realizēšanai. Optiskais platjoslas signāls tiek pārraidīts caur X tipa optisko sazarotāju, optiskās šķiedras cilpas un polarizācijas kontroliera, no kura viena signāla daļa tiek pārraidīta līdz pirmajam FBG, bet otra signāla daļa līdz otrajam un trešajam šķiedras Brega režģim. Prototipā ir izmantoti divi fotodetektori, kas attiecīgi pielāgoti optiskās jaudas atstarojuma noteikšanai otrajam un trešajam FBG, kuru spēj nolasīt un noteikt vadības iekārta.

[003] Prototipa galvenais trūkums ir tas, ka radītāja daļā izmantotā erbija leģētā šķiedra (EDF) ne tikai darbosies kā ierosināmā vide platjoslas gaismas avotam, bet arī pastiprinās sensora atstaroto signāla spektru, kā rezultātā signāla raksturlīkne kļūs trokšņaina, dēļ EDF trokšņainās vides, kas var novest pie nekorektas informācijas ieguvi no sensora. Otrs būtisks trūkums ir tas, ka prototipā pēc pumpējošā optiskā lāzera nav iestrādāts optiskais izolators, kas novērš atstarotā signāla no optiskās šķiedras cilpas spoguļa nokļūšanu līdz lāzera avotam.

Optiskajam signāla nokļūstot līdz optiskajam lāzera avotam, tas var tikt neatgrieziniski sabojāts, kā rezultātā sistēma nefunkcionēs. Trešais būtiskais trūkums ir tas, ka prototipa sistēmas modelis ir pielietojams tikai sensoriem, kas balstīti uz optiskā signāla viļņa garuma izmaiņām, bet nav pielietojams sensoriem, kas balstīti uz intensitātes izmaiņām.

Izgudrojuma izklāsts

[004] Izgudrojuma mērķis ir izstrādāt sensoru signālu apstrādes iekārtu ar integrētu optiskā laika apgabala reflektometru (no angļu valodas *Optical Time Domain Reflectometer*, OTDR), lai veiktu objekta tehniskā stāvokļa uzraudzību ne tikai ar optiskiem FBG sensoriem, bet arī ar optiskajiem intensitātes sensoriem, un vienlaikus veiktu optiskā tīkla tehniskā stāvokļa uzraudzību. Šāda iekārta ir universāla, ērti lietojama servisa pakalpojumu sniedzējiem, samazina bojājumu novēršanas laiku, kā arī ļauj sensoru tīklā vienlaikus izmantot dažāda tipa sensorus, kas ir balstīti gan uz optiskā signāla viļņa garuma, gan intensitātes izmaiņām. Optisko sensoru signāla apstrādes iekārta nodrošina ilgtspējīgu sensoru darbību vismaz 20 km attālumā. Izgudrojums ir savietojams ar viļņgarumdales blīvētām pasīvām optiskām piekļuves sistēmām (no angļu valodas *Wavelength Division Multiplexed Passive Optical Network*, WDM PON), kas ļauj izmantot esošo šķiedru optisko tīklu infrastruktūru [2].

[005] Izgudrojuma iekārtas blokshēma ir attēlota 1. zīmējumā. Tā sastāv no sensoru signālu apstrādes iekārtas un optiskās pārraides līnijas ar ieintegrētu optisko FBG un intensitātes sensora tīklu. Izgudrojums atšķiras no prototipa ar to, ka sensoru signālu apstrādes iekārta ietver optiskā laika apgabala reflektometru (no angļu valodas *Optical Time Domain Reflectometer*, OTDR) (1), superluminiscējošo diodi (no angļu valodas *Superluminescent Light Emitting Diode*, SLED) (2), optisko cirkulatoru (3) un optisko apvienotāju (4) , kā arī FBG sensora atstarotā signāla centrālo frekvenču noteikšanai tika izmantots signāla centrālo frekvenču detektors (13).

[006] Sensoru signāla apstrādes iekārtas (SSAI) raidošā daļa sastāv no OTDR (1) un SLED (2). OTDR (1) ģenerē īslaicīgus optiskos impulsus pie 1625 nm centrālā viļņa garuma, un vienlaikus darbojas kā optiskais uztvērējs, analizējot atstaroto signālu. SLED (2) izstaro optisko signālu 55 nm plašā joslā ar centrālo viļņa garumu 1550 nm. SSAI ir izmantots optiskais cirkulators (3), kas sastāv no 3 portiem A, B, C un veic signāla plūsmu atdalīšanu. Optiskais cirkulators (3) atļauj pārraidi no A porta uz B portu un no B porta uz C portu. Taču signāls tiks bloķēts – novājināts (vismaz par 50 dB) no B porta uz A portu un no C uz A portu. SLED (2) un OTDR (1) ģenerētais signāls tika apvienots ar Y (50:50 %) tipa optisko apvienotāju (4). Optiskais slēdzis (5) sastāv no 8 fiziskiem kanāliem un veic pieslēgšanos katram kanālam konkrētā laika intervālā.

[007] Pie četriem optiskā slēdža (5) kanāliem ir pieslēgtas optiskās pārraides līnijas ar ieintegrētu optisko FBG un intensitātes sensoru tīklu. Optiskā slēdža (5) pirmajam kanālam (ch_1) ir pieslēgts signāla pārskaņojams optiskais vājinātājs (6), divas vienmodas optiskās šķiedras (SMF) (7) pārraides līnijas, šķiedras Brega režģa deformācijas sensors (8) un optiskais intensitātes sensors (9). Optiskā slēdža (5) otrajam kanālam (ch_2) pieslēgtas identiskas komponentes kā pirmajam, izņemot šķiedras Brega režģa deformācijas sensora (8) vietā ir pieslēgts šķiedras Brega režģa temperatūras sensors (FBG_t) (10). Attiecīgi septītais kanāls (ch_7) ir identisks otrajam kanālam tikai nesatur optiskās intensitātes sensoru (OIS) (9) un FBG_t (10) aizstāts ar šķiedras Brega režģa mitruma sensoru (11), bet astotais kanāls (ch_8) sastāv no diviem SMF (7) pārraides līnijas posmiem un diviem optiskās intensitātes sensoriem (9). OIS (9) ir ērti pielietojami sakaru kabeļu uzmavās (mitruma uzraudzībā) un ēkās (drošības risinājumos).

[008] SSAI uztverošā daļa sastāv no virknē saslēgta spektrometra (12), signāla centrālo frekvenču detektora (13), digitālā signāla apstrādes bloka (14) un vadības bloka (15). Spektrometrs (12) optisko signālu attēlo frekvenču apgabalā. Signāla centrālo frekvenču detektors (13) detektē optiskā signāla centrālo frekvenci pie signāla jaudas līmeņa koeficienta 0,9. Digitālā signāla apstrādes bloks (14) matemātiski aprēķina reālas sensora parametra (piem. temperatūra, deformācija) vērtības reālā laikā, izmantojot datus no signāla centrālo frekvenču detektora (13). Vadības bloks (15) satur programmatūru, kas ļauj veikt ārēju pieslēgšanos ar datoru un veikt iekārtas elementu, sensoru konfigurēšanu un nodrošina informācijas attēlošanu grafiskā formā.

[009] Izgudrojums ir paskaidrots ar šādiem zīmējumiem:

1. zīm. Optisko sensoru signālu apstrādes iekārta ar integrētu OTDR funkciju: optiskais laika apgabala reflektometrs (1), superluminiscējošā diode (2), optiskais cirkulators (OC) (3), optiskais apvienotājs (4), optiskais slēdzis (OS) (5), pārskaņojams signāla optiskais vājinātājs (no angļu valodas *Variable Optical Attenuator*, VOA) (6), vienmodas optiskā šķiedra (7), šķiedras Brega režģa deformācijas sensors (FBG_s) (8), optiskais intensitātes sensors (OIS) (9), šķiedras Brega režģa temperatūras sensors (FBG_t) (10), šķiedras Brega režģa mitruma sensors (FBG_h) (11), spektrometrs (12), signāla centrālo frekvenču detektors (SCFD) (13), digitālā signāla apstrādes bloks (no angļu valodas *Digital Signal Processing*, DSP) (14), vadības bloks (15).

2. zīm. FBG optiskā sensora darbības princips.

3. zīm. Nomērītā un aproksimētā FBG optiskā temperatūras sensora raksturlīkne diapazonā no 14,0 līdz 40,1 ºC.

4. zīm. Nomērītās signāla centrālās frekvences diviem FBG sensoriem pie standarta pīķa (pie maksimālas signāla jaudas) un izgudrojumā iestrādātā (pie signāla jaudas līmeņa koeficienta 0,9) detektēšanas algoritma.

Izgudrojuma īstenošanas piemēri

[010] Izgudrojuma realizācijai pie optiskā cirkulatora (3) porta A pieslēgta superluminiscējošā diode (2), bet pie porta B ir pieslēgts optiskais apvienotājs (4) (1.zīm.), kas apvieno divas signāla plūsmas. Pie optiskā apvienotāja (4) otras ieejas pieslēgts OTDR (1). Optiskā apvienotāja (4) izeja ir savienota ar optiskā slēdža (5) ieeju. Pie optiskā slēdža (5) izejas pirmā kanāla (ch_1) ir virknē pieslēgts pārskaņojams signāla optiskais vājinātājs (6), SMF (7) pārraides līnija, šķiedras Brega režģa deformācijas sensors (8), SMF (7) pārraides līnija un optiskais intensitātes sensors (9). Pārskaņojamā optiskā vājinātāja (6) signāla vājinājuma vērtība ir noteikta atkarībā no pirmā SMF (7) līnijas posma ienestā vājinājuma. SMF (7) līnijas posma un VOA (6) signāla summārajam vājinājumam jābūt vismaz 3 dB (šāds nosacījums jāievēro arī otrajam un septītajam kanālam). Ja SMF (7) līnijas posma vājinājums ir lielāks par 3 dB, tad signāla VOA (6) komponente nav jāizmanto. Pie optiskā slēdža (5) izejas otrā kanāla (ch_2) ir pieslēgts signāla VOA (6), SMF (7) pārraides līnija, (FBG_t) (10), SMF (7) un OIS (9). Optiskā slēdža (5) izejas septītā kanāla (ch_7) ir pieslēgts signāla VOA (6), SMF (7), (FBG_h) (11) un SMF (7). Optiskā slēdža (5) izejas ostotā kanāla (ch_8) ir pieslēgta SMF (7) pārraides līnija, OIS (9), SMF (7) un OIS (9). Pie optiskā cirkulatora (3) porta C pieslēgts spektrometrs (12). Spektrometra (12) izejā pieslēgts signāla centrālo frekvenču detektors (13) un tā izejā pieslēgts digitālā signāla apstrādes bloks (14). Pie DSP (14) izejas ir pieslēgts vadības bloks (15).

[011] SLED (2) platjoslas avota signāls (signāla joslas platums 55 nm) ir pārraidīts uz optiskā cirkulatora (3) A portu. No optiskā cirkulatora (3) porta A signāls plūst līdz portam B, no kura signāls ir pārraidīts līdz Y tipa (50:50 %) optiskā apvienotāja (4) ieejai. Optiskā apvienotāja (4) otrā ieejā ir ievadīti OTDR (1) īslaicīgi optiskie impulsi pie 1625 nm viļņa garuma. OTDR (1) tipiski var lietot arī pie 1550 nm viļņa garuma, taču pie šādas realizācijas, to nevar lietot, jo notiks spektrālā pārklāšanās. Lai lietotu OTDR (1) pie 1550 nm viļņa garuma nepieciešams pēc SLED (2) ievietot optisko joslas filtru. Optiskais apvienotājs (4) veic signālu apvienošanu pēc optiskās jaudas. Apvienotais signāls ir pārraidīts uz optisko slēdža (5) ieeju un optiskais sēdzis (5) veic pārslēgšanos no porta uz portu pēc iepriekš uzdota laika intervāla.

[012] Optiskais slēdzis (5) ir komponente, kas ļauj veikt 8 dažādu sensoru tīklu paralēlu uzraudzību reālā laikā. Konkrētā risinājuma optiskajam slēdzim (5) netiek noslogoti no trešā

līdz sestajam kanālam, bet iekārta spēj nodrošināt paralēlu darbību visiem 8 kanāliem. Pie OS (5) kanāliem pieslēgta VOA (6) komponente novājina optisko signālu, lai novērstu FBG sensora radīto dubulto atstarošanos. Optiskais signāls caur SMF (7) līniju tiek pārraidīts līdz FBG optiskiem sensoriem (8, 10, 11) un OIS (9). Pievadot uz FBG sensora platjoslas gaismas avota signālu, tad režģis atstaros šaurjoslas spektrālo komponenti, kas atbilst režģa Braga rezonanses viļņa garumam λ_B, bet pārējās viļņa garuma komponentes tiek pārraidītas tālāk (2. zīm.). FBG sensora darbojas lineāri – temperatūrai pieaugot par 1 grādu centrālais viļņa garums nobīdīsies par x pm, bet ja temperatūra pieaugs par 2 grādiem, tad $2 \cdot x$ pm (3. zīm.). FBG optiskā sensora darbību raksturojama ar sekojošu matemātiku izteiksmi [3]:

$$\lambda_B = 2 \cdot n_{eff} \cdot \Lambda, \qquad (1)$$

kur: λ_B – atstarotais viļņa garums (Brega viļņa garums), nm; n_{eff} – efektīvais grupas laušanas koeficients optiskai šķiedrai; Λ – režģa periods, nm.

[013] OIS (9) ir izveidoti uz makrolocījuma bāzes un balstīti uz signāla intensitātes izmaiņām. Optiskais signāls tiek atstarots no OIS (9) makrolocījuma vietas un tika apstrādāts un analizēts ar OTDR (1) komponenti. Veicot deformācijas mērījumus ar FBG sensoru, nepieciešams nodrošināt temperatūras kompensēšanu konkrētā objektā, kas ir realizēta otrajā (ch_2) kanālā ar FBG_t (10) sensoru. Tā kā otrais un septītais kanāls pie konkrētās realizācijas atrodas blakus, tad mituma sensoram temperatūras kompensācijai var izmantot otrā kanāla FBG_t (10) sensoru. Izgudrojums pieļauj arī vairāku FBG sensoru izvienošanu uz viena kanāla, kas ļauj 2 objektos nodrošināt, piemēram, ēkas drošības risinājumu, objekta mitruma, u.c. parametru uzraudzību. Gan FBG, gan OIS sensoru uzraudzībā ir analizēts atstarotais signāls. Atstarotais signāls no OS (5) tika pārraidīts uz optisko apvienotāju (4), kas konkrētā gadījumā darbosies kā sazarotājs, kas signālu sadalīs pēc jaudas divās vienādās plūsmās, no kura viena plūsma ir pārraidīta uz OTDR (1), bet otra uz OC (3). OTDR (1) uzkrāj un analizē atstarotos signālus un rezultātu attēlo reflektogrammā – signālu jaudas atkarībā no līnijas garuma. Tas ļauj ne tikai izmantot IOS (9) risinājumos, bet vienlaikus veikt optiskās līnijas tehniskā stāvokļa uzraudzību, piemēram, nosakot līnijas bojājuma vietu.

[014] OC (3) atstarotais signāls tika pārraidīts no porta B uz C, un nonāk spektrometrā (12), kas optisko signālu laikā pārveido frekvenču apgabalā – signāla spektrā. Nomērītais optiskā signāla spektrs tiek pārraidīts uz signāla centrālo frekvenču detektoru (13), kas detektē signāla centrālo frekvenci pie 90 % no signāla maksimālās jaudas (4. zīm.). Tā kā atstarotā signāla spektrs var būt nevienmērīgs un trokšņains, tādēļ centrālo frekvenču noteikšanai nedrīkst izmantot algoritmus, kas balstīt uz signāla jaudas pīķa noteikšanu (4. zīm.). Noteiktās centrālo frekvenču vērtības ir pārraidīta uz DSP bloku (14), kas matemātiski aprēķina reālas sensora

parametra (piemēram, temperatūra, deformācija, mitrums u.c.) vērtības un vizuāli attēlo atkarība no laika ar vadības bloka (15) palīdzību. Vadības bloks (15) nodrošina pieslēgšanos ar datoru un OTDR(1), SLED (2), visu FBG sensoru (8, 10, 11), spektrometra (12), SCFD (13) un DSP (14) konfigurēšanu.

Izmantotie informācijas avoti

1.	US patent 6,647,160 B1 - FIBER BRAGG GRATING SENSOR SYSTEM, 9 lpp., 2003.

2.	Senkans U., Spolitis S. and Bobrovs V., "Evaluation and research of FBG optical temperature sensors network," *2017 Advances in Wireless and Optical Communications (RTUWO)*, Riga, 2017, pp. 79-89.

3.	Qiao X., Shao Z., Bao W., Rong Q., "Fiber Bragg Grating Sensors for the Oil Industry," *Sensors* 2017, 17, 429.

PRETENZIJAS

1. Sensoru signālu apstrādes iekārta sastāv no optiskā slēdža (5), spektrometra (12), digitālā signālu apstrādes bloka (14), vadības bloka (15), kas atšķiras ar to, ka sensoru signālu apstrādes iekārta ietver integrētu optiskā laika apgabala reflektometrs (OTDR) (1), platjoslas superlumiscējošo diodi (SLED) (2), kas izstaro optisko signālu 55 nm plašā joslā (pie -3 dB signāla jaudas krituma) ar centrālo viļņa garumu 1550 nm, savukārt optiskā signālu (caurejošo un atstaroto) plūsmu atdalīšanai ir izmantots 3 portu optiskais cirkulators (3), kā arī FBG sensora atstarotā signāla centrālo frekvenču noteikšanai ir izmantots signāla centrālo frekvenču detektors (13).

2. Sensoru signālu apstrādes iekārta saskaņā ar 1. pretenziju, kas atšķiras ar to, ka sensoru signālu apstrādes iekārtā tiek izmantota platjoslas superlumiscējošā diode (SLED) (2), kas izstaro optisko signālu joslā no 1522,5–1577,5 nm (pie -3 dB signāla jaudas krituma), kas ir savienota ar 3 portu optisko cirkulatoru (3) optisko signālu plūsmu atdalīšanai, pie kura B porta pieslēgts optiskais apvienotājs (4), kas apvieno optiskos signālus no OTDR (1) un SLED (2), taču FBG optiskos sensora atstarotā signāla centrālo frekvenču noteikšanai ir izmantots signāla centrālo frekvenču detektors (13).

3. Paņēmiens, kuru realizē iekārta saskaņā ar 1. vai 2. pretenziju, kas ietver šādus secīgus soļus:

i.   parametra uzstādīšanu – sakonfigurēšanu platjoslas SLED (2) gaismas avotam un optiskā laika apgabala reflektometram (1) un optiskā signāla pārraides uzsākšanu;

ii. optiskais cirkulators (3) nodrošina SLED (2) signāla pārraidi virzienā no A uz B portu un no B uz C portu, taču bloķē (novājina par 50 dB, jeb 100000 reizes) signāla izplatību virzienā no B uz A portu un no C uz A portu;

iii. OTDR (1) un SLED (2) signālus apvieno ar optisko apvienotāju un pārraida uz optisko slēdzi, kura kanāliem ir pieslēgtas signāla pārskaņojamā optiskā vājinātāja (6), vienmodas optiskās šķiedras (7), optiskā intensitātes sensora (9) komponentes un šķiedras Brega režģa sensori (8, 10, 11), kuri veic deformācijas, temperatūras un mitruma mērījumus;

iv. vienmodas optiskās šķiedras (7) pārraides līnijas sensoru atstaroto signālu caur optiskā apvienotāja (4) un optiskā cirkulatora (3) komponentēm pārraida līdz spektrometram (12), kas optisko signālu attēlo optisko signālu frekvenču joslā – signāla spektrā;

v.   signāla centrālo frekvenču detektors (13) centrālo frekvenci aprēķina matemātiski, sasummējot optiskā spektra labā un kreisā pusē noteiktās frekvences vērtības (pie 90 % no maksimālās signāla jaudas) un izdalot summas vērtību ar divi, tad noteikto
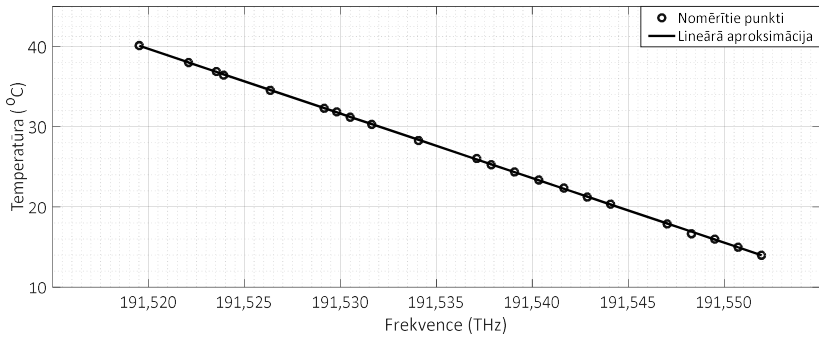
vērtību pārraida uz digitālā signāla apstrādes bloku (14), kas matemātiski nosaka reālās sensora parametra (piemēram, temperatūra, deformācija, mitrums u.c.) vērtības un grafiski, atkarība no laika, attēlo ar vadības bloka (15) palīdzību.
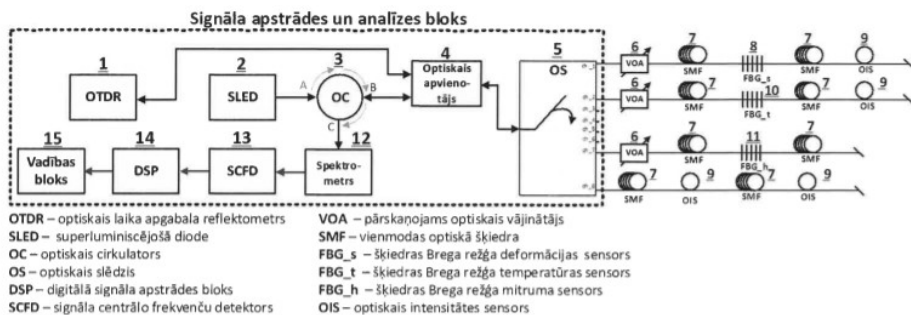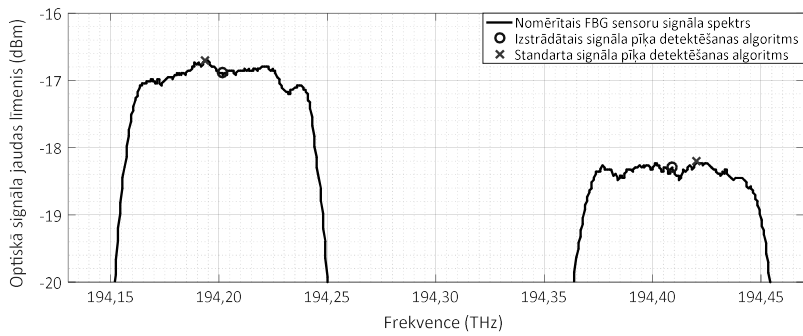
1. zīm.
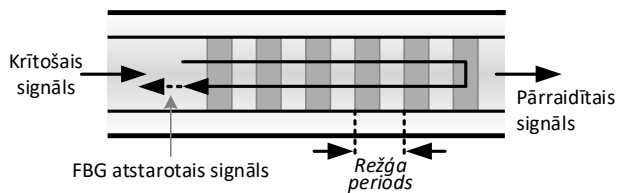
2.zīm.

3.zīm.

4.zīm.

Braunfelds J., Senkans, U., Skels, P., Janeliukstis, R., Salgals, T., Redka, D., Lyashuk, I., Porins, J., Spolitis, S., Haritonovs, V., Bobrovs, V. FBG-based sensing for structural health monitoring of road infrastructure, Journal of Sensors, **2021**, pp. 1-9.

Research Article

FBG-Based Sensing for Structural Health Monitoring of Road Infrastructure

Janis Braunfelds [1] **Ugis Senkans,[1] Peteris Skels,[2] Rims Janeliukstis,[3] Toms Salgals,[1] Dmitrii Redka,[1,4] Ilya Lyashuk,[1] Jurgis Porins,[1] Sandis Spolitis,[1] Viktors Haritonovs,[2] and Vjaceslavs Bobrovs[1]**

[1]*Institute of Telecommunications, Riga Technical University, Azenes st. 12, LV-1048 Riga, Latvia*
[2]*Department of Roads and Bridges Riga Technical University, Kipsalas st. 6B, LV-1048 Riga, Latvia*
[3]*Institute of Materials and Structures, Riga Technical University, Kipsalas st. 6B, LV-1048 Riga, Latvia*
[4]*Saint-Petersburg Electrotechnical University "LETI" (ETU), 5 Prof. Popova Street, Saint Petersburg 197376, Russia*

Correspondence should be addressed to Janis Braunfelds; janis.braunfelds@rtu.lv

Public road infrastructure is developed all around the world. To save resources, ensure public safety, and provide longer-lasting road infrastructure, structural health monitoring (SHM) applications for roads have to be researched and developed. Asphalt is one of the largest used surface materials for the road building industry. This material also provides relatively easy fiber optical sensor technology installment, which can be effectively used for SHM applications—road infrastructure monitoring as well as for resource optimization when road building or their repairs are planned. This article focuses on the research of the fiber Bragg grating (FBG) optical temperature and strain sensor applications in road SHM, which is part of the greater interdisciplinary research project started at the Riga Technical University in the year 2017. Experimental work described in this article was realized in one of the largest Latvian road sites where the FBG strain and temperature sensors were installed into asphalt pavement, and experiments were carried out in two main scenarios. Firstly, in a controlled environment with a calibrated falling weight deflectometer (FWD) to test the installed FBG sensors. Secondly, by evaluating the real-time traffic impact on the measured strain and temperature, where different types of vehicles passed the asphalt span in which the sensors were embedded. The findings in this research illustrate that by gathering and combining data from calibrated FWD measurements, measurements from embedded FBG optical sensors which were providing the essential information of how the pavement structure could sustain the load and information about the traffic intensity on the specific road section, and the structural life of the pavement can be evaluated and predicted. Thus, it enables the optimal pavement future design for necessary requirements and constraints as well as efficient use, maintenance, and timely repairs of the public roads, directly contributing to the overall safety of our transportation system.

1. Introduction

Public roads with asphalt surface material are typically considered as a structure that is exposed to the vibration, strain, and temperature impact on a daily basis. The dangers of underdesign of the road pavement lead to the permanent deformation and even collapsing of the road, which is resulted from significantly higher strain than accounted for in the initial design. Essentially, because the damage done to the roads might not be initially easily and visually observed as well as evaluated, it is important to detect the damage in the early stages of its development [1]. The most common failure modes in asphalt pavement include rutting, cracking, and subsidence [2] caused by channelized traffic and pavement overloading [3].

In order to save the resources and provide longer-lasting infrastructure, a structural health monitoring (SHM) paradigm is rapidly being adopted for the maintenance framework of civil infrastructure including but not limited to roads, buildings [1], bridges [4, 5], or slopes with landslide

possibilities [6]. It is achieved by ensuring a real-time observation and collection of an accurate measurement data related to the structural integrity of the monitored structure or component using transducer technologies. Within the SHM framework, it is possible to detect the damage or specific parameters of interest, initially allowing the responsible authority to react before any serious structural damage has propagated [4]. Thus, the urgency for SHM implementation with time has increased and still is nowadays. However, the complexity of pavement materials due to composition uncertainty, temperature sensitivity, viscoelasticity characteristics [2], and level of compaction [7] is an issue hampering the development of effective means for damage detection and monitoring of road structures.

Fiber optical sensors (FOS) are an effective tool adopted by civil, mechanical, and aerospace engineering communities for temperature and strain monitoring in different structures. Offering numerous advantages, such as multiplexing abilities, robustness, easy integration, lightweight, small size, passive nature, resistance to electromagnetic interference (EMI), and corrosion resistance, [8–10] is compared to the conventional electronic sensors. However, there are only few limitations—fragility of the bare sensors, high cost, and efficiency for transduction mechanisms, as well as interrogation systems complexity. These optical sensors can be integrated into public roads for continuous monitoring. Besides, with further research and commercialization, it is expected that at least some of the disadvantages are about to extinct in the near future [8]. A particular attention in the research community has been on fiber Bragg grating (FBG) optical sensors. In FBG technology, a periodic grating has been inscribed into an optical fiber [11]. The period of grating is influenced by strain and temperature of the surroundings enabling sensing of these physical quantities. According to the Fiber to the Home (FTTH) council organization [12], European governments have been improving their digital infrastructure plans in order to concentrate more on fiber and 5G technologies, leading to wider availability of public funds that are dedicated to enhancing fiber-based networks. This trend will lead to SHM applications to be more integrated within the fiber optical environment, thus using fiber optical sensors to remotely monitor, for instance, public roads and buildings. For example, by using the already deployed fiber optical infrastructure, the FBG sensor interrogation unit can be located 20 km or even further from the installed passive FBG sensors, while previously deployed optical lines can be used as a transport layer for the carrying of optical sensors' information.

Numerous studies exist on application of FBG sensors in monitoring of the roads. Several studies have been devoted to a design of appropriate encapsulation of bare fibers before integration into pavements as the fibers themselves are fragile and can easily break [13–15]. In [16], authors, firstly, applied a simple layer of an epoxy resin curing and toughening agents and, subsequently, provided a steel casing encapsulation ($E = 198$ GPa) for increased safety, as laying of pavement implies the use of a heavy (about 30 tons) road rollers. In [17], a special fiber-reinforced polymer with linear elasticity, good fatigue resistance, corrosion resistance, and lightweight

for encapsulation of FBG sensors was proposed. Authors argued that this kind of packaging ensures large enough measurement range, ease of application, good durability, long-term stability, and resistance to elevated temperatures. In [18], researchers developed a new FBG sensor encapsulation approach based on compliance of elastic modulus of FBG sensor packaging and surrounding asphalt pavement. This implies the use of low-modulus coatings for FBG optical fibers in order to prevent the strain field, as sensed by FBG sensors, from distortion. In [19], commercial solution from *Monitor Optics Systems* Ltd. was proposed, and it consisted of glass fiber composite optical sensing cable, in which several optical fibers can be embedded. The cable itself can reach several kilometers in length, and it can be tailored to enable a proper transfer of mechanical stresses from a structure to the sensor. It is compatible with epoxy resin adhesives for better surface bonding or embedment of sensors. The cable can also be surface treated for added protection regarding the environmental effects. The system was successfully deployed for highway pavement monitoring in Australia.

The performance of embedded FBG sensors within asphalt pavement was researched in studies [13–15]. Static tests of asphalt concrete specimens, with embedded FBG sensors, showed a linear relationship between wavelength shift and strain of the asphalt concrete thus satisfactory repeatability of the test [16]. The authors also studied the response of the sensors to understand the impact of loading heavy traffic under high speeds by simulating it with a drop hammer. The findings were that the relationship between the frequency of impacts and asphalt concrete strain can be approximated with a cubic function with a coefficient of determination equal to 0.9978. Two distinct phases were noticed in the growth of strain with increasing frequency of impacts—faster growth of cumulative plastic strain initially and a more stable growth in the later phase. Three FBG sensors were interconnected in a 3D manner for measuring strains in vertical and two transverse directions simultaneously [17]. This assembly was then embedded into highway pavement for strain monitoring. Researchers in [2] proposed a novel "self-healing" FBG optical sensor technology for pavement monitoring. This technology implies the use of self-repair sensor nodes that are based on the "smart" light switching where the light impulses are necessary for sensor operation and are still transmitted through the path, even if the sensors are damaged. FBG optical sensors can also be used in carrying out quality control of compaction of an asphalt pavement. This study was presented in [7]. For this purpose, the traditional FBG sensor was modified with a load-bearing plate. Fixing part and support legs were used for increased stability. This sensor was then embedded into an asphalt mixture. The differences between strain, as measured by this sensor, indicate the areas where asphalt is under compaction or over compaction. In [20], the FBG sensor network was employed to measure the hydrodynamic pressure of an asphalt pavement surface at different vehicle speeds. It was found that the correlation coefficient between the wavelength shift of the sensors and the pressure is 0.99, suggesting a solid application of an FBG sensor technology in the evaluation of hydrodynamic pressure at the surface of asphalt pavement. The

SLED– superluminescent light emitting diode
OC – optical circulator
OS– optical switch
DSP– digital signal processor

SMF– single mode fiber
FBG_s– fiber Bragg grating strain sensor
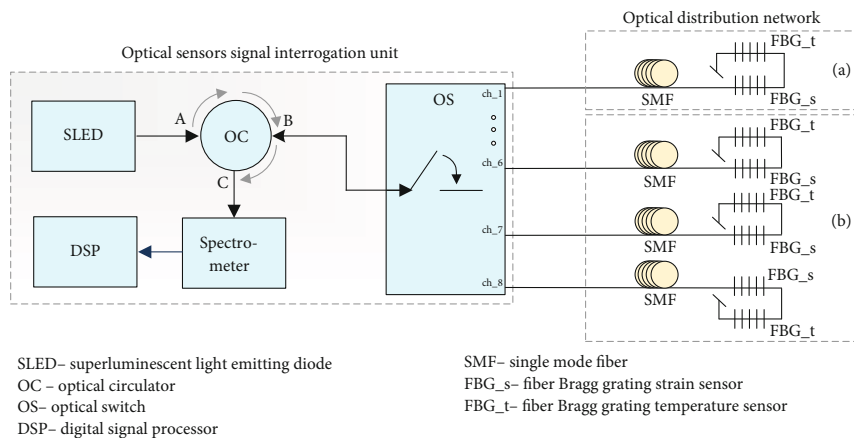FBG_t– fiber Bragg grating temperature sensor

FIGURE 1: The FBG optical sensor measurement system with optical sensor signal interrogation unit and optical distribution network.

TABLE 1: FBG sensor parameters.

Measured parameter	Strain	Temperature	Strain	Temperature	Strain	Temperature
Sensor's integration location	a	a	b	b	b	b
Central wavelength (nm)	1531.24	1565.19	1536.02	1560.22	1569.64	1549.80
Temperature range (˚C)	-20–60	-40–80	-20–60	-40–80	-20–60	-40–80

accumulated deformations in various layers of the asphalt (with FBG sensor network) at different temperatures were monitored in [3]. It was found that the accumulated deformation has a tendency to propagate from middle layers to deeper layers with increasing temperature, and also that, in general, the accumulated deformation increases with temperature for top and bottom layers, but not for the middle layers. This phenomenon was also observed and approved during this research, when strain parameters were measured in different seasons (shown in Section 3.1.). In [13], authors employed a novel FBG sensor laying technique for laying asphalt pavements. This implied a cross-sectional laying so that FBG sensors would simultaneously be capable of measuring strain in longitudinal and transverse directions. FBG sensors are known to have a drawback of not being able to effectively distinguish between strain and temperature field measurements if used as a single sensor. The potential solution to this problem is proposed in [21], where a reference grating sensor (for temperature measurements only) is combined with a dual-wavelength grating sensor, in which two FBG sensors are superimposed in order to discern between temperature and strain responses. Adding to that, research [22] shows that based on the FBG's strain and temperature sensing principles, dual FBG temperature compensation is important. While using two different fiber Bragg gratings that are inscribed into one optical fiber (where one is affected by strain and temperature, while the other one is strain isolated), it is possible to gather more accurate data, thus ensuring the possible solutions that can be appealing for a long-term structural monitoring system application. This method,

for distinguishing between strain and temperature, was also used in this research experiments. It can be further concluded that it is of paramount importance to develop reliable and effective mechanical strain monitoring technologies for asphalt pavement structures in order to, firstly, provide the means for early warning of deterioration of road quality and secondary—contribute to an accurate scientific basis to modify the existing scientific theories of asphalt mechanics.

In the current study, the FBG FOS was used for interconnected experimental scenarios as described in this paper. The first scenario deals with a falling weight deflectometer (FWD) to numerically and visually evaluate the response of the optical sensors that were integrated within the road that is being built. The second experimental scenario describes the integration of FBGs within the surface of the public road asphalt, where real-time traffic was observed, especially focusing on the heavy trucks that induce the highest strain in the pavement.

Further sections are organized as follows. Section 2 describes the experimental setup and scenarios with the falling weight deflectometer and real-time traffic monitoring. Results are presented in Section 3. Finally, conclusions are made, showing the methodology and future research directions.

2. Experimental Methods

The experiments described in the following subsections are very topical for Northern and Eastern Europe including Latvian road pavement designers in order to forecast the
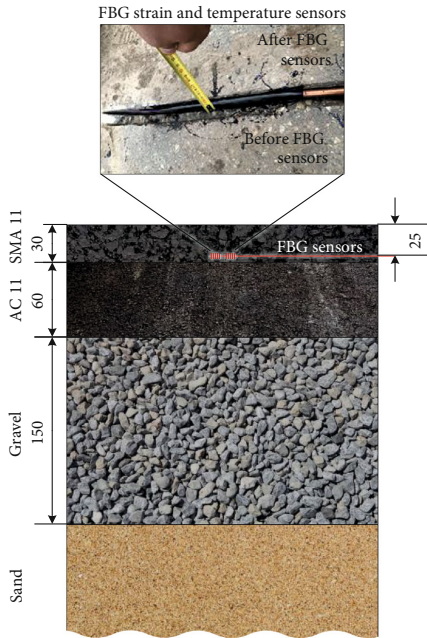
FBG strain and temperature sensors

FIGURE 2: The structure of road layers in location (a).

FIGURE 3: Embedded FBG sensors on the carriageway in the location (b).

structural integrity of the designed roads. Two different but interconnected experimental measurement scenarios involve using falling weight deflectometer (FWD) (for assessment of the FBG sensor operation) and measurements of the real-time strain traffic.

Both of the scenarios were realized as a field measurement by using the setup shown in Figure 1.

For our experimental research, it was necessary to plan the overall scheme of components and networks. Here, for both measurement scenarios, we used specially developed multichannel optical sensor signal interrogation unit that was used for processing of our acquired data regarding fiber optical sensor information during our research phases. Remote operation distance for optical sensor signal interrogation is more than 40 km. This unit was connected with the optical distribution network (ODN) where our FBG temperature and strain optical sensors were positioned.

Figure 1 shows the experimental measurement setup used for tests with FWD and monitoring of real-time traffic, having two main parts—optical sensor signal interrogation unit (OSSIU) and ODN with embedded FBG optical sensor network. High power superluminescent emitting diode (SLED) source with a central wavelength of 1550 nm and 3-dB bandwidth of 55 nm fully covering the optical C band (1530 nm to 1565 nm) is used in the OSSIU unit as a broadband light source. This unit also has optical time-domain reflectometer (OTDR) capability, which is in parallel to FBG sensor interrogation that was used for monitoring of the ODN, to avoid possible damage, faults, or excessive macrobending of the optical fibers attached to these optical

sensors. In Figure 1, the optical sensor signal interrogation unit is not shown, as it is not the focus of this article.

The output of SLED is connected to the optical circulator's (OC) port number 3 for separation of the optical signal flows. SLED's signal is transmitted from port A to port B, while FBG sensors reflected signal—from port B to port C. Afterward, port B of the OC is connected to the input of the optical switch (OS). The optical switch has 8 fiber channels, and it was used to connect each channel at a specific time interval. Four channels of the optical switch were used for the connection of the ODN sensor network, but the rest of the channels were not necessary for the described experiments. Each of the ODN sensor network channels consist of the ITU-T G.652 single-mode optical fiber (SMF), FBG strain, and temperature sensors. In the ODN (location a), part (OS fiber port 1) represents the connection for first measurement scenario—the setup for measurements with falling weight deflectometer (FWD), but (location b) represents second measurement scenario (OS fiber ports 6 to 8)—real-time applied traffic strain measurements of the road with integrated FBG optical sensors (FBG sensors parameters shown in Table 1.), as it is further discussed in Section 3.2.

Additional FBG temperature sensors were used to compensate temperature changes in strain measurements. FBG sensor reflected signal is transmitted from OC, port C, to the spectrometer with a 10 kHz maximal scan frequency for 1 optical channel. The digital signal processor receives spectrometer data, detects sensor signal central frequency, and mathematically calculates temperature and strain values. The results of the measurements are then plotted against time.

2.1. Embedding FBG Sensors for Strain Monitoring. The location for FBG optical sensor integration into the real pavement structure was chosen in accordance with the recommendation given in European Weigh–In–Motion (WIM) specifications COST-323 [23]. This document states that the site of sensor embedment should satisfy the following requirements:
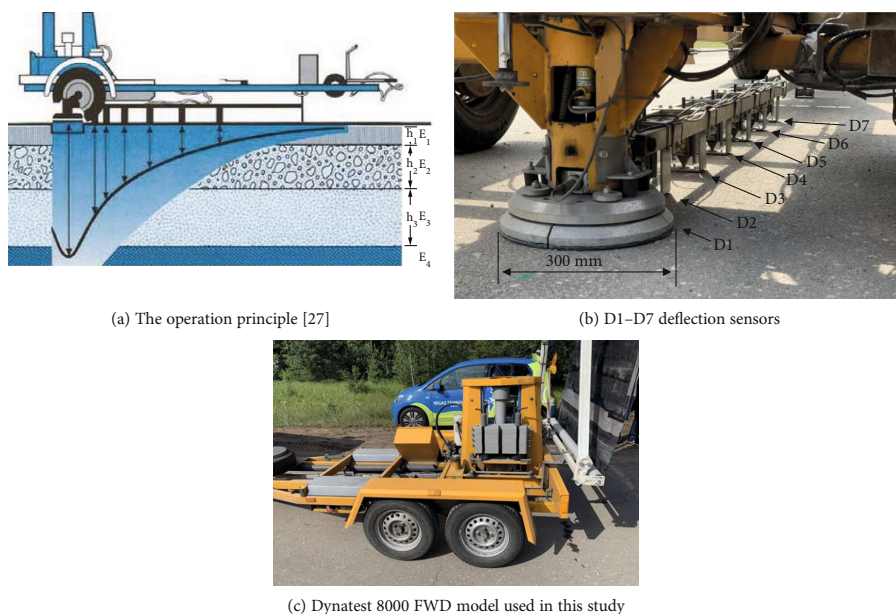
(a) The operation principle [27]

(b) D1–D7 deflection sensors

(c) Dynatest 8000 FWD model used in this study

FIGURE 4: FWD equipment for testing the pavement structure.

(i) Longitudinal slope < 1%

(ii) Transverse slope < 1%

(iii) Radius of curvature > 2500 m

(iv) The surface shall be smooth and maintained in a condition that complies with the International Roughness Index (m/km)—0-4

For embedding of the FBG sensors and measurements, it was found that the pavement structure in Latvia is going to be built in the construction season of 2019-2020. With the help of the contracting company "Binders" Ltd., which is performing the pavement reconstruction projects of the main road, the A2 Riga-Sigulda-Estonian border km 25.50-39.40 (both carriageways) was chosen for embedding the FBG strain and temperature sensors in 2 locations. This road section connects Riga (the capital of Latvia) with the Estonian border.

According to the location (a), commercial FBG sensors were implemented between SMA11 (stone mastic asphalt) (30 mm thick layer from the top coat) and AC11 (asphalt concrete) (60 mm thick layer) asphalt layers. To provide the protection of the FBG sensors and correct operation, strain sensors are integrated into glass/epoxy composite patches (250 × 15 mm), but temperature sensors in ceramic tube. FBG's temperature sensor ceramic tube (diameter: 3 mm, length: 23 mm) isolated strain changes. Length of the FBG strain sensor's grating, according to the specification provided by the manufacturer, was 10 mm. In our solution, we used this FBG sensor thus—optical fiber, and positioned it between 2 glass/epoxy composite material plates.

The operation temperature range of temperature sensors is -40–80°C, but strain sensors -20–60°C. The graphical representation of these layers is shown in Figure 2. The FBG strain and temperature sensors were fixed on the cross-section of the asphalt at the 25 mm depth. In this location, FWD equipment is used for testing of the sensor's integration quality and pavement structure. Tests with FWD equipment were realized in seven different scenarios (when FWD was located to the sensors in range of 300, 600, or 900 mm after the FBG strain sensor).

In location (a), FBG sensors are integrated into the road with geographical location point coordinates: 57°07′18.4″N 24°40′02.6″E. The FBG implementation in both locations is realized after the construction of the road.

As for location (b), FBG strain and temperature sensors (the same sensors as in location (a)) were embedded on the border in a 70 mm thick homogeneous AC 11 one-layer system. Both strain sensors were fixed on the section of asphalt (exactly the same as for location (a)). Long cut was created, and sensors were attached to the cut walls—1 on the one side and 1 on the other one, at the following depth—25 mm on both sides (the same depth as in location (a)). The temperature sensors were fixed in the predrilled holes next to the strain sensors. In location (b), the FBG sensors are embedded in the entry to the A2 temporary road with geographical location point coordinates: 57°07′07.4″N 24°39′04.1″E (see Figure 3).
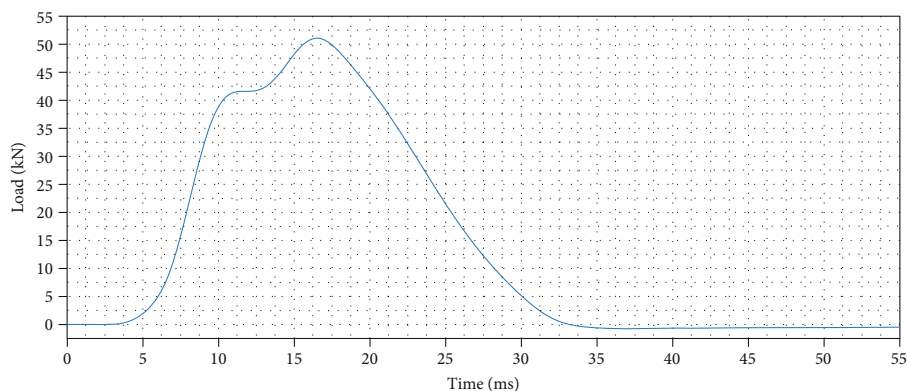
FIGURE 5: Measured FWD pulse load result for the last drop when distance between FWD and embedded FBG strain sensor is 300 mm.

2.2. Experiments with the Falling Weight Deflectometer and Embedded FBG Sensors.
Falling weight deflectometers (FWDs) are in widespread use for nondestructive pavement testing and used as a research or structural evaluation method [24–26]. FWD data is most often used to calculate stiffness-related parameters of the pavement structure. The process of calculating the elastic modulus of individual layers in a multilayer system based on the surface deflections is known as "back-calculation", as there is no closed-form solution [27–29]. When using the FWD, surface deflection measurements are necessary for processing back-calculations of specific material properties. Such properties are based on assumptions for the pavement response to a load, thus allowing applying the strain value that is deliberate for the pavement structural and fatigue analysis. Therefore, the precision of the results (strain at the critical location in the pavement structure) is dependent on the assumptions made during the analysis [28].

FWD equipment is typically used to measure the road pavement deflection with its deflection sensors (D1–D7), but in this research, this equipment was used for getting the fixed and calibrated load values that were made from the circular load plate.

In the measurement session, an FWD equipment, optical sensors signal interrogation unit (OSSIU), and FBG strain as well as temperature sensors were embedded in the road pavement 2 laptops–1 for FWD and 1 for OSSIU controlling that were also used. The load is applied by dropping a known weight, and it is transmitted to the road pavement through a circular load plate—300 mm in diameter (see Figure 4(a)). A load cell is mounted on the top of the load plate, and it measures the load that is imparted to the pavement surface. According to the European practice, the typical load for the road testing is 50 kN giving about 707 kPa pressure under the load plate. Deflection sensors (geophones; force-balance seismometers) are mounted radially from the center of the load plate in order to measure the deformation of the pavement in response to the load [27]. The FWD system is equipped with seven (D1-D7) deflection sensors, and offsets between sensors are from 0 to 1800 mm with increments of 300 mm (see Figure 4(b)). The *Dynatest 8000* FWD equipment (shown in Figure 4(c)) owned by the
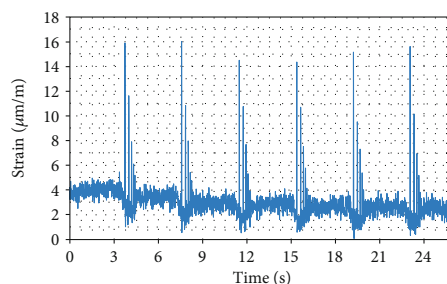

FIGURE 6: Strain versus time measured by the FBG sensor, embedded 25 mm under FWD and center of the FWD load plate, is located 900 mm after FBG sensor.

State Joint Stock Company Latvian State Roads was used for testing the pavement structure. The depth profile of the road in location (a) and the embedded FBG sensors (FBG strain sensor and FBG temperature sensor for temperature compensation) were located within the structure in between the pavement structure layers as are shown in Figure 2.

FWD equipment was used in a mode of six weight drops with a fixed 50 kN load at four different scenarios, where in the first scenario, the center of the FWD load plate was located directly on the FBG strain sensor. In other scenarios, distance between the FWD load plate and FBG strain sensor was 300, 600, or 900 mm. It is important to note that the FBG sensor is integrated on the right side of the road pavement layer (see the upper part of Figure 2), corresponding to "FWD 300 mm after FBG sensor". In FWD software, all drops were set with the same load, which is 50 kN. The FWD equipment after the drop measured drops' load with its sensors. It was observed that in full measurement, session the load variated till 1%. This described measurement session was realized in summer 2019, when, during the measurement day the road pavement temperature varied from +18.7 to +22.5°C (temperature measured with FBG sensor).

TABLE 2: Measured strain (μm/m) by FBG sensor that is embedded 25 mm under FWD when 6 drops by 48.9 ± 0.5 kN load are performed (with temperature compensation enabled).

No. of FWD drop	Center location of the FWD plate with respect to the FBG sensor (mm)			
	0	300	600	900
1	162.5	91.5	24.6	12.5
2	145.9	77.6	27.0	13.1
3	142.7	80.5	24.2	12.2
4	149.5	73.4	28.3	12.1
5	161.6	85.8	25.7	13.2
6	148.5	71.2	25.1	13.2
Average value of measured strain (μm/m)	151.8 ± 9.9	80.0 ± 10.2	25.8 ± 2.1	12.7 ± 0.6
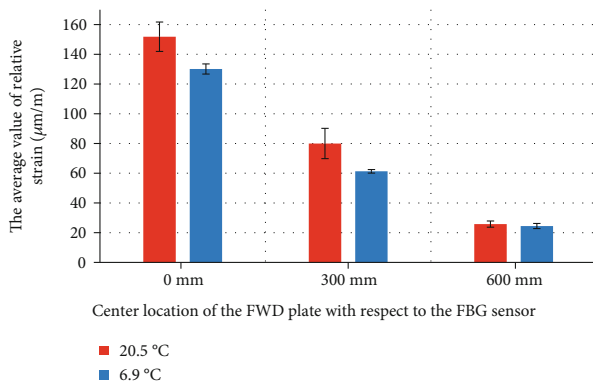
FIGURE 7: Average value of strain for FWD drops when road temperature is 6.9°C and 20.5°C.
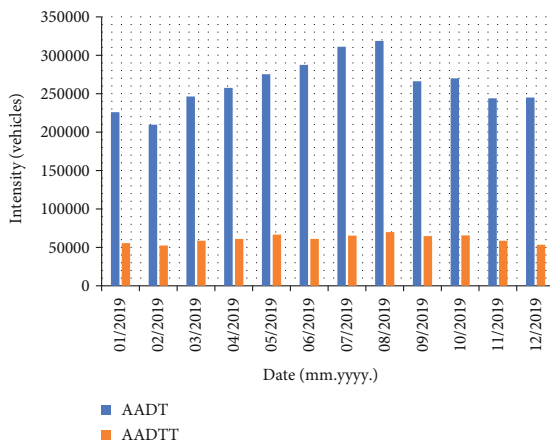
FIGURE 8: Traffic intensity in 2019 at highway A2 76th km [30].

3. Results

3.1. Strain Measurements from FWD Drops with the FBG Sensors. The load of the falling weight versus time for one drop of circular load plate (pulse) was measured with FWD to analyze equipment's working principle (see Figure 5). The total duration of load pulse initiated by FWD equipment drop is 30.35 ms, and load peak value 51.09 kN is achieved at 16.5 ms.
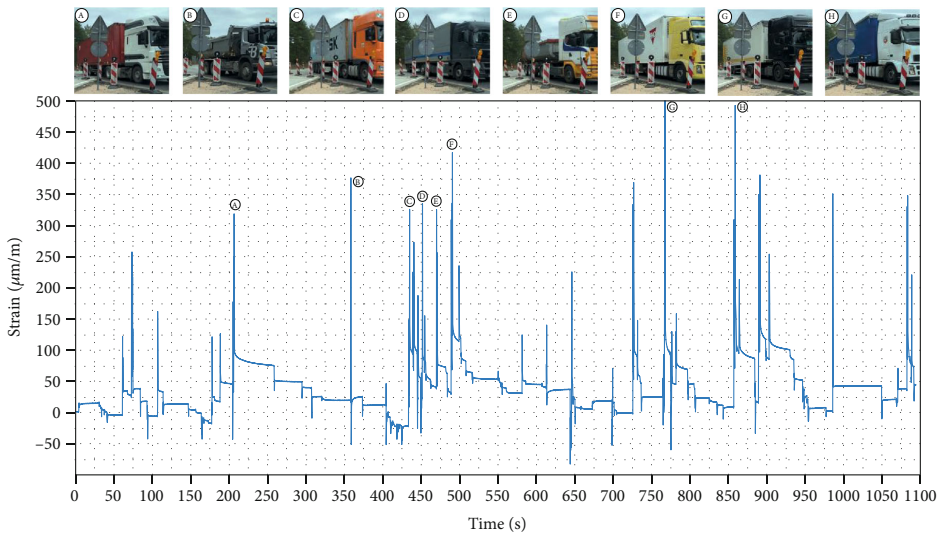
FIGURE 9: Measured real-time strain graph of passing traffic by the embedded FBG sensor.
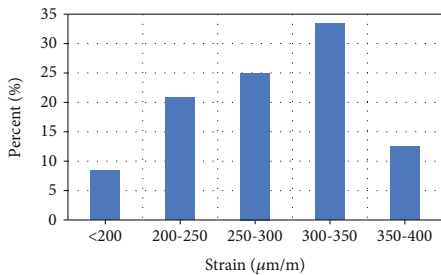
FIGURE 10: Histogram of truck generated strain values measured with embedded FBG sensors.

The strain that was measured with the FBG sensor embedded 25 mm under the FWD load of 6 drops is illustrated in Figure 6 (in scenario—when the center of the FWD load plate was located 900 mm after FBG sensor (see Figure 6)).

Six stable peaks can be observed. The relative scatter of 4.7% (Figure 6) over all six drops of the FWD plate was registered for a mean load of 48.9 ± 0.5 kN. Peaks with smaller strain amplitude can be seen after every major peak. Those represent FWD amortization drops for equipment stabilization and positioning at rest.

In Table 2, measured strain can also be seen. They are also known as a relative deformation values that represent FBG optical sensors after temperature compensation for each drop. These strain values that are showed in Table 2 represent the difference between strain minimum (strain floor) and measured peak maximum.

As it can be seen in Table 2, results gathered with the FBG sensors show the possibility to precisely (the relative scatter

4.8–12.8%) detect the strain values, which allows to evaluate the real operation of the pavement structure under load.

FBG strain sensors are fixed to the asphalt side, then monitoring with high accuracy can be realized from the side where the sensor is embedded. This is the main disadvantage of this method, which must be taken into account when applying the integration process of the sensors. For fixed one-way traffic, it does not create monitoring restrictions, but if the traffic direction is changing, then it is necessary to integrate FBG sensors on both sides.

In order to evaluate the impact of the road surface temperature on the measured strain, another session of measurements, therefore, was repeated in autumn 2019. The measured average strain values after temperature compensation for each drop are shown in Figure 7 where comparison is made of the strain values between the ones that were gathered during summer versus the other ones—during autumn, when road pavement temperatures measured with FBG sensors were 20.5°C and 6.9°C. In the graph, error bars represent strain relative scatter. The same loading parameters were used in the autumn session (6 drops with 50 kN load each) with the mean measured load of drops equal to 51.98 ± 0.94 kN.

These values are equal to the difference between strain minimum (strain floor) and measured peak maximum. As it can be seen, the highest strain value (averaging $151.8 \pm 9.9 \, \mu$m/m) is detected when the center of the FWD load plate is located over the embedded FBG strain sensor. In the light of these findings, the sensor placement with respect to the direction of passing vehicles plays an important role. As can also be seen, all values of the measured strain were lower in autumn compared to summer. Same tendency was observed in [3] research. The strain values were higher in warmer weather, because of the stiffness that decreases at higher temperatures; so, as a result, strain values are

increasing. Therefore, it is very important to take into account the temperature of the road when carrying out the second part of our research—strain measurements from passing vehicles.

3.2. Real-Time Traffic Analysis. Monitoring of the real-time vehicle traffic described in this article was realized in September 2019, in the temporary road section—location (b) shown in Figure 3, where FBG optical sensors were used without using FWD equipment. The average temperature for the road pavement (measured with FBG temperature sensor) during the measurements was +25.2°C. For embedding of the sensors, we chose the location, where there is a high annual average daily traffic (AADT) and annual average daily truck traffic (AADTT). The data of the nearest traffic counting point (station No. 6) showed that there were 3.15 million vehicle intensity in 2019 with an average speed of 86.4 km/h. From all the passing vehicles, 23.3% or 735 000 were specifically truck intensity (see Figure 8) [30]. In this location, the sensors were embedded in the temporary road section provided by Binders Ltd., which is the largest Latvian road construction company.

Figure 9 can be seen in a short time period of the measured vehicle traffic strain changes gathered from the FBG sensor no. 2 (fixed on the right side—depth 25 mm, exactly the same as for location (a)). Parallel to the real-time strain measurements, a video was taken in order to be certain that the road traffic changes are calibrated with the strain measurements, as well as to see the "strain-pattern" of different vehicles, mainly trucks. It can be seen that the truck traffic in particular is generating the highest strain in the pavement structure. If the graph is zoomed in, then the number of vehicle axis and the strain value of each vehicle axis can be detected. From the measured FBG strain, sensor data shows that the "G" truck's last axis (5th) creates the highest strain or relative deformation value, which is 375.6 μm/m. The second highest strain value (356.4 μm/m) was created by the "B" gravel truck that has 3 axes. It is important to note that in Figure 9, upper part visually does not show all of the trucks that were passing by, for example, at the time spans of 73, 728, 891, 986, and 1084 s. Measured strain values are comparable and similar to those shown in [13] research.

The summary of the measurements gathered by the road truck traffic while using FBG sensors is shown in Figure 10. Here, a focus is made on the road's truck traffic, not the traffic made by the passenger cars, as trucks cause the highest applied strain values and damage to the road pavement. The graph represents the generated truck strain value histogram. It is important to add that the strain value histogram contains all the measurement data, not only those presented in Figure 9.

As it can be seen in the histogram, trucks most often (33% of the time) can be put into the category that generates strain of 300-350 μm/m. If all of the data is collected and compared, then trucks, on average, generate 282 μm/m strain value each.

4. Conclusions

In this paper, a framework for implementation of FBG optical sensors for structural health monitoring of road pavement was demonstrated. The framework consists of the sensor integration into the A2 road Riga-Sigulda-Estonia, and validation of sensor strain and temperature readings through the use of the falling weight deflectometer (FWD) equipment, which, according to the European practice, is typical for load testing of roads. FWD equipment with the calibrated load was used to help testing the sensor's integration method and evaluating the accuracy of the measurements.

A parametric study was conducted where the measured strain readings from the embedded FBG sensors were compared in summer and autumn sessions when the temperature difference of the road pavement was about 13°C (as measured with the embedded FBGs) and at different locations of falling load plate of the FWD with respect to the location of the FBG sensor. It was found that, first of all, the strain values were higher in warmer weather. This can be explained because of the stiffness that decreases at higher temperatures so as a result, strain values are increasing.

As it can be seen in the results with FBG sensors, it is possible to precisely detect (the relative scatter 4.8–12.8%) strain values, which allows the evaluation of the real operation of the pavement structure under load circumstances.

Finally, a monitoring of the real-time truck traffic on a temporary road with a high annual average daily car traffic and annual average daily truck traffic was conducted. From the monitoring results, the typical strain values generated by the passing trucks were determined to be, on average, 282 μm/m, but the most probable value (33%) is within the range of 300-350 μm/m (325 μm/m averagely). When the road pavement is underdesigned, the applied strain is sufficiently higher, which might cause fatigue failures under repeated loads.

When using FBG sensors solutions, it can be determined at what time the relative deformation limits for a particular road pavements concrete material are exceeded that allows validating and verifying the designed road construction solutions.

Although it has been shown that the installation of FBG sensors into road pavements provides effective means of monitoring the structural integrity of roads under traffic, there are challenges. Firstly, providing the necessary protection of the bare optical fibers in a form of durable packaging, secondly, to account for the varying seasonal temperatures when analyzing the measured strain values.

Based on the obtained results, authors are continuing the research, where the FBG sensors are integrated in the road pavement during the asphalt laying process. Further investigating of the FWD and FOS combination approach would help to understand the structural behavior of the pavement structure, including back-calculations and forward calculations in the pavement design.

Therefore, by using FBG sensors, which can be integrated into the road construction process or after that, the fatigue of such road structures can be monitored over time. This approach could be used for the prediction of different road pavement structure life cycles, so enabling efficient use, maintenance, and timely repairs of the public roads lead to the overall safety of the transportation system.

Data Availability

The data used to support the findings of this study are available from the first author upon request.

Conflicts of Interest

The authors declare that there is no conflict of interest regarding the publication of this paper.

Acknowledgments

References

[1] A. Abdelgawad and K. Yelamarthi, "Internet of Things (IoT) platform for structure health monitoring," *Wireless Communications and Mobile Computing*, vol. 2017, Article ID 6560797, 10 pages, 2017.

[2] H. Wang, W. Liu, J. He et al., "Functionality enhancement of industrialized optical fiber sensors and system developed for full-scale pavement monitoring," *Sensors*, vol. 14, no. 5, pp. 8829–8850, 2014.

[3] J. Xie, H. Li, L. Gao, and M. Liu, "Laboratory investigation of rutting performance for multilayer pavement with fiber Bragg gratings," *Construction and Building Materials*, vol. 154, pp. 331–339, 2017.

[4] W. Zhaoxia, Y. Dongmei, and L. Zhiquan, "Bridge structure monitoring system based on practical FBG," in *2008 IEEE International Conference on Automation and Logistics*, pp. 1–4, Qingdao, China, September 2008.

[5] Q. Jin, Z. Liu, J. Bin, and W. Ren, "Predictive analytics of in-service bridge structural performance from SHM data mining perspective: a case study," *Shock and Vibration*, vol. 2019, Article ID 6847053, 11 pages, 2019.

[6] H. Xu, F. Li, W. Zhao, S. Wang, Y. Du, and C. Bian, "A high precision fiber Bragg grating inclination sensor for slope monitoring," *Journal of Sensors*, vol. 2019, Article ID 1354029, 7 pages, 2019.

[7] T. Yiqiu, W. Haipeng, M. Shaojun, and X. Huining, "Quality control of asphalt pavement compaction using fibre Bragg grating sensing technology," *Construction and Building Materials*, vol. 54, pp. 53–59, 2014.

[8] G. Rajan, Ed., *Optical Fiber Sensors: Advanced Techniques and Applications*, University of New South Wales, School of Electrical Engineering and Telecommunications, UNSW Australia, CRC Press Taylor & Francis Group, 2015.

[9] M. D. Fatima, F. Domingues, and A. Radwan, *Optical Fiber Sensors for IoT and Smart Devices*, Springer Briefs in Electrical and Computer Engineering, I3N & Physics Department, University of Aveiro, Portugal, 2017.

[10] Y. C. Manie, R. K. Shiu, P. C. Peng et al., "Intensity and wavelength division multiplexing FBG sensor system using a Raman amplifier and extreme learning machine," *Journal of Sensors*, vol. 2018, Article ID 7323149, 11 pages, 2018.

[11] K. O. Hill, Y. Fujii, D. C. Johnson, and B. S. Kawasaki, "Photosensitivity in optical fiber waveguides: application to reflection filter fabrication," *Applied Physics Letters*, vol. 32, no. 10, pp. 647–649, 1978.

[12] R. Montagne, "FTTH Forecast for Europe, Europe broadband status, market forecast by 2020 and 2025," in *FTTH Council Europe Conference*, Netherlands, Amsterdam, March 2019.

[13] P. Kara De Maeijer, W. Van den Bergh, and C. Vuye, "Fiber Bragg grating sensors in three asphalt pavement layers," *Infrastructures*, vol. 3, no. 2, p. 16, 2018.

[14] P. Kolisoja, N. Vuorimies, A. Kurki, and T. Saarenketo, "Open structural monitoring data from two extensively instrumented road sections – case Aurora," in *Proceedings of the XVII European Conference on Soil Mechanics and Geotechnical Engineering: Geotechnical Engineering, foundation of the future. The Icelandic Geotechnical Society, IGS*, pp. 1–8, Reykjavik, Iceland, 2019.

[15] P. Skels, R. Janeliukstis, and V. Haritonovs, "Review on structural health interrogation using fiber bragg grating sensors," *Engineering for Rural Development*, vol. 17, pp. 1346–1353, 2018.

[16] K. Li and J. G. Xie, "Experiment and research of using fiber Bragg grating to monitor the dynamic response of asphalt concrete," *Applied Mechanics and Materials*, vol. 97-98, pp. 301–304, 2011.

[17] Z. Zhou, W. Liu, Y. Huang et al., "Optical fiber Bragg grating sensor assembly for 3D strain monitoring and its case study in highway pavement," *Mechanical Systems and Signal Processing*, vol. 28, pp. 36–49, 2012.

[18] L. Meng, L. Wang, Y. Hou, and G. Yan, "A research on low modulus distributed fiber optical sensor for pavement material strain monitoring," *Sensors*, vol. 17, no. 10, p. 2386, 2017.

[19] G. Nosenzo, B. E. Whelan, M. Brunton, D. Kay, and H. Buys, "Continuous monitoring of mining induced strain in a road pavement using fiber Bragg grating sensors," *Photonic Sensors*, vol. 3, no. 2, pp. 144–158, 2013.

[20] Y. Lei, X. Hu, H. Wang, Z. You, Y. Zhou, and X. Yang, "Effects of vehicle speeds on the hydrodynamic pressure of pavement surface: measurement with a designed device," *Measurement*, vol. 98, pp. 1–9, 2017.

[21] J.-N. Wang, J.-L. Tang, and H.-P. Chang, "Fiber Bragg grating sensors for use in pavement structural strain-temperature monitoring," in *Smart Structures and Materials 2006: Sensors and Smart Structures Technologies for Civil, Mechanical, and Aerospace Systems*, vol. 6174, San Diego, United States, March 2006.

[22] Z. Zhou and J. Ou, "Techniques of temperature compensation for FBG strain sensors used in long-term structural monitoring," in *Fundamental Problems of Optoelectronics and Microelectronics II*, Khabrovsk, Russian Federation, June 2005.

[23] COST 323, *European WIM Test Program 1996-1998 (CET & CMT), Technical report of the Management Committee, draft 2, COST323/WAVE, EC/DGVII*, COST Transport, 1996.

[24] P. Ullidtz, *Modelling Flexible Pavement Response and Performance*, Polyteknisk Forlag, Denmark, 1998.

[25] L. Korkiala-Tanttu, *Calculation Method for Permanent Deformation of Unbound Pavement Materials*, VTT Technical Research Centre of Finland, Espoo, Finland, 2008.

[26] T. Saevarsdottir and S. Erlingsson, "Deformation modelling of instrumented flexible pavement structure," *Procedia Engineering*, vol. 143, pp. 937–944, 2016.

[27] M. Y. Shahin, *Pavement Management for Airports, Roads, and Parking Lots*, Springer, 2 edition, 2017.

[28] P. Kara De Maeijer, W. Van den Bergh, S. Vanlanduit et al., "Inverse modelling approach-fiber Bragg grating (FBG) measurements in comparison to falling weight deflectometer (FWD) measurements: a review," in *7th International Conference Bituminous Mixtures and Pavements*, p. 11, Thessaloniki, Greece, 2019.

[29] P. Kara de Maeijer, G. Luyckx, C. Vuye et al., "Fiber optics sensors in asphalt pavement: state-of-the-art review," *Infrastructures*, vol. 4, no. 2, p. 36, 2019.

[30] "SJSC Latvian State Roads, online traffic intensity at highway A2 76th km," January 2020, https://lvceli.lv/traffic/.

Braunfelds J., Senkans U., Skels P., Janeliukstis R., Porins J., Spolitis S., Bobrovs V. Road Pavement Structural Health Monitoring by Embedded Fiber Bragg Grating Based Optical Sensors. Sensors, **2022**, pp.1-13.

Road Pavement Structural Health Monitoring by Embedded Fiber-Bragg-Grating-Based Optical Sensors

Janis Braunfelds [1,2,*], Ugis Senkans [1], Peteris Skels [3], Rims Janeliukstis [4], Jurgis Porins [2], Sandis Spolitis [1,2] and Vjaceslavs Bobrovs [2]

1   Communication Technologies Research Center, Riga Technical University, LV-1048 Riga, Latvia; ugis.senkans@rtu.lv (U.S.); sandis.spolitis@rtu.lv (S.S.)
2   Institute of Telecommunications, Riga Technical University, LV-1048 Riga, Latvia; jurgis.porins@rtu.lv (J.P.); vjaceslavs.bobrovs@rtu.lv (V.B.)
3   Department of Roads and Bridges, Riga Technical University, LV-1048 Riga, Latvia; peteris.skels_1@rtu.lv
4   Institute of Materials and Structures, Riga Technical University, LV-1048 Riga, Latvia; rims.janeliukstis_1@rtu.lv
*   Correspondence: janis.braunfelds@rtu.lv; Tel.: +371-2238-5936

Abstract: Fiber Bragg grating (FBG) optical sensors are state-of-the-art technology that can be integrated into the road structure, providing real-time traffic-induced strain readings and ensuring the monitoring of the road's structural health. By implementing specific FBG sensors, it is possible to detect each vehicle's axle count and the induced strain changes in the road structure. In this study, FBG sensors are embedded at the top of the 240-mm-thick cement-treated reclaimed asphalt pavement mixture layer of the road (specifically, 25 mm deep within the road). Optical sensors' signal interrogation units are used to measure the strain and temperature and collect data of the road's passing vehicles, starting from passenger cars that have two axles and up to heavy trucks that have six axles. Passenger cars with 2 axles generate a typical (90% events) strain of 0.8–4.1 μm/m, the 2-axle minibus 5.5–8.5 μm/m, 2–3-axle trucks 11–26 μm/m, but 4–6-axle trucks 14–36 μm/m per each axle. A large number of influencing parameters determine the pavement design leading to the great uncertainty in the prediction of the strain at the boundary between the asphalt surface and cement-treated base layers. Real-time strain and temperature measurements help to understand the actual behavior of the pavement structure under an applied load, thus assisting in validating the proposed pavement design.

Keywords: fiber Bragg grating (FBG); fiber optical sensors (FOS); structural health monitoring (SHM); strain measurements

1. Introduction

Traffic volume on the Latvian road network had been continually increasing until 2019, when the average annual daily traffic (AADT) reached 6525 vehicles in 24 h. Even though the AADT (based on traffic counting data) decreased by 7% in 2020 [1], the general trend shows an increase in overall traffic volumes and road loading by equivalent 10-ton axle loads.

With the rapid growth of worldwide fiber optical networks, all the related technology has also advanced and been adopted for industry purposes. One of such perspective technologies is fiber optical sensors (FOS). FOS have multiple advantages such as an immunity to corrosion [2–4] and electromagnetic interference [3–7], the capability for distributed and long-distance measurements [8,9], harsh environment and high-temperature durability [10], high precision [8,11], easy integration [8,11] and high sensitivity [3,9,12], which can be efficiently utilized for necessary applications.

FBG technology allows for the relatively easy and convenient implementation of FOS into a necessary architecture. FBG sensors are versatile in the matter of the parameters to

be measured; for instance, strain [13,14], temperature [9,15], pressure [16], humidity [9,17], and many more can be measured and monitored. With regard to industry, FBG FOS realization is topical in structural health monitoring (SHM) applications for dams [10,18], pipelines [10,16], slopes [10], tunnels [10,19], bridges [10,20], railroads [21], roads [14,22], and so on.

The changes in traffic volumes and road loading have a direct impact on the rate of deterioration of the road pavement. SHM applications, by incorporating FOS inside the pavement, are a valuable tool for infrastructure managers. SHM tools assist in the planning of reconstruction and maintenance smartly and justifiably, based on real-time data. Such tools help in making appropriate decisions for planning the maintenance and reconstruction works and validate the design assumptions by measuring actual pavement structural layers' responses under the load conditions. Since new materials and structural layers are introduced, such as modified new types of asphalts, stabilized base layers, cement-treated reclaimed asphalt pavement (RAP) mixture layers, etc., the increased importance for such solutions needs to be researched.

Our research process is structured into three main parts—preparation, the calibration of the implemented FOS with a falling weight deflectometer (FWD), and the experimental study of real transport traffic and strain measurements. Further paper sections are organized as follows. Construction and analysis of the experimental setup are described in Section 2. Section 3 discusses the FWD application method for calibration purposes with regard to the operation of FBG optical sensors, while Section 4 focuses on real-time transport traffic strain monitoring for SHM by using FBG optical sensors that are integrated within road infrastructure. In the end, the results are concluded, and the effectiveness of the proposed technique is evaluated.

2. The Working Principle of Our Optical Sensor Signal Interrogation Unit and FBG Optical Sensors

During the whole research process, it is necessary to use the authors' previously individually developed [14] mobile optical sensors signal interrogation unit (OSSIU), which is suitable for field use to provide different sorts of strain measurements in real-time (including induced strain by real-time transport traffic). The main parameters of this device are described in Table 1.

Table 1. The main parameters of the developed and used optical sensors signal interrogation unit.

| Parameters	Value
Wavelength operation band	1520–1575 nm
Max scan frequency for single optical channel	10 kHz
Wavelength resolution	1 pm
Remote maximum operation distance	40 km

The OSSIU unit consists of a superluminescent emitting diode (SLED) (parameters mentioned in further paragraphs), an optical circulator (OC) necessary for the separation of the directions of the optical signals, as well as a spectrometer and digital signal processor (DSP) to investigate the received optical spectrum and data from the FBG optical sensors.

As for the optical sensors, a pair of commercial FBG strain and temperature sensors were chosen. A temperature sensor (Xi'an Aurora Technology Co., Xi'an, China) is necessary to ensure the FBG optical strain sensor's calibration during the whole research period, thus excluding the ambient temperature's effect on the received strain values. The main parameters of the used optical FBG sensors are summarized in Table 2.

The experimental working principle of our FBG strain sensor is depicted in Figure 1. Here, for an optical input signal, a high-power SLED broadband light source with a central wavelength of 1550 nm and a 3-dB bandwidth of 55 nm is chosen and has already been integrated inside our OSSIU unit.

Table 2. The main parameters of the FBG temperature and strain sensor.

FBG No.	Measured Parameter	Central Wavelength	Accuracy	Measurement Range
1	Strain	1544.800 nm	<1 μm	±5000 με
2	Temperature	1554.558 nm	±0.3 °C	−40–120 °C
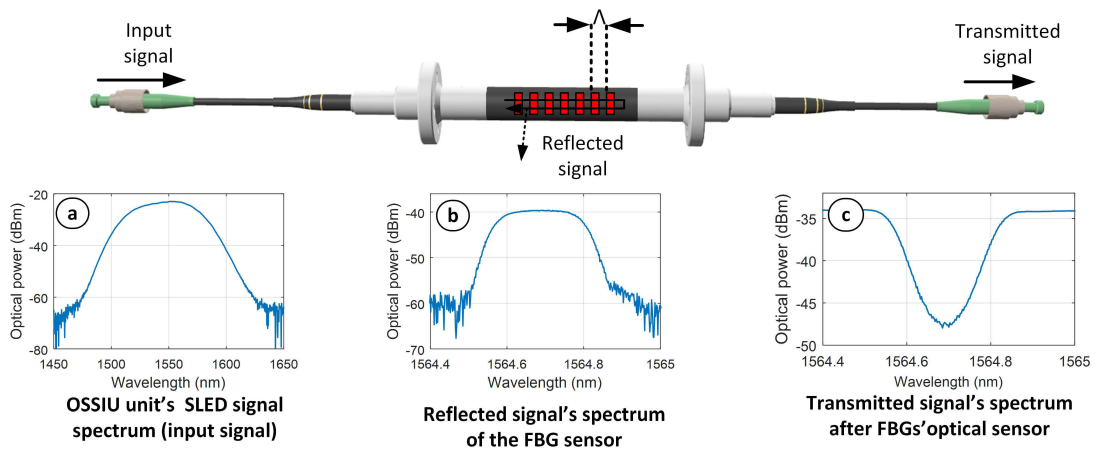
Figure 1. The characteristic and measured spectrum of commercial [23] FBG strain sensor.

The optical spectrum of the input signal is visible in Figure 1a. The optical signal is transmitted through the optical fiber as shown in the middle-upper part of Figure 1, where the FBGs sensors are inscribed. The reflected optical signal of the FBG sensor at the reference wavelength can be seen in Figure 1b. This reflected optical spectrum of the strain sensor is processed and observed in our mobile OSSIU unit. Figure 1c, on the other hand, shows the transmitted optical signal after passing the FBG strain optical sensor.

Integration of optical FBG sensors within the road architecture during the construction process allows for monitoring of the reflected optical sensors' wavelength or frequency changes induced by the strain in the long term. In this research, the strain shift is generated with either a falling weight deflectometer or real-time transport traffic (vehicles passing over the FBG sensors). The induced strain and its shift can provide information about the vehicles or objects on top of the road structure and, no less important—the integrity or structural health of the road construction at that specific time. The strain shift is calculated (see Table 3 for the received strain data with the FWD experiment and Table 4 for real-time received transport traffic strain data) in this research using an equation [23]:

$$\Delta\varepsilon = \frac{\Delta\lambda - B \times \Delta T}{A \times \Delta l} + (\Delta T \times CTE \times \Delta l_2) \qquad (1)$$

where:

$\Delta\lambda = \frac{\lambda_{act} - \lambda_0}{\lambda_0}$

$\Delta T = (T_{act} - T_0)$

$\Delta l = \frac{l_{FAL}}{l_{FFL}}$

$\Delta l_2 = \frac{(l_{FAL} - l_{FFL})}{l_{FAL}}$

$\Delta\varepsilon$—Strain shift (μm/m);

λ_0—Initial strain wavelength (nm);

λ_{act}—Actual strain wavelength (nm);

T_0—Initial temperature (°C);

T_{act}—Actual temperature (°C);
l_{FAL}—Anchoring length (m);
l_{FFL}—Free fiber length (m);
CTE—Coefficient of thermal expansion [$\mu \cdot \varepsilon \cdot °C$];
A—Coefficient [$\mu \cdot \varepsilon^{-1}$];
B—Coefficient [$°C^{-1}$];

Similar to the strain shift calculation, it is possible to calculate wavelength versus temperature shifts by using an equation:

$$\Delta T = \frac{\lambda_{act} - \lambda_0}{k} \tag{2}$$

where:

ΔT = Temperature shift (°C);
λ_{act} = Actual wavelength (nm);
λ_0 = Initial wavelength at time "0" (nm);
k = Monomial coefficient $\left(\frac{\text{pm}}{°C} \right)$.

3. Integration of the FBG Sensors into Asphalt Pavement

Once the setup and all the preparation work have been completed, the location for the experiment is chosen and carried out in a construction site, where FBG optical sensors are embedded. FBG optical sensors are integrated into the road with geographical locations, Latvia. Available online: https://google/maps/hkxm4er4slcqcaff7 (accessed on 24 May 2022). Here a contracting company, "Binders" Ltd., (Riga, Latvia) and a joint stock company, "ACB", (Riga, Latvia), was performing reconstruction on the road of national importance (A8 Riga-Jelgava-Meitene border km 19.20–29.95 km). This particular road connects Riga city (capital of Latvia) with the border of Lithuania.

Firstly, an experimental setup (please see Figure 2) for real-time transport traffic strain monitoring is developed to display the overall method for the investigation of SHM applications.
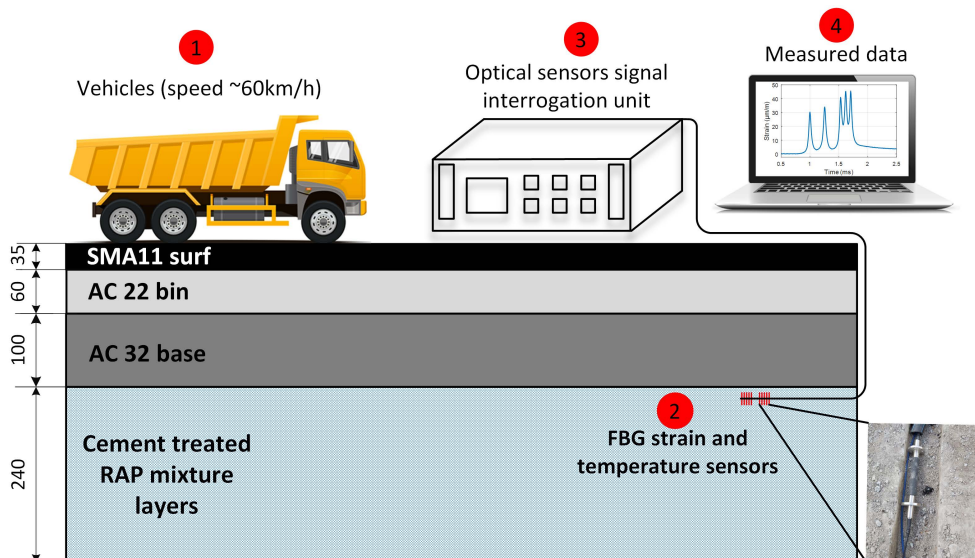

Figure 2. Schematic setup of the FBG optical sensors' integration (mm deep) and placement for strain measurement experiments.

As can be observed in Figure 2, the FBG strain and temperature sensors are embedded in the upper part of the 240-mm-thick cement-treated RAP mixture layer, specifically, 25 mm deep inside the cement-treated RAP mixture layer, that is, under 35-mm-thick SMA11 (stone mastic asphalt), 60-mm-thick AC22 and 100-mm-thick AC32 (asphalt concrete) layers and monitored remotely with OSSIU. It detects all the induced strain (and thus reflected wavelength/frequency shifts of the FBG optical sensor) by the vehicles passing the upper layer of the road. Unlike our previous research [14], where FBG optical sensors were embedded within the temporary road—between 30-mm-thick SMA11 and 60-mm-thick AC11 layers—in this research, we have chosen a different approach by studying the embedment of deeper FBG optical sensors in the cement-treated RAP mixture layer (~220 mm from the surface, see the left side of Figure 3) and strain measurement detection, and hence also test such technologies' performance in permanent road infrastructure. In this research, new types of optical sensors are also chosen, providing a more reliable embedment realization in road infrastructure.

Figure 3. Photos from the construction process of road infrastructure where FBG sensors are integrated.

FBG strain and temperature sensors are integrated into a position so that the majority of passing transportation would almost certainly drive over that specific position. Optical sensors and all of their connecting armored optical patches are inserted into sawn grooves (visible on the left side of Figure 3). The width of the groove where FBGs optical sensors are inserted is 60 mm, and its depth is 50 mm, while the part of the groove where only optical patches are inserted is reduced to 35 mm, as it is not necessary for a wider groove in that position. Connecting optical fibers of the FBG sensors are inserted within the heat-resistant and mechanically durable pipe with a diameter of 30 mm. This is done to provide for the longevity of the FBG optical sensors and their fibers.

Some of the main difficulties that can be encountered and need to be dealt with during the embedment process are firstly choosing a specifically suitable road embedment type of strain FBG sensor, as some of the FBGs that are attached to the material's surface might not position well. Secondly, additional optical fibers' protection from the mechanical influence (as the asphalt laying machine was driving over the embedment position during the construction process) and temperature influence (which was increased as the hot asphalt layer was poured on) has to be completed as discussed in the previous paragraph. Last but not least, it was also important to ensure that the FBG sensors were embedded so that there would not be any air gaps between the surface and the layers on the road under the position where the FBGs were placed.

Once the sensors are installed and the construction process of the road infrastructure is finished, it is possible to use the FWD device, calibrate the measurements of the optical FBG sensors, measure the data acquired, and start the real-time transport traffic monitoring

for comprehensive data acquisition. The performed experiments are discussed in the next sections of this article.

4. The Initial Experiments and Calibration Process of the Embedded FBG Sensors

FWD applications (see Figure 4) for evaluation of the collected strain data are necessary to ensure proper installment of the realized FBG optical sensors. To make certain that the sensors' response data are correct, it is necessary to calibrate the acquired strain data concerning the related timeline. FWD is widely used [24–26] for non-destructive road pavement testing and as a research test tool. Mostly, FWD gathered data are used to estimate the stiffness parameters of the underlying pavement structure. A single pulse load of 50 kN generates about 707 kPa of pressure (which is relatively equivalent to the amount of pressure generated by the heavy type of passing trucks—equivalent to a 10-ton axle load) under the load plate and is depicted in Figure 5, where load versus time data can be observed. Such parameters are typical to the European practice for road infrastructure testing, thus allowing us to ensure that FOS applications in road SHM complies with the road-building industry's needs and standards.

Figure 4. Realization of FWD experiments for calibration purposes of the embedded optical sensors.
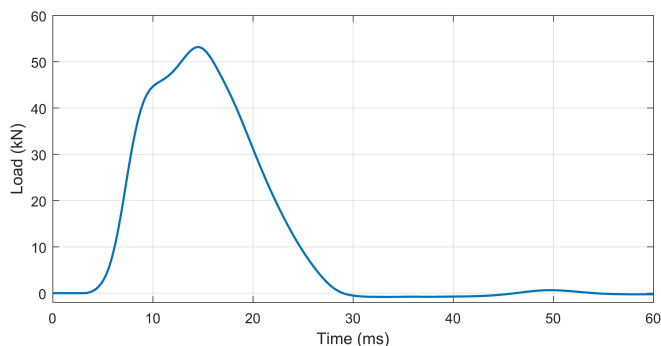

Figure 5. Measured pulse load that is induced by the FWD.

As seen in Figure 5, FWDs' generated pulse load lasts approximately 25 ms, reaching the highest load of ~53 kN after 15 ms from the initial start. In a larger time scale, to analyze strain versus time by the same FWD, 3 series with 3 drops in each series (with a 4 ms

pause between each drop) are made, and more detailed response information can be seen in Figure 6, where one of those series is shown. There, an FBG strain sensor's response data show the detected strain values when the horizontal distance between the FWD load plate center and the sensor is 50 cm (explained in more detail in the next subsection). With this distance between the optical strain sensor and the FWD's load plate, for each drop, the average measured strain $\Delta \varepsilon$ is approximately 14 µm/m. Resonant oscillations are also observed after each drop (approximately for 0.5 s) until the momentum of the strain applied to the road infrastructure evens out. Parallel to the strain measurements, we also measure temperature by using the FBG optical sensor that is embedded into the cement-treated RAP mixture layer. The material temperature within the cement-treated RAP mixture layer, during experimental measurements, varied within a range of 1–1.5 °C and is measured by our embedded FBG temperature optical sensor.
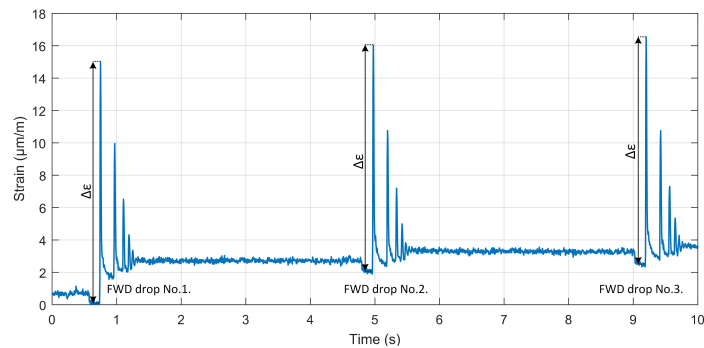

Figure 6. Monitoring of the strain versus time induced by FWD (3 drops) when the horizontal distance between the center of the FWD load plate and the embedment position of the optical sensor is 50 cm.

Afterward, 15 separate FWD load drops (with 50 kN load each) are made on the top of the location where the FBG optical strain sensor is implemented. Based on the measured data, the distribution of received strain values made by FWD drops (see Figure 7) is analyzed. This is performed to be certain that the installment process ensures precise strain detection (and that of its values) under continuous load conditions during the time. As it also does on the road infrastructure, when real-time transport traffic passes the road pavement, leaving multiple strain-induced changes in a quick period.
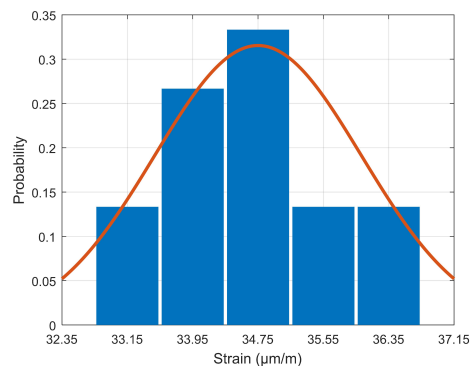

Figure 7. FBG sensor's measured strain distribution of FWD drops when the FWD load plate is located on top of (directly on) the position under where the FBG strain sensor is embedded.

On average, 34.63 µm/m for each of the series is estimated, and a strong correlation between the 15 sets of experimental FWD load data could be observed. In addition to that, the measured strain distribution of the FWD drops shows a Gaussian type of model. From what was previously mentioned, we can state that a stable operation of the SHM system model can be realized with the real-time transport traffic and the correct gathering of strain data, allowing for monitoring of both low- and high-intensity traffic over the road infrastructure.

4.1. Horizontal Distance from the FBG Optical Sensors Concerning FWD's Load Plate Position

FWD experiments are further investigated by realizing different test scenarios. The acquired strain values are compared regarding the load positioning of the load plate concerning the embedded optical FBG sensor. Table 3 consists of all the data gathered when the horizontal distance between the central point of the fiber optical sensor and the FWD's load plate is changed from the "on top of" position (0 cm away) to 50 cm with a step of 10 cm. This allows us to observe how large the difference is for the received average strain shift $\Delta\varepsilon$_avg (µm/m) as well as the relative deviation (%) by the distance of the load plate on top of the road layer.

Table 3. Received strain measurement values induced by the FWD in its different positions regarding the implemented FBG optical strain sensor.

Horizontal distance between the FWD load plate center and FBG sensor	0 cm	10 cm	20 cm	30 cm	40 cm	50 cm
$\Delta\varepsilon$_avg (µm/m)	34.63	30.21	28.16	23.13	19.71	14.03
Coefficient of variation (%)	4.26	6.64	3.28	5.24	5.59	6.26

As can be observed, the average strain shift $\Delta\varepsilon$_avg is 34.63 µm/m in a scenario when the load plate is directly on the road's top layer position (beneath of which is the embedded FBG optical strain sensor). However, as expected, this value decreases with the additional horizontal distance further away from the optical sensor, showing 14.03 µm/m when the load plate is 50 cm further away from the starting position. This means that a 50 cm large horizontal distance decreases the average detected strain shift value by approximately 20.60 µm/m compared to the highest (starting) value (34.63 µm/m). Moreover, as can be seen in Table 3, the coefficient of variation ranges from 3.28% up to 6.64%. From the observed data, we can state that the adjacent lane and traffic over it have a negligible effect on the measured strain data towards the lane where the FBGs are embedded. In this research, we studied the scenario where two lanes are built in both driving directions—thus, the road is wider and the impact from the adjacent traffic lane is even smaller.

The numerical data gathered and shown in Table 3 are also visually depicted in Figure 8. Here, a correlation between the received strain values (measured with the FBG optical strain sensor) and FWD's load plate centrum distance position (according to the FBG optical sensors' embedment position) is observed. In the graph, blue dots with lines represent the average strain values and the measurement variation range.

As can be seen in Figure 8, there is a strong linear correlation between the received strain shift values and the position distance of the FWD's plate (concerning the FBG's embedment). Thus, approving the proper installment of our FBG optical strain sensor and its correct operation, we can state that if an FBG optical strain sensor that has a sensitivity and protective coating as described in the previous section is implemented beneath the 220 mm of road infrastructure layers (SMA11—35 mm, AC22—60 mm, AC32—100 mm, cement treated RAP mixture layer—25 mm), then such a configuration will provide an accurate linear equation in regards to the sensor's working range diapason.
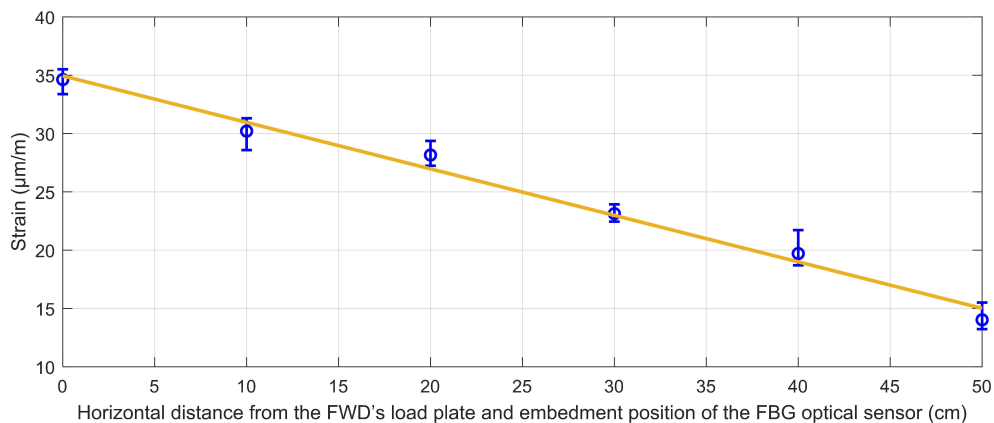
Figure 8. Correlation between the received strain values (measured with FBG strain optical sensor) and FWD's load plate centrum distance position (according to the FBG optical sensors' embedment position).

4.2. Correlation between the Applied Stress and Measured Strain Values

Further into our research, to evaluate the precision of our previously mentioned real-time transport traffic strain measurement experiments (discussed in more detail in Section 5), further repeated tests are made (approximately half a year later from the time of the first experiments) by using the same FWD device. The temperature of the road's cement-treated RAP mixture layer in these experiments is measured by our embedded FBG temperature's optical sensor and is in the range of 24.8–25.1 °C. The effect of the temperature on the received strain amount is explained in more detail in Section 4.3. Here, we position the dropping plate of the FWD device right on the embedment position of the FBG strain optical sensor. Then, by changing the FWD's applied stress values (from 470 kPa to 1170 kPa, with a step of ~200 kPa between the minimal and maximal values), we measure and record the received strain (μm/m) values. For each level of applied stress, 10 drops (5 times in a row, in 2 series) are made. In Figure 9, the received strain (μm/m) values at FWD's generated stress levels (kPa) are shown, as the blue dots with lines represent the average strain and stress values, as well as the strain and stress measurement variation range.
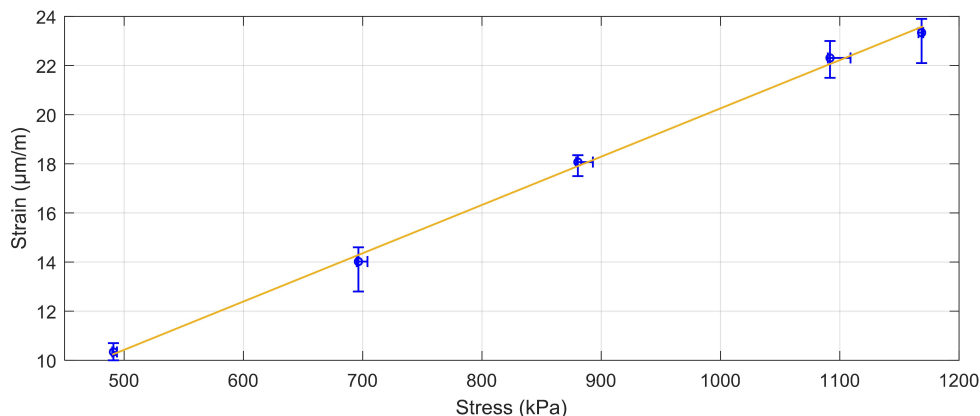

Figure 9. Received average FBG optical strain sensor's strain values (μm/m) for every induced stress (kPa) level made by the FWD device.

As can be seen in Figure 9, a clear linear correlation can be observed between the received FBG optical strain sensor's strain values (μm/m) and the FWD device's induced stress (kPa) level. Numerically, 470 kPa of high stress leads to ~10.3 μm/m amount of strain, while 1170 kPa leads to ~23 μm/m. This means that previously gathered and measured data are accurate enough for SHM monitoring applications. No less important, this also proves that our embedment technique and methods (discussed in Sections 3 and 4) can ensure the proper installment, longevity (at least half a year later, as shown in this research), and received data accuracy of such FBG strain optical sensor's realization in road SHM applications.

4.3. The Effect of Temperature on the Received Strain Values

In this subsection, the received strain values at different temperatures (periods when measurements are taken) are analyzed and compared. The FWD device is positioned right on the embedment position of the FBG strain and temperature sensors. FWD load drops are fixed to 50 kN for each drop. The numerical data gathered aew shown in Table 4.

Table 4. Received strain measurement values induced by the FWD devices versus ambient temperature.

The temperature of the cement-treated RAP mixture layer during the experiments	1–1.5 °C	24.8–25.1 °C
$\Delta\varepsilon$_avg (μm/m)	34.63	13.70
Coefficient of variation (%)	4.26	6.57

As can be seen in Table 4, with the temperature range of 1–1.5 °C (winter time), the received average relative strain value at the recycled layer is 2.5 times higher than at 24.8–25.1 °C (summertime). Such results can be explained by the temperature's effect on the different layers of the road structure. As the environmental temperature decreases, so do the temperatures of the road's layer materials. With lower temperatures, for example, during wintertime, the upper asphalt layers become stiffer, and thus the induced strain by the FWD device (or any other transport traffic vehicle) is more freely carried over to deeper layers of the road's recycled layer. Thereby, a larger amount of the total strain is received at the FBG optical strain sensor that (in this scenario) is embedded in the cement-treated RAP mixture layer. When the environmental temperature has significantly increased (as shown in Table 4), so has the temperature in the upper layers of the road. Then, the upper layers of the road are not as stiff compared to the colder conditions, leading to more dissipation of the applied strain within those layers. Dissipation of the strain then can be observed as a smaller strain amount sensed directly with the FBG strain optical sensor.

5. Real-Time Transport Traffic Strain Monitoring Experiments

As experiments with the FBG strain optical sensor and FWD device approved the stable and correct operation, the next research phase consists of real-time transport traffic strain monitoring experiments. The temperature within the cement-treated RAP mixture layer during experimental measurements varies within a range of 1–1.5 °C. We have measured and recorded traffic that was passing over the road's (specific location mentioned in the Section 3 of this article) pavement above the FBG's embedment position. Moving vehicles there consisted of 2-axle passenger cars and up-to-6-axle heavy trucks. As there are different types of transportation passing the road, to better comprehend the strain-induced changes and their amount, we categorize all of the transport into four classes by the most common transport types passing the specific road. Those classes are: 2-axle passenger cars (Figure 10a), 2-axle minibuses (Figure 10b), 2–3-axle trucks (Figure 10c) and 4–6-axle trucks (Figure 10d–f).
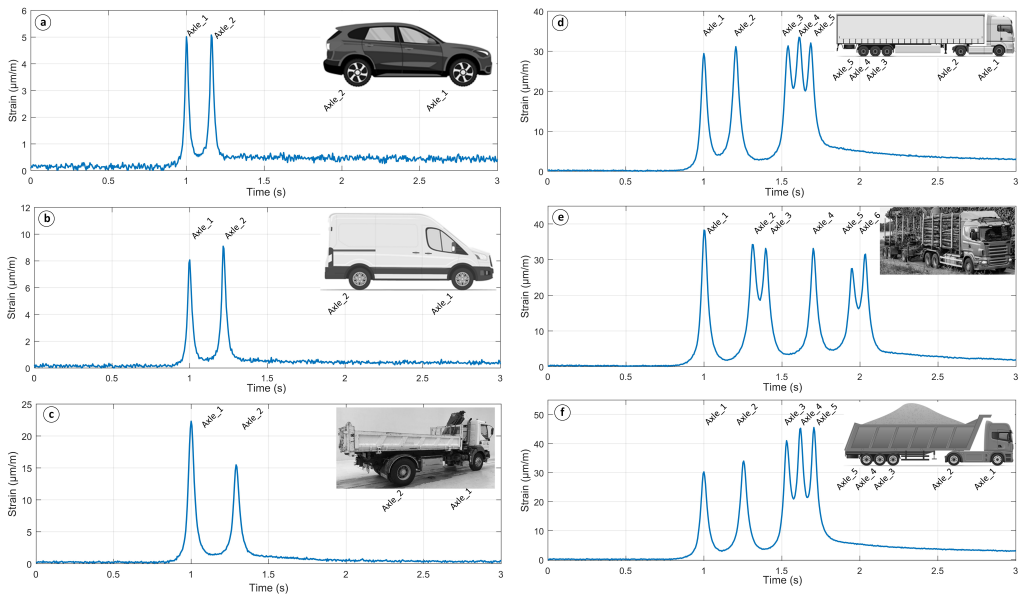
Figure 10. Real-time transport traffic strain measurements and visual data acquired from vehicles passing over the surface of the road where the FBG optical sensor was integrated.

Figure 10. shows typical strain-induced changes (μm/m) in time (s) for all four classes of transport mentioned previously. As seen in Figure 10, an embedded FBG optical strain sensor allows for the precise detection of the strain-induced changes in time for transport with different amounts of axles. It is also possible to evaluate how much strain is induced from each axle of the passing vehicle. For instance, Figure 10a shows the strain measurements made by BMW X5 (distance between axles 2.975 m), where the measured time between the strain peaks (axle points) is 0.164 ms. Based on this data, we can calculate the movement speed of this car as follows:

$$v = \frac{s}{t} = \frac{2.975}{0.164} = 18.14 \left(\frac{\mathrm{m}}{\mathrm{s}} \right) = 65.3 \left(\frac{\mathrm{km}}{\mathrm{h}} \right) \tag{3}$$

Thus, additionally, such realization of FBG optical sensors can provide information about the movement speed of the transport on the road where sensors are used. This valuable data can then be processed for various solutions—not only for the SHM but also to support fiber optic and Internet of Things applications, for instance, in traffic planning and road safety control. It is also important to state that due to the different amounts of induced strain by every axle of the specific vehicle, the relaxation time to reach the 0 strain level after the impact is also diverse. For some lighter (2-axle) vehicles, full relaxation to the zero micro-strain level might typically require up to an additional 3 s since the last contact, while for the heavier vehicles (5+-axle trucks) this is typically up to 5 s. Considering that the strain shift is determined as shown in Figure 8, then the strain-induced relaxation process has no adverse effect on the measurements regarding the induced strain by the next passing vehicle. Thus, it is important to highlight that with high-intensity traffic, the complete relaxation of the strain level might be observed rarely. However, there is a wide range of factors that affect the relaxation process and time. Some of the most important ones include the overall traffic intensity, type of the passing vehicle, its weight, load on each axle, passing trajectory (horizontal distance between the embedded sensor's location and the vehicle's tire) as well as the environmental (material's) temperature.

Numerically, we also estimate the induced strain shift range (μm/m) of the previously mentioned transportations classes (Table 5).

Table 5. Measured induced strain shift range and calculated typical strain shift of real-time transport traffic.

Induced strain shift range (μm/m)	0.7–6	4.6–13	10–38	12–42
Typical (90% event) strain shift range (μm/m)	0.8–4.1	5.5–8.5	11–26	14–36

All of the numerical values put in Table 5 show the strain-induced values for each axle of the specific mode of transportation as the road pavement and specific reference point on the road receive individual axle's induced strain at one particular moment. However, as the mass of a specific vehicle depends on the brand and type of it, as well as the cargo carried, some of these values are clearly out of the typical measurement range (compared to other vehicles in their transport class) and are very unique. Thus, to better understand the more common strain-induced shift values, a typical strain (90% events) shift range (μm/m) is also calculated. For 2-axle passenger cars, it is 0.8–4.1 μm/m, for 2-axle minibuses 5.5–8.5 μm/m, for 2–3-axle trucks 11–26 μm/m, but for 4–6-axle trucks it is 14–36 μm/m per each axle.

For comparison, as seen in Table 5, the axle of the passenger car typically induces approximately 2–10 times less strain than the axle of the 2-axle minibus. Meanwhile, typically, axles of the passenger car induces approximately 3–45 times less strain than the axle of a heavy 4–6-axle truck.

6. Conclusions

Pavement SHM applications completed by realizing fiber optical sensors not only assists in making appropriate decisions for planning maintenance and reconstruction works but also validates the proposed design solution. Such an aspect is gaining increased importance since new materials and structural layers are introduced under changing traffic volumes and road loading conditions.

This research approved the successful integration of the FBG optical strain and temperature sensors that were embedded during the construction of a road of national importance. FBG sensors were integrated within the permanent infrastructure—into the cement-treated RAP mixture layer (220 mm deep). Short-term and long-term experiments with the FWD device and real-time transport traffic were carried out over half a year. We calculated and concluded that the received strain levels in this particular configuration are dependent upon various factors. The major ones are the horizontal distance from the embedment position of the optical strain sensor and strain inducer (FWD or real-time transport traffic in this research), the amount and intensity of the load that induces strain, and last but not least—the temperature of the environment (road layers).

As described in the article, by using the FWD, we concluded that the received strain amount decreases with the additional distance further away from the optical sensor, showing a 14.03 μm/m large strain when the load plate is 50 cm further away from the embedment position. This means that a 50 cm large horizontal distance decreased the average detected strain shift value by approximately 20.60 μm/m compared to the highest (starting) value (34.63 μm/m) recorded on top of the embedment position. In addition, by changing the applied stress values of the FWD (from 470 kPa to 1170 kPa), we concluded that 470 kPa

high stress leads to ~10.3 μm/m for the amount of received strain, while 1170 kPa leads to ~23 μm/m when the stress is induced on top of the embedment position. As for the real-time transport traffic—2-axle passenger cars generated 0.8–4.1 μm/m large strain per axle, 2-axle minibuses 5.5–8.5 μm/m, 2–3-axle trucks 11–26 μm/m, but 4–6-axle trucks 14–36 μm/m per each axle. The axle of a passenger car induced approximately 2–10 times less strain than the axle of a 2-axle minibus. Meanwhile, the axle of the passenger car induces approximately 3–45 times less strain than the axle of a heavy 4–6-axle truck. As for the recycled layer's temperature factor, we estimated that the temperature range of 1–1.5 °C (winter time) leads to the received average relative strain values that are 2.5 times higher than the ones recorded when the temperature is ranging between 24.8–25.1 °C (summertime). As explained in the article, different temperatures determine the stiffness of the road's upper layers, and thus also the number of received strain values.

The sensing setup developed, the methods described and used, and the components utilized can be realized for further large-scale FBG optical strain and temperature realizations within the construction of road infrastructure, thus providing for the capability to use, study and develop the road SHM industry as well as other spheres where such solutions are appealing.

Author Contributions: Conceptualization, J.B., P.S., U.S., R.J., S.S. and V.B.; methodology, J.B., P.S. and U.S.; software, J.B., S.S., U.S. and P.S.; validation, J.B., U.S., P.S. and S.S.; formal analysis, S.S., P.S., R.J. and J.P; investigation, J.B., P.S., U.S. and J.P.; resources, P.S., U.S. and J.B.; data curation, J.B.; writing—original draft preparation, J.B., U.S. and P.S.; writing—review and editing, U.S, J.B., P.S., R.J. and S.S.; visualization, J.B., U.S. and P.S.; supervision, J.B, P.S., U.S., S.S. and V.B.; project administration, S.S., V.B. and J.P.; funding acquisition, J.P., S.S. and V.B. All authors have read and agreed to the published version of the manuscript.

Data Availability Statement: The data used to support the findings of this study are available from the first author upon request.

Conflicts of Interest: The authors declare that there is no conflict of interest regarding the publication of this paper.

References

1. SJSC Latvian State Roads, State Road Network Statistics. Available online: https://lvceli.lv/wp-content/uploads/2021/07/LVC-Statistika-2020-20210729-1335.pdf (accessed on 24 May 2022).
2. Fan, L.; Bao, Y. Review of fiber optic sensors for corrosion monitoring in reinforced concrete. *Cem. Concr. Compos.* **2021**, *120*, 104029. [CrossRef]
3. Budnicki, D.; Parola, I.; Szostkiewicz, Ł.; Markiewicz, K.; Hołdyński, Z.; Wojcik, G.; Makara, M.; Poturaj, K.; Kuklińska, M.; Mergo, P.; et al. All-Fiber Vector Bending Sensor Based on a Multicore Fiber With Asymmetric Air-Hole Structure. *J. Light. Technol.* **2020**, *38*, 6685–6690. [CrossRef]
4. Ekechukwu, G.K.; Sharma, J. Well-scale demonstration of distributed pressure sensing using fiber-optic DAS and DTS. *Sci. Rep.* **2021**, *11*, 12505. [CrossRef] [PubMed]
5. Lu, F.; Wright, R.; Lu, P.; Cvetic, P.C.; Ohodnicki, P.R. Distributed fiber optic pH sensors using sol-gel silica based sensitive materials. *Sens. Actuators B Chem.* **2021**, *340*, 129853. [CrossRef]
6. Liu, Y.; Zhou, A.; Yuan, L. Multifunctional fiber-optic sensor, based on helix structure and fiber Bragg gratings, for shape sensing. *Opt. Laser Technol.* **2021**, *143*, 107327. [CrossRef]
7. Senkans, U.; Braunfelds, J.; Lyashuk, I.; Porins, J.; Spolitis, S.; Bobrovs, V. Research on FBG-Based Sensor Networks and Their Coexistence with Fiber Optical Transmission Systems. *J. Sens.* **2019**, *2019*, 6459387. [CrossRef]

8. Zheng, X.; Shi, B.; Zhang, C.C.; Sun, Y.; Zhang, L.; Han, H. Strain transfer mechanism in surface-bonded distributed fiber-optic sensors subjected to linear strain gradients: Theoretical modeling and experimental validation. *Measurement* **2021**, *179*, 109510. [CrossRef]
9. He, C.; Korposh, S.; Correia, R.; Liu, L.; Hayes-Gill, B.R.; Morgan, S.P. Optical fibre sensor for simultaneous temperature and relative humidity measurement: Towards absolute humidity evaluation. *Sens. Actuators B Chem.* **2021**, *344*, 130154. [CrossRef]
10. Wijaya, H.; Rajeev, P.; Gad, E. Distributed optical fibre sensor for infrastructure monitoring: Field applications. *Opt. Fiber Technol.* **2021**, *64*, 102577. [CrossRef]
11. Lenner, M.; Frank, A.; Yang, L.; Roininen, T.M.; Bohnert, K. Long-Term Reliability of Fiber-Optic Current Sensors. *IEEE Sens. J.* **2020**, *20*, 823–832. [CrossRef]
12. Bašić, P. Fiber Optic Sensor Cable Based on Hollow Capillary Tube with Three Tightly Encapsulated Optical Fibers. In Proceedings of the 2nd International Colloquium on Smart Grid Metrology, Split, Croatia, 9–12 April 2019; pp. 1–4.
13. Kerrouche, A.; Najeh, T.; Jaen-Sola, P. Experimental Strain Measurement Approach Using Fiber Bragg Grating Sensors for Monitoring of Railway Switches and Crossings. *Sensors* **2021**, *21*, 3639. [CrossRef] [PubMed]
14. Braunfelds, J.; Senkans, U.; Skels, P.; Janeliukstis, R.; Salgals, T.; Redka, D.; Lyashuk, I.; Porins, J.; Spolitis, S.; Haritonovs, V.; et al. FBG-Based Sensing for Structural Health Monitoring of Road Infrastructure. *J. Sens.* **2021**, *2021*, 8850368. [CrossRef]
15. Wang, H.; Gao, S.; Yue, X.; Cheng, X.; Liu, Q.; Min, R.; Qu, H.; Hu, X. Humidity-Sensitive PMMA Fiber Bragg Grating Sensor Probe for Soil Temperature and Moisture Measurement Based on Its Intrinsic Water Affinity. *Sensors* **2021**, *21*, 6946. [CrossRef]
16. Shu, Q.; Wu, L.; Lu, S.; Xiao, W. High-sensitivity structure based on fiber Bragg grating sensor and its application in nonintrusive detection of pipeline pressure change. *Measurement* **2022**, *189*, 110444. [CrossRef]
17. Montanini, R. Wavelength-encoded optical psychrometer for relative humidity measurement. *Rev. Sci. Instrum.* **2007**, *78*, 025103. [CrossRef] [PubMed]
18. Cheng, L.; Zhang, A.; Cao, B.; Yang, J.; Hu, L.; Li, Y. An experimental study on monitoring the phreatic line of an embankment dam based on temperature detection by OFDR. *Opt. Fiber Technol.* **2021**, *63*, 102510. [CrossRef]
19. Song, H.; Pei, H.; Zhu, H. Monitoring of tunnel excavation based on the fiber Bragg grating sensing technology. *J. Int. Meas. Confed.* **2021**, *169*, 108334. [CrossRef]
20. Cocking, S.; Alexakis, H.; DeJong, M. Distributed dynamic fibre-optic strain monitoring of the behaviour of a skewed masonry arch railway bridge. *J. Civ. Struct. Health Monit.* **2021**, *11*, 989–1012. [CrossRef]
21. Yüksel, K.; Kinet, D.; Moeyaert, V.; Kouroussis, G.; Caucheteur, C. Railway monitoring system using optical fiber grating accelerometers. *Smart Mater. Struct.* **2018**, *27*, 105033. [CrossRef]
22. Bado, M.F.; Casas, J.R. A Review of Recent Distributed Optical Fiber Sensors Applications for Civil Engineering Structural Health Monitoring. *Sensors* **2021**, *21*, 1818. [CrossRef]
23. ES-01 Embeddable Strain Sensor. Available online: https://www.sylex.sk/wp-content/uploads/2018/09/ES-01-Embeddable-strain-sensor.pdf (accessed on 24 May 2022).
24. Ullidtz, P. *Modelling Flexible Pavement Response and Performance*; Polyteknisk Forlag: Lyngby, Denmark, 1998.
25. Korkiala-Tanttu, L. *Calculation Method for Permanent Deformation of Unbound Pavement Materials*; VTT Technical Research Centre of Finland: Espoo, Finland, 2008.
26. Saevarsdottir, T.; Erlingsson, S. Deformation modelling of instrumented flexible pavement structure. *Procedia Eng.* **2016**, *143*, 937–944. [CrossRef]

Braunfelds J., Senkans U., Skels P., Murans I., Porins J., Spolitis S., Bobrovs V. Fiber Bragg Grating Optical Sensors for Road Infrastructure Monitoring Applications, Applied Industrial Optics, **2022**, pp.1-2.

Fiber Bragg Grating Optical Sensors for Road Infrastructure Monitoring Applications

J. Braunfelds[1,2], U. Senkans[1], P. Skels[3], I. Murans[2], J. Porins[1], S. Spolitis[1,2], V. Bobrovs[1]

[1]*Institute of Telecommunications, Riga Technical University, Riga, Latvia.*
[2]*Communication Technologies Research Center, Riga Technical University, Riga, Latvia.*
[3]*Department of Roads and Bridges Riga Technical University, Riga, Latvia.*
Author e-mail address: janis.braunfelds@rtu.lv; ugis.senkans@rtu.lv; peteris.skels_1@rtu.lv; ints.murans@rtu.lv; jurgis.porins@rtu.lv; sandis.spolitis@rtu.lv; vjaceslavs.bobrovs@rtu.lv.

Abstract: Application of fiber Bragg grating (FBG) optical sensors for road infrastructure allows to use the measured data for transport traffic monitoring, structural health monitoring applications, architecture's structural integrity estimation and temperature monitoring. © 2022 The Author(s)

1. Introduction

Fiber optical sensors, especially those that utilize fiber Bragg grating technology are topical research area for different applications and industries, for instance, automotive sector [1], structural health monitoring (SHM) solutions [2], energy industry [3] etc. Mainly due to the optical sensors' various advantages, such as robustness [4,5], remote long-distance realization capabilities [6], immunity to electromagnetic interference [5] and so on, provides an opportunity for efficient realization in modern industries. Capability to measure wide range of physical parameters, for example, strain [5], temperature [5,7] and pressure [5], allows to use FBG optical sensors for precise and accurate data measurements and provide parameter compensation, when applicable.

Previous studies show that FBGs' can be realized for crack detection of reinforced concrete structures [9], thus also suggesting the further investigation possibilities of FBGs application for road infrastructure as shown in this article. In addition to that, as proved by our researchers - FBG optical sensor networks can be successfully unified with the fiber optical data transmission systems [8], showing that optical sensors can be integrated into modern data transmission metro and metro-access communication systems. Such opportunity is appealing for FBG optical sensors' embedment in the road architecture, as it would provide the media for sensing data transmission over the built optical links. In our research, during the construction process of permanent road architecture, we have successfully embedded and installed FBG strain and temperature optical sensors within the road layers, discussed in more details in further sections. Thereby allowing for short-term (real-time transportation traffic induced strain) and long-term (comprehensive structural health monitoring) measured data acquisition and experiments.

2. Experimental measurement setup and results

The integration of optical FBG strain and temperature sensors was realized into road pavement's recycled (depth 225 mm) and middle of asphalt layers - AC22 (asphalt concrete) layer (depth 65 mm) with geographical location in one of the largest Latvian road sites A8 (A8 Riga-Jelgava-Meitene border km 19.20 – 29.95 km), see in fig. 1.

Table 1.   FBG sensors main parameters

Measured parameter	Central wavelength	Measurement range	Accuracy
Strain	1552.8 nm	-5000 to 5000 $\mu\varepsilon$	<0.23% FS*
Temperature	1554.558 nm	-40°C to 120°C	±0.3°C

Optical FBG strain and temperature sensors integration in the road pavement
Fig.1. Setup of FBG sensors integration and measurement process

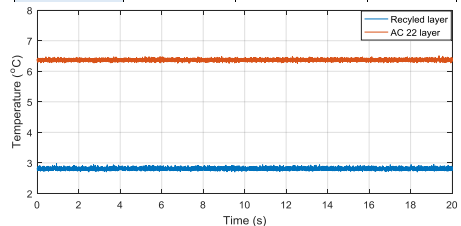

Fig.2. Real-time temperature measurements data of the road where FBG optical sensors were integrated
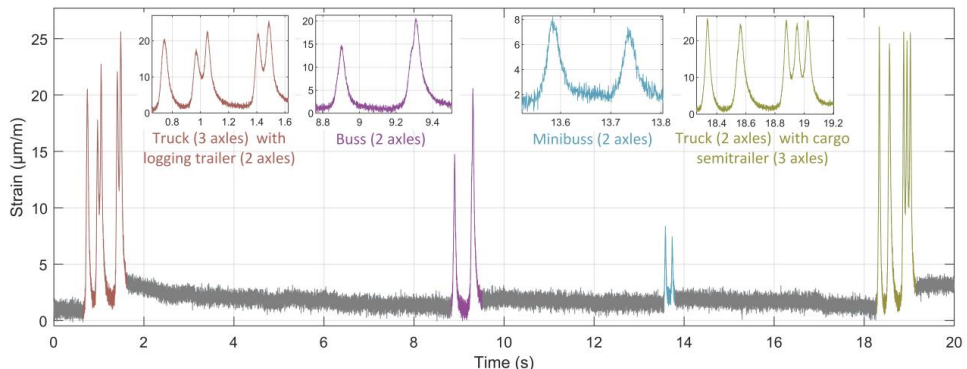
Fig.3. Real-time traffic strain measurements data acquired from vehicles passing over the surface of the road where FBG optical sensors were integrated (recycled layer).

FBG sensors are embedded that way so that the vehicles passing over the road would almost certainly be detected and strain - measured. For temperature and strain measurements, FBG sensors interrogation unit is used, and for data analysis – a computer. FBG sensors' main parameters are summarized in Table.1. Measurements are realized in March 2022, during morning time, when air temperature is 8.5 ℃, but asphalt's surface temperature is 7 ℃. As we can see in Fig.2 recycled layer temperature is 2.8 ℃, but AC22 layer 6.4 ℃. During night time, as the environmental temperature decreases – so does the temperature for whole road infrastructure. However, during day time, temperature firstly increase in the upper asphalt layer and only then, in deeper recycled layer.

As we can see in Fig.3., the FBG sensors are very sensitive and can detect strain values for each vehicles' axle in real-time. Fig.3. represents only short time slot from all the measurement sessions. Vehicles there move at an average speed of 50-70 km/h. The highest relative strain values are detected for truck ($axle_1$=25μm/m; $axle_2$=23.4 μm/m) with semitrailer ($axle_1$=24 μm/m; $axle_2$=23.6 μm/m; $axle_3$=23.9 μm/m). Based on this data, we can conclude that load on the axles is proportionally balanced and is similar. Relatively high strain value is detected for buss ($axle_1$=13.2; $axle_2$=19.6), because all the load is divided to 2 axles.

Conclusion

Experiments and measured results are very topical to local and international road pavement designers and road management services to forecast the potential collapse of the road, permanent deformation, weight of the vehicles and number of their axles, as well as for traffic monitoring, and road pavement temperature monitoring. These data also can be used for smart road solutions for traffic flow analysis, vehicle counting and free parking lots analysis.

Acknowledgment

References

[1] Falcetelli F, Martini A, Di Sante R, Troncossi M. Strain Modal Testing with Fiber Bragg Gratings for Automotive Applications. Sensors. 2022; 22(3):946. https://doi.org/10.3390/s22030946

[2] Soman R, Wee J, Peters K. Optical Fiber Sensors for Ultrasonic Structural Health Monitoring: A Review. Sensors. 2021; 21(21):7345. https://doi.org/10.3390/s21217345

[3] Rong Q. and Qiao X., "FBG for Oil and Gas Exploration," J. Lightwave Technol. 37, 2502-2515 (2019)

[4] Li J. W., Chan M. H., Yang Z. Q., Manie Y. C. and Peng P. C., "Robust Remote Sensing FBG Sensor System Using Bidirectional-EDFA Techniques," 2021 IEEE International Conference on Consumer Electronics-Taiwan, 2021, pp. 1-2, doi: 10.1109/ICCE-TW52618.2021.9602898.

[5] He J., Xu B., Ju S., Hou M., Guo K., Xu X., Wang Y., Liu S., and Wang Y., "Temperature-insensitive directional transverse load sensor based on dual side-hole fiber Bragg grating," Opt. Express 29, 17700-17709 (2021)

[6] Hayle S.T., Guo B. Y., Manie Y. C., Hsu Y. T., Li J. W. and Peng P.C., "Long-distance FBG Sensor System for Remote Sensing and Internet of Things (IoT) Applications," 2020 IEEE International Conference on Consumer Electronics - Taiwan (ICCE-Taiwan), 2020, pp. 1-2, doi: 10.1109/ICCE-Taiwan49838.2020.9258336

[7] Guo H. Y., Wang Z. B., Li H. Y., "Development and Commissioning of High Temperature FBG Solid Pressure Sensors", Journal of Sensors, vol. 2018, Article ID 2056452, 8 pages, 2018. https://doi.org/10.1155/2018/2056452

[8] Zhang Q., Xiong Z., "Crack Detection of Reinforced Concrete Structures Based on BOFDA and FBG Sensors", Shock and Vibration, vol. 2018, Article ID 6563537, 10 pages, 2018. https://doi.org/10.1155/2018/6563537

[9] Senkans U., Braunfelds J, Lyashuk I., Porins J., Spolitis S., Bobrovs V., "Research on FBG-Based Sensor Networks and Their Coexistence with Fiber Optical Transmission Systems", Journal of Sensors, vol. 2019, 13, 2019. https://doi.org/10.1155/2019/6459387

Jānis Braunfelds dzimis 1994. gadā Talsos. Rīgas Tehniskajā universitā- tē (RTU) ieguvis inženierzinātņu bakalaura grādu elektrozinātnē (2016) un inženierzinātņu maģistra grādu telekomunikācijās (2018). Kopš 2016. gada strādā RTU, ieņemot zinātniskā asistenta amatu. Patla- ban ir RTU pētnieks un lektors. Kopš 2019. gada 1. decembra ir Elektro- nikas un telekomunikāciju fakultātes domes loceklis, kopš 2021. gada 4. janvāra – RTU Zinātnes padomes loceklis, kopš 2022. gada 1. marta – RTU padomes loceklis.

Stažējies Eindhovenas Tehniskās universitātes Fotonikas integrācijas institūtā Nīderlandē un Dānijas Tehniskajā universitātē. Saņēmis vairā- kus apbalvojumus: Latvijas Drošības un aizsardzības industriju federā- cijas Gada balvu zinātnē un pētniecībā (2019); RTU Studenta parlamen- ta balvu "Gada fakultātes studentu atbalsts 2019", Latvijas Studentu apvienības balvu "Gada jaunais zinātnieks 2020"; "RTU Studentu gada balvu valorizācijā 2020".